N-H···X (X=O, N, π) Hydrogen-bonded Interactions of Pyrrole: Matrix Isolation Infrared and Computational Studies

By

Shubhra Sarkar

Enrolment Number: CHEM 02 2015 04 010

Indira Gandhi Centre for Atomic Research, Kalpakkam

A thesis submitted to the

Board of Studies in Chemical Sciences in partial,

Fulfillment of requirements

for the Degree of

DOCTOR OF PHILOSOPHY

of

HOMI BHABHA NATIONAL INSTITUTE

March 2021

Homi Bhabha National Institute

Recommendations of the Viva Voce Committee

As members of the Viva Voce Committee, we certify that we have read the dissertation prepared by ***Shubhra Sarkar*** entitled "**N-H···X (X=O, N, π) Hydrogen-bonded Interactions of Pyrrole: Matrix Isolation Infrared and Computational Studies**" and recommend that it may be accepted as fulfilling the thesis requirement for the award of Degree of Doctor of Philosophy.

Chairman – Prof. T. R. Ravindran Ravindran 15/3/2021

Guide / Convener – Dr. K. Sundararajan 15/3/2021

Examiner - Dr. Bhalamurugan Sivaraman 15th MAR '21

Member 1- Prof. M. Joseph 15/3/21

Member 2- Prof. D. Ponraju D. Pon 15/3/2021

Final approval and acceptance of this thesis is contingent upon the candidate's submission of the final copies of the thesis to HBNI.

I hereby certify that I have read this thesis prepared under my direction and recommend that it may be accepted as fulfilling the thesis requirement.

Date: 15/3/2021

Place: Kalpukkam

Signature:

Guide: K SUNDARARAJAN

STATEMENT BY AUTHOR

This dissertation has been submitted in partial fulfillment of requirements for an advanced degree at Homi Bhabha National Institute (HBNI) and is deposited in the Library to be made available to borrowers under rules of the HBNI. Brief quotations from this dissertation are allowable without special permission, provided that accurate acknowledgement of source is made. Requests for permission for extended quotation from or reproduction of this manuscript in whole or in part may be granted by the Competent Authority of HBNI when in his or her judgment the proposed use of the material is in the interests of scholarship. In all other instances, permissions may be sought from the author.

Shubhra Sarkar

Shubhra Sarkar

DECLARATION BY THE AUTHOR

I, hereby declare that the investigation presented in the thesis has been carried out by me. The work is original and has not been submitted earlier as a whole or in part for a degree / diploma at this or any other Institution / University.

Shubhra Sarkar

Shubhra Sarkar

List of Publications arising from the thesis

Journals

Published:

1. Pyrrole Multimers and Pyrrole-Acetylene Hydrogen Bonded Complexes Studied in N_2 and *para*-H_2 Matrixes Using Matrix Isolation Infrared Spectroscopy and *ab initio* Computations.

Shubhra Sarkar, N. Ramanathan, R. Gopi, K. Sundararajan, *J. Mol. Struct.*, **2017**, 1149, 387-403.

2. Effect of Methyl Substitution on the N-H⋯O Interaction in Complexes of Pyrrole with Water, Methanol and Dimethyl ether: Matrix Isolation Infrared Spectroscopy and *ab initio* Computational Studies.

Shubhra Sarkar, N. Ramanathan, K. Sundararajan, *J. Phys. Chem. A*, **2018**, 122, 2445-2460.

3. Experimental Evidence of Synergistic Interactions in Pyrrole-Phenol Complexes at Low Temperatures under Isolated Conditions.

Shubhra Sarkar, N. Ramanathan, K. Sundararajan, *J. Phys. Chem. A*, **2018**, 122, 9073-9083.

4. Conformations of Diethyl ether and its Interaction with Pyrrole at Low Temperatures.

Shubhra Sarkar, N. Ramanathan, P. K. Sruthi, K. Sundararajan, *Spectrochim. Acta A*, **2019**, 213, 361-369.

5. Experimental Evidence of N–H⋯N Hydrogen Bonding in the Heterodimers of Pyrrole with Nitrogen Bases.

Shubhra Sarkar, P. K. Sruthi, N. Ramanathan, K. Sundararajan, *J. Mol. Struc.*, **2019**, 1204, 127511.

6. Computational and Experimental Evidence of N-H⋯π and Cooperative $\pi_N \cdots \pi^*$ Interactions in Pyrrole⋯Benzene and Pyrrole⋯Ethylene Heterodimers at Low Temperatures.

Shubhra Sarkar, N. Ramanathan, P. K. Sruthi, K. Sundararajan, *J. Mol. Struc.*, **2020**, 1209, 127983(1-17).

Other Publications (Not to be included in this thesis)

1. Photolysis of PCl_3/$POCl_3$ with Oxygen Dopant Using 193 nm ArF Excimer at Low Temperatures: Oxygen Insertion through ‘Phosphadioxirane’ Pathway.

N. Ramanathan, Shubhra Sarkar, K. Sankaran, K. Sundararajan, *ChemistrySelect*, **2019**, 4, 417.

2. Influence of Branching on the Conformational Space: Case Study of Tri-sec-butyl Phosphate Using Matrix Isolation Infrared Spectroscopy and DFT Computations.

N. Ramanathan, Shubhra Sarkar, K. Sundararajan, Aditi Chandrasekar, K. Sankaran, A. Suresh, *J. Phys. Chem. A*, **2018**, 122, 8229-8242.

3. Pentavalent Phosphorus as a Unique Phosphorus Donor in $POCl_3$ Homodimer and $POCl_3$–H_2O Heterodimer: Matrix Isolation Infrared Spectroscopic and Computational Studies.

P. K. Sruthi, N. Ramanathan, Shubhra Sarkar, K. Sundararajan, *Phys. Chem. Chem. Phys*., **2018**, 20, 22058-22075.

4. Elusive Hypervalent Phosphorus···π Interactions: Evidence for Paradigm Transformation from Hydrogen to Phosphorus Bonding at Low Temperatures.

P. K. Sruthi, Shubhra Sarkar, N. Ramanathan, K. Sundararajan, *Phys. Chem. Chem. Phys*., **2019**, 21, 12250-12264.

5. Prototypical Cyclohexane Dimers: Spectroscopic Evidence for σ-Stacking at Low Temperatures.

N. Ramanathan, Shubhra Sarkar, K. Sundararajan, *Phys. Chem. Chem. Phys.*, **2020**, 22, 905-913.

6. Exploring Reactive Species of Chlorocarbons and Evidence for the Formation of Oxygen Atoms and Ozone at Low Temperatures Using the *'In House'* Developed Electron Gun Assembly.

N. Ramanathan, K. Sundararajan, Shubhra Sarkar, P. K. Sruthi, *Chem. Phys*., **2019**, 525, 110389(1-9).

7. Strong Proton-Shared Hydrogen Bonding in a Methyl Imidazole···HCl Complex: Evidence from Matrix Isolation Infrared Spectroscopy and *ab initio* Computations.

Shubhra Sarkar, P. K. Sruthi, N. Ramanathan, K. Sundararajan, *New J. Chem.*, **2020**, 44, 7116-7128.

8. Experimental Evidence for Pentavalent phosphorous bonded P···Cl Interactions in Phosphoryl Chloride-Halocarbon Heterodimers at Low Temperatures.

P. K. Sruthi, Shubhra Sarkar, N. Ramanathan, K. Sundararajan. *Communicated to Chemical Physics* (Under review).

9. A Flickering Tale of Bonding between Pyrrole and PCl_3. Shubhra Sarkar, Swaroop Chandra, N. Ramanathan, K. Sundararajan, (*Manuscript under preparation*).

10. Multifaceted Interactions of Pyrrole: a Matrix Isolation Infrared Spectroscopy and Electron Density Analysis. Shubhra Sarkar, N. Ramanathan, P. K. Sruthi, K. Sundararajan (*Manuscript under preparation*).

Conference Presentations:

1. Pyrrole Multimers and Pyrrole-Acetylene Complexes studied in N_2 and *para*-H_2 matrixes using Matrix Isolation Infrared Spectroscopy.

Shubhra Sarkar, R. Gopi, N. Ramanathan, K. Sundararajan

(Presented as Poster at International Conference on the Perspectives of Vibrational Spectroscopy **2016**)

2. Probing N-H···O interactions in Pyrrole with Water and Methanol systems using Matrix Isolation Infrared Spectroscopy and *ab initio* studies.

Shubhra Sarkar, N. Ramanathan, K. Sundararajan

(Presented as Poster in International Conference on Spectroscopy of Biomolecules and Advanced Materials, Christian College, Chengannur, Kerala, 4-7 October **2017**)

3. (a) Pyrrole-Phenol Complexes in Nitrogen matrix.

Shubhra Sarkar, N. Ramanathan, K. Sundararajan

(Oral presentation in Astrochemistry in Terahertz, Chennai, 30-31 October **2017**)

(b) Interaction of phosphorus chloride with water and its dimerization.

Sruthi P. K., N. Ramanathan, *Shubhra Sarkar,* K. Sundararajan

(Oral presentation in Astrochemistry in Terahertz, Chennai, 30-31 October **2017**)

4. Can PCl_3 interact through Phosphorous with π-cloud of Pyrrole?

Shubhra Sarkar, N. Ramanathan, K. Sundararajan

(Presented as Poster in Research Scholars Meet on Materials Science and Engineering of Nuclear Materials, Indira Gandhi Centre for Atomic Research, Kalpakkam, 7-9 May **2018**)

5. (a) Comparative study on the hydrogen bonded heterodimers of Pyrrole with Ammonia and Pyridine: A Matrix Isolation FTIR spectroscopy and *ab initio* study.

Shubhra Sarkar, P. K. Sruthi, N. Ramanathan, K. Sundararajan

(Oral presentation in National Conference on Advances in Spectroscopy: Molecules to Materials, Institute of Infrastructure, Technology, Research and Management (IITRAM), Ahmedabad, 4-6 October **2018**)

(b) Exploration of phosphorus bonding in unsaturated carbon systems with Phosphoryl Chloride: A matrix isolation infrared spectroscopy and *ab initio* computations.

Sruthi P. K., *Shubhra Sarkar*, N. Ramanathan, K. Sundararajan

(Poster presentation in National Conference on Advances in Spectroscopy: Molecules to Materials, Institute of Infrastructure Technology Research and Management (IITRAM), Ahmedabad, Gujarat, 4-6 October **2018**).

6. (a) N-H…O Interactions of pyrrole at Low Temperatures.

Shubhra Sarkar, N. Ramanathan, P. K. Sruthi, K. Sundararajan

(Oral presentation in National Conference on Light Matter Interaction at Nanoscale, Indira Gandhi Centre for Atomic Research, Kalpakkam, 15-17 July **2019**)

(b) Pentavalent Phosphorus bonding interaction of $POCl_3$ with Carbon tetrachloride, Methylene Chloride: A matrix isolation infrared spectroscopy and *ab initio* computations.

Sruthi P. K, *Shubhra Sarkar*, N. Ramanathan, K. Sundararajan

(Oral presentation in National Conference on Light Matter Interaction at Nanoscale (LMIN), Indira Gandhi Center for Atomic Research (IGCAR), Kalpakkam, Chennai, 15-17 July **2019**)

7. Multifaceted Interactions of Pyrrole.

Shubhra Sarkar, N. Ramanathan, K. Sundararajan

(Oral and Poster presentations at 23rd International Conference on "Horizons in Hydrogen Bond Research" (HBOND2019), Vrije Universiteit Amsterdam, the Netherlands, 24-27 September **2019**)

8. Revisiting the Pyrrole-Benzene Heterodimer: T-shaped structure or a partial π stacked structure?

Shubhra Sarkar, N. Ramanathan, P. K. Sruthi, K. Sundararajan

(Poster Presentation at the 17th Conference on Spectroscopy and Dynamics of Molecular Clusters (SDMC 2020), Fateh Safari Lodge, Kumbhalgarh, near Udaipur, Rajasthan, on 20th to 23rd February, **2020**).

Shubhra Sarkar

Shubhra Sarkar

Dedicated to my beloved Parents and Husband

And

To the Frontline Warriors of COVID19

Acknowledgements

I would take the opportunity to convey my whole-hearted thanks to my supervisor Dr. K. Sundararajan. This thesis would not have been possible without his tactful guidance, understanding, invaluable inputs, timely corrections, unflinching support and advices- both on academic and personal fronts. I really consider myself lucky to have been under the careful supervision of a person like him. I deeply acknowledge the valuable inputs and scientific discussions with Dr. N. Ramanathan. His dedication towards science was always awe-inspiring, which in turn instilled in me the passion for addressing new findings in non-covalent interactions. I am grateful to my Doctoral Committee Chairman Prof. T. R. Ravindran, and members Prof. M. Joseph and Prof. D. Ponraju for their constant motivation and timely evaluation at each stage of my research. I sincerely convey my gratitude to Prof. N. Sivaraman, former Dean, Chemical Sciences and Director, MC&MFCG, for his constant support, encouragement and providing excellent research facilities and scientific atmosphere at Chemistry Group. I am grateful to Dr. C. V. S. Brahmananda Rao, Dean-Chemical Sciences, for helping me with the paperwork and encouragement. I express my thanks to Prof. A. K. Bhaduri, Director, IGCAR, for providing me with the research facilities and allowing me to stay at JRF Enclave. I convey my gratitude to Dr. Vidya Sundararajan, Dean, Student Affairs, for her constant encouragement since the dawn of my PhD tenure, and for providing adequate facilities at JRF Enclave.

I am grateful to Department of Atomic Energy, India for providing a research fellowship.

I want to show my gratitude to Dr. K. Sankaran, former Head, Analytical Chemistry and Spectroscopy Section, for helping me to carry on the research and avail the facilities in the initial stages of my tenure. I have always enjoyed his brilliant presence in the lab and outstanding knowledge in matrix isolation technique and spectroscopy. My sincere thanks to Dr. Siuli Maji Gayen, Dr. Pavan Kr. Narayanam and Dr. Satendra Kumar for academic and scientific discussions, and for imparting their knowledge to me in Spectroscopy and Lasers. I am grateful to Mr. T. Ramamurthy for helping me to bring Liquid Nitrogen essential for my experiments from the plant, whenever required.

My deep regards to my former senior lab members Dr. Vijayalakshmi, Mrs. Hemalatha, Mrs. Uma Maheshwari, Mr. Sriram, Mr. J. K. Sekar, Mrs. Usha Lakshmi and Mrs. Annapoorani for their support, motivation and the good times we had spent together.

I thank Mrs. Hemalatha for helping me to procure important chemicals for my research experiments.

I am thankful to Dr. Gopi Raghupathy, who was my senior, for teaching me the Matrix Isolation technique, helping me with the research work, invaluable scientific discussions and constant encouragement. I also enjoyed playing badminton with him in the first year. I want to thank my brilliant juniors Sruti, Swaroop, Rini, Surya and Nandalal for extensive discussions on science, and for the amusing moments, both inside and outside lab.

I cannot thank all my friends enough, and especially the ones I made during my PhD tenure. Without their constant presence, motivation, love, care and support, it would not have been feasible. They have been the mentors and role models whose positive influence kept me going. All the times spent together will forever, be etched in my heart. I was lucky to have my pet dog, Teenu and pet cat, Bulbuli who are my family and dependents at JRF Enclave and made me feel needed every single day.

Last but not the least, I am grateful to my family, my father Late Sushil Chandra Sarkar, my mother Mrs. Ratna Sarkar and brother Mr. Sudipto Sarkar for their sacrifices, blessings and faith on me. My heartfelt thanks to my husband, Mr. Janajit Bagchi, who has always been a friend in need, a guardian, an adviser, and supported me in all situations with patience and unconditional love. I am also grateful to my father-in-law Mr. Tushar Bagchi and mother-in-law Mrs. Santasri Bagchi for their blessings, care, moral support, and for staying with me during the time of thesis writing.

Shubhra Sarkar

Shubhra Sarkar

Table of Contents

List of Figures

List of Tables

Chapter 7 Summary and Future Scope of Thesis

7.1 Summary

The final chapter summarises the experimental and theoretical results of multifaceted interactions of pyrrole with number of proton donors and acceptors using matrix isolation infrared spectroscopy and adequately supported by *ab initio* and DFT computational methodologies. Since, pyrrole can show dichotomic behavior as proton donor and acceptor through N-H bond and aromatic electron cloud, respectively, a variety of non-covalent complexes can be formed with different electron donors. The N-H···π interaction of C_4H_5N was studied with C_2H_2, C_2H_4 and C_6H_6 systems. The N-H···O interaction was probed through C_4H_5N with H_2O, CH_3OH, C_6H_5OH and $C_2H_5OC_2H_5$ and the N-H···N interaction was explored by interacting C_4H_5N with NH_3, C_5H_5N and C_9H_7N. In all the systems studied, the global minima are primarily stabilized by N-H···X (where X= π, O, N) interaction, except for C_4H_5N-C_2H_2 (PA-A) and C_4H_5N-C_6H_5OH (PP-A) system, where the lowest energy structures are stabilized by C-H···π, π···π* and O-H···π interactions, respectively. The N-H···π (PA-B) and N-H···O (PP-C) structures are the local minima on the potential energy surface.

- **Chapter 1** Introduction gives a brief account of various non-covalent interactions (NCI) and different spectroscopic methods to understand NCIs were illustrated. A short description of matrix isolation infrared spectroscopy was demonstrated. The most prevalent NCI, hydrogen bond and its importance was explored, followed by the different categories of hydrogen bonding common in the biological, chemical and material world. Finally the justification of seeking pyrrole (C_4H_5N) as a model to understand the nature of hydrogen bonds from weak to moderate to strong was investigated. An extensive literature review for the interactions of pyrrole with a variety of proton donors and acceptors studied so far using various techniques and computations was explored.

- **Chapter 2** This chapter gives a brief description of matrix isolation and the various components associated with the technique. A short account of sample preparation, selection of matrix gases and generation of p-H_2 gas were described. A brief introduction to the quantum chemical calculations used to arrive at the optimized geometries of the heterodimers and various other parameters such as stabilization energies, vibrational wavenumbers, Atoms-in-Molecules (AIM), Natural Bond Orbital (NBO) and Energy Decomposition Analyses (EDA) were discussed.
- **Chapter 3** An account of the infrared spectra of pyrrole in different inert matrixes such as Ne, Ar, Kr, Xe, N_2 and p-H_2 was discussed elaborately with referring the literature data. Furthermore, the infrared spectra for the dimer, trimer and tetramer of pyrrole were extensively investigated and compared at B3LYP and MP2 level of theories with 6-311++G (d, p) and aug-cc-pVDZ basis sets. Although N_2 and Ar matrixes exhibited multiple site splitting of the N-H stretching and bending mode of C_4H_5N monomer, yet the infrared absorption peaks were distinct and well resolved. Hence, these two matrixes were chosen to study the hydrogen bonded interaction of C_4H_5N. Furthermore, MP2/aug-cc-pVDZ level of theory was selected to be the appropriate level to simulate the geometries and calculate the wavenumbers of the complexes, because of better correlation of the computed shifts of pyrrole multimers with experimental wavenumber shifts.
- **Chapter 4** This chapter explores the weak N-H$\cdots\pi$ interactions of C_4H_5N with C_2H_2, C_2H_4 and C_6H_6 in N_2 and Ar matrixes. Due to the dual role of pyrrole acting as a proton donor and acceptor, a variety of heterodimers with C_2H_2, C_2H_4 and C_6H_6 were obtained. In this chapter, the co-existence of co-operative $\pi_N\cdots\pi^*/\pi\cdots\pi^*$ interactions along with

the predominant π···σ* interactions in the heterodimers of C_4H_5N with C_6H_6, C_2H_4 and C_2H_2 was highlighted through both experimental and computational methodologies. The presence of such multiple interactions lead to the deviations from linearity when correlating the BSSE corrected stabilisation energies, second order perturbation energies, electron densities at the bond critical points, change in N-H bond length and hydrogen bond distance with the experimental wavenumber shifts in both the matrixes. Pyrrole is therefore a paradigmatic system which encourages both π···σ* (through N-H bond) and π_N···π* interactions (through aromatic π cloud) in its heterodimers with π systems that eventually results in the deviation from the T-shaped geometry. Overall, in this work, the possibility of partial π-stacking in the otherwise N-H···π dominated structures is comprehensively explored using model pyrrole with π-systems. The existence of co-operative π_N···π* interactions along with the predominant π···σ* was found for all the systems. No direct correlation was obtained when comparing the experimental wavenumber shift with the computed parameters such as BSSE corrected stabilization energies, second order perturbation energies, electron densities at the bond critical points, change in N-H bond length and hydrogen bond distance could be due to the presence of multiple interactions prevailing in these heterodimers.

- **Chapter 5** The moderately strong N-H···O hydrogen bonded heterodimers of pyrrole with H_2O, CH_3OH, C_6H_5OH and $C_2H_5OC_2H_5$ were investigated. The effect of alkyl and phenyl group on the hydrogen bond strength was explored and was found that the alkyl group leads to strengthening, while phenyl group leads to weakening of the hydrogen bond. This phenomenon reverberated when comparing the BSSE corrected stabilization energies, calculated and experimental vibrational shifts in the N-H stretching mode of C_4H_5N, hydrogen bond distances, changes in the N-H bond length of C_4H_5N sub-unit in the heterodimers, electron densities at the bond critical points of N-H···O hydrogen bond and the second order perturbation energies (E_2) of the N-H···O hydrogen bonded heterodimers of C_4H_5N with H_2O, CH_3OH, $C_2H_5OC_2H_5$, and C_6H_5OH.

- **Chapter 6** This chapter gives a depiction of strong N-H···N complexes formed with pyrrole as the donor and NH_3, C_5H_5N and C_9H_7N as acceptors. The experimental shifts in Ar matrix from PAm-A< PPy-A< PQ-A, correlates with the computed wavenumber shift, BSSE corrected stabilization energies, change in the N-H bond length and electron densities at the intermolecular bond critical points. But the trend of experimental shifts in N_2 matrix is PPy-A < PQ-A < PAm-A probably due to the effect of the matrix. The 1:2, 2:1, 2:2, 1:3, 1:4 C_4H_5N-NH_3 higher clusters of pyrrole with ammonia were identified in both the matrixes.

Figure 7.1 illustrate the experimental shift in N_2, Ar matrixes and the computed shifts of the various homodimers and heterodimers of pyrrole. The plot shows from N-H···π → N-H···O → N-H···N heterodimers, there is a gradual increase of computed and experimental vibrational shifts, clearly demonstrating that the strength of the dimers follows the order weak → moderate → strong. It can be also concluded that computational predictions show a fine corroboration in Ar matrix. Even though, experimentally in N_2 matrix all the heterodimers were trapped and identified, there is a considerable deviation of the experimental shift with the computed shifts in the corresponding heterodimers. The reason for this anomalous behaviour of the matrix on to the heterodimers is yet to be explored and requires further refinement of the computational methodology to mimic these effects.

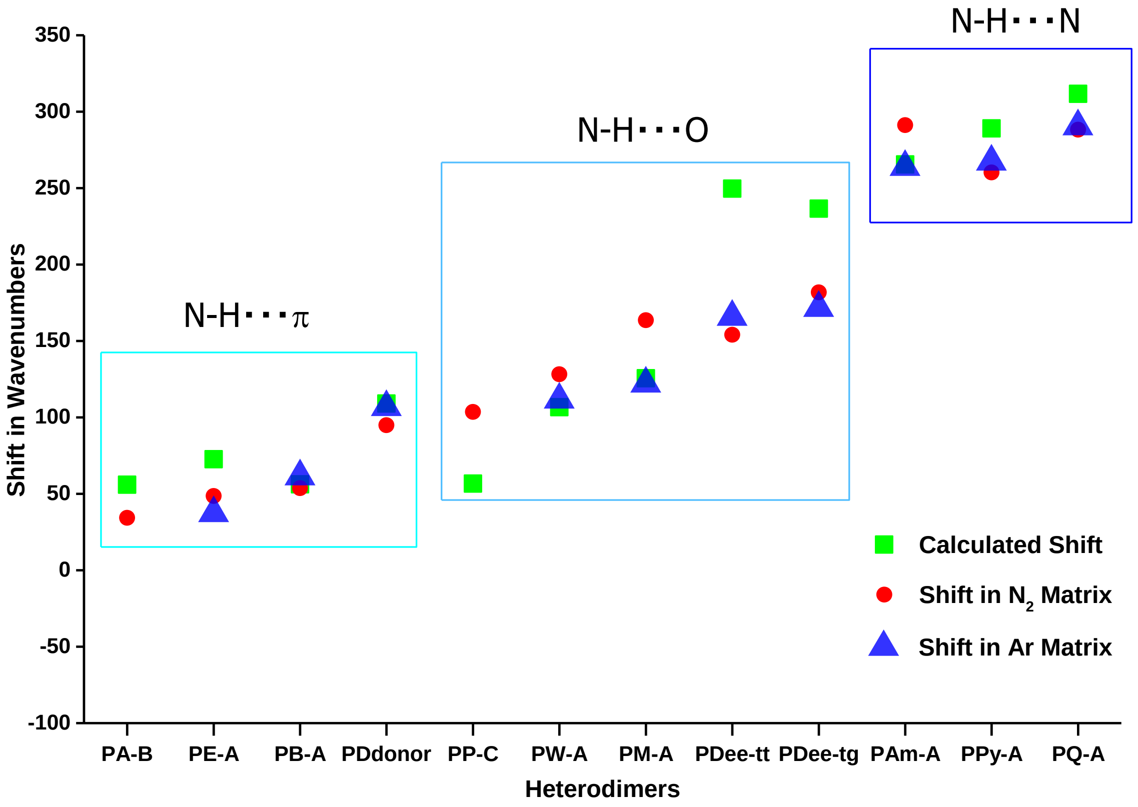

Figure 7.1 The depiction the computed as well as experimental N-H shifts against the homo and heterodimers of pyrrole with acetylene, ethylene, benzene, pyrrole, phenol, water, methanol, diethyl ether, ammonia, pyridine and quinoline.

7.2 Future Scope

- The current project can be extended to N-H⋯S, N-H⋯X (X=F, Cl, Br, I) and N-H⋯P type of hydrogen bonded systems which have strong biological relevance.
- The protein data bank (PDB) and Cambridge structural databases (CSD) can be probed to obtain the presence of these interactions.
- The current project can also be carried out with substituted pyrroles and indoles, in different media, such as gas phase, inert liquid and inert gas matrixes.
- The *para*-H_2 matrix can be explored for the study of all these interactions discussed in this thesis involving pyrrole monomer which can possibly throw new insights with respect to the intrinsic nature of *para*-H_2.

Synopsis

Hydrogen bonding is ubiquitous and one of the most important non-covalent interactions. Although there are numerous reports available on this interaction, studies on hydrogen bonding are always evergreen due to their prevalence in many organic crystals, polymers, and bio-macromolecules. In the last two decades, many experimental and theoretical reports have provided evidences for the π-electron cloud acting as electron donors or hydrogen bond acceptors. There are several varieties of π-hydrogen bonding like O-H···π, N-H···π and C-H···π interactions. Among these, the strength of the interaction follows the order, O-H···π > N-H···π > C-H···π. Similarly, there are numerous studies on the O-H···O, C-H···O and N-H···O types of hydrogen bonded interactions, where oxygen lone pair acts as electron donor or proton acceptor. In diverse biological systems, the nitrogenous compounds are omnipresent and as an example, the derivatives of pyrrole are found in haemoglobin, chlorophyll, alkaloids, tryptophan and proteins.

In this thesis, pyrrole is taken as a model compound to study its multitudinous interactions like N-H···π, O-H···π, N-H···O, C-H···π, π···π* and N-H···N interactions. Pyrrole is one of the simplest heterocyclic aromatic molecules that can show contrasting property as a proton donor and acceptor through its weakly acidic N-H bond and the aromatic π-electron cloud, respectively. For the same reason, pyrrole can undergo self-association by forming dimers, trimers and tetramers through multiple N-H···π interactions.

One of the objectives of this thesis is to study the spectroscopic properties of pyrrole monomer and multimers in Ar, Xe, Ne, Kr, N_2 and p-H_2 matrixes and compare the experimental vibrational wavenumbers of the pyrrole aggregates in different matrixes with the gas phase spectra, in correlation with the computed wavenumbers.

Secondly, the important types of hydrogen bonding interactions of pyrrole such as N-H···π, N-H···O, and N-H···N are also explored using matrix isolation infrared spectroscopy and supported by *ab initio* and DFT computational methodologies. The N-H···π interaction is studied in pyrrole-acetylene (PA), pyrrole-ethylene (PE) and pyrrole-benzene (PB) systems. The N-H···O interaction is probed through interaction of pyrrole with water (PW), methanol (PM), phenol (PP) and diethyl ether (Pyr-DEE) and the N-H···N interaction is explored by allowing interactions of pyrrole with ammonia (PAm), pyridine (PPyr) and quinoline (PQ). Interestingly, in all the systems studied, the global minimum complexes are primarily stabilized by N-H···X (where X= π, O, N) interaction and the local minimum geometries are stabilized by C-H···π, π···π* and O-H···π interactions. Among the 1:1 N-H···π complexes, pyrrole dimer shows the highest vibrational wavenumber shift in N-H stretching region followed by PB-A, PE-A and PA-B and this trend is running parallel to the stabilization energy of the complexes. However, a deviation from the computed wavenumbers with respect to experimental shifts was noticed. This variance in trend between the experimental and computed wavenumbers is likely due to the matrix effect on the complexes, and also due to multiple cooperative interactions existing in the complexes. The strong pyrrole dimer shows a higher vibrational shift, while the weakest complex PA-B shows the lowest vibrational shift. Comparison of the various computed parameters with experimental vibrational wavenumbers of the N-H···O complexes of pyrrole with phenol, water, methanol, and diethyl ether, revealed that the successive replacement of the hydrogen atoms of water with an alkyl group leads to the strengthening of the N-H···O hydrogen bond whereas the substitution of phenyl group weakens the interaction. Hence, PP-C is the weakest complex, while py-DEE-*tt/tg*$^{\pm}$ is the strongest complex, and the results did match well with the theoretical predictions.

In case of N-H···N complexes, computations indicated that the magnitude of computed shift ($\Delta\nu_{N\text{-}H}$) in the vibrational wavenumber follows the order PQ-A > PPy-A > PAm-A. Experimentally, the above trend was observed in Ar matrix. In N_2 matrix, due to the likely interaction of matrix with the complexes, the trend in the $\Delta\nu_{N\text{-}H}$ vibrational wavenumber shift follows the order PAm-A > PQ-A > PPy-A. It was experimentally observed that among the different types hydrogen bonding interactions of pyrrole, the N-H···N type of interaction was the strongest followed by N-H···O and N-H···π. This observation was further supported by NBO, ED and AIM analyses.

Chapter 1 Introduction

The chemistry of life depends on a plethora of non-covalent interactions (NCI), such as hydrogen bonding [1-11], halogen [12-21], chalcogen [22-27], pnicogen [28-34], aerogen [35], regium [36-42], spodium (named after a derivative of the first element of the group, ZnO or spodium) [43-44], triel [45-46] and tetrel bondings [47-48], covering almost the entire periodic table. There are other novel interactions such as $\pi\cdots\pi^*$, $n\cdots\pi^*$, $\sigma\cdots\sigma^*$ [49] that have been found to be responsible in several bio-catalytic, enzymatic and protein functions. The hydrogen bonding interactions have been explored extensively in the past by varieties of experimental and theoretical methods and it still continues to intrigue the researchers. The simultaneous ability of these interactive forces to hold an assembly together or to get dissipated on slight alteration of surrounding factors like temperature, pressure, pH, concentration, etc., makes them crucial for chemical and biological processes.

The diverse techniques such as UV, NMR [50-51], microwave [52-53], Raman [54-55], neutron scattering [56-57], two-color resonant two photon ionization (2C-R2PI) [58-59], time-of-flight mass spectroscopy (TOF-MS) [60], cavity ring down coupled with IR spectroscopy [61-62], IR-UV or UV-UV double resonance techniques [63-64], and ultracold He-Nano droplet technique [65-66] are being used to study the hydrogen bonded interactions. Among all these techniques, infrared spectroscopy has been found to be a very sensitive and useful technique to study the hydrogen bonded interactions [6, 10-11]. Recently, terahertz spectroscopy (20-2000 cm^{-1}) has been growing as an alternate technique to directly measure the vibrational frequency of hydrogen bonds [67-73] rather than measuring the perturbation in the vibrational modes as a result of hydrogen bonding.

Due to the broadening effects (Natural, Doppler, Collision and Pressure broadening mechanism) that operate in gases, liquids and solids, the infrared spectra are broad and the

FWHM in solids and liquids can vary from ~20-300 cm^{-1}, while it is ~1-5 cm^{-1} in gas phase with multiple rotation-vibration lines leading to spectral congestion. It is undesirable to have a broad spectral feature, particularly in experiments where the wavenumber shifts are smaller due to the interaction and the complex formation could not be identified. Furthermore, two closely lying features can be unambiguously assigned if the peak widths are small compared to the separation between the peaks. Therefore, it is always desirable to have spectral features with smaller peak widths.

It is also found that the most of the broadening mechanisms (Doppler, Collision and Pressure broadening) depend on the temperature of the sample. By lowering the temperature of the sample, the width of the speed distribution decreases. As a result, the Doppler broadening which is proportional to $(T)^{1/2}$ decreases. Further, the effect of lowering the temperature restricts the population to only a few vibrational and rotational states which gives a simpler spectrum, devoid of rotational congestion. It is therefore apparent that by reducing the temperature of the sample, one can possibly reduce the spectral width. In reality, the spectral width increases drastically by lowering the temperature. The reason for the broad spectral feature is due to the intermolecular interaction which becomes dominant at low temperatures. In order to obtain a narrow spectral width, it is therefore necessary to cool the samples with simultaneous minimization of the intermolecular interactions, by isolating the molecules from each other. Conventional sampling methods cannot combine both low temperature and the much-needed isolation condition. It is therefore necessary to look beyond the conventional sampling methodology to produce cold isolated molecules. Matrix Isolation technique is one such technique, where the vapors of the sample of interest are mixed with large excess of inert gases (Ne, Ar, Kr, Xe) or diatomic gases (N_2, p-H_2) and deposited at low temperatures.

Among the various types of NCIs, hydrogen bonding still continues to enthrall theoreticians, chemists, biologists and physicists. The century old concept still remains exciting due to the stupendous role, it plays in chemical [74-80], polymeric [81-85], biological [86-88] fields, as well as in crystals [89], materials and electronic fields [90-91]. The IUPAC defines hydrogen bonding as an *'attractive interaction between a group X–H and an atom or group of atoms Y in the same or different molecule(s), where there is evidence of bond formation'* [1]. Hydrogen bonds can be classified based upon their energetics as strong, moderate and weak, which in turn reflect the strength of bond formation. Hydrogen bonds are also classified based upon the shift in infrared bands (X-H stretching vibrational mode) on complexation, since infrared spectroscopy is one of the most sensitive techniques to identify hydrogen bonded interactions. The shift of the infrared band towards lower wavenumber from the monomer absorption band is known as red-shift and it is termed as red-shifted hydrogen bond. A red-shift in the infrared spectrum arises due to the lengthening of the bond length (X-H) which results in bond weakening owing to the electrostatic pull on the H atom by the other electronegative atom (Y). In some cases, the infrared band shows a blue-shift, where the peak is shifted towards higher wavenumber from the monomer absorption band due to the shortening of the bond length (X-H) and is termed as blue-shifted hydrogen bond. [92-96].

An excellent book by Desiraju and Steiner [11] describes the weak hydrogen bond that occurs between the less electronegative atoms X and A, while moderately strong hydrogen bonding takes place when either of X or A is substantially electronegative, whereas a strong hydrogen bond can be formed when X and A are both highly electronegative. There are numerous research articles on 'strong hydrogen bonds' [87, 88-106] where, the length of the covalent bond H-A is almost equal to the hydrogen bond H···X, i.e. proton is shared. In extreme cases, the proton is transferred to the acceptor and the entities exist as an ion-pair, typically an acid and its conjugate base [102]. Proton shared interactions have been found to play a prominent role in enzyme catalysis [107-108]. The presence of strong hydrogen bonded interactions was confirmed by Legon and co-workers through gas phase rotational spectroscopy in a series of systems such as $NH_3\cdots HBr$, $NH_3\cdots HCl$, Amine···HCl, Trimethylamine···HF and Trimethylphosphine···HCl systems [109-114].

The current thesis explores a variety of weak to moderate to strong hydrogen bonded interactions of pyrrole with various proton acceptors or electron donors such as oxygen, nitrogen and π-electron systems. Pyrrole is of immense importance due to its presence as a building block in several biomolecules like, chlorophyll, chlorin, haemoglobin and other protein moieties [115-120]. A review article on the synthesis of C_4H_5N and its analogs reported that it has widespread applications in therapeutic drugs, indigoid dyes, and corrosion inhibitors to preservatives [116]. During the past few years, several groups have studied C_4H_5N and its interactions by theoretical and experimental methods [121-130]. C_4H_5N has a dichotomic behavior where the hydrogen attached to the nitrogen and the π-electron can act as a proton donor and acceptor, respectively. Due to this dual behavior, C_4H_5N forms N-H···π type of hydrogen bonding as evident in $(C_4H_5N)_2$ (proton donor and acceptor simultaneously). Herman et al. assigned the vibration-rotation absorption bands observed between 500 and 12000 cm^{-1} to C_4H_5N and furan (C_4H_4O) molecules. The assignments were corroborated with *ab initio* computations performed at the MP2 level of theory [131]. Claude et al. studied the hydrogen-bonded interaction of self-association of C_4H_5N by infrared spectroscopic technique and found that C_4H_5N is more associative than dimethylamine and N-methylaniline, and it readily forms dimer that exists only in a narrow range of concentrations and temperature [132]. The rotational spectra of $(C_4H_5N)_2$ have been identified and measured using the pulsed-nozzle Fourier Transform Microwave spectrometer. The structure of the $(C_4H_5N)_2$ was found to be analogous to the T-shaped benzene dimer with an N-H···π interaction, and the bond distance was experimentally calculated to be 2.28 Å, indicating a stronger hydrogen bonding between the C_4H_5N monomers [133]. There are several theoretical and experimental reports on the $(C_4H_5N)_2$, which confirm the formation of a T-shaped N-H···π type hydrogen bonded heterodimer [124,128,134,135]. Gómez-Zavaglia and Fausto for the first time reported the structure of multimers of C_4H_5N using matrix isolation infrared spectroscopy in Ar and Xe matrixes [130]. A slanting T-shaped geometry was found for the $(C_4H_5N)_2$ [124,133,134,135,136], cyclic geometries for the $(C_4H_5N)_3$ and $(C_4H_5N)_4$ [130]. The spectroscopic studies were correlated with the calculations performed for the C_4H_5N monomer and multimers computed at B3LYP/6-311++G(d,p) level of theory. Recently, the self-association of C_4H_5N was studied by Beuckeleer and Herrebout in liquid Xenon and was characterized using infrared spectroscopy [137]. They extensively analyzed the IR spectra using a least-square approach and found that apart from the vibrational spectra of the monomer, intense absorption bands originating from pyrrole trimers were also observed in almost every spectral region. The predominant presence of cyclic C_4H_5N trimers over dimers was attributed to the strong cooperative effect, which shifts the equilibrium towards the trimer side, thus reducing the formation of dimers and tetramers.

Matsumoto and Honma used cavity ring-down spectroscopy coupled with infrared spectroscopy to study the formation of various C_4H_5N clusters. Computations performed at B3LYP/6-311++G(d,p) level of theory were correlated with the experimental results. They have used slit and large pinhole pulsed nozzle, to generate a distribution of clusters with different size in a supersonic jet. The analysis of infrared spectra in the N-H stretching region evidenced the formation of dimer, trimer and tetramer and the results were compared with the condensed phase spectra [126].

Several groups have studied the self-association of pyrrole using different experimental and theoretical methods [124-128,130-133,135,137-139]. There are a few experimental reports on pyrrole multimers using matrix isolation infrared spectroscopy. The infrared spectra of pyrrole monomer and multimer were reported to be broad and site split that makes the definitive assignments in Ar and Xe matrixes rather difficult. Hence, to understand and unambiguously assign the multimer feature, the matrix isolation infrared experiments were performed in Ar, Xe, Kr, Ne and diatomic N_2 and para-hydrogen (p-H_2) matrixes. Since, p-H_2 has to be produced afresh for experiments, briefly discusses about the preparation of p-H_2 matrix and the third chapter of the thesis explores the vibrational spectra of pyrrole monomer and its multimers in different matrixes under cold isolated conditions. Computations were performed at different levels of theory using varied basis sets to optimize the geometry of pyrrole monomer and multimers. The computed vibrational wavenumbers of the optimized structure of the monomer and multimers are correlated with the experimental wavenumbers obtained in different matrixes.

The theoretical and experimental reports on the interaction studies of C_4H_5N were limited to highlight the dichotomic behaviour of C_4H_5N. The fourth chapter of the thesis gives a detailed account of the experimental and computational studies on the interactions of pyrrole with π-electron systems such as benzene (C_6H_6), ethylene (C_2H_4), and acetylene (C_2H_2).

A survey on the π-acceptors revealed a few reports available in the literature on the interaction of C_4H_5N with C_6H_6. Leutwyler et al. observed a T-shaped geometry for the C_4H_5N-C_6H_6 heterodimer using IR-UV double resonance technique supported by computations at DFT-D, SCS-MP2 and SCS-CC2 level of theories [138]. Experimentally, a red-shift of ~59 cm^{-1} was observed in the N-H stretching of C_4H_5N. Dauster et al. have also reported a T-shaped structure for the $C_4H_5N\cdots C_6H_6$ heterodimer through pulsed jet experiments [139] and observed a red-shift of ~46 cm^{-1} in the N-H stretching region of C_4H_5N. In another report, Ahnen et al. performed computations on the equilibrium structures of T-shaped imidazole ($C_3H_4N_2$)···C_6H_6 and C_4H_5N···C_6H_6 heterodimers using explicitly-correlated coupled-cluster theory with aug-cc-pVQZ basis set. However, all these reports did not discuss the computed vibrational wavenumbers of the C_4H_5N···C_6H_6 T-shaped heterodimer to correlate with the experimental shift.

Futami et al. performed DFT computations on the interaction of C_4H_5N with C_2H_4 and C_2H_2 and predicted that the heterodimers are stabilized by N-H···π hydrogen bonding, where the N-H bond of C_4H_5N was perpendicular to the CC bond of C_2H_4 and C_2H_2 [140]. Recently, Goyal et al. elucidated the mechanism by which the chemical denaturants unfolded proteins. They explored the nature of urea-aromatic interactions pertinent to the urea (CH_4N_2O)-assisted protein denaturation. Their studies showed the unique ability of urea to form π-stacking and N-H···π interactions with the aromatic residues of proteins. The π-stacking interactions of CH_4N_2O···nucleobase have been shown to be crucial in stabilizing CH_4N_2O assisted RNA unfolding. They also observed in proteins that a delicate balance of different types of intramolecular interaction made the folded states of proteins more stable than unfolded states [141]. Molecular dynamics coupled with thermodynamic simulations and quantum mechanical calculations were performed to investigate the nature of interactions responsible for maximum affinity between CH_4N_2O and aromatic groups as compared to other functional groups in proteins. It was found through free energy calculations and analysis of geometric features that the importance of distortion of hydrophobic core along the unfolding of Tryptosine-cage mini protein was stabilized by stacking and N-H···π interactions. It is now known that CH_4N_2O transporters use stacking interactions to discriminate and regulate CH_4N_2O permeation across cell membranes. On deriving experimental observations of such interaction, it is proved that CH_4N_2O-aromatic stacking interactions are crucial in shifting the protein equilibrium process involving aromatic amino acids. Therefore, it is intriguing to investigate the presence of N-H···π and cooperative π-stacking interaction of C_4H_5N with C_2H_4, C_2H_2 and C_6H_6 that would be explicitly discussed in Chapter 4.

The N-H···O interaction of C_4H_5N with water (H_2O) have been studied by several groups [142-146]. Martoprawiro and Bacskay performed theoretical studies on the $C_4H_5N\cdots H_2O$ and $C_5H_5N\cdots H_2O$ heterodimers [147]. They had used SCF+MP2 theory with double zeta plus polarization basis set to arrive at the equilibrium geometries, harmonic vibrational frequencies and ^{14}N nuclear quadrupole coupling constants. At the SCF level, they found two structures, crossed (C_s) and hinged (C_{2v}) geometries for the $C_4H_5N\cdots H_2O$ heterodimers. Both these structures correspond to local minima on the potential energy surface with the crossed structure being ~0.5 kcal mol^{-1} more stable than the hinged one, where the N-H-O angle in crossed structure was 32.6º. At counterpoise corrected MP2 level, a more stable $C_4H_5N\cdots H_2O$ heterodimer (C_{2v}) was predicted, where the water molecule is perpendicular to the C_4H_5N. Microwave studies of C_4H_5N-H_2O complex revealed the presence of N-H···O type of interaction with the hydrogen bond distance of 2.02 Å [148]. Engdahl et al. studied the interaction of H_2O with aromatic π electrons using matrix isolation infrared spectroscopy [149]. They observed similar band structures for the $C_6H_6\cdots H_2O$ heterodimers in Ar and Kr matrixes, whereas it was different in N_2 matrix. They attributed that this difference was due to the matrix environment and the heterodimer may be trapped in more than one trapping site. Since $C_4H_5N\cdots H_2O$ is a potential prototype for studying protein interactions, Desfrancüois et al. have carried out gas phase study of this interaction using Rydberg Electron Transfer (RET) spectroscopy and determined the very weak excess electron binding energies of the heterodimer anions [150]. Li et al. have performed multiphoton ionization using a time-of-flight mass spectrometer and *ab initio* calculations on the C_4H_5N-$(H_2O)_n$ at two different laser wavelengths 355 and 532 nm [151]. At both wavelengths, a series of C_4H_5N-$(H_2O)_n^+$ and protonated C_4H_5N-$(H_2O)_nH^+$ products were obtained. The *ab initio* calculations showed that in the protonated products, the proton prefers to link with the α-carbon of C_4H_5N rather than nitrogen.

Matsumoto and Honma studied heterodimers of C_4H_5N with methanol (CH_3OH) using infrared cavity ring-down spectroscopy [152]. They compared the shifts in the N-H stretching region of C_4H_5N with $C_4H_5N\cdots H_2O$, $C_4H_5N\cdots CH_3OH$ and $C_4H_5N\cdots C_2H_5OH$ heterodimers. The magnitude of shift in the N-H stretching mode of C_4H_5N in the heterodimers was 83, 117 and 123 cm^{-1}, respectively, depending on the proton affinities of the solvents. Calculations performed at MP2/6-31+G(d, p) and B3LYP/6-311+G(d, p) levels of theory yielded two structures- one with π-type and another with σ-type of bonding, in which the σ-type was the global minimum. Higher clusters for both $C_4H_5N\cdots H_2O$ and $C_4H_5N\cdots CH_3OH$ were also identified. Recently, matrix isolation experiments were reported on C_4H_5N with CH_3OH by Du et al. [153]. The objective of their work was to compare the nature of interaction of CH_3OH with various heterocyclic entities, and C_4H_5N was one of the heterocyclic molecules. They performed the experiments in Ar matrix and the results were compared with B3LYP/aug-cc-pVTZ level of theory for compounds containing oxygen and nitrogen, and B3LYP/aug-cc-pV(d+T)Z for compounds containing sulfur. For the $C_4H_5N\cdots CH_3OH$ interaction, the formation of both N-H···O (proton donor) and O-H···π (proton acceptor) heterodimers in Ar matrix was experimentally observed. On the contrary, in our work the weak acidic nature of the N-H bond of C_4H_5N is casted through its strong nature of interaction with H_2O, CH_3OH and CH_3OCH_3. Fuson and co-workers performed the experiment on the effect of solvent upon N-H stretching of C_4H_5N using 14 different solvents and solvent mixtures [154]. They found that C_4H_5N follows Kirkwood-Bauer relationship in non-polar solvents, but it showed deviation in polar solvents, which is due to the formation of hydrogen bonding in the molecular heterodimers.

Another interesting N-H$\cdots$O system studied was pyrrole (C_4H_5N) with phenol (C_6H_5OH) since, both the precursors and its derivatives are well known for their role in biology, drug activities [9,10,116,155,156] and as a conducting polymer [157-162]. Several reports are available on the self-aggregating nature of C_4H_5N and C_6H_5OH [128,130,137,163,164]. C_6H_5OH can form dimers through O-H$\cdots$O linkages [163] O-H of one C_6H_5OH moiety interacting with the oxygen of the other; whereas C_4H_5N can form dimers and multimers through N-H$\cdots\pi$ networks, the N-H of one C_4H_5N interacting with the π-cloud of the other [124,134,139].

Several groups have carried out theoretical and experimental studies on the interaction of C_6H_5OH with H_2O [165-183]. Sodupe et al. have performed calculations at MP2 and B3LYP levels of theory on the ionization of $C_6H_5OH\cdots H_2O$ and $C_6H_5OH\cdots NH_3$ hydrogen bonded heterodimers [173] and have concluded that B3LYP level of theory was the more accurate method for the neutral as well as for the cationic heterodimers of C_6H_5OH with H_2O and NH_3. It was found that the geometrical relaxation leads to a non-proton transferred heterodimer in $C_6H_5OH\cdots H_2O$ and a proton-transferred heterodimer in $C_6H_5O\text{-}NH_4^+$. The gas phase photo-ionization behavior of C_6H_5OH with H_2O, CH_3OH and CH_3OCH_3 was studied by Courty et al. using semi-empirical model and by recording the ZEKE photoelectron spectra, one-color mass spectra and two-color fragmentation spectra. As a result of these experiments, the gas phase binding energy of the hydrogen bonded heterodimers was obtained [184]. Iwasaki et al. studied the hydrogen bonded clusters of C_6H_5OH with NH_3, $N(CH_3)_3$, $NH(C_2H_5)_2$ and $N(C_2H_5)_3$ using IR-UV double resonance spectroscopy and *ab initio* calculations [185]. They had found that the increase in the $\nu_{O\text{-}H}$ shifts of the heterodimers were consistent with the proton affinities of the amines. Mikami et al. using IR-UV double resonance spectroscopy and B3LYP/6-31G(d,p) level of theory studied the N-H···π interaction of C_6H_5OH with C_2H_2, C_2H_4 and C_6H_6 in the neutral and cationic ground states [186]. They observed that the frequency shifts in the O-H vibrational mode of C_6H_5OH did not depend on the source of the π-electrons and found that the shifts were lesser for the $C_6H_5OH \cdots C_6H_6$ heterodimer even though the C_6H_6 π-cloud has a high proton affinity. The reason for the lower shift was attributed to the formation of secondary C-H···π interaction between the $C_6H_5OH \cdots C_6H_6$ heterodimer. Pujarini et al. have revisited the O-H···π interaction by performing matrix isolation experiments through a series of fluorine substituted C_6H_5OH with C_6H_6 [187]. They discerned that the occurrence of red-shift in the vibrational wavenumbers of the heterodimers indeed depends upon the pK_a values of the fluorophenols. Maity et al. have studied that the participation of C_6H_5OH in hydrogen bonding is entirely due to the acidic nature of O-H bond, which makes C_6H_5OH a proton donor. On the other hand, forming a hydrogen bond with a more acidic species, may turn C_6H_5OH into a proton acceptor, and in none of the cases, the aromatic π-cloud would participate in the bonding [188]. Earlier, the heterodimers of C_6H_5OH with C_2H_2 were investigated using matrix isolation infrared spectroscopy which was supported by computations performed at B3LYP/6-311++G (d p) level of theory [189]. Computations yielded three optimized structures for the $C_6H_5OH \cdots C_2H_2$ heterodimers with O-H···π, C-H···O and C-H···π interactions and experimentally, the O-H···π and C-H···O $C_6H_5OH \cdots C_2H_2$ heterodimers were observed in Ar matrix. In the C_6H_5OH-C_4H_5N system, the O-H of C_6H_5OH and the N-H of C_4H_5N can act as proton donor and the π-electron cloud in both the molecules can simultaneously act as proton acceptor. Such heterogeneous sites, in these molecules, aid in the synergistic interaction where multiple hydrogen bonds lead to the stability of the heterodimers. Furthermore, the geometry of the heterodimer depends on the relative hydrogen bonding abilities of the donor and acceptor molecules, which depends on the Etter's and Legon-Millen rule. There are several reports on C_4H_5N π-electron cloud participating in hydrogen bonding, [137-139] but there are a few studies involving the C_6H_5OH π-electron cloud [188].

Diethyl ether (DEE, $C_2H_5OC_2H_5$), a dipolar aprotic solvent is extensively used in organic synthesis. Extensive theoretical and experimental studies were performed by several groups on the conformers of rotationally flexible DEE molecule [190-195]. DEE has four different rotational isomers with an increasing energy given in the order $tt<tg^{\pm}<g^{\pm}g^{\pm}<g^{\pm}g^{\mp}$ where t=trans and g=gauche. The tt and $tg^{\pm}$ conformers of DEE were found to be present in hot cores and have astrochemical relevance [196-198]. DEE has been shown to exist as tt conformer in solid, liquid and gaseous states, $tg^{\pm}$ conformer in the liquid and gaseous states, whereas the $g^{\pm}g^{\pm}$ and $g^{\pm}g^{\mp}$ forms are energetically unfavorable [194]. Taga et al. have performed the conformational analyses of DEE and its organosilicon derivatives of $CH_3MH_2OM'H_2CH_3$ (M, M'= C and Si) using B3LYP level of theory with 6-31G* and 6-311+G** basis sets and have recorded the Raman spectra for these molecules in the liquid and solid states [199]. They have observed for the DEE that tt and $tg^{\pm}$ were the stable conformers in the liquid state, while the tt form exists in the solid state. Barnes studied the heterodimer of DEE with hydrogen halide in Ar matrix [200]. Andrews et al. studied the heterodimers of hydrogen halides with dimethyl ether (CH_3OCH_3) and diethyl ether ($C_2H_5OC_2H_5$) [201]. They identified two different orientations of DEE···HF heterodimer in solid Ar, tt-DEE···HF (major one) and $tg^{\pm}$-DEE···HF (minor one) and proposed that the matrix cage inhibits the conversion of tt-DEE conformer whereas on annealing the matrix, they observed a small fraction of $tg^{\pm}$-DEE heterodimer. Biswal and Wategaonkar have studied the O-H···O and O-H···S hydrogen bonded interaction of *p*-cresol (*p*-CR) with diethyl ether (DEE) and diethyl sulphide (DES) using IR-UV Double Resonance Spectroscopy and *ab initio* computations [202]. From the red-shifts in the O-H stretching

frequency of *p*-cresol, they obtained evidences for the formation of *p*-CR···*tt*-DEE heterodimer, and for the p-CR with DES, they observed three heterodimers with *tt*, $tg^{\pm}$ and $g^{\pm}g^{\pm}$ conformers under supersonic jet expansion. Yamaguchi et al. studied the vibrational dynamics of the N-H stretching mode of pyrrole-base heterodimers in carbon tetrachloride (CCl_4) using sub-picosecond infrared pump-probe spectroscopy [203]. The decay time for the N-H stretching mode was found to be frequency dependent for all the pyrrole-base heterodimers and that on the lower frequency side was shorter. Chapter 5 describes the detailed account of the interaction of C_4H_5N with H_2O, CH_3OH, C_6H_5OH and C_2H_5-O-C_2H_5 using matrix isolation infrared and computational methods.

The experimental and computational results of the N-H···N interactions of C_4H_5N with ammonia (NH_3), pyridine (C_5H_5N) and quinoline (C_9H_7N) studied using matrix isolation infrared spectroscopy and computational methods are described in Chapter 6.

Earlier investigations on the photo dissociation of the N-H bond of C_4H_5N in presence of NH_3 produced NH_4 radical [204-206]. Three different mechanisms were proposed for the formation of NH_4 radical due to the ejection of an N-H proton from the C_4H_5N molecule. David et al. studied the excited state hydrogen-atom transfer (ESHT) reaction in C_4H_5N···NH_3 clusters. The clusters were produced by supersonic jet expansion and the products were probed by using TOF mass spectrometer. Calculations performed at CASSCF/CASMP2 level confirm the experimental observation, and provide hints regarding the reaction mechanism [204]. Velocity map imaging experiments have been carried out to study the photodynamics of the hydrogen transfer reaction in C_4H_5N-NH_3 clusters of different sizes through non-resonant ionization detection of the $NH_4(NH_3)_{m=2\text{–}4}$ radical products [205]. Zilberg et al. highlighted the role of the hydrogen bonding in the C_4H_5N···NH_3 clusters in Rydberg states in addition to the general H-bonding in the electronic excited state [207]. The formation of the $C_4H_5N\cdots NH_4^+$ is achieved due to the Rydberg Centre Shift (RCS), where the Rydberg orbital is located on the C_4H_5N or NH_3 components forming the cluster. This hypothesis explains the transition to the 2-body dissociation funnel through the $C_4H_5N\cdots NH_4^+$ cluster in agreement with the experimental results of $C_4H_5N\cdots NH_3$ cluster. However, the $C_4H_5N\cdots NH_3$ heterodimer and the higher clusters of NH_3 with C_4H_5N in low temperature matrixes and computations were never studied.

The self-aggregation of NH_3 is very well known that results from its small molecular size, which encourages diffusion within low temperature matrixes [208-216], Nishiya et al. have studied the clusters of NH_3 in Ar, Kr and N_2 matrixes using short pulsed supersonic beams to produce higher clusters of NH_3 [215]. They have identified the features due to $(NH_3)_2$, $(NH_3)_3$ and $(NH_3)_4$, and established a mechanism for the formation of the higher clusters based upon the quenched reaction model. But this model was applicable only at higher concentrations of NH_3 and also when the molecules are assumed to be mobile before condensing into the matrixes. At low concentrations, serious deviations lead to the belief that the higher aggregates can diffuse too, and form even higher clusters on associating with monomers and dimers. Further, studies on $(NH_3)_n$ were carried out by Nelson Jr. et al. (1985) [209], Barnes (1990) [212], Perchard (1991) [213], Janeiro-Barral (2006) [216], Yu (2010) [217] and Beuckeleer et al. (2016) [137]. Infact, NH_3 can readily associate with H_2O to form strong $H_3N\cdots H_2O$ heterodimers, and studies of $NH_3\cdots H_2O$ dimers were performed by Nelander et al. in Ar and N_2 matrixes [218]; whereas, a microwave-infrared double resonance spectroscopic study in a molecular beam yielded a wide account of the various perturbed vibrations due to the NH_3 umbrella mode in $NH_3\cdots H_2O$ dimers [219].

The solid and matrix isolated infrared spectra of C_5H_5N and its deuterated derivative were determined between 4000 to 200 cm^{-1} by Castelucci et al. [220]. Further, the interaction studies involving C_5H_5N in inert matrixes at low temperatures were performed with H_2O [221], HCl [222], HBr [223], CH_3OH [224], and C_2H_2 [225]. So far there are no reports available in the literature to understand the biomimetic $C_4H_5N \cdots C_5H_5N$ interaction. In fact, interesting articles were found on the photodynamics study of the $C_4H_5N \cdots C_5H_5N$ system [226-227]. Zhenggang et al. proposed that a highly polar charge transfer state of $^1\pi\pi^*$ drives the proton transfer from C_4H_5N to C_5H_5N, leading to a conical intersection of S_1 and S_0 energy surfaces. On the other hand, Linnell et al. and Vinogradov et al. carried out the viscosity measurements of C_5H_5N and C_4H_5N. Infrared spectra of the C_5H_5N and C_4H_5N in CCl_4 solution supported the formation of 1:1 $C_4H_5N \cdots C_5H_5N$ heterodimer [228,229]. But none of these reported the infrared spectra nor discussed the structural aspects of the hydrogen bonded structures.

Recent literature survey showed the potential of C_9H_7N scaffolds as anti-cancer drug development since its derivatives can act as growth inhibitors by cell cycle arrest, apoptosis, inhibition of angiogenesis, disruption of cell migration and modulation [230-232]. C_9H_7N trapped in solid Ar and H_2O matrixes at 15 K were reported by Bernstein et al. [233] To identify the IR spectra of C_9H_7N and phenanthridine in interstellar medium, they performed the matrix isolation experiments in H_2O matrix and compared the spectra with that in Ar matrix. It was observed that the infrared spectrum of phenanthridine is similar in both Ar and H_2O matrixes, whereas C_9H_7N showed a shift of 16 cm^{-1} in H_2O when compared to Ar matrix. Similar to NH_3 and C_5H_5N systems, $C_4H_5N \cdots C_9H_7N$ can serve as a model for photodynamic study. An article by Omidyan et al. provides a theoretical account of the geometry, electronic transition energies, and photophysics of isoindole-pyridine and $C_4H_5N \cdots C_9H_7N$ heterodimers [234]. They have determined the hydrogen bonded geometries of both the heterodimers at MP2 and CC2 methods to be perpendicular, and also found that the first electronic transitions due to UV absorption are governed by $^1\pi\pi^*$ nature, while a charge transfer $^1\pi\pi^*$ state, governs the non-radiative relaxation processes of both heterodimers. The $C_4H_5N \cdots C_9H_7N$ system can be of biological relevance, as well as astrochemical importance as is evident from the probations made by Bernstein et al. [233], Mattioda et al. [235] and Frutos et al. [226], respectively.

1.1. Scope of the Thesis

The presence of hydrogen bonding in C_4H_5N with C_4H_5N, C_2H_2, C_2H_4, C_6H_6 (N-H···π), H_2O, CH_3OH, C_6H_5OH, $C_2H_5OC_2H_5$ (N-H···O), NH_3, C_5H_5N and C_9H_7 (N-H···N) were investigated. The experimental evidence of the heterodimer formation was obtained from the shifts in the vibrational modes of the precursors. The experimental results were correlated with the quantum chemical calculations performed at B3LYP, B3LYP-GD3 and MP2 levels, with 6-311++G (d,p) and aug-cc-pVDZ basis sets. Atoms-In-Molecules (AIM), Natural Bond Orbital (NBO) and Energy Decomposition (ED) analyses were carried to further understand the various interactions prevailing in the hydrogen bonded heterodimers.

---

1. Definition of the hydrogen bond (IUPAC Recommendations 2011) E. Arunan, G. R. Desiraju, R. A. Klein, J. Sadlej, S. Scheiner, I. Alkorta, D. C. Clary, R. H. Crabtree, J. J. Dannenberg, P. Hobza, H. G. Kjaergaard, A. C. Legon, B. Mennucci, D. J. Nesbitt. *Pure Appl. Chem.*, **2011**, 83(8), 1637–1641.

2. The arrangement of electrons in atoms and molecules. I. Langmuir, *J. Am. Chem. Soc.,* **1919**, 41, 868–934.

3. G. N. Lewis and the Chemical Bond, L. Pauling, *J. Am. Chem. Soc.,***1984**, 61(3), 201-203.

4. The Nature of the Chemical Bond— an Introduction to Modern Structural Chemistry. 3rd Edition, L. Pauling, **1960,** *Cornell University Press*, Ithaca, New York, 10-13.

5. The hydrogen bond, A. D. Buckingham, J. E. Del Bene, S. A. C. McDowell, *Chem. Phys. Lett.*, **2008**, 463, 1–10.

6. The Hydrogen Bond, G. C. Pimentel, A. L. McClellan, **1960**, *W. H. Freeman & Co.*, San Francisco.

---

7. Theoretical Treatments of Hydrogen Bonding, D. Hadzˇi (Ed.), **1997**, *John Wiley & Sons*, Chichester.

8. Hydrogen Bonding. A Theoretical Perspective, S. Scheiner, **1997**, *Oxford University Press*.

9. Hydrogen Bonding in Biology and Chemistry, G. A. Jeffrey, W. Saenger, **1991**, *Springer-Verlag*, Berlin.

10. An Introduction to Hydrogen Bonding, G. A. Jeffrey, **1997**, *Oxford University Press*.

11. An Introduction to Hydrogen Bonding, G. R. Desiraju, T. Steiner, **1999**, *Oxford University Press*.

12. Halogen bonding: an interim discussion, P. Politzer, J. S. Murray, *ChemPhysChem.*, **2013**, 14, 278 – 294.

13. A Low Temperature Infrared Study of Hydrogen Bonding in *N*-Alkylacetamides, M. C. Bernard-Houplain, C. Sandorfy, *Can. J. Chem.*, **1973**, 51, 3640 –3647.

14. On the hydrogen bond breaking ability of fluorocarbons containing higher halogens, T. Di Paolo, C. Sandorfy, *Can. J. Chem.*, **1974**, 52, 3612 – 3622.

15. J.-M. Dumas, M. Kern, J. L. Janier-Dubry, *Bull. Soc. Chim. Fr*. **1976**, 1785 –1787.

16. J.-M. Dumas, H. Peurichard, M. J. Gomel, *J. Chem. Res*. **1978**, 54 – 57.

17. Charge-transfer interactions of amines with tetrahalomethanes: X-ray crystal structures of the donor-acceptor complexes of quinuclidine and diazabicyclo [2.2.2] octane with carbon tetrabromide, S. C. Blackstock, J. P. Lorand, J. K. Kochi, *J. Org. Chem*. **1987**, 52, 1451 – 1460.

18. Halogen Bonding in Solution: thermodynamics and applications, T. M. Beale, M. G. Chudzinski, M. G. Sarwar, M. S. Taylor, *Chem. Soc. Rev*. **2013**, 42, 1667–1680.

19. The Halogen Bond, G. Cavallo, P. Metrangolo, R. Milani, T. Pilati, A. Priimagi, G. Resnati, G. Terraneo, *Chem. Rev*. **2016**, 116, 2478– 2601.

---

20. An overview of halogen bonding, T. Clark, M. Hennemann, J. S. Murray, P. Politzer, *J. Mol. Model.*, **2007**, 13, 291– 296.

21. Current Opinion in Solid State and Materials Science, M. Fourmigué, **2009**, 13, 36–45.

22. The origin of chalcogen-bonding interactions, D. J. Pascoe, K. B. Ling, S. L. Cockroft, *J. Am. Chem. Soc.*, **2017**, 139, 15160-15167.

23. A Survey of the Role of Noncovalent Sulfur Interactions in Drug Design, B. R. Beno, K. -S.Yeung, M. D. Bartberger, L. D. Pennington, N. A. Meanwell, *J. Med. Chem.,* **2015**, 58, 4383-4438.

24. Simultaneous Sigma-Hole and Hydrogen Bonding by Sulfur- and Selenium Containing Heterocycles, J. S. Murray, P. Lane, P. Politzer, *Int. J. Quantum Chem*. **2008**, 108, 2770–2781

25. σ-hole bonding: molecules containing group VI atoms, J. S. Murray, P. Lane, T. Clark, P. Politzer, *J. Mol. Model.,* **2007**, 13, 1033–1038.

26. Expansion of the σ-hole concept, J. S. Murray, P. Lane, P. Politzer, *J. Mol. Model.*, **2009**, 15, 723– 729.

27. Chalcogen Bonding in Solution: Interactions of Benzotelluradiazoles with Anionic and Uncharged Lewis Bases, G. E. Garrett, G. L. Gibson, R. N. Straus, D. S. Seferos, M. S. Taylor, *J. Am. Chem. Soc*. **2015**, 137, 4126–4133.

28. A predicted new type of directional noncovalent interaction, J. S. Murray, P. Lane, P. Politzer, *Int. J. Quantum Chem.*, **2007**, 107, 2286–2292.

29. Pnicogen bonds: a new molecular linker? S. Zahn, R. Frank, E. Hey-Hawkins, B. Kirchner, *Chem. - Eur. J.*, **2011**, 17, 6034–6038.

30. Halogen, Chalcogen, and Pnicogen Bonding involving Hypervalent Atoms, S. Scheiner, J. Lu, *Chem. Eur. J.*, **2018**, 24, 8167–8177.

---

[31]. The pnicogen bond in review: Structures, energies, bonding properties, and spin-spin coupling constants of heterodimers stabilized by pnicogen bonds, J. E. Del Bene, I. Alkorta, J. Elguero, Vol. 19 (Ed.: S. Scheiner), *Springer*, Dordrecht, **2015**, 191–263.

[32]. Modulating intramolecular P···N pnictogen interactions**,** G. Sánchez-Sanz, C. Trujillo, I. Alkorta, J. Elguero, *Phys. Chem. Chem. Phys*., **2016**, 18, 9148-9160.

[33]. Sensitivity of noncovalent bonds to intermolecular separation: hydrogen, halogen, chalcogen, and pnicogen bonds, S. Schiener, *CrystEngComm*, **2013**, 15, 3119-3124.

[34]. The Pnicogen Bond: Its Relation to Hydrogen, Halogen, and Other Noncovalent Bonds, S. Scheiner, *Acc. Chem. Res.*, **2013**, 462280-462288.

[35]. Aerogen Bonding Interaction: A New Supramolecular Force? A. Bauzá, A. Frontera, *Angew. Chem., Int. Ed*. **2015**, 54, 7340–7343.

[36]. Regium-π bonds: An unexplored link between noble metal nanoparticles and aromatic surfaces, A. Frontera, A. Bauzá, *Chem. Eur. J*., **2018**, 24, 7228–7234.

[37]. A. C. Legon, N. R. Walker, What's in a name? 'Coinage-metal' non-covalent bonds and their definition. Tetrel, pnictogen and chalcogen bonds identified in the gas phase before they had names: A systematic look at non-covalent interactions. *Phys. Chem. Chem. Phys*., **2018**, 20, 19332–19338.

[38]. Tetrel, pnictogen and chalcogen bonds identified in the gas phase before they had names: A systematic look at non-covalent interactions, A. C. Legon, N. R. Walker, *Phys. Chem. Chem. Phys*., **2017**, 19, 14884–14896.

[39]. Synergistic and diminutive effects between triel bond and regium bond: Attractive interactions between π-hole and σ-hole. J. Zhang, Z. Wang, S. Liu, J. Cheng, W. Li, Q. Li, *Appl. Organomet. Chem*., **2019**, 33, 4806.

---

[40]. Understanding regium bonds and their competition with hydrogen bonds in Au2:HX heterodimers. G. Sánchez-Sanz, C. Trujillo, I. Alkorta, J. Elguero, *ChemPhysChem*, **2019**, 20, 1572–1580.

[41]. $(CF_3)_3Au$ as a highly acidic organogold(III) fragment. A. Pérez-Bitrián, M. Baya, J. M. Casas, L. R. Falvello, A. Martín, B. Menjón, *Chem. Eur. J.*, **2017**, 23, 14918–14930.

[42]. Regium bonds formed by MX (M = Cu, Ag, Au; X = F, Cl, Br) with phosphine-oxide/phosphinous acid: Comparisons between oxygen shared and phosphine-shared heterodimers. B. Zheng, Y. Liu, Z. Wang, F. Zhou, Y. Liu, X. Ding, T. Lu, *Mol. Phys.*, **2019**, 117, 2443–2455.

[43]. Trends in molecular geometries and bond strengths of the homoleptic d10 metal carbonyl cations $[M(CO)_n]x^+$ (Mx+ = Cu+, Ag+, Au+, Zn2+, Cd2+, Hg2+; n =1–6): A theoretical study. A. J. Lupinetti, V. Jonas, W. Thiel, S. H. Strauss, G. Frenking, *Chem. Eur. J.*, **1999**, 5, 2573–2583.

[44]. Monomeric 16-electron π-diborene heterodimers of Zn(II) and Cd(II), S. R. Wang, M. Arrowsmith, H. Braunschweig, R. D. Dewhurst, M. Dömling, J. D. Mattock, C. Pranckevicius, A. Vargas, *J. Am. Chem. Soc.*, **2017**, 139, 10661–10664.

[45]. Boron and other triel Lewis acid centers: From hypovalency to hypervalency. S. J. Grabowski, *ChemPhysChem.*, **2014**, 15, 2985–2993.

[46]. A computational analysis of the bonding in boron trichloride and their heterodimers with ammonia. T. Brinck, J. S. Murray, P. Politzer, *Inorg. Chem.*, **1993**, 32, 2622–2625.

[47]. Tetrel-Bonding Interaction: Rediscovered Supramolecular Force? A. Bauzá, T. J. Mooibroek, A. Frontera, *Angew. Chem. Int. Ed.*, **2013**, 52, 12317– 12321.

[48]. Mutual interplay between pnicogen–π and tetrel bond in PF3⊥X–Pyr… SiH_3CN heterodimers: NMR, SAPT, AIM, NBO, and MEP analysis, A. Gholipour, *Struc. Chem.*, **2018**, 29(5), 1255-1263.

---

[49]. Prototypical cyclohexane dimers: spectroscopic evidence for σ stacking at low temperatures,
N. Ramanathan, S. Sarkar, K. Sundararajan, *Phys. Chem. Chem. Phys.*, **2020**, 22, 905-913.

[50]. Direct Observation of Hydrogen Bonds in Nucleic Acid Base Pairs by Internucleotide $^{2}J_{\mathrm{NN}}$ Couplings, A. J. Dingley, S. Grzesiek, *J. Am. Chem. Soc.*, **1998**, 120, 8293-8297.

[51]. NMR studies of hydrogen bonding interactions with secondary amide and urea groups, M. J. Deetz, J. E. Fahey, B. D. Smith, *J. Phys. Org. Chem.*, **2001**, 14, 463–467.

[52]. Radiofrequency and Microwave Spectrum of the Hydrogen Fluoride Dimer; a Nonrigid Molecule, T. Dyke, B. J. Howard, W. Klemperer, *J. Chem. Phys.*, 1969, 56, 2442-2454.

[53]. Microwave spectrum and structure of hydrogen bonded water dimer, T. Dyke, J.S. Muenter, *J. Chem. Phys.*, **1974**, 60, 2929-2930.

[54]. Matrix infrared and Raman spectra of the inequivalent submolecules in the ammonia dimer,
J. P. Perchard, R. B. Bohn, L. Andrews, *J. Phys. Chem.*, **1991**, 85, 2707-2712.

[55]. Supersonic jet CARS spectra of small water clusters, S. Wuelfert, D. Herren, S. Leutwyler, *J. Chem. Phys.*, **1987**, 86, 3751-3753.

[56]. Hydrogen-Bond Spectroscopy of Water by Neutron Scattering, S. –H. Chen, K. Toukan, C. –K. Loong, D. L. Price, J. Teixeira, *Phys. Rev. Lett.*, **1984**, 53, 1360-1363.

[57]. A neutron diffraction study of hydrogen bonding in isostructural potassium and ammonium lanthanoidates, A. J. Emerson, A. J. Edwards, S. R. Batten, D. R. Turner, *CrystEngComm*, **2014**, 16, 1625-1631.

[58]. Nature of the N−H···S Hydrogen Bond, H. S. Biswal, S. Wategaonkar, *J. Phys. Chem. A*, **2009**, 113, 12763–12773

---

[59]. O−H···O versus O−H···S Hydrogen Bonding. 3. IR−UV Double Resonance Study of Hydrogen Bonded Heterodimers of *p*-Cresol with Diethyl Ether and Its Sulfur Analog, H. S. Biswal, S. Wategaonkar, *J. Phys. Chem. A*, **2010**, 114, 5947–5957.

[60]. The propargylbenzene dimer: C–H···π assisted π–π stacking, A. Kundu, S. Sen, G. Naresh Patwari, *Phys. Chem. Chem. Phys*., **2015**, 17, 9090-9097.

[61]. NH stretching vibrations of pyrrole clusters studied by infrared cavity ringdown spectroscopy, Y. Matsumoto and K. Honma, *J. Chem. Phys*., **2007**, 127, 184310

[62]. Contribution of the π electron to the N–H···O═C hydrogen bond: IR spectroscopic studies of the jet-cooled pyrrole–acetone binary clusters, Y. Matsumoto, Jun-ichi Iwamoto, K. Honma, *Phys. Chem. Chem. Phys*., **2012**, 14, 12938-12947.

[63]. Spectroscopic and *ab initio* investigation of 2,6-difluorophenylacetylene–amine heterodimers: coexistence of C–H···N and lone-pair···π heterodimers and intermolecular coulombic decay, S. I. Mondal, A. Dey, S. Sen, G. N. Patwari, D. Ghosh, *Phys. Chem. Chem. Phys*., **2015**, 17, 434-443.

[64]. Hydrogen Bonding to Multifunctional Molecules: Spectroscopic and ab Initio Investigation of Water Heterodimers of Fluorophenylacetylenes, S. Maiti, G. N. Patwari, *J. Phys. Chem. A*, **2009**, 113, 1760-1769.

[65]. Dynamics of hydrogen–HF heterodimers in helium nanodroplets, D. T. Moore, R. E. Miller, *J. Chem. Phys*., **2003**, 118, 9629-9636.

[66]. Superfluid Helium Droplets: A Uniquely Cold Nanomatrix for Molecules and Molecular Heterodimers, J. P. Toennies, A. F. Vilesov, *Angew. Chem. Int. Ed*., **2004**, 43, 2622-2648.

[67]. Terahertz spectroscopy, M.C. Beard, G.M. Turner, C.A. Schmuttenmaer, *J. Phys. Chem. B*, **2002**, 106, 7146–7159.

[68]. Terahertz time-domain spectroscopy of solids: A review. M. Hangyo, M. Tani, T. Nagashima, *Int. J. Infrared Millim. Wave*, **2005**, 26, 1661–1690.

---

[69]. Cutting-edge terahertz technology. M. Tonouchi, *Nat. Photon*., **2007**, 1, 97–105.

[70]. Analytical terahertz spectroscopy, Y. Ueno, K. Ajito, *Anal. Sci*., **2008**, 24, 185–192.

[71]. Recent pharmaceutical applications of Raman and terahertz spectroscopies, C. M. McGoverin, T. Rades, K. C. Gordon, *J. Pharm. Sci*., **2008**, 97, 4598–4621.

[72]. Terahertz time-domain spectroscopy of gases, liquids, and solids, M. Theuer, S. S. Harsha, D. Molter, G. Torosyan, R. Beigang, *ChemPhysChem*, **2011**, 12, 2695–2705.

[73]. Terahertz spectroscopy: A powerful new tool for the chemical sciences? A. I. McIntosh, B. Yang, S. M. Goldup, M. Watkinson, R. S. Donnan, *Chem. Soc. Rev*., **2012**, 41, 2072–2082.

[74]. Applications of metal-organic frameworks in adsorption/separation processes via hydrogen bonding interactions, I. Ahmed, S. Hwa Jhung, *Chem. Eng. J*., **2017**, 310, 197–215.

[75]. Effects of Intra- and Intermolecular Hydrogen Bonding on O–H Bond Photodissociation Pathways of a Catechol Derivative, C. Grieco, A. T. Hanes, L. Blancafort, B. Kohler, *J. Phys. Chem. A*, **2019**, 123, 5356-5366.

[76]. G. Caron, J. Kihlberg, G. Ermondi, *Med. Res. Rev*., **2019**, 1–23.

[77]. Supramolecular Self-Sorting Networks using Hydrogen-Bonding Motifs, H. M. Coubrough, S. C. C. van der Lubbe, K. Hetherington, A. Minard, C. Pask, M. J. Howard, C. F. Guerra, A. J. Wilson, *Chem. Eur. J*., **2019**, 25, 785–795.

78. Hydrogen bonding in ionic liquids, P. A. Hunt, C. R. Ashworth, R. P. Matthews, *Chem. Soc. Rev*., **2015**, 44, 1257-1288.

79. Hydrogen-Bonding and Hydrophobic Groups Contribute Equally to the Binding of Hyperactive Antifreeze and Ice-Nucleating Proteins to Ice, A. Hudait, Y. Qiu, N. Odendahl, V. Molinero, *J. Am. Chem. Soc*., **2019**, 141, 7887-7898.

---

80. A twist-bend nematic phase driven by hydrogen bonding, S. M. Jansze, A. Martnez-Felipe, J. M. D. Storey, A. T. M. Marcelis, C. T. Imrie, *Angew. Chem. Int. Ed.*, **2015**, 54, 643 –646.

81. Exploring structural variations of hydrogen-bonding patterns in cellulose during mechanical pulp refining of tobacco stems, D. Zhao, Y. Deng, D. H., L. Tan, Y. Dinga, Z. Zhou, H. Xu, Y. Guo, *Carbohydr. Polym*., **2019**, 204, 247–254.

82. Novel insights into membrane fouling caused by gel layer in a membrane bioreactor: Effects of hydrogen bonding, Y. Chena, J. Tenga, L. Shena, G. Yua, R. Lia, Y. Xua, F. Wanga, B.-Q. Liaob, H. Lin, *Bioresour. Technol.*, **2019**, 276, 219–225.

83. Self-healing epoxy nanocomposites via reversible hydrogen bonding, L. Guadagnoa, L. Vertuccioa, C. Naddeoa, E. Calabresea, G. Barraa, M. Raimondoa, A. Sorrentinob, W.H. Binderc, P. Michaelc, S. Rana, *Compos. B. Eng*., **2019**, 157, 1–13.

84. Characterization of Hydrogen Bonding Formation and Breaking in Semiconducting Polymers under Mechanical Strain, A. Gasperini, G.-Ji N. Wang, F. Molina-Lopez, H.-Chin Wu, J. Lopez, J. Xu, S. Luo, D. Zhou, G. Xue, Jeffery B.-H. Tok, and Zhenan Bao, *Macromol*., **2019**, 52, 6, 2476-2486.

85. Polymer Soft-Landing Isolation of Acetylene on Polystyrene and Poly(vinylpyridine): A Novel Approach to Probing Hydrogen Bonding in Polymers, Y. Li, C. Samet, *J. Phys. Chem. B*, **2015**, 119, 12336-12344.

86. Understanding enzymic catalysis: the importance of short, strong hydrogen bonds, J. A Gerlt, M. M. Kreevoy, W.W. Cleland, P. A Frey, *Chem. Biol.*, **1997**, 4, 259-267.

[87]. “Strong” Hydrogen bonds in Chemistry and Biology, C. L. Perrin, and J. B. Nielson, *Annu.* Rev. Phys. Chem., **1997**, 48, 511–544.

88. Low-barrier hydrogen bonds and enzymatic catalysis, W. W. Cleland, *Arch. Biochem. Biophys*, **2000**, 382, 1–5.

---

[89]. Hydrogen Bridges in Crystal Engineering: Interactions without Borders, G. R. Desiraju, *Acc. Chem. Res*., **2002**, 35, 565-573.

90. Weak hydrogen bonding enables hard, strong, tough, and elastic hydrogels, X. Hu, M. Vatankhah-Varnoosfaderani, J. Zhou, Q. Li, S. S. Sheiko, *Adv. Mater*., **2015**, 27, 6899–6905.

91. Multiple hydrogen bonding enables the self-healing of sensors for human–machine interactions, J. Cao, C. Lu, J. Zhuang, M. Liu, X. Zhang, Y. Yu, Q. Tao, *Angew. Chem. Int. Ed*., **2017**, 56, 8795 –8800.

[92]. On Differences between Hydrogen Bonding and Improper Blue-Shifting Hydrogen Bonding, W. Zierkiewicz, P. Jurecka, P. Hobza, *Chem. Phys. Chem*., **2005**, 6, 609-617.

[93]. Blue-shifting Hydrogen Bonds, P. Hobza, Z. Havlas, *Chem. Rev*., **2000**, 100, 4253-4264.

[94]. Experimental Evidence for Blue-Shifted Hydrogen Bonding in the Fluoroform-Hydrogen Chloride Heterodimer: A Matrix-Isolation Infrared and ab Initio Study, R. Gopi, N. Ramanathan, K. Sundararajan, *J. Phys. Chem. A*, **2014**, 118, 5529-5539.

[95]. Experimental evidence for the blue-shifted hydrogen-bonded heterodimers of CHF_3 with π-electron donors, R. Gopi, N. Ramanathan, K. Sundararajan, *Spectroch. Acta Part A*, **2017**, 181, 137–147.

[96]. Blue-shift of the C-H stretching vibration in CHF3-H2O heterodimer: Matrix isolation infrared spectroscopy and ab initio computations, R. Gopi, N. Ramanathan, K. Sundararajan, *Chem. Phys*., **2016**, 476, 36–45.

[97]. Short Strong Hydrogen Bonds: A Valence Bond Analysis, S. Humbel, *J. Phys. Chem. A*, **2002**, 106, 5517-5520.

[98]. Strong hydrogen bonding in molecules and enzymatic heterodimers, P. A. Frey, *Magn. Reson. Chem*. **2001**, 39, S190–S198.

---

[99]. Energy considerations show that low-barrier hydrogen bonds do not offer a catalytic advantage over ordinary hydrogen bonds. A. Warshel, A. Papazyan, *Proc. Natl. Acad. Sci*., **1996**, 93, 13665–13670.

[100]. Infrared Spectra of the Ammonia-Hydrochloric Acid Complex in Solid Nitrogen, B. S. Ault, G. C. Pimentel, *J. Phys. Chem*., **1973**, 77, 1649-1653.

101. Infrared Spectrum of the H_3N-HCl Complex in Solid Ne, Ne/Ar, Ar, and Kr. Matrix Effects on a Strong Hydrogen-Bonded Complex, L. Andrews, X. Wang, Z. Mielke, *J. Phys. Chem. A*, **2001**, 105, 6054-6064.

[102]. Strongly Hydrogen-bonded Molecular Complexes Studied by Matrix-isolation Vibrational Spectroscopy. Part 1: The Ammonia-Hydrogen Chloride Complex, A. J. Barnes, T. R. Beech, Z. Mielke, *Faraday Trans. 2*, **1984**, 80, 455.

[103]. Strongly Hydrogen-bonded Molecular Complexes Studied by Matrix-isolation Vibrational Spectroscopy. Part 2: Amine-Hydrogen Chloride Complex, A. J. Barnes, J. N. S. Kuzniarski, Z. Mielke, *Faraday Trans. 2*, **1984**, 80, 465-476.

[104]. Strongly Hydrogen-bonded Molecular Complexes Studied by Matrix-isolation Vibrational Spectroscopy. Part 3: Ammonia-Hydrogen Bromide and Amine-Hydrogen Bromide Complexes, A. J. Barnes, M. P. Wright, *Faraday Trans. 2*, **1986**, 82, 153-164.

[105]. Strongly Hydrogen-bonded Molecular Complexes Studied by Matrix-isolation Vibrational Spectroscopy. Part 4: Dimethyl Sulphoxide-Hydrogen Halide Complexes, A. J. Barnes, M. P. Wright, *Faraday Trans. 2*, **1986**, 82, 165-172.

[106]. Isotope effects in the characterization of low barrier hydrogen bond, P. A. Frey, In Isotope effects in chemistry and biology (eds A Kohen, H-H Limbach), **2006**, 975–993. Boca Raton, FL: *CRC press*.

---

[107]. An *ab Initio* Study of Anharmonicity and Field Effects in Hydrogen-Bonded Complexes of the Deuterated Analogues of HCl and HBr with NH_3 and $N(CH_3)_3$, J. Bevitt, K. Chapman, D. Crittenden, M. J. T. Jordan, J. E. Del Bene, *J. Phys. Chem. A*, **2001**, 105, 3371-3378.

[108]. Unraveling Environmental Effects on Hydrogen-Bonded Complexes: Matrix Effects on the Structures and Proton-Stretching Frequencies of Hydrogen-Halide Complexes with Ammonia and Trimethylamine, J. T. Jordan, J. E. Del Bene, *J. Am. Chem. Soc*., **2000**, 122, 2101-2115.

[109]. Nature, geometry, and binding strength of the ammonia–hydrogen chloride dimer determined from the rotational spectrum of ammonium chloride vapor, N. W. Howard, A. C. Legon, *J. Chem. Phys*., **1988**, 88, 4694-4701.

[110]. An investigation of the hydrogen bonded dimer $H_3N\cdots HBr$ by pulsed nozzle, Fourier transform microwave spectroscopy of ammonium bromide vapor, N. W. Howard, A. C. Legon, *J. Chem. Phys*., **1987**, 86, 6722-6730.

[111]. The Extent of Proton Transfer from X to N in the Gas-Phase Dimers $(CH_3)_{3-n}H_nN\cdots HX$. Evidence From Rotational Spectroscopy, A. C. Legon, C. A. Rego, *Chem. Phys. Lett*., **1989**, 162, 369-375.

[112]. ^{14}N-and D-Nuclear Quadrupole Coupling in The Rotational Spectrum Of $(CH_3)_3{}^{14}N\cdots H(D)F$: Modification of The Electric Field Gradients At The N And D Nuclei, A. C. Legon, C. A. Rego, *Chem. Phys. Lett*., **1989**, 157, 243-250.

113. Rotational spectrum of $(CH_3)_3P\cdots HCl$ and a comparison of properties within the series of axially symmetric dimers $R_3Y\cdots HCl$, where Y = N or P and R = H or CH_3, A. C. Legon, C. A. Rego, *Faraday Trans*., **1990**, 86, 1915-1921.

[114]. The rotational spectrum and nature of the heterodimer in trimethylammonium bromide vapor, A. C. Legon, A. L. Wallwork, C. A. Rego, *J. Chem. Phys*., **1990**, 92, 6397-6407.

---

[115]. H. Fischer, Akademische Verlag: Die Chemie Des Pyrrols, Leipzig, Vol. I, **1934**, **1937**, **1940**.

[116]. Pyrrole: A Resourceful Small Molecule in Key Medicinal Hetero-Aromatics, V. Bhardwaj, D. Gumber, V. Abbot, S. Dhiman, P. Sharma, *RSC. Adv*., **2015**, 5, 15233–15266.

117. Pyrrole, Pyrrolidine, Pyridine, Piperidine and Tropane Alkaloids, D. O’Hagan, *Nat. Prod. Rep*. **2000**, 17, 435–446.

118. Metalated Heterocycles and Their Applications in Synthetic Organic Chemistry, R. Chinchilla, Nájera, C.; Yus, M. *Chem. Rev*., **2004**, 104, 2667–2722.

[119]. R. A. Jones, Pyrroles: The synthesis and the Physical and Chemical Aspects of the Pyrrole Ring. *Wiley-Interscience*, New York, **1990**.

120. Total synthesis of Pyrrolnitrin, a New Antibiotic, H. Nakano, S. Umio, K. Kariyone, K. Tanaka, T. Kishimoto, H. Noguchi, I. Ueda, H. Nakamura, T. Morimoto, *Tetrahedron Lett*., **1966**, 7, 737–740.

[121]. The Vibrational Spectra of Pyrrole and Some of Its Deuterium Derivatives, R. C. Lord, Jr., F. A. Miller, *J. Chem. Phys*., **1942**, 10, 328-341.

[122]. A Photoabsorption and Mass Spectrometry Study of Pyrrole. E. E. Rennie, C. A. F. Johnson, J. E. Parker, R. Ferguson, D. M. P. Holland, D. A. Shaw, *Chem. Phys*., **1999**, 250, 217–236.

[123]. Effect of Hydrogen Bonding on the N-H Stretching Raman Band of Pyrrole, A. Lautie, A. Novak, *J. Chem. Phys*. **1972**, 56, 2479–2481.

[124]. Experimental and Quantum Chemical Study of Pyrrole Self-association through N–H···π Hydrogen Bonding, V. Stefov, L. Pejov, B. Soptrajanov, *J. Mol. Struct*., **2003**, 649, 793-805.

[125]. The N-H Stretch in Pyrrole: A Study of the Fundamental ($\Delta v=1$) and Third Overtone ($\Delta v=4$) Bands in the Bulk Gas and in a Molecular Beam, C. Douketis, J. P. Reilly, *J. Chem. Phys*. **1992**, 96, 3431–3440.

---

[126]. N-H Stretching Vibrations of Pyrrole Clusters Studied by Infrared Cavity Ringdown Spectroscopy, Y. Matsumoto, K. Honma, *J. Chem. Phys*., **2007**, 127**,** 184310(1-9).

[127]. Solvated Structures of Pyrrole–Acetonitrile Binary Clusters Studied by Infrared Cavity Ringdown Spectroscopy, J. Iwamoto, Y. Matsumoto, K. Honma, *J. Chem. Phys*., **2013**, 419, 184–192.

[128]. Tracing dynamic Self-disassociation Behavior of Pyrrole with Novel T-shaped Hydrogen Bonding, S. Sun, H. Tang, P. Wu, *Phys. Chem. Chem. Phys*., **2009**, 11, 7611-7618.

[129]. Molecular Orbital Theory of the Hydrogen Bond: Pyrrole and Imidazole as Proton Donors and Proton Acceptors, J. E. D. Bene, I. Cohen, *J. Am. Chem. Soc*., **1978**, 100:17, 5285–5290.

[130]. Self-Aggregation in Pyrrole: Matrix Isolation, Solid State Infrared Spectroscopy, and DFT Study, A. Gomez-Zavaglia, R. Fausto, *J. Phys. Chem. A*, **2004**, 108, 6953-6967.

131. The vibrational spectrum of pyrrole (C_4H_5N) and furan (C_4H_4O) in the gas phase, A. Mellouki, J. Lievin, M. Herman, *J. Chem. Phys*., **2001**, 271, 239-266.

132. Low temperature infrared study of hydrogen bonding in dissolved pyrrole and indole, Marie-Claude, Bernard-Houplain, C. Sandorfy, *Can. J. Chem*., **1973**, 51, 1075-1082.

133. Pure rotational spectrum, quadrupole coupling constants and structure of the dimer of pyrrole, G. Columberg, A. Bauder, *J. Chem. Phys*., **1997**, 106, 504-510.

134. Ab initio investigations of the pyrrole dimer: a direct observation of the π-facial hydrogen bond, H. Park, S. Lee, *Chem. Phys. Lett*., **1999**, 301, 487-492.

135. Pathways of relaxation of the N–H stretching vibration of pyrrole in liquids, J. R. Ambroseo, R. M. Hochstrasser, *J. Chem. Phys*., **1988**, 89, 5956-5957.

136. Complete vapor phase assignment for the fundamental vibrations of furan, pyrrole and thiophene, T. D. Klots, R. D. Chirico, W. V. Steele, Spectrochim. Acta A, **1994**, 50A, 765-795.

---

[137]. The Self-Associating Behavior of Pyrrole in Liquid Xenon, L. I. De Beuckeleer, W. A. Herrebout, *J. Mol. Struct*., **2016**, 1108, 71-79.

138. N–H···π hydrogen-bonding and large-amplitude tipping vibrations in jet-cooled pyrrole–benzene, C. Pfaffen, D. Infanger, P. Ottiger, H. -M. Frey, S. Leutwyler, *Phys. Chem. Chem. Phys*., **2011**, 13, 14110-14118.

[139]. N–H···*π* Interactions in Pyrroles: Systematic Trends from the Vibrational Spectroscopy of Clusters, I. Dauster, C. Rice, P. Zielke, M. Suhm, *Phys. Chem. Chem. Phys*., **2008**, 10, 2827-2835.

140. Frequencies and absorption intensities of the fundamental and the first overtone of NH stretching vibrations of pyrrole···acetylene and pyrrole···ethylene complexes studied by density-functional-theory calculation, Y. Futami, Y. Ozaki, Y. Hamada, Y. Ozaki, *Vib. Spectrosc*., **2014**, 72, 124-127.

141. Role of Urea–Aromatic Stacking Interactions in Stabilizing the Aromatic Residues of the Protein in Urea-Induced Denatured State, S. Goyal, A. Chattopadhya, K. Kasavajhala, U. D. Priyakumar, *J. Am. Chem. Soc*., **2017**, 139, 14931-14946.

[142]. Excited State Dynamics in Pyrrole–Water Clusters: First-principles Simulation, I. Frank, K. Damianos, *Chem. Phys*., **2008**, 343, 347–352.

[143]. Natures of Benzene-Water and Pyrrole-Water Interactions in the forms of σ and π types: Theoretical Studies from Clusters to Liquid Mixture, W. Gao, J. Jiao, H. Feng, X. Xuan, L. Chen, *J. Mol. Model.*, **2013**, 19, 1273–1283.

[144]. Photo-ejection of Electrons from Pyrrole into an Aqueous Environment: ab initio Results on Pyrrole-Water Clusters, A. L. Sobolewski, W. Domcke, *Chem. Phys. Lett*., **2000**, 321, 479–484.

[145]. The Thermodynamics and Kinetics of the Reaction Between Pyrrole and Water, K. L. Ding, Y. Luo, S. S. Wang, *Energy Sources, Part A*, **2014**, 36, 929–937.

---

[146]. Ground State Structures and Excited State Dynamics of Pyrrole-Water Heterodimers: Ab initio Excited State Molecular Dynamics Simulations, A. Kumar, M. Kołaski, K. S. Kim, *J. Chem. Phys.*, **2008**, 128, 034304(1-6).

[147]. Quantum Chemical Studies of the Pyrrole-Water and Pyridine-Water Heterodimers, M. A. Martoprawiro, G. B. Bacskay, *Mol. Phys.*, **1995**, 85, 573–585.

[148]. Microwave Spectrum and Structure of a Hydrogen-Bonded Pyrrole-Water Heterodimer. M. J.Tubergen, A. M. Andrews, R. L. Kuczkowski, *J. Phys. Chem.*, **1993**, 97, 7451–7457.

[149]. A Matrix Isolation Study of the Interaction between Water and the Aromatic π-Electron System, A. Engdahl, B. Nelander *J. Phys. Chem.*, **1987**, 91, 2253–2258.

[150]. Gas-Phase Experimental and Theoretical Studies of Adenine, Imidazole, Pyrrole, and Water Non-Covalent Heterodimers, S. Carles, F. Lecomte, J. P. Schermann, C. Desfrancüois, *J. Phys. Chem. A*, **2000**, 104, 10662–10668.

[151]. Multiphoton Ionization and ab Initio Calculation Studies of the Hydrogen-Bonded Clusters C_4H_5N-$(H_2O)_n$, Y. Li, X. H. Liu, X. Y. Wang, N. Q. Lou, *J. Phys. Chem. A,* **1999**, 103, 2572–2579.

[152]. Hydrogen-bonded Sructures of Pyrrole-solvent Clusters: Infrared Cavity Ringdown Spectroscopy and Quantum Chemical Calculations, Y. Matsumoto, K. J. Honma, *Chem. Phys.*, **2009**, 130, 054311(1–11).

[153]. Matrix Isolation FTIR Study of Hydrogen-bonded Heterodimers of Methanol with Heterocyclic Organic Compounds. X. Jiang, S. Liu, N. T. Tsona, S. Tang, L. Ding, H. Zhao, L. Du, *RSC Adv.*, **2017,** 7, 2503–2512.

[154]. Infrared Study of the Effect of Solvent upon υ(NH) in Pyrrole, M. L. Josien, N. Fuson, *J. Chem. Phys.*, **1954**, 22, 1169–1177.

[155]. Phenolics: From Chemistry to Biology. D. M. Pereira, P. Valentão, J. A. Pereira, P. B. Andrade, *Molecules*, **2009**, 14, 2202-2211.

---

156. Noncovalent Interactions: A Challenge for Experiment and Theory, K. Müller-Dethlefs, P. Hobza, *Chem. ReV.*, **2000**, 100, 143-168.

157. Phenol substituted Polymethylsilane: a Soluble Conducting Polymer with Low Cross-linking Density, W. Pu, X. Li, G. Li, *Polym. Bull.*, **2015**, 72, 779-790.

[158]. Synthesis and Characterization of Phenol-based Biaryl Proton Conducting Polymers. C. Nagamani, J. Guo, S. J. Thayumanavan, *Polym. Sci. A*, **2012**, 50, 1187–1196.

159. Structural Study of Two Conducting Polymers: Poly(Pyrrole) and Poly(Thiophene).B. J. Orchard, B. Froidenreich, S. K. Tripathy, *Polym.*, **1986**, 27, 1533-1541.

[160]. Conductive Polymer Composites and Copolymers of Pyrrole and N-Vinylcarbazole, U. Geissler, M. L. Hallensleben, L. Toppare, *Synth. Met.*, **1991**, 40, 239-246.

[161]. Colored electrically conducting polymers from furan, pyrrole, and thiophene. M. Armour, A. G. Davies, J. Upadhyay, A. Wassermann, *J. Polym. Sci. A-1 Polym. Chem.*, **1967**, 5, 1527–1538.

[162]. Conducting Polymers Derived from Pyrrole. In: Organic Molecular Aggregates. G. B. Street, R. H. Geiss, S. E. Lindsey, A. Nazzal, P. Pfluger, P. Reineker, H. Haken, H.C. Wolf, **1983**, 49. Springer Series in Solid-State Sciences, *Springer*, Berlin, Heidelberg.

[163]. The Self-Association of Phenol under Cryogenic Matrix Conditions, H. Tylli, H. Konschin, *J. Mol. Struc.*, **1986**, 142, 571-57.

164. Dimers of phenol in argon and neon matrixes, A. M. Plokhotnichenko, E. D. Radchenko, P. Yu., V. A. Karachevtsev, *Low Temp. Phys.*, **2001**, 27, 666-675.

165. An Experimental and Theoretical Investigation into the Excited Electronic States of Phenol. D. B. Jones, G. B. Silva, R. F. C. Neves, H. V. Duque, L. Chiari, E. M. Oliveira, M. C. Lopes, R.F. Costa, M. T. N. Varella, M. H. F Bettega, M. A. P. Lima, M. J. Brunger, *J. Chem. Phys.*, **2014**, 141, 074314(1-8).

---

166. Interaction of Phenol with Xenon and Nitrogen: Spectroscopic and Computational Characterization, Q. Cao, N. Andrijchenko, A. E. E. Ahola, X. Domanskaya, M. Räsänen, A. Ermilov, A. Nemukhin, L. Khriachtchev, *J. Chem. Phys*., **2012**, 137, 134305(1-11).

167. The Vibrational Spectra of Phenol and Phenol-OD. J. C. Evans, *Spectrochim. Acta*, **1960**, 16, 1382-1392.

168. Direct Observation of Weak Hydrogen Bonds in Microsolvated Phenol: Infrared Spectroscopy of O-H Stretching Vibrations of Phenol-CO and -CO_2 in S0 and D0, A. Fujii, T. Ebata, N. Mikami, *J. Phys. Chem. A*, **2002**, 106, 10124-10129.

169. Formation of Hydrogen-bonded Heterodimers between Phenol and Some Heterocyclic Bases in Carbon Tetrachloride, M. Orban, A. Kiss, L. Barcza, *J. Chem. Soc.- Perkin Trans. 2.*, **1987**, 1815-1817.

170. Complete Infrared Spectroscopic Characterization of Phenol-Borane-Trimethylamine Dihydrogen-Bonded Heterodimer in the Gas Phase. G. N. Patwari, A. Fujii, N. Mikami, *J. Chem. Phys*., **2006**, 124, 241103(1-4).

[171]. A Density Functional, Infrared Linear Dichroism, and Normal Coordinate Study of Phenol and its Deuterated Derivatives: Revised Interpretation of the Vibrational Spectra. G. Keresztury, F. Billes, M. Kubinyi, T. Sundius, *J. Phys. Chem. A*, **1998**, 102, 1371-1380.

[172]. Structure, Spectroscopy, and Dynamics of the Phenol-(Water)2 Cluster at Low and High Temperatures. N. R. Samala, N. Agmon, *J. Chem. Phys*., **2017**, 147, 234307(1-15).

[173]. Theoretical Study of the Ionization of Phenol-Water and Phenol-Ammonia Hydrogen-Bonded Heterodimers. M. Sodupe, A. Oliva, J. Bertrán, *J. Phys. Chem. A*, **1997**, 101, 9142-9151.

[174]. Characterization of the Hydrogen-Bonded Cluster Ions [Phenol-$(H_2O)_n$]+ (n=1-4), $(Phenol)_2$+, and (Phenol-Methanol)+ as Studied by Trapped Ion Infrared Multiphoton

---

Dissociation Spectroscopy of their O-H Stretching Vibrations, T. Sawamura, A. Fujii, S. Sato, T. Ebata, N. Mikami. *J. Phys. Chem.*, **1996**, 100, 8131-8138.

[175]. Matrix-isolation Study of the Phenol–Water Heterodimer and Phenol Dimer. G. Y. Gor, S. Tapio, A. V. Domanskaya, M. Räsänen, A. V. Nemukhin, L. Khriachtchev, *Chem. Phys. Lett*. **2011**, 517, 9-15.

[176]. Accurate Theoretical Determination of the Structure of Aromatic Heterodimers is Complicated: The Phenol Dimer and Phenol···Methanol Cases. M. Kolářand, P. Hobza, *J. Phys. Chem. A*, **2007**, 111, 5851-5854.

[177]. High Resolution UV Spectroscopy of Phenol and the Hydrogen Bonded Phenol-Water Cluster. G. Berden, W. L. Meerts, M. Schmitt, K. Kleinermanns, *J. Chem. Phys*., **1996**, 104, 972-982.

[178]. Intermolecular Bonding and Vibrations of Phenol-H_2O (D_2O).M. Schutz, T. Burgi, S. Leutwyler, T. Fischer, *J. Chem. Phys*., **1993**, 98, 3763-3776.

[179]. Ab initio Calculations on Phenol-Water. H. Y. Helen, T. V. Mourik, *Chem. Phys. Lett*., **2001**, 350, 565-572.

[180]. Hydrogen Bonding in Phenol, Water, and Phenol-Water Clusters. R. Parthasarathi, V. Subramanian, N. Sathyamurthy, *J. Phys. Chem. A*, **2005**, 109, 843-850.

[181]. O-H Stretching Vibrations of Phenol- (H_2O)n (n=1-3) Heterodimers Observed by IR-UV Double-Resonance Spectroscopy. S. Tanabe, T. Ebata, M. Fujii, N. Mikami, *Chem. Phys. Lett*., **1993**, 215, 346-352.

[182]. Size-Selected Vibrational Spectra of Phenol-$(H_2O)_n$ (n=1–4) Clusters Observed by IR–UV Double Resonance and Stimulated Raman-UV Double Resonance Spectroscopies. T. Watanabe, T. Ebata, S. Tanabe, N. Mikami, *J. Chem. Phys*., **1996**, 105, 408-419.

[183]. OH Stretching Vibrations of Phenol-$(H_2O)^1$ and Phenol-$(H_2O)^3$ in the S1 State. T. Ebata, N. Mizuochi, T. Watanabe, N. Mikami, *J. Phys. Chem*., **1996**, 100, 546-550.

---

[184] Ionization, Energetics, and Geometry of the Phenol-S Heterodimers (S = H_2O, CH_3OH, and CH_3OCH_3), A. Courty, M. Mons, I. Dimicoli, F. Piuzzi, V. Brenner, P. Millie, *J. Phys. Chem. A*, **1998**, 102, 4890-4898

[185] Infrared Spectroscopy of Hydrogen-Bonded Phenol-Amine Clusters in Supersonic Jets. A. Iwasaki, A. Fujii, T. Watanabe, T. Ebata, N. Mikami, *J. Phys. Chem.*, **1996**, 100, 16053-16057.

[186] An Infrared Study of π-Hydrogen Bonds in Micro-solvated Phenol: OH Stretching Vibrations of Phenol-X (X =C_6H_6, C_2H_4, and C_2H_2) Clusters in the Neutral and Cationic Ground States. A. Fujii, T. Ebata, N. Mikami, *J. Phys. Chem. A*, **2002**, 106, 8554-8560.

[187] Correlation of νOH Spectral Shifts of Phenol-Benzene O-H$\cdots\pi$ Hydrogen-Bonded Heterodimers with Donor's Acidity: A Combined Matrix Isolation, Infrared Spectroscopy, and Quantum Chemistry Study, P. Banerjee, T. Chakraborty, *J. Phys. Chem. A*, **2014**, 118, 7074-7084.

[188] Phenylacetylene: A Hydrogen Bonding Chameleon, S. Maity, M. Guin, P. C. Singh, G. N. Patwari, *ChemPhysChem.*, **2011**, 12, 26-46.

[189] Acetylene–Phenol Heterodimers: A Matrix Isolation Infrared and ab initio Study. K. Sundararajan, N. Ramanathan, *J. Mol. Struc.*, **2009**, 920, 369-376.

[190] Vibrational spectra and a valence force field for conformers of diethyl ether and deuterated analogues , H. Wieser, W. G. Laidlaw, P. J. Krueger, H. Fuhrer, *Spectrochim. Acta*, **1973**, 24, 1055-1089.

[191] Low frequency infrared and Raman spectra of certain aliphatic ethers, A. D. H. Clague, A. Danti, *Spectrochim. Acta*, **1968**, 24, 439-441.

[192] Vibrational analysis of ten simple aliphatic ethers: Spectra, assignments, valence force field and molecular conformations, R. G. Snyder, G. Zerbi, *Spectrochim. Acta.*, **1967**, 23, 391-437.

---

[193]. Interpretation and prediction of vibrational absorption intensities: methylethyl ether and diethyl ether, B. Galabov, S. Ilieva, T. Duoev, H. V. Phan, J. R. Durig, *Spectrochim. Acta*, **1993**, 49, 2093-2103.

[194]. Experimental determination of the *trans–gauche* energy difference of gaseous *n*-pentane and diethyl ether, I. Kanesaka, R. G. Snyder, H. L. Strauss, *J. Chem. Phys.*, **1986**, 84, 395-397.

[195]. L. Schriver, A. Loutellier, A. Burneau, *Chem. Phys. Lett.*, **1979**, 60, 471-475.

[196]. The Millimeter- And Submillimeter-Wave Spectrum Of Methyl Carbamate $[CH_3OC(:O)NH_2]$, I. Medvedev, M. Winnewisser, F.C. De Lucia, E. Herbst, E. Yi, L. P. Leong, R. P. A. Bettens, E. Biankowska-Jaworska, O. Desyatnyk, L. Pszczo´nkowski, Z. Kisiel, *Astrophys. J. Suppl. S.*, **2003**, 148, 593-597.

[197]. Submillimeter-wave spectrum of *anti–anti* and *anti–gauche* diethyl ether, A. Walters, H. S. P. Muller, F. Lewen, S. Schlemmer, *J. Mol. Spectr.*, **2009**, 257, 24-28.

[198]. The millimeter- and submillimeter-wave spectrum of the *trans–gauche* conformer of diethyl ether, I. Medvedev, M. Winnewissera, F. C. De Lucia, E. Herbst, E. Białkowska-Jaworsk, L. Pszczo΄łkowski, Z. Kisiel, *J. Mol. Spect.*, **2004**, 228, 314–328.

[199]. Raman spectra and conformational analyses for a series of diethyl ether and its organosilicon derivatives, $CH_3MH_2OM'H_2CH_3$ (M, M'=C and Si), by density functional theory, K. Taga, K. Kawasaki, Y. Yamamoto , T. Yoshida, K. Ohno, H. Matsuura, *J. Mol. Struct.*, **2006**, 788, 159-175.

[200]. Molecular complexes of the hydrogen halides studied by matrix isolation infrared spectroscopy, A. J. Barnes, *J. Mol. Struct.*, **1983**, 100, 259-280.

[201]. FTIR spectra of the dimethyl ether-hydrogen fluoride complex and related complexes in solid argon, L. Andrews, G. L. Johnson, S. R. Davis, *J. Phys. Chem.*, **1985**, 89, 1710-1715.

---

[202]. O−H···O versus O−H···S Hydrogen Bonding. 3. IR−UV Double Resonance Study of Hydrogen Bonded Complexes of *p*-Cresol with Diethyl Ether and Its Sulfur Analog, H. S. Biswal, S. Wategaonkar, *J. Phys. Chem A*, **2010**, 114, 5947-5957.

[203]. Frequency Dependence of Vibrational Energy Relaxation and Spectral Diffusion of the N–H Stretching Band of Pyrrole–Base Complexes in Solution, S. Yamaguchi, M. Banno, K. Ohta, K. Tominaga, *J. Phys. Chem. A*, **2013**, 117, 6323-6331.

[204]. O. David, C. Dedonder-Lardeux, C. Jouvet, H. Kang, S. Martrenchard, T. Ebata, A. L. Sobolewski, *J. Chem. Phys*., **2004**, 102, 10101-10110.

[205]. Photodissociation of pyrrole-ammonia clusters by velocity map imaging: Mechanism for the H-atom transfer reaction, L. Rubio-Lago, G. A. Amaral, A. N. Oldani, J. D. Rodrıguez, M. G. González, G. A. Pinoc, L. Bañares, *Phys. Chem. Chem. Phys*., **2011**, 13, 1082–1091.

[206]. Photodissociation of pyrrole-ammonia clusters below 218 nm: Quenching of statistical decomposition pathways under clustering conditions, J. D. Rodríguez, M. G. González, L. Rubio-Lago, L. Bañares, *J. Chem. Phys*., **2012**, 137, 094305(1-8).

[207]. The photo-dissociation of the pyrrole-ammonia complex - The role of hydrogen bonding in Rydberg states photochemistry, S. Zilberg, A. Kahan, Y. Haas, *Phys. Chem. Chem. Phys*., **2012**, 14, 8836–8841.

[208]. Infrared spectroscopic evidence for the rotation of the ammonia molecule in solid argon and nitrogen, D. E. Milligan, R. M. Hexter, K. Dressler, *J. Chem. Phys*., **1961**, 34, 1009-1012.

[209]. Ammonia dimer: A surprising structure, D. D. Nelson Jr., G. T. Fraser, W. Klemperer, *J. Chem. Phys*., **1985**, 83, 6201-6208.

[210]. Infrared spectra of ammonia suspended in solid nitrogen, G. C. Pimentel, M. O. Bulanin, M. Van Thiel, *J. Chem. Phys*., **1962**, 36, 500-506.

---

[211]. FTIR spectra of ammonia clusters in noble gas matrixes, S. Süzer, L. Andrews, *J. Chem. Phys*. **1987**, 87, 5131-5140.

[212]. Studies of intermolecular interactions by matrix isolation vibrational spectroscopy: self-association of ammonia, A. J. Barnes, *J. Mol. Struct*., **1990**, 237, 19-32.

[213]. Matrix infrared and Raman spectra of the inequivalent submolecules in the ammonia dimer, J. P. Perchard, R. B. Bohn, L. Andrews, *J . Phys. Chem*., **1991**, 95, 2707-2712.

[214]. Rotational tunnelling and ammonia sites in Ar and N_2 matrixes, M. Havighorst, M. Prager, W. Langel, *Physica B*, **1992**, 180 & 181, 674-676.

[215]. Identification of ammonia clusters in low-temperature matrixes using the FTIR short-pulsed matrix isolation technique, T. Nishiya, N. Hirota, H. Shinohara, N. Nishi, *J. Phys. Chem*., **1985**, 89, 2260-2264.

[216]. Identification of ammonia clusters in low-temperature matrixes using the FTIR short-pulsed matrix isolation technique, P. E. Janeiro-Barral, M. Mella, *J. Phys. Chem. A*, **2006**, 110, 11244-11251.

[217]. Study on structures and properties of ammonia clusters $(NH_3)_n$ (n=1–5) and liquid ammonia in terms of *ab initio* method and atom-bond electronegativity equalization method ammonia-8*P* fluctuating charge potential model, L. Yu, Z. Z. Yang, *J. Chem. Phys*., **2010**, 132, 174109.

[218]. Complex between water and ammonia, B. Nelander, L. Nord, *J. Phys. Chem*. **1982**, 86, 4375-4379.

[219]. G. T. Fraser, R. D. Suenram, *J . Phys. Chem*., **1992**, 96, 7287.

[220]. Infrared Spectra of Crystalline and Matrix Isolated Pyridine and Pyridine-D_5, E. Castellucci, G. Sbrana, F. D. Verderame, *J. Chem. Phys*., **1969**, 51, 3762-3770.

[221]. Matrix isolation FT-IR studies and ab initio calculations of hydrogen-bonded complexes of molecules modeling cytosine or isocytosine tautomers. 1. Pyridine and pyrimidine

---

complexes with water in argon matrixes, A. Destexhe, J. Smets, L. Adamowicz, G. Maes, *J. Phys. Chem.*, **1994**, 98, 1506-1514.

[222]. *Ab initio* theoretical and matrix isolation experimental studies of hydrogen bonding: vibrational consequences of proton position in 1:1 complexes of HCl and 4-X-pyridines, J. E. Del Bene, W. B. Person, K. Szczepaniak, *Chem. Phys. Lett.*, **1995**, 247, 89-94.

[223]. *Ab initio* theoretical and matrix isolation experimental studies of hydrogen bonding. IV. The HBr:Pyridine complex, K. Szczepaniak, P. Chabrier, W. B. Persona, J. E. Del Bene, *J. Mol. Struct.*, **1997**, 436-437, 367-386.

224. Methanol–pyridine complexes trapped in argon and nitrogen matrixes: Infrared induced isomerization and theoretical calculations, S. Coussan, V. Brenner, J. P. Perchard, W. Q. Zheng, *J. Chem. Phys.*, **2000**, 113, 8059-8069.

[225]. A matrix isolation and ab initio study of the hydrogen bonded complexes of acetylene with pyridine, K. Sundararajan, K. Sankaran, K.S. Viswanathan, *J. Mol. Struct.*, **2005**, 733, 187–192.

[226]. Photoinduced Electron and Proton Transfer in the Hydrogen-Bonded Pyridine− Pyrrole System, L. M. Frutos, A. Markmann, A. L. Sobolewski, W. Domcke, *J. Phys. Chem. B,* **2007**, 111, 6110–6112.

[227]. Photochemistry of hydrogen-bonded aromatic pairs: Quantum dynamical calculations for the pyrrole–pyridine complex, Z. Lan, L. M. Frutos, A. L. Sobolewski, W. Domcke, *Proc. Natl. Acad. Sci.*, **2008**, 105, 12707–12712.

[228]. The System PyridinePyrrole and Hydrogen Bonding, R. H. Linnell, *J. Chem. Phys.*, **1953**, 21, 179-180.

[229]. The System Pyridine-Pyrrole and the Association of Pyrrole, S. N. Vinogradov, R. H. Linnell, *J. Chem. Phys.*, **1955**, 23, 93-97.

---

[230]. Comprehensive review on current developments of quinoline-based anticancer agents, S. Jain, V. Chandra, P. K. Jain, K. Pathak, D. Pathak, A. Vaidya, *Arab. J. Chem.*, **2019**, 12, 4920-4946.

[231]. A review on anticancer potential of bioactive heterocycle quinoline, O. Afzal, S. Kumar, Md. R. Haider, Md R. Ali, R. Kumar, M. Jaggi, S. Bawa, *Eur. J. Med. Chem.*, **2015**, 97, 871-910.

[232]. A review on quinoline hydrazone derivatives as a new class of potent antitubercular and anticancer agents, M. C. Mandewale, U. C. Patil, S. V. Shedge, U. R. Dappadwad, R. S. Yamgar, *Beni-Seuf Univ. J. Appl. Sci.*, **2017**, 6, 354–361.

[233]. Laboratory infrared spectra of polycyclic aromatic nitrogen heterocycles: Quinoline and phenanthridine in solid argon and H_2O, M. P. Bernstein, A. L. Mattioda, S. A. Sandford, D. M. Hudgins, *Astrophys. J.*, **2005**, 626, 909–918.

[234]. A theoretical exploration of the nonradiative deactivation of hydrogen-bond complexes: isoindole–pyridine and quinoline–pyrrole, R. Omidyan, M. Salehi, G. Azimi, *RSC Adv.*, **2015**, 5, 97619-97628.

[235]. Infrared spectroscopy of matrix-isolated polycyclic aromatic compounds and their ions. 6. Polycyclic aromatic nitrogen heterocycles, A. L. Mattioda, D. M. Hudgins, C. W. Bauschlicher Jr, M. Rosi, L. J. Allamandola, *J. Phys. Chem. A*, **2003**, 107, 1486-1498.

Chapter 2 Experimental and Computational Methodology

This chapter gives a brief description of the experimental and computational methodologies.

2.1. Experimental Method: Matrix Isolation technique

The matrix isolation technique was first introduced by George Pimentel and co-workers in the mid-1950s, at UCL, Berkeley, California [1-3]. This technique was originally developed to trap and detect unstable intermediates such as free radicals, by reducing the temperature and diluting with inert gases.

The method of matrix isolation involves mixing the sample of interest with large excess of inert gas and deposition onto a cold substrate (~10 K). The deposited sample can be probed by a variety of spectroscopic methods such as infrared, UV-visible, fluorescence and electron spin resonance (ESR). A high matrix to sample ratio in a typical matrix isolation experiment ensures that the sample is distributed uniformly in the matrix gas that results in the isolation of sample molecules of interest at low temperatures. The inert gases such as neon, argon, krypton and xenon are used as matrix gases. Apart from these gases, diatomic nitrogen and para-hydrogen (p-H_2) are also used as matrix gases.

Matrix isolation when coupled with infrared spectroscopy (MI-IR) is a high-resolution technique where the vibrational spectra of sample molecules surrounded by solid matrix have very sharp line widths when compared to gas, liquid and solid spectra. Since, the experiment is performed at a low temperature, the Doppler broadening is reduced and the rotational motion of sample molecules is arrested due to the rigid cage which leads to a simpler spectrum devoid of spectral congestion. Furthermore, the matrix gases prevent the sample molecules from interacting with each other, thus preventing the broadening due to intermolecular interactions. Hence, the MI technique is used to study a) Intermolecular interactions b) Conformations c) Radicals, reactive species and intermediates generated using vacuum pyrolysis or photolysis

[4-7].

The gas mixtures (sample + inert gases) are prepared using manometric procedures in the mixing chamber and then allowed to flow through the 1/8″ copper lines at a controlled rate by a fine dozing valve and deposited onto a cold KBr substrate. A controlled flow rate of the gas mixture is necessary to produce a uniform solid film on the cold substrate. Typically, in all the experiments, deposition lasted for about ~1 hour at a rate of ~1 Torr per min.

The mixing and the deposition chambers are continuously pumped by diffusion pump and turbo pump backed by rotary pumps, respectively, where the base pressure in both chambers was $< 10^{-7}$ Torr.

2.2 Components of Matrix Isolation Set-up

2.2.1 Cryostat

Low temperature experiments were performed using a closed cycle helium compressor cooled cryostat RDK-408D2 Model (Sumitomo Heavy Industries Ltd.). The Sumitomo cryostat can attain a minimum temperature of 2.5 K and works on the principle of the Gifford-McMahon cycle. The cooling is achieved by the continuous compression and expansion of helium gas in an enclosed space. Helium is first compressed to a pressure of about ~ 20 bars and the heat due to compression is removed by circulating cold water. The helium is then delivered to the cold head, where it expands against a piston, and eventually cools the regenerator. The expanded helium is then returned to the compressor for the next cycle. The temperature of the cold head was measured using a Cernox (ceramic oxynitrides) resistor. Lakeshore temperature controller (Model 336) is used to read the temperature of the cold substrate and it can be varied through the nichrome resistive heater wire (25Ω, 2A, 100W) wound on the cold head.

2.2.2 Vacuum Pumps

It is always desirable to perform MI experiments in a clean environment where the atmospheric impurities such as H_2O, CO_2, O_2 and N_2 are in the ppm to ppb levels. These impurities will affect the quality of the matrix and in extreme cases it can interact with sample which will lead to undesirable results in the IR spectra. In order to maintain an impurity less environment, the sample chamber containing the cold substrate (i.e., the cryo chamber) is continuously pumped by a turbo molecular pump (Edwards TIC Pumping Station, model-nEXT300D 160 W; pumping speed of 300 l/s) backed by a rotary pump. On the other hand, a diffusion pump (Diffstak MK2 100/300; pumping capacity of 280 l/s) backed by a rotary pump, is connected to the mixing chamber and pumped continuously. The ultimate vacuum of the entire system is below ~10^{-7} Torr.

2.2.3 Pressure Gauge

Pressure gauges are inevitable components in the matrix isolation set-up. The gas mixtures (sample + inert gas) are prepared using capacitance manometers (Baratron, measurement range: 10-5000 Torr and Pfeiffer, CMR 362; measurement range: 7.5×10^{-2}-75 Torr). To measure the vacuum in the system, a cold-cathode gauge is connected near the diffusion pump (Pfeiffer, PKR 251, measurement range: 5×10^{-11} to 200 Torr).

2.2.4 Infrared Spectrophotometer

Bruker Vertex 70 FTIR spectrometer was used to record infrared spectra of the deposited and annealed samples at low temperatures. The spectrometer is equipped with a KBr beam splitter and a globar source. The instrument has a provision for having two detectors; Lanthanum doped Deuterated Tri-glycine Sulphate (La-DTGS) and Mercury Cadmium Telluride (MCT) detectors. Liquid nitrogen coolant (LN_2) was used to cool the MCT detector to minimize the thermal noise. All the IR spectra reported in this thesis were recorded using MCT detector. The IR spectra are recorded by co-adding 32 individual scans in the range 400-4000 cm^{-1} with a resolution of 0.5 cm^{-1}. The matrix isolation experimental set-up along with FTIR spectrometer is illustrated in Figure 2.1.

2.3 Preparation of sample

2.3.1 Premixing and co-deposition through a single and double jet nozzle

The sample and the matrix gas were mixed in desired ratios using standard manometric procedure. Initially, the liquid samples are subjected to several freeze-pump-thaw cycles to remove the volatile impurities. Sample vapor pressure is controlled through the vacuum valve and directly added into the mixing chamber and then diluted with the inert gas. In another method, the sample bulb is kept inside the ethanol+LN_2 slurry, which is maintained at a particular temperature to obtain the desired vapor pressure and equilibrated to the mixing chamber for about ~30 minutes, following which the matrix gas is added to obtain a desired sample to matrix ratios (Sample 1 in Figure 2.1). The gas mixture thus prepared by either of the above two methods was deposited onto the cold substrate (~10 K) using a single jet nozzle assembly through a fine dosing valve.

For very low vapor pressure samples, the sample bulb is connected to the one arm of the double jet nozzle assembly and the vapor pressure of the sample is controlled dynamically at a given temperature using the ethanol-LN_2 slurry and deposited at low temperature (Sample 2 in Figure 2.1). Through the second arm of the nozzle the matrix gas from the mixing chamber is allowed to flow at a controlled rate using the fine dosing valve and deposited on to the cold substrate.

2.3.2 Matrix gases

Ultrahigh pure (99.9995%) matrix gas used in the MI technique should have the following important properties: a) It should be chemically inert b) It must be easily available with high purity and it should be transparent in the wavelength region of interest c) It should have sufficient vapor pressure at room temperature and be able to form rigid matrix at low temperature and prevent diffusion of guest molecules. Inert gases such as Ne, Ar, Kr, Xe and diatomic gas N_2 meet the above criteria and hence are commonly used as matrix gases.

Recently, *p*-H_2 gas has emerged as a promising matrix material for use in MI technique [8]. The schematic of the para-hydrogen (*p*-H_2) set-up is shown in Figure 2.2. Normal hydrogen (99.999%, Chemtron) has 3:1 ortho/para ratio and the production of enriched *p*-H_2 is obtained by passing the normal hydrogen through a copper bobbin filled with a hydrated ferric oxide catalyst. The copper bobbin is connected to the cold head of the closed cycle helium cryostat and the temperature of the cold head is maintained at 13.5 K (triple point of hydrogen). Normal hydrogen gas passing through the copper bobbin that exists in a dynamic equilibrium at the temperature of 13.5 K, in presence of catalyst gets converted into *p*-H_2. By using infrared spectroscopy, the purity of the *p*-H_2 matrix was found to be >99%. The details of the preparation of *p*-H_2 gas and the determination of impurities are reported elsewhere [8]. The *p*-H_2 gas thus prepared is used for the matrix isolation experiment.

2.4 Computational Methods

Based on electronic structure theory, the quantum chemical calculation gives molecular geometries, energies, transition states, IR, UV-vis, NMR spectra, thermochemical parameters, reaction pathways, etc [9-12]. GAUSSIAN09 [13] package loaded on a Fujitsu machine with Intel 2X XEON E5-2687W v2 processors, with 64 GB RAM, was used to perform the calculations. DFT methods such as B3LYP, B3LYP-D3 and *ab initio* MP2 level of theory with 6-311++G (d, p) and aug-cc-pVDZ basis sets were used to optimize the geometry.

2.4.1 Geometry Optimization

Geometry optimization refers to locating a stationary point or, an equilibrium state of a molecule/molecular heterodimer on the potential energy surface (PES). Starting from the optimized monomer geometries, the geometries of the heterodimers were then optimized. All geometrical parameters were left free during the optimization process. The structures of the various types of heterodimers shown in the thesis were drawn using Chemcraft software [14]. Various properties such as stabilization energies, structural parameters, vibrational wavenumbers and s were computed. Vibrational frequency calculation was performed for the optimized geometries to characterize the nature of stationary point and to obtain zero-point energies (ZPE). All the normal modes of vibration must be positive for the optimized structure to be characterized as a minimum on the PES. Furthermore, the computed vibrational wavenumber is compared with the experimental wavenumber. Generally, a comparison of the vibrational shift (Δν) between the experimental and computed wavenumbers of a particular mode as shown in equation (1), which are characteristics of H-bonded interaction, was accomplished.

$$\boldsymbol{\Delta\nu_{\mathrm{experimental/computed}} = \nu_{\mathrm{(heterodimer)}} - \nu_{\mathrm{(monomer)}}} \text{ ---------------------(1)}$$

The raw stabilization energies (**ΔE**) (not corrected for ZPE and BSSE) and the ZPE corrected energies (**ΔE_{zpe})** of the heterodimers are computed using the equations 2 and 3 respectively. E_A, E_B are the energies of the monomers and E_{AB} is the energy of the heterodimer.

$$\boldsymbol{\Delta E = E_{(AB)} – E_{(A)} - E_{(B)}} \text{ ----------------------------------(2)}$$

$$\boldsymbol{\Delta E_{zpe} = E_{zpe(heterodimer)} – \Sigma\, E_{zpe\ (monomers)}} \text{ -------------(3)}$$

Stabilization energies obtained by the method (2) is erroneous because the number of basis functions used to optimize the heterodimer and monomer geometry are different and this is referred as basis set superposition error (BSSE). In order to correct this error, counterpoise (CP) correction suggested by Boys and Bernardi [15] is used. In this method, the energies of monomer E_A, E_B and the heterodimer E_{AB} are optimized in the same basis set spanned by the functions of the heterodimer AB and the difference in energies is obtained as follows.

$$\Delta E = E_{AB}\,(AB) – \{E_A\,(AB) + E_B\,(AB)\} \text{ ------------ (4)}$$

Where, E_A (AB) = Energy of the monomer A using the basis set AB

E_B (AB) = Energy of the monomer B using the basis set AB

E_{AB} (AB) = Energy of the heterodimer AB using the basis set AB

In this thesis, the RAW, ZPE and BSSE corrected stabilization energies are listed for all the heterodimers.

2.5 Atoms-in-Molecules Analysis

Bader proposed the concept of quantum theory of AIM (QTAIM) method, which is extensively used to study the nature of chemical bond based on the electron density topology [16-18]. An analysis of electron density topology $\rho(r)$ leads directly to the chemical concepts of atoms, molecules, structures and bonds. A quantitative way to analyze the topology of $\rho(r)$ is to consider the first derivative (gradient) $\nabla\rho(r)$. At certain points, called critical points, this gradient vanishes. The characteristic of these points is determined by the Hessian of $\rho(r)$, which is second derivative $\nabla^2\rho(r)$. The Hessian is the (3×3) symmetric matrix of partial second derivatives. By diagonalization of this matrix, the off-diagonal terms become zero, and one obtains the three principal axes of curvature. These principal axes will correspond to symmetry axes, if the critical point lies on a symmetry element. The sum of the diagonal terms is called the symmetry element. The sum of the diagonal terms is called the Laplacian of ρ, $\nabla^2(\rho)$, and is of fundamental importance. It is defined as,

$$\nabla^2(\rho) = \partial^2\rho/\partial x^2 + \partial^2\rho/\partial y^2 + \partial^2\rho/\partial z^2 \quad \text{--------(5)}$$

At critical points, the eigenvalues of the hessian matrix are real and generally non-zero. The rank of the critical point is defined as the number of non-zero eigenvalues, while the signature is defined as the algebraic sum of the signs of the eigenvalues. These two characteristics are used to label a critical point (rank, signature). A (3, -1) is a bond critical point (b, BCP), (3, +1) is a ring critical point (r, RCP) and (3, +3) is a cage critical point (c, CCP). The number of critical points that can coexist in a topological space is based upon the Poincaré-Hopf relationship, where n is the number of atoms

$$n - b + r - c = 1 \text{---------(6)}$$

The wavefunction of the optimized geometry of the monomers and heterodimers are used as input in the AIMPAC package to generate the electron density topology. From the electron density plots, various properties at the BCP were examined: the electron density

($\rho(r_c)$), Laplacian of electron density ($\nabla^2\rho(r_c)$) and the eigen values.

A shared or covalent interaction between the two nuclei is always associated with $\nabla^2\rho(r_c) < 0$ while $\nabla^2\rho(r_c) > 0$ implies the interaction is of closed-shell type. The latter is found in hydrogen bonds, ionic bonds and van der Waals heterodimers where the interactions are dominated by requirements of Pauli Exclusion Principle [16,19].

2.6 Natural Bond Orbital Analysis

The NBO analysis is very useful in analyzing the intra and intermolecular bonding. It is a helpful tool for understanding the delocalization of electrons and hyperconjugative or charge transfer interactions [20-21]. The concept of natural orbitals was introduced by Löwdin [22] in order to delineate the unique set of orthonormal 1-electron functions $\phi i(r)$, that are intrinsic to the N-electron wavefunctions $\psi(1,2,\ldots,N)$. The 1-electron functions $\phi i(r)$ are the best possible orbitals of ψ to describe the electron density $\rho(r)$ of ψ. The ψ forms the natural orbitals and they are necessarily symmetry adapted, superposition of states and more delocalized. In order to remove the spurious effects due to the symmetry adaption or delocalization, one can formulate the localized criterion for orbitals that have the analogous maximum occupancy (natural) character in localized 1-center and 2-center regions of the molecule**.** Because the maximum occupancy of an orbital is inherently limited to a pair of electrons by the Pauli Exclusion Principle, local 1- and 2-center orbitals, with occupancies sufficiently close to 2.000 can serve equally well as “true” natural orbitals for describing ψ. Such natural bond orbitals (NBOs) provide the most accurate possible “natural Lewis structure” picture of ψ, because all orbital details (polarization coefficients, atomic hybrid compositions, etc.) are mathematically chosen to include the highest possible percentage of the electron density. This percentage (denoted %-ρ_L) gives an intrinsic measure of the accuracy of the natural Lewis structure picture, and is often found to be >99% for common organic molecules, which is reasonable to test the accuracy of Lewis's concept. The NBOs are one of a sequence of natural localized orbital sets that include natural atomic orbitals (NAO), natural hybrid orbitals (NHO), natural bond orbitals (NBO) to natural localized molecular orbitals (NLMO) and molecular orbitals (MO).

Each bonding NBO σ_{AB} (the donor) can be written in terms of two directed valence hybrids (NHOs) h_A, h_B on atoms A and B, with corresponding polarization coefficients c_A, c_B:

$$\boldsymbol{\sigma_{AB} = c_A h_A + c_B h_B} \quad \text{-------------} \ (7)$$

The bonds vary smoothly from covalent ($c_A = c_B$) to ionic ($c_A >> c_B$) limit.

Each valence bonding NBO σ must be paired with a corresponding valence antibonding NBO σ* (the acceptor) to complete the span of the valence space:

$$\boldsymbol{\sigma_{AB}^* = c_A h_A - c_B h_B} \quad \text{-------------} \ (8)$$

The stabilization due to σ→σ* donor-acceptor interactions can be estimated by E_2 (second order perturbation energy). In addition to bonding orbital as electron donor, the non-bonding orbital such as lone pair of electrons, the bonding π orbital and antibonding σ orbitals with reasonably higher occupancy can equally be considered as electron donors to the acceptor orbitals.

The orbital overlap picture between the donor-acceptor can be viewed using Chemcraft package in conjunction with the NBO 6.0 [23] package associated with Gaussian software.

2.7 Energy Decomposition Analysis

EDA is an extremely useful tool to dissect the physical origin of intra and intermolecular interactions of molecules. The most popular and well-known EDA methods are the one based on Morokuma [24-26] implemented in Gaussian and Gamess and the Extended Transition State (ETS) of Ziegler and Rauk [27-29] implemented in the ADF program package [30] and localized molecular orbital energy decomposition analysis (LMO-EDA) developed by Su et al. [31]. In the EDA methods, the total interaction energy is defined as the difference between the energy of the heterodimer and the energy of the monomers or fragments and it is decomposed into electrostatic, exchange repulsion, polarization (as a result of charge-transfer effects) and dispersion components. The electrostatic energy term can be defined as the interaction between the static charge densities of each monomer within the heterodimer. This term includes the attractive Coulomb interactions between nuclei of one monomer with the electrons of the other monomer, repulsive Coulomb interactions between the nuclei of monomer and between the electrons of each monomer. The total electrostatic interaction is normally attractive. The Pauli term contains the exchange and repulsion energies, which are stabilizing and destabilizing respectively. The exchange interaction arises due to the antisymmetric nature of a wave function that allows electrons to exchange between monomers. The repulsion interaction originates largely from other types of 2-electron integral terms for monomer orbitals. On the other hand, the dispersion term computed in this method is an attractive term, which arises due to electron correlation [32]. In the ADF-EDA method, the interaction energy is decomposed into three main components: electrostatic, Pauli repulsion and orbital interaction terms. Finally, Steinmann et al. introduced the dispersion corrections by dDXDM method in self-consistent DFT and identified it as an independent energy component in EDA [33].

So the scheme adopted in this work is,

$$\Delta E = ES + PL + OI + DISP$$

where, ES is the electrostatic interaction which takes into account the Coulombic forces of attraction or repulsion between all permanent charges or multipoles, PL for Pauli repulsion, OI is orbital interaction that accounts for both charge transfer and electron exchange terms and DISP is for dispersion energy.

In this thesis, ED analysis was performed on the different types of heterodimers of pyrrole using extended Transition State (ETS) method of Ziegler and Rauk [27-30] implemented in the ADF-2016 package to clearly delineate the contribution of different energy components and the role of other dominant interactions in stabilizing the heterodimers. ED analysis was performed at dispersion corrected B3LYP-D3/TZ2P level of theory. The TZ2P (Triple Zeta with two Polarization functions) basis set was chosen, which has a comparable quality with aug-cc-pVDZ basis set. The input geometries of the different heterodimers for such ED analysis were essentially the optimized geometries at MP2/aug-cc-pVDZ level of theory.

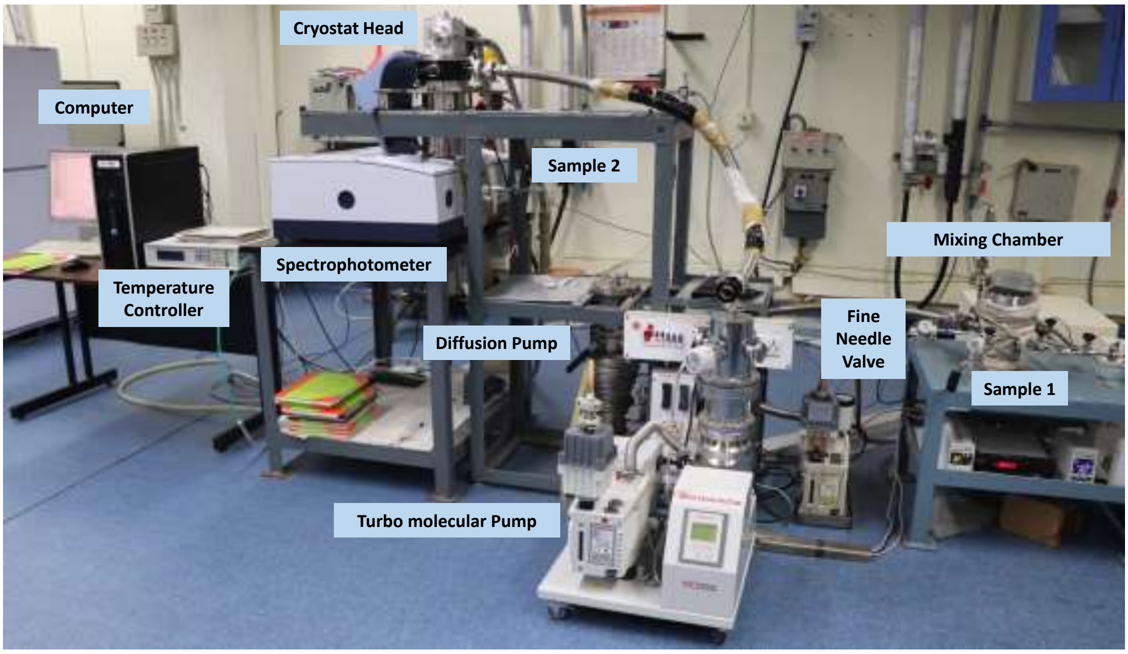

Figure 2.1 Experimental Set-up of Matrix Isolation Infrared Technique.

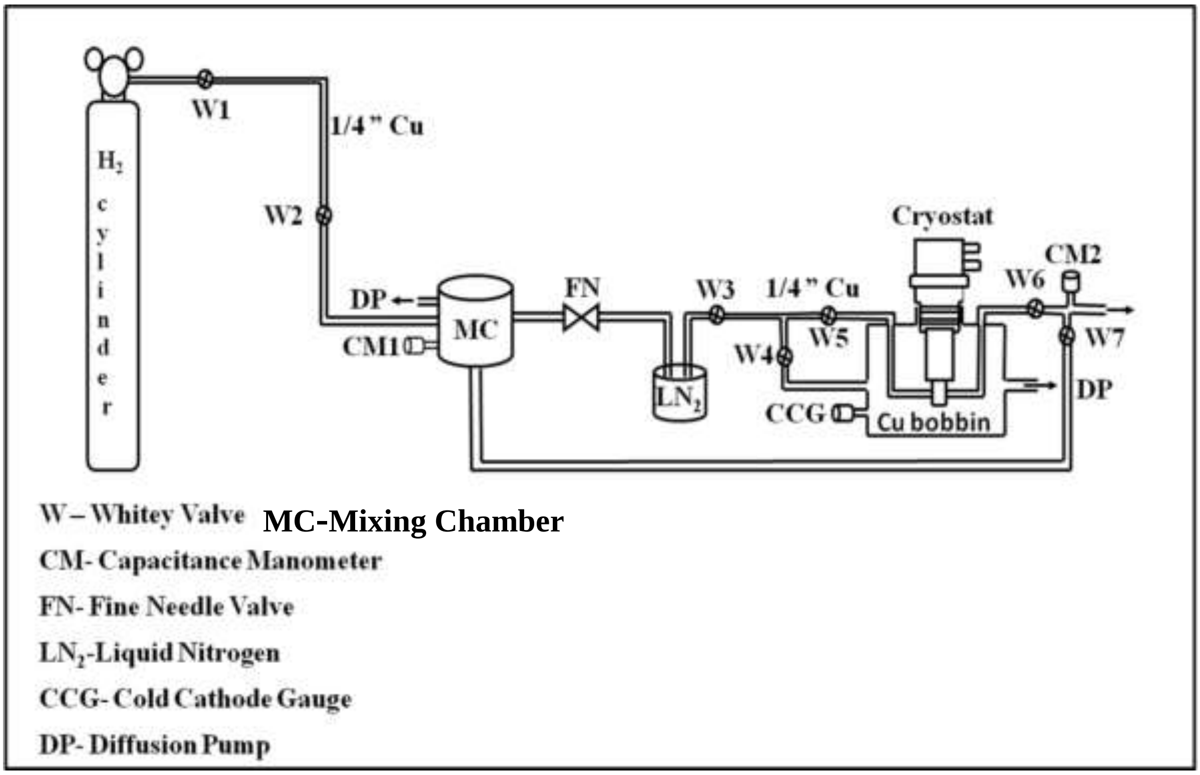

Figure 2.2 Schematic of *para*-Hydrogen generation Set-up.

References

---

1. Matrix Isolation Method for the Experimental Study of Unstable Species, E. Whittle, D. A. Dows, G. C. Pimentel, *J. Chem. Phys.*, **1954**, 22, 1943.

2. Spectroscopic Studies of Reactive Molecules by the Matrix Isolation Method, Edwin D. Becker *and* George C. Pimentel, *J. Chem. Phys.*, **1956**, 25, 224-228.

3. G. C. Pimentel, S.W. Charles, *Pure Appl. Chem.*, **1963**, 7, 111

4. Matrix Isolation Techniques: A Practical Approach; I. R. Dunkin, *Oxford University Press*, **1998.**

5. Matrix isolation; T. Bally, *Wiley-Interscience*: New York, **2004**.

6. Matrix Isolation: A technique for the study of reactive inorganic species, S. Cradock, A. J. Hinchliffe, *Cambridge University Press*, Cambridge, **1975**.

7. Hydrogen Dichloride Radical: Infrared Detection through the Matrix Isolation Technique, P. N. Noble, G. C. Pimentel, *J. Chem. Phys.*, **1968**, 49, 3165-3169.

8. Production and characterization of para-hydrogen gas for matrix isolation infrared spectroscopy, K. Sundararajan, K. Sankaran, N. Ramanathan, R. Gopi, *J. Mol. Struct.*, **2016**, 1117, 181-191.

9. Computational Chemistry: Introduction to theory and applications of Molecular and Quantum Mechanics, E. Lewars, *Kluwer Academic Publishers*, Boston, **2003**.

10. *ab initio* molecular orbital theory, W. J. Hehre, L. Radom, P. V. R. Schleyer J. A. Pople, *John Wiley and Sons*, New York, **1985**.

11. Quantum Chemistry, J. P. Lowe, *Academic Press*, New York, **1978**.

12. Hand book of Computational Chemistry: A practical guide to Chemical Structure and Energy Calculations, T. A. Clark, *John Wiley & sons*, New York, **1985.**

---

13. M. J. Frisch, G. W. Trucks, H. B. Schlegel, G. E. Scuseria, M. A. Robb, J. R. Cheeseman, G. Scalmani, V. Barone, B. Mennucci, G. A. Petersson, H. Nakatsuji, M. Caricato, X. Li, H. P. Hratchian, A. F. Izmaylov, J. Bloino, G. Zheng, J. L. Sonnenberg, M. Hada, M. Ehara, K. Toyota, R. Fukuda, J. Hasegawa, M. Ishida, T. Nakajima, Y. Honda, O. Kitao, H. Nakai, T. Vreven, J. A. Montgomery, Jr., J. E. Peralta, F. Ogliaro, M. Bearpark, J. J. Heyd, E. Brothers, K. N. Kudin, V. N. Staroverov, R. Kobayashi, J. Normand, K. Raghavachari, A. Rendell, J. C. Burant, S. S. Iyengar, J. Tomasi, M. Cossi, N. Rega, J. M. Millam, M. Klene, J. E. Knox, J. B. Cross, V. Bakken, C. Adamo, J. Jaramillo, R. Gomperts, R. E. Stratmann, O. Yazyev, A. J. Austin, R. Cammi, C. Pomelli, J. W. Ochterski, R. L. Martin, K. Morokuma, V. G. Zakrzewski, G. A. Voth, P. Salvador, J. J. Dannenberg, S. Dapprich, A. D. Daniels, Ö. Farkas, J. B. Foresman, J. V. Ortiz, J. Cioslowski, and D. J. Fox, *Gaussian Inc*., Wallingford CT, **2009**.

14. Chemcraft - graphical software for visualization of quantum chemistry computations. https://www.chemcraftprog.com

15. The Calculation of Small Molecular Interactions by the Differences of Separate Total Energies. Some Procedures with Reduced Errors, S. F. Boys, T. F. Bernardi, *Mol. Phys*., **1970**, 19, 553-566.

16. Atoms in Molecules: A Quantum Theory; R. F. W. Bader, *Oxford Univ. Press*: Oxford, U.K., **1990**.

17. Identifying and Analyzing Intermolecular Bonding in van der Waals Molecules. R. G. A. Bone, R. F. W. Bader, *J. Phys. Chem*., **1996**, 100, 10892-10911.

18. Aim 2000, Version 1.0, F. Biegle-Koning, R. F. W. Bader, W. H. Tang, *J. Comput. Chem*. **2000**, 96, 6796.

19. The Quantum Theory of Atoms in Molecules, C. F. Matta, R. J. Boyd, *WILEY-VCH Verlag GmbH & Co. KGaA*, Weinheim, **2007**.

---

20. Valency and Bonding: A Natural Bond Orbital Donor-Acceptor Perspective, F. Weinhold, C. Landis, *Cambridge University Press*: Cambridge, U.K., **2005**.

21. Intermolecular Interactions From A Natural Bond Orbital, Donor-Acceptor Viewpoint, A. E. Reed , L. A. Curtiss , F. Weinhold, *Chem. Rev.*, **1988**, 88, 899-926.

22. Natural orbitals in the quantum theory of two-electron systems, P. O. Lowdin, H. Shull, *Phys. Rev.*, **1956**, 101, 1730.

23. NBO 6.0, E. D. Glendening, J. K. Badenhoop, A. E. Reed, J. E. Carpenter, J. A. Bohmann, C. M. Morales, C. R. Landis, F. Weinhold, Theoretical Chemistry Institute, University of Wisconsin: Madison, **2013**.

24. Molecular orbital Studies Of Hydrogen Bonds. An Ab Initio Calculation For Dimeric H_2O, K. Morokuma, L. Pedersen, *J. Chem. Phys*., **1968**, 48, 3275.

25. Why Do Molecules Interact? The Origin Of Electron Donor-Acceptor Heterodimers, Hydrogen Bonding, and Proton Affinity, K. Morokuma, *Acc. Chem. Res.*, **1977**, 108, 294-300.

26. The Origin of Hydrogen Bonding. An Energy Decomposition Study, H. Umeyama, K. Morokuma, *J. Am. Chem. Soc*., **1977**, 99, 1316-1332.

27. Chemistry with ADF, G. Te Velde, F. M. Bickelhaupt, E. J. Baerends, C. Fonseca Guerra, S. J. A. Van Gisbergen, J. G. Snijders And T. Ziegler, *J. Comp. Chem*., **2001**, 22, 931-967.

28. A theoretical study of the ethylene-metal bond in complexes between copper(1+), silver(1+), gold(1+), platinum(0) or platinum(2+) and ethylene, based on the Hartree-Fock-Slater transition-state method, T. Ziegler, A. Rauk, *Inorg. Chem*., **1979**, 18, 1558-1565.

29. Carbon monoxide, carbon monosulfide, molecular nitrogen, phosphorus trifluoride, and methyl isocyanide as σ donors and π acceptors. A theoretical study by the Hartree-Fock-Slater transition-state method, T. Ziegler, A. Rauk, *Inorg. Chem*., **1979**, 18, 1755-1759.

30. F. M. Bickelhaupt, E. J. Baerends, K. B. Lipkowitz, D. B. Boyd, Rev.Comput. Chem. 15, Wiley-VCH, New York, **2000**.

---

31. Energy decomposition analysis of covalent bonds and intermolecular interactions, P. Su and H. Li, *J. Chem. Phys*., **2009**, 131, 014102(1-2).

32. London dispersion in molecular chemistry - reconsidering steric effects, J. P. Wagner, P. R. Schreiner, *Angew. Chem. Int. Ed*., **2015**, 54, 12274-12296.

33. Dispersion-Corrected Energy Decomposition Analysis For Intermolecular Interactions Based On The Blw And Ddxdm Methods, S. N. Steinmann, C. Corminboeuf, W. Wu, Y. Mo, *J. Phys. Chem. A*, **2011**, 115, 5467–5477.

Chapter 3 Pyrrole and its Multimers in Different Matrixes

This chapter deals with the intermolecular interactions of pyrrole. The infrared spectra of pyrrole monomer and multimers are explored in different matrixes like N_2, Kr, Ne, p-H_2 and compared with Ar and Xe matrixes. *Ab initio* and Density functional theory (DFT) calculations were carried out for the multimers and the vibrational wavenumbers were compared with the experiments.

Although pyrrole and its higher clusters were studied in Ne, Ar and Xe matrixes, the same is not explored in N_2, Kr and p-H_2 matrixes. A clear delineation of the multimers of pyrrole is required for the assignment of the spectral features of heterodimers of pyrrole involving N-H···X (X=O, N, π) interactions. With the computed wavenumbers therefore, the vibrational features due to pyrrole multimers in different matrixes were assigned. This chapter thus provides the preamble for the following chapters in this thesis.

3.1 Computations on Pyrrole Multimers

DFT and *ab initio* calculations were carried out to optimize the structure of C_4H_5N dimer, trimer and tetramer using G09 program [1]. Gómez-Zavaglia and Fausto have elaborately reported on the geometries of the C_4H_5N multimers ($(PyH)_n$ (n=1-4)) computed at B3LYP/6-311++G (d, p) level of theory [2]. They have assigned the vibrational modes of pyrrole and its higher clusters in Ar and Xe matrixes at low temperatures. Computations yielded three and four optimized geometries for C_4H_5N trimers and tetramers, respectively, with the cyclic N-H···π structures being the most stable geometries. The fact that cooperative hydrogen bonding enhances the strength of the pyrrole multimers was quantitatively measured by dividing the binding energy with the number of hydrogen bonds present in the cluster. Furthermore, Matsumoto and Honma have performed computations for the most

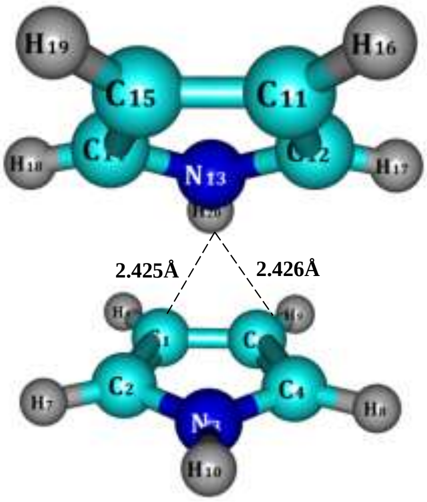

Pyrrole Dimer

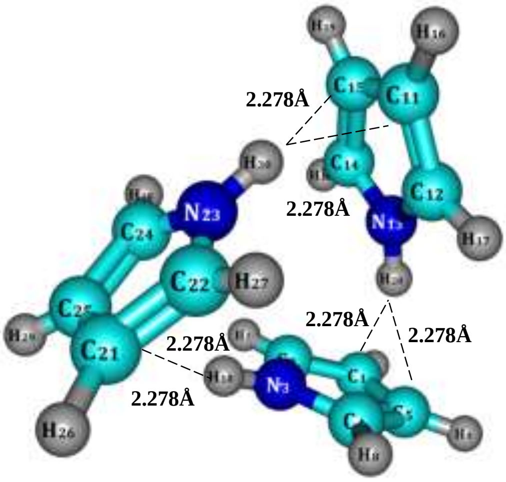

Pyrrole Trimer

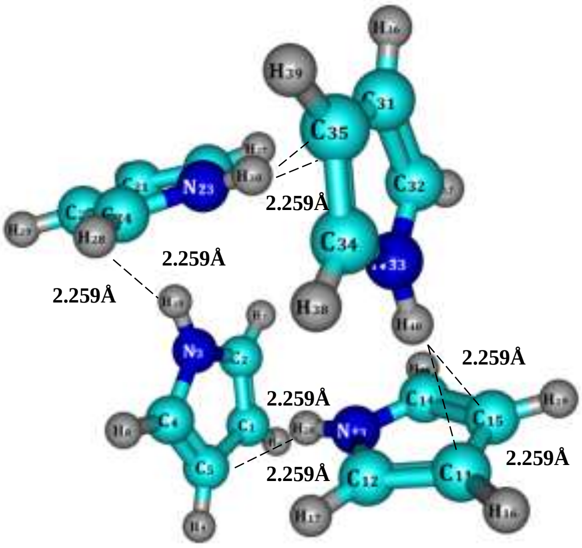

Pyrrole Tetramer

Figure 3.1 Structures of pyrrole dimer, trimer and tetramer computed at MP2/aug-cc-pVDZ level of theory.

Table 3.1 Comparing the Stabilization Energies (in kcal mol^{-1}) of the Dimer, Trimer and Tetramer of Pyrrole at B3LYP/6-311++G (d, p) and MP2/aug-cc-pVDZ Level of Theories.

Systems	**B3LYP/6-311++G(d, p)**	**MP2/aug-cc-pVDZ**
	S.E. (Raw/ZPE/BSSE)	S.E. (Raw/ZPE/BSSE)
Dimer	-3.4/-2.7/-3.0	-10.4/-9.6/-7.1
Trimer	-11.3/-9.5/-10.4	-33.7/-31.5/-23.4
Tetramer	-16.7/-14.5/-14.2	-45.4/-[a]/-30.8
Dipole Moment		
Dimer	2.99	1.95
Trimer	0.02	0.00
Tetramer	0.00	0.00

[a] Vibrational wavenumber calculation could not be performed for the tetramer.

stable structure of C_4H_5N multimers at B3LYP/6-311++G (d, p) level of theory [3]. In this chapter C_4H_5N monomer and its multimers were studied in different matrixes such as N_2, Kr, Ne, *p*-H_2 and compared with Ar and Xe matrixes. Computations were carried out at MP2/aug-cc-pVDZ level of theory to optimize the structures, stabilization energies and vibrational wavenumbers of pyrrole and its higher clusters, which were compared with the counterparts at B3LYP/6-311++G (d, p) level. Table 3.1 compares the stabilization energies (raw, zero point corrected vibrational energy and basis set superposition error corrected) and the dipole moments of the dimer, trimer and tetramer of pyrrole computed at the aforementioned levels of theory. Figure 3.1 illustrates the structures of the dimer, trimer and tetramer of pyrrole at MP2/aug-cc-pVDZ level, where the pyrrole units are inter-associated through N-H···π bonds. Table 3.2 gives an account of the selected structural parameters of the monomer, dimer, trimer and tetramer of pyrrole. In the pyrrole dimer, the intermolecular bond distance between the N-H of one pyrrole (acting as proton donor, PD) and the π-cloud of the other pyrrole (acting as proton acceptor, PA) are 2.626/2.621Å and 2.425/2.426Å at B3LYP/6-311++G (d,p) and MP2/aug-cc-pVDZ level, respectively, indicating a strengthening of hydrogen bonded interaction as result of inclusion of dispersion effects in MP2 methods. The N13-H20 bond in pyrrole (PD) where the proton is donated, gets elongated by 0.004 Å and 0.006 Å at B3LYP/6-311++G (d, p) and MP2/aug-cc-pVDZ levels of theory, respectively, while the N3-H10 bond of the pyrrole (PA) acting as the proton acceptor remains almost the same. Following the same trend in trimer and tetramer, the bond distances do not just reduce but the cyclic structures become symmetric with almost the same bond distances. The elongation of the N-H bond length in pyrrole subunits of the trimer and tetramer is larger than the dimer at MP2 level. Hence, the N-H vibrational wavenumber red-shift in the trimer and tetramer should be substantial. In essence, the cyclic structures of trimer and tetramer must exhibit the same bond distances, which is obtained at the MP2 level in contrast to the slightly different bond distances at the DFT level. Therefore, the superiority of the *ab initio* theory in optimizing the molecular geometries of pyrrole trimer and tetramer is confirmed.

3.2 Experimental Result

The N-H bending and stretching modes of pyrrole are exceptionally sensitive to hydrogen bonding out of its other modes of vibration. Hence, in the current and following chapters, these two modes of pyrrole are probed for the identification of heterodimers. Figure 3.2 and Figure 3.3 grid A show the as-deposited spectra and grid B, the annealed spectra corresponding to the N-H stretching region of C_4H_5N while grid C shows the annealed spectra of the N-H bending region of C_4H_5N- in N_2 and *p*-H_2 matrixes, respectively.

In the as-deposited spectra, C_4H_5N monomer has absorptions at 3519.3, 3514.2, 3510.9 and 3508.9 cm^{-1}, owing to site splitting within N_2 matrix, which agree well with the reported literature value [2]. The peak at 3514.2 cm^{-1} becomes 3513.8 cm^{-1} on annealing. In the *p*-H_2 matrix, the C_4H_5N monomer shows an intense single absorption at 3519.5 cm^{-1}.

When C_4H_5N concentration was increased, new features started appearing in the as-deposited spectra in the N-H stretching region in N_2 matrix at 3500.8, 3423.4, 3413.7, 3386.5, 3371.3 and 3364.8 cm^{-1} and in *p*-H_2 matrix at 3512.3, 3423.6, 3417.3 and 3384.8 cm^{-1}. When the matrix was annealed these features increased in intensity and in addition new peaks started appearing in N_2 matrix at 3503.4, 3417.3, 3414.2, 3385.5, 3335.9, 3331.0 cm^{-1} and in *p*-H_2 matrix at 3514.5 cm^{-1}.

In the N-H bending region, C_4H_5N monomer absorption band appears as a site split feature at 520.2, 527.2 cm^{-1} in N_2 matrix and the corresponding feature was observed at 494.4 cm^{-1} in the *p*-H_2 matrix. On annealing, new features were observed at 534.0, 543.4, 545.7, 550.6, 572.1, 573.5, 585.8, 590.1, 592.8, 596.4 and 599.8 cm^{-1} in N_2 and 518.7, 572.0 cm^{-1} in *p*-H_2 matrix. Figure 3.4 to Figure 3.7 illustrate the IR spectra of the N-H stretching (grid A) and N-H bending (grid B) modes of pyrrole in Ar, Xe, Kr and Ne matrixes. All the matrix isolated spectra shown in the figures were annealed at 35 K(Ar), 50 K(Xe), 45 K(Kr) and 9 K(Ne). In each of the figures, traces ‘a’ and ‘b’ correspond to the as-deposited and annealed spectra, respectively. Although the infrared bands of pyrrole monomer and multimers in the N-H stretching and bending modes were already assigned in Ar and Xe matrixes, for comparison with N_2, Ne, Kr and p-H_2 matrixes, the spectra are discussed. The IR spectra of pyrrole monomer in Ar matrix were similar to the earlier report however some variation was noted in Xe matrix.

In Figure 3.5, although the features at 3504.9, 3500.8, 3498.9, 3495.8 were observed in the as-deposited spectra [2,4], annealing the Xe matrix triggered the formation of new peaks at 3492.6, 3490.7, 3408.0, 3403.2, 3387.8, 3381.7, 3379.3, 3372.8 and 3369.2 cm^{-1}. Similarly, in the N-H bending mode, on annealing the new bands were produced at 593.5, 588.7, 585.8, 515.4, 513.0, 509.6, and a shoulder at 484.8 cm^{-1}.

In the as-deposited spectrum of Fig. 3.6 (trace ‘a’), features due to the N-H stretching mode was found at 3510.2, 3506.1 and 3498.9 cm^{-1}. On annealing the Kr matrix, new bands were observed at 3412.8, 3395.5 and 3376.2 cm^{-1}. On the other hand, in the N-H bending region the monomer features were seen at 486.2 and 485.0 cm^{-1}, but no new features were observed on annealing the Kr matrix.

The IR spectrum of N-H stretching region of pyrrole in Ne matrix was recently reported by Oswald et al. [5]. Figure 3.7 grids A and B show the infrared spectra of pyrrole in Ne matrix. The infrared features of the N-H stretching region of pyrrole in Ne matrix agreed well with the earlier report. In the N-H bending region the monomer features were observed at 477.0, 479.0, 480.9, 483.6, 507.7, 568.9 and 592.3 cm^{-1}. On annealing the matrix new features were observed at 509.6, 499.7 and 495.6 cm^{-1}.

Table 3.2 Selected Structural Parameters for the Monomer, Dimer, Trimer and Tetramer of Pyrrole at B3LYP/6-311++G(d,p) and MP2/aug-cc-pVDZ Levels of Theory.

B3LYP/6-311++G(d,p)		**MP2/aug-cc-pVDZ**	
Monomer			
N3-H10	1.006	**N3-H10**	1.012
∠C4-N3-H10	125.0	**∠C4-N3-H10**	124.8
∠C5-C4-N3-H10	180.0	**∠C5-C4-N3-H10**	180.0
Dimer			
N3-H10	1.007	**N3-H10**	1.013
N13-H20	1.010	**N13-H20**	1.018
H20-C1	2.621	**H20-C1**	2.425
H20-C5	2.626	**H20-C5**	2.426
∠N13-H20-N3	130.0	**∠N13-H20-N3**	100.2
∠N13-H20-N3-H10	-0.5	**∠N13-H20-N3-H10**	0.08
∠N13-H20-C1-C2	48.9	**∠N13-H20-C1-C2**	-5.1
∠N13-H20-C5-C4	-49.8	**∠N13-H20-C5-C4**	5.1
Trimer			
N3-H10/N13-H20/ N23-H30	1.013	**N3-H10/N13-H20/ N23-H30**	1.022
H10-C25/C21	2.589/2.587	**H10-C25/C21**	2.278
H20-C1/C5	2.589/2.594	**H20-C1/C5**	2.278
H30-C15/C11	2.596/2.599	**H30-C15/C11**	2.278
∠N23-H30-C11-C12	26.5	**∠N23-H30-C11-C12**	36.7
∠N23-H30-C15-C14	-26.5	**∠N23-H30-C15-C14**	-36.7
∠N3-H10-C21-C22	28.8	**∠N3-H10-C21-C22**	36.7
∠N3-H10-C25-C24	-29.4	**∠N3-H10-C25-C24**	-37.0
∠N13-H20-C1-C2	-28.0	**∠N13-H20-C1-C2**	-36.6
∠N13-H20-C5-C4	28.7	**∠N13-H20-C5-C4**	37.0
Tetramer			
N3-H10/N13-H20/ N23-H30/N33-H40	1.014	**N3-H10/N13-H20/ N23-H30/N33-H40**	1.021
H20-C1/C5	2.501	**H20-C1/C5**	2.259
H10-C21/C25	2.501	**H10-C21/C25**	2.259

H30-C31/C35	2.501	**H30-C31/C35**	2.259
H40-C15/C11	2.501	**H40-C15/C11**	2.259
∠N3-H10-C21-C22	-89.0	**∠N3-H10-C21-C22**	-104.5
∠N3-H10-C25-C24	89.4	**∠N3-H10-C25-C24**	105.0
∠N13-H20-C1-C2	-89.0	**∠N13-H20-C1-C2**	-104.6
∠N13-H20-C5-C4	89.3	**∠N13-H20-C5-C4**	104.9
∠N33-H40-C11-C12	89.2	**∠N33-H40-C11-C12**	104.8
∠N33-H40-C15-C14	-89.2	**∠N33-H40-C15-C14**	-104.8
∠N23-H30-C31-C32	-89.3	**∠N23-H30-C31-C32**	-105.0
∠N23-H30-C35-C34	89.0	**∠N23-H30-C35-C34**	104.6

Bond lengths are in Ǻ,
Bond angles and dihedral angles in °.

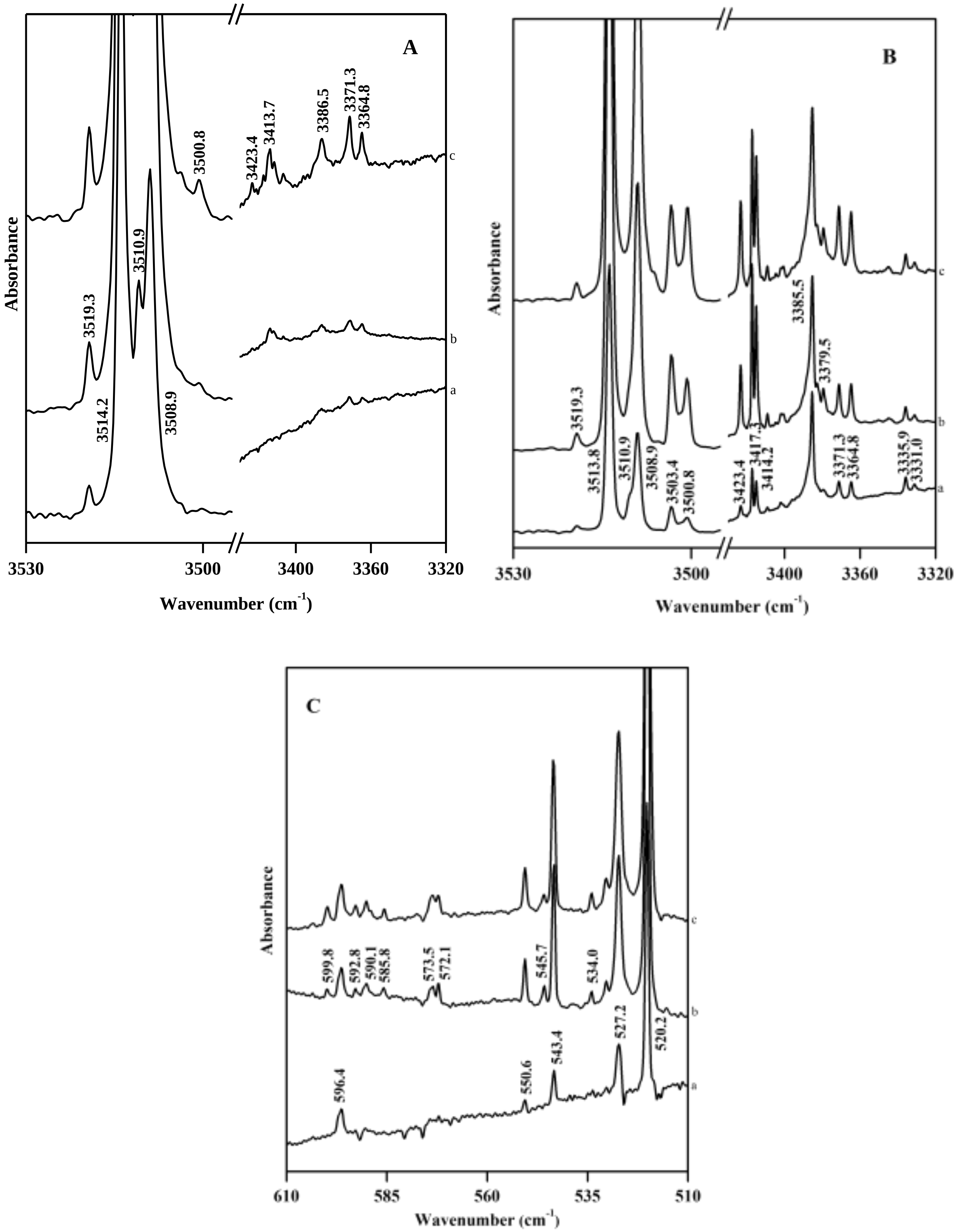

Figure 3.2 Infrared spectra of Pyrrole are illustrated in N_2 matrix. Blocks A and B correspond to 12 K and 30 K annealed spectra in the N-H stretching region, while Block C corresponds to the 30 K annealed spectra in the N-H bending region of C_4H_5N. Typical C_4H_5N/N_2 concentrations are a) 0.2/1000 b) 0.5/1000 and c) 1.0/1000.

3.3 Vibrational Assignments of Pyrrole multimers

Table 3.3 Table 3.3 gives the comparison of experimental shift in N_2, *p*-H_2, Kr, and Ne matrixes with the calculated vibrational wavenumbers of C_4H_5N dimer, trimer and tetramer computed at B3LYP/6-311++G(d, p) level of theory. Experimentally, new features observed in the N-H stretching and bending region of C_4H_5N in N_2 matrix at 3423.4, 3417.3, 3414.2 cm^{-1} and 572.1, 573.5 cm^{-1}, amounting to a shift of -94.9 and 49.1 cm^{-1}; the corresponding features were observed in *p*-H_2 matrix at 3423.6, 3417.3 cm^{-1} and 572.0 cm^{-1}, with a shift of -99.0 and 77.6 cm^{-1}. The experimental shift matches well with the computed shift of -71.8 and 96.8 cm^{-1} for the C_4H_5N dimer, where C_4H_5N acts as a proton donor. Furthermore, features observed at 3503.4, 3500.8 cm^{-1} and 543.4, 545.8, 550.6 cm^{-1} in N_2 matrix, which amounts to a shift of -11.1 and 22.9 cm^{-1} and in *p*-H_2 matrix at 3514.5, 3512.0 cm^{-1} and 518.7 cm^{-1}, with a shift -6.3 and 24.3 cm^{-1} matches well with the computed shift of -5.6 and 42.6 cm^{-1} of the proton accepting N-H mode of C_4H_5N dimer. As the concentration of C_4H_5N was increased, new features started appearing in the N-H stretching region in N_2 matrix at 3371.3, 3364.8 and in *p*-H_2 at 3384.8, at shifts of -145.2 and -134.7 cm^{-1}, respectively and in the N-H bending region in N_2 matrix at 585.8, 590.1, 592.8 cm^{-1}, at an average shift of 65.9 cm^{-1}, deviating a little from the computed shift of -101.4 and 121.9 cm^{-1} for the C_4H_5N trimer (Figure 3.2 and Figure 3.3).

Computations showed that the N-H stretching and bending modes of the C_4H_5N tetramer are shifted by -121.4 and 125.4 cm^{-1} from the C_4H_5N monomer absorption. Experimentally, new feature was observed at 3344.8 cm^{-1} in N_2 matrix in the N-H stretching region, a shift of -168.4 correlates with the computed shift of -121.4 cm^{-1}. New features could not be discerned in the N-H bending region for the C_4H_5N tetramer in *p*-H_2 and N_2 matrixes and also in the N-H stretching region of *p*-H_2 matrix. A strong feature observed at

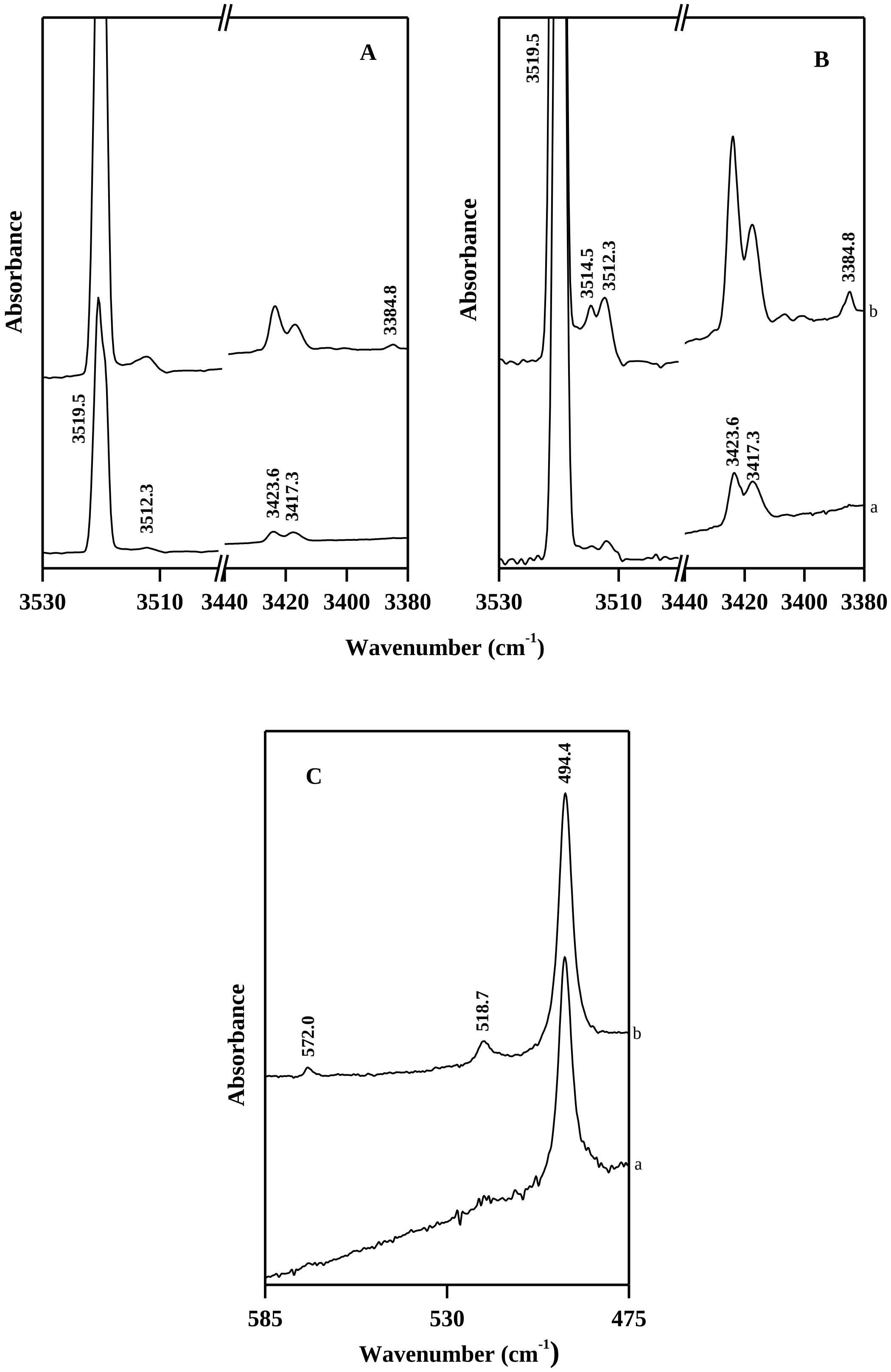

Figure 3.3 Infrared spectra of pyrrole are illustrated in *p*-H_2 matrix. Blocks A and B correspond to 2.5 K and 5.0 K annealed spectra in the N-H stretching region while Block C corresponds to the 5.0 K annealed spectra in the N-H bending region of C_4H_5N. Typical C_4H_5N/*p*-H_2 concentrations are a) 0.5/1000 and b) 1.0/1000.

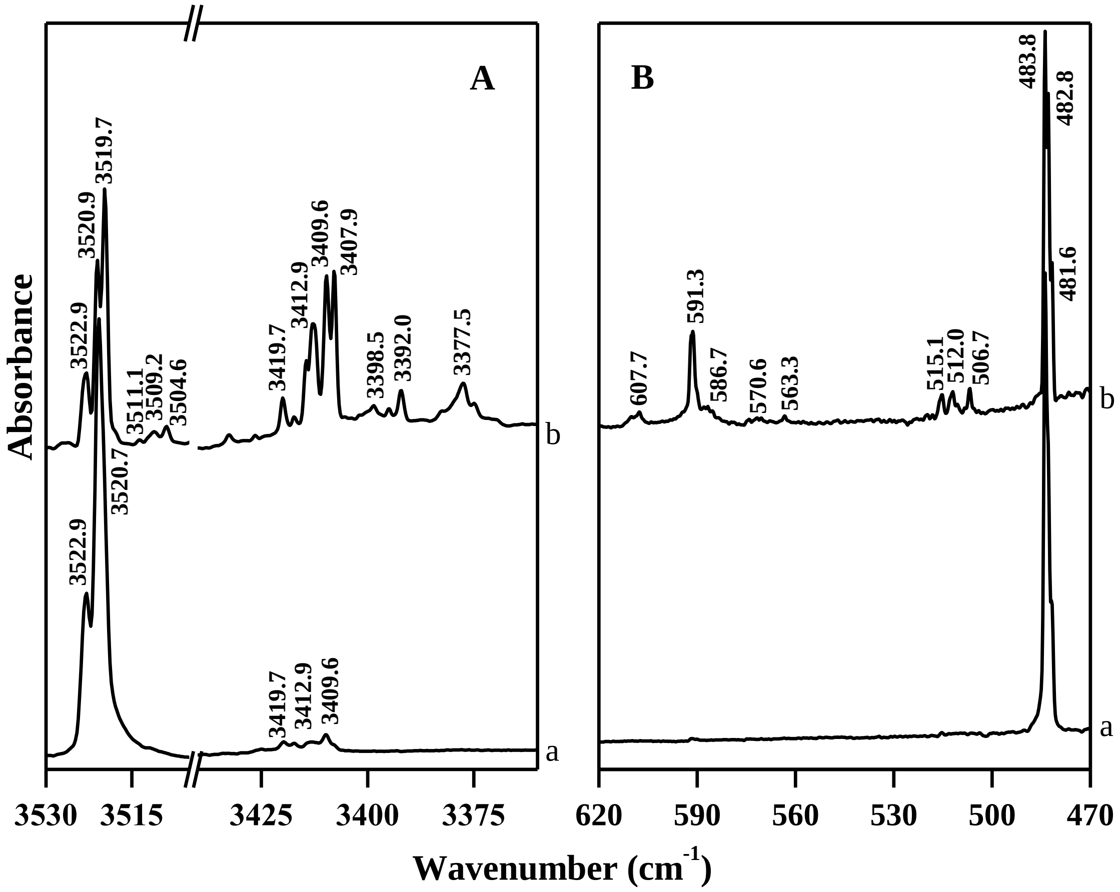

Figure 3.4 Infrared spectra of pyrrole are illustrated in Ar matrix. Blocks A and B correspond to the N-H stretching and bending regions of pyrrole in Ar matrix; (a) as deposited and (b) annealed spectrum at 35 K. Typical C_4H_5N/Ar concentration was 1/1000.

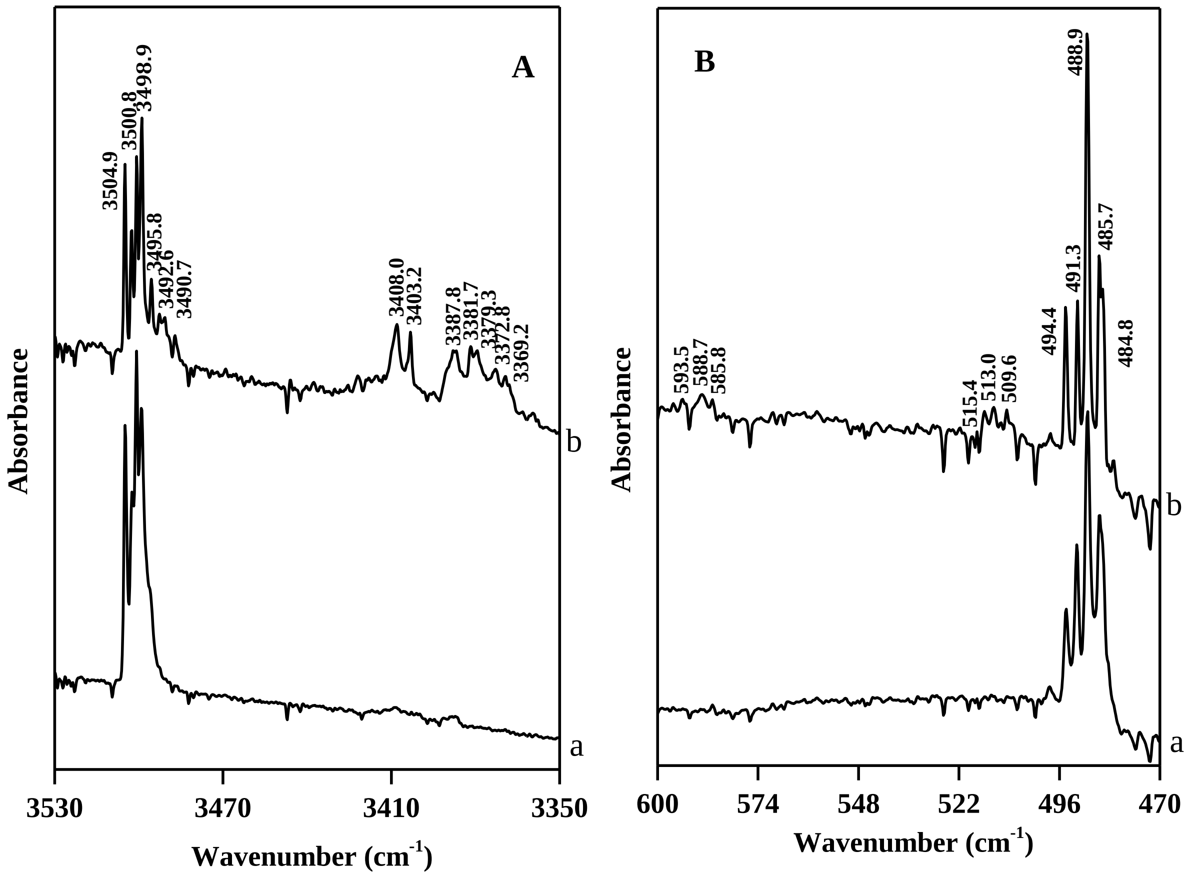

Figure 3.5 Infrared spectra of pyrrole are illustrated in Xe matrix. Blocks A and B correspond to the N-H stretching and bending regions of pyrrole in Xe matrix; (a) as deposited spectrum and (b) 50 K annealed spectrum. Typical C_4H_5N/Xe concentration was 1/1000.

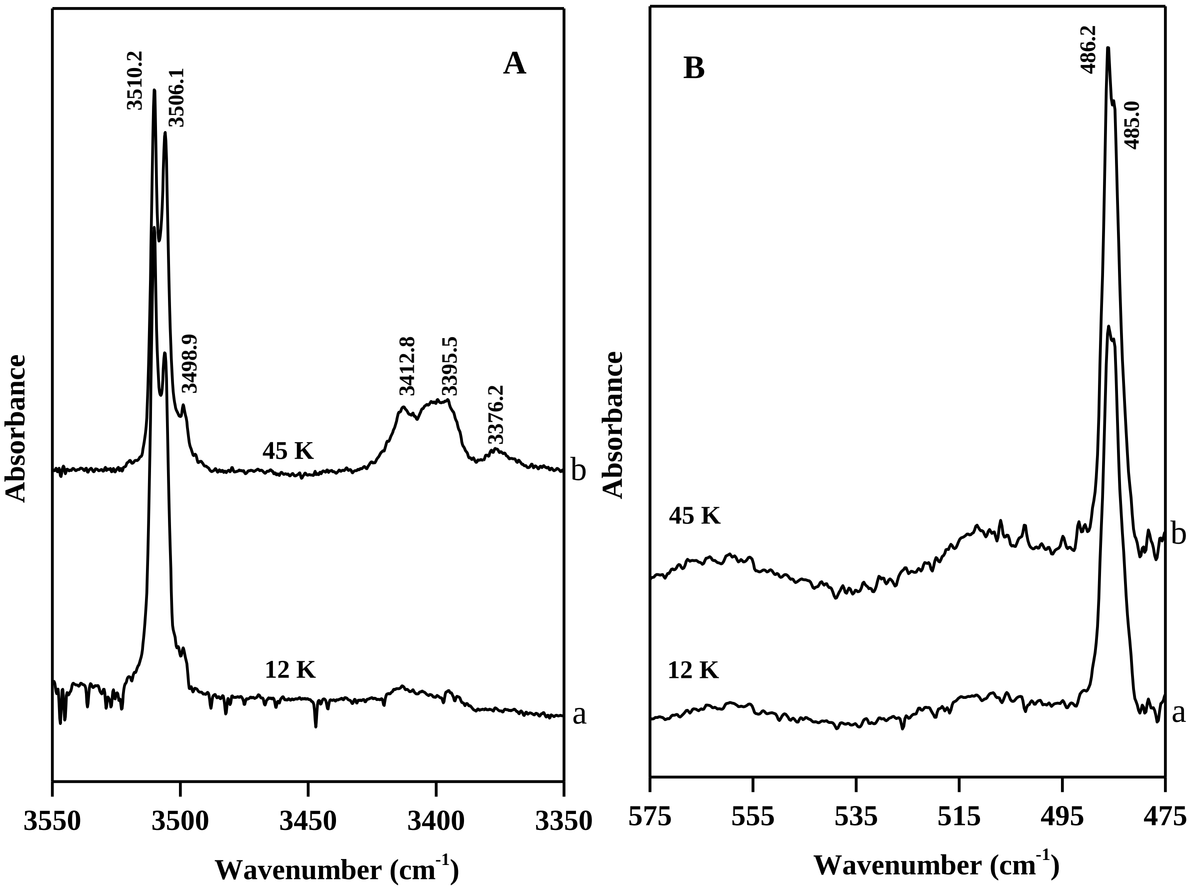

Figure 3.6 Infrared spectra of pyrrole are illustrated in Kr matrix. Blocks A and B correspond to the N-H stretching and bending regions of pyrrole in Kr matrix; (a) as deposited spectrum and (b) 45 K annealed spectrum. Typical C_4H_5N/Kr concentration was 1/800.

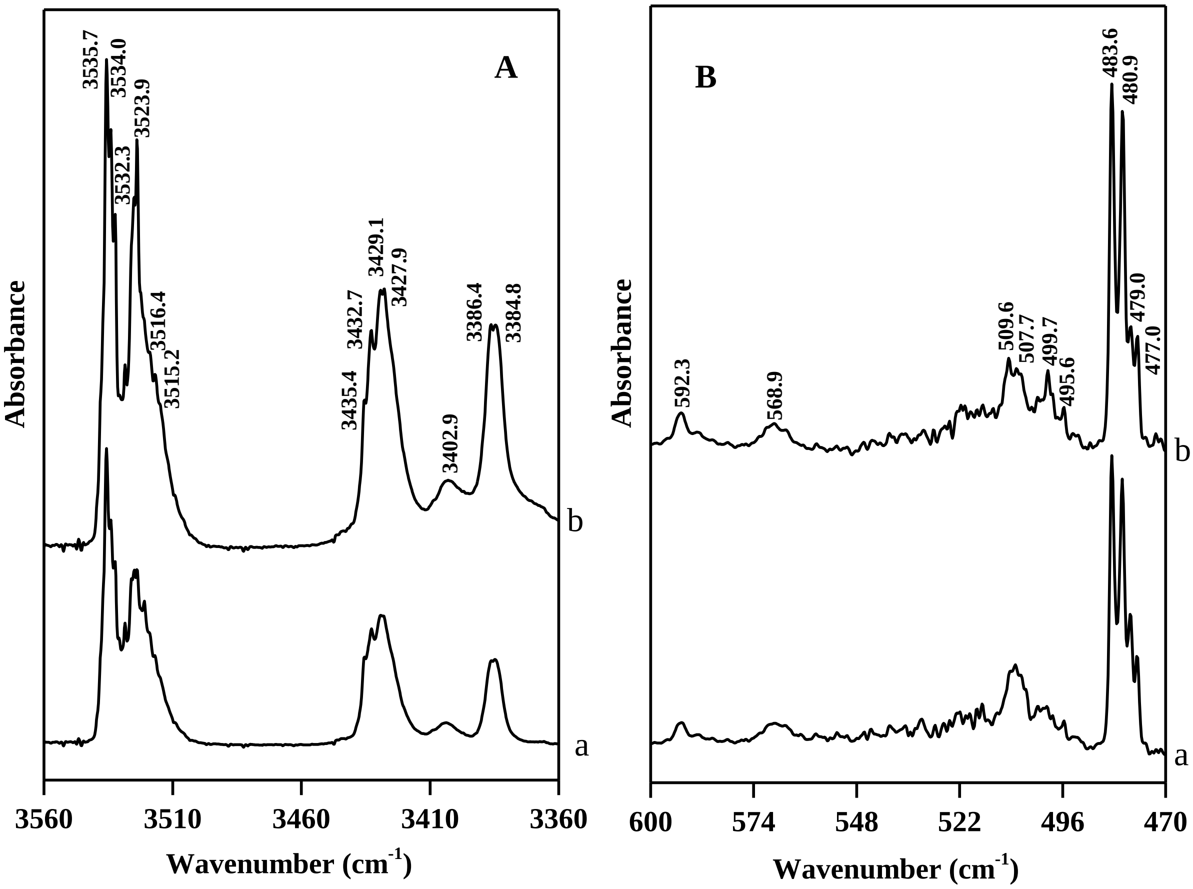

Figure 3.7 Infrared spectra of pyrrole are illustrated in Ne matrix. Blocks A and B correspond to the N-H stretching and bending regions of pyrrole in Ne matrix; (a) as deposited spectrum (b) 9 K annealed spectrum. Typical C_4H_5N/Ne concentration was 1/1000.

3385.5/3379.5 and 596.4 cm^{-1} in the N-H stretching and bending region of C_4H_5N in N_2 matrix is due to C_4H_5N-H_2O heterodimer in nitrogen matrix, which will be discussed in detail in Chapter 5.

Even though the infrared spectra of C_4H_5N monomer in Xe matrix have been reported, the formation of higher aggregates is still elusive in this matrix. As can be seen from Figure 3.5, on annealing the Xe matrix new peaks were observed at 3492.6/3490.7 and 3408.0/3403.2 cm^{-1} with an average shift of -8.5 and -94.5 cm^{-1}, respectively matching well with the computed shifts of -5.6 and -71.8 cm^{-1} for the $(C_4H_5N)_2$. Apart from the dimer features new bands were observed at 3387.8, 3381.7, 3379.3 cm^{-1}, a red-shift of -117.2 cm^{-1}, correlates with the computed shift of -101.4 cm^{-1} for C_4H_5N-trimer. Further, the computed shift of -121.4 cm^{-1} for C_4H_5N tetramer matches closely with the experimental red-shift of -129.1 cm^{-1} for the features observed at 3372.8/3369.2 cm^{-1}. The N-H bending modes of C_4H_5N also show infrared features at 515.4/513.0/509.6, 585.8 and 593.5/588.7 cm^{-1} corresponding to the C_4H_5N dimer, trimer and tetramer, respectively

In Kr matrix, annealing (Figure 3.6) at 45 K generated new bands at 3498.9 and 3412.8 cm^{-1} which amounts to a red-shift of -9.2 and -95.3 cm^{-1} agrees with the computed shifts as mentioned before, for the C_4H_5N dimer. The broad peak at 3395.9 cm^{-1} and a small hump at 3376.2 cm^{-1} which are red-shifted by -112.2 cm^{-1} and -131.9 cm^{-1} from the C_4H_5N monomer, were assigned to the trimer and tetramer, respectively. No new features could be observed for the higher cluster of C_4H_5N in the N-H bending region.

Compared to the other inert matrixes Ne matrix is relatively less reactive with the guest molecules. Surprisingly, in this matrix the infrared feature of C_4H_5N monomer has multiple site split bands similar to the other matrixes. The features in the N-H stretching mode matches very well with the earlier reported spectra by Oswald et al. [5] and the bands in the N-H bending mode were assigned for the first time. Apart from the monomer peaks at 3535.7/3534.0/3532.3

cm^{-1} in the N-H stretching and the corresponding feature in the N-H bending region at 483.6/480.9/479.0/477.0 cm^{-1}, new peaks due to dimer were observed on annealing (9 K) at 3523.9/3516.4/3515.2, 3435.4/3432.7/3429.1/3427.9, 495.6/499.7/507.7/509.6 and 568.9 cm^{-1} at a red-shifts of -15.7 and -100.2 cm^{-1} and a blue-shift of 23.1 and 88.8 cm^{-1}, matches well with the computed shift for the C_4H_5N dimer. C_4H_5N-trimer feature was observed at 3386.4/3384.8, 592.3 cm^{-1} at a shift of -145.9 and 112.2 cm^{-1} compares well with the computed shift of -101.4 and 121.9 cm^{-1}. For the tetramer, no peak was observed in the N-H stretching and bending region of pyrrole in Ne matrix.

Although in the present chapter DFT computation was used to corroborate with the experiments, in the following chapters the experimental data will be compared with the MP2/aug-cc-pVDZ level of theory. Table 3.4 represents a fine correlation between the computed shifts at MP2/aug-cc-pVDZ level of theory with the experimental shifts in various matrixes. Computing the vibrational wavenumber for the pyrrole tetramer at aforementioned level of theory was not possible with the existing computational facility, therefore DFT level of theory was chosen to compare the experimental and computed shifts. Henceforth, in the following chapters, MP2/aug-cc-pVDZ level will be used to correlate with the experimental results.

3.4 Summary

Table 3.5 compares the vibrational wavenumbers in the N-H stretching and bending region of C_4H_5N monomer and multimers in solid N_2, *p*-H_2, Xe, Ne, Ar, and Kr with the gas phase. The experimental wavenumbers were obtained in different matrixes and the gas phase data was taken from literature [6]. It is clear from the table that the N-H stretching and bending mode of C_4H_5N monomer in the gas phase has a small splitting whereas a single peak was found for the higher multimers. Invariably, in solid Ar, Kr, Ne, N_2 and Xe matrixes, the pyrrole monomers and multimers features are multiple site split due to the interaction of the solid host with the guest molecules. As expected, in *p*-H_2 matrix due to large ZPE and quantum nature of the solid, a single absorption was observed. In *p*-H_2 matrix, the multimer features are broader and relatively free from site splitting compared to other solid matrixes. In Kr matrix, site-splitting is comparatively lesser for the monomer and the multimers, but those of the higher clusters overlap, and form a broad hump with barely discernible dimer and trimer peaks. Notably, the features due to C_4H_5N monomers and multimers were well resolved in N_2 matrix. The monomer peaks are broad and split to multiplets in the Ne and Xe matrixes, any weak heterodimer with a small shift of 2-5 cm^{-1} would hardly be resolved from the monomer bands. The FWHM of the monomer as well as dimer bands of C_4H_5N were on the higher side in *p*-H_2, Ne, Kr and Xe matrixes, and hence weak heterodimers may not be differentiated from the monomer/multimers of C_4H_5N. Hence, to study the weak, intermediate and strong heterodimers of C_4H_5N, N_2 and Ar matrixes were chosen.

Table 3.3 Comparison of shifts in the Experimental Vibrational Wavenumbers in N_2, Kr, Ne and *p*-H_2 Matrixes with the Computed Wavenumbers of Pyrrole Monomer, Dimer, Trimer and Tetramer. Computations were performed at B3LYP/6-311++G (d, p) Level of Theory.

Computed ν (cm^{-1})		**Experimental ν (cm^{-1})**								**Mode Assignment**
		N_2		***p*-H_2**		**Kr**		**Ne**		
ν	**Δν**	**N**	**Δν**	**ν**	**Δν**	**ν**	**Δν**	**ν**	**Δν**	
Pyrrole										
478.9 (78)	-	520.2 527.2	-	494.4	-	486.2 485.0	-	483.6 480.9 479.0 477.0	-	N-H bending mode of pyrrole
3674.2 (68)	-	3519.3 3513.8 3510.9 3508.9	-	3519.5	-	3510.2 3506.1	-	3535.7 3534.0 3532.3	-	N-H str. mode of pyrrole
Pyrrole Dimer										
521.5 (99)	42.6	543.4 545.8 550.6	22.9[d]	518.7	24.3	-[a]	-	495.6 499.7 507.7 509.6	23.05	N-H bending mode of pyrrole dimer (PA)[b]
575.7 (27)	96.8	572.1 573.5	49.1[d]	572.0	77.6	-[a]	-	568.9	88.8	N-H bending mode of pyrrole dimer (PD)[c]
3668.6 (76)	-5.6	3503.4 3500.8	-11.1[d]	3514.5 3512.0	-6.3[d]	3498.9	-9.2	3516.4 3515.2 3523.9	-15.7	N-H str. mode of pyrrole dimer (PA)[b]

3602.4 (330)	-71.8	3423.4 3417.3 3414.2	-94.9[d]	3423.6 3417.3	-99.0[d]	3412.8	-95.3	3435.4 3432.7 3429.1 3427.9	-100.2	N-H str. mode of pyrrole dimer (PD)[c]
Pyrrole Trimer										
600.8 (45)	121.9	585.8 590.1 592.8	65.9[d]	-[a]	-	-[a]	-	592.3	112.2	N-H bending mode of pyrrole trimer
3571.7 (476) 3574.0 (486)	-101.4[d]	3371.3 3364.8	-145.2[d]	3384.8	-134.7	3395.9	-112.2	3386.4 3384.8	-145.9	N-H str. mode of pyrrole trimer
Pyrrole Tetramer										
604.3 (53)	125.4	-[a]	-	-[a]	-	-[a]	-	-[a]	-	N-H bending mode of pyrrole tetramer
3552.8 (950)	-121.4	3344.8	-168.4	-[a]	-	3376.2	-131.9	-[a]	-	N-H str. mode of pyrrole tetramer

[a] Experimental features are not observed;
[b] Proton Acceptor;
[c] Proton Donor;
[d] Average multiplet experimental wavenumbers of the monomers and multimers were taken to compute the experimental shift in the pyrrole dimer, trimer and tetramer.

Table 3.4 Comparing the Computed Vibrational Wavenumber shifts of the Dimer and Trimer of Pyrrole at MP2/aug-cc-pVDZ Level of Theory with the Experimental shifts.

Computed Δν (cm^{-1})	**Experimental Δν (cm^{-1})**				**Mode Assignment**
	N_2	***p*-H_2**	**Kr**	**Ne**	
Pyrrole Dimer					
30.1	22.9	24.3	-	23.05	N-H bending mode of pyrrole dimer (PA)
80.2	49.1	77.6	-	88.8	N-H bending mode of pyrrole dimer (PD)
-16.3	-11.1	-6.3	-9.2	-15.7	N-H str. mode of pyrrole dimer (PA)
-109.0	-94.9	-99.0	-95.3	-100.2	N-H str. mode of pyrrole dimer (PD)
Pyrrole Trimer					
94.9	65.9	-	-	112.2	N-H bending mode of pyrrole trimer
-169.4	-145.2	-134.7	-112.2	-145.9	N-H str. mode of pyrrole trimer

Vibrational wavenumber calculation for the pyrrole tetramer at MP2/aug-cc-pVDZ level was not completed due to the existing computational facility, and hence eliminated from the table.

Table 3.5 Comparison of the Vibrational Wavenumbers of Pyrrole Monomer, Dimer, Trimer and Tetramer in Gas Phase, Xe, Ar, N_2, Kr, Ne and *p*-H_2 Matrixes.

System	Gas Phase	Xe		Ar		N_2		*para*-H_2		Kr		Ne	
		$\nu_{\text{N-H}}$ str	$\nu_{\text{N-H}}$ bend	$\nu_{\text{N-H}}$ str	$\nu_{\text{N-H}}$ bend	$\nu_{\text{N-H}}$ str	$\nu_{\text{N-H}}$ bend	$\nu_{\text{N-H}}$ str	$\nu_{\text{N-H}}$ bend	$\nu_{\text{N-H}}$ str	$\nu_{\text{N-H}}$ bend	$\nu_{\text{N-H}}$ str	$\nu_{\text{N-H}}$ bend
Monomer	3531.0 3530.8	3504.9 3500.8 3498.9 3495.8	494.4 491.3 488.9 485.7 484.8	3522.9 3520.9 3519.7	483.8 482.8 482.6	3519.3 3513.8 3510.9 3508.9	520.2 527.2	3519.5	494.4	3510.2 3506.1	486.2 485.0	3535.7 3534.0 3532.3 3523.9	483.6 480.9 479.0 477.0
Dimer-PA	3524.0	3492.6 3490.7	515.4 513.0 509.6	3511.1 3509.2 3504.6	515.1 512.0 506.7	3503.4 3500.8	543.4 545.8 550.6	3514.5 3512.0	518.7	3498.9	-[a]	3516.4 3515.2	495.6 499.7 507.7 509.6
Dimer-PD	3444.0	3408.0 3403.2	-[a]	3419.7 3412.9 3409.6 3407.9	563.3	3423.4 3417.3 3414.2	572.1 573.5	3423.6 3417.3	572.0	3412.8	-[a]	3435.4 3432.7 3429.1 3427.9	568.9
Trimer	3393.0	3387.8 3381.7 3379.3	585.8	3398.5 3392.0	570.6 607.7	3371.3 3364.8	585.8 590.1 592.8	3384.8	-[a]	3395.9	-[a]	3386.4 3384.8	592.3
Tetramer	-[a]	3372.8 3369.2	593.5 588.7	3377.5	586.7 591.3	3344.8	-[a]	-[a]	-[a]	3376.2	-[a]	-[a]	-[a]

PA-Proton Acceptor; PD-Proton Donor

[a] Features not observed

References

---

1. M. J. Frisch, G. W. Trucks, H. B. Schlegel, G. E. Scuseria, M. A. Robb, J. R. Cheeseman, G. Scalmani, V. Barone, B. Mennucci, G. A. Petersson, H. Nakatsuji, M. Caricato, X. Li, H. P. Hratchian, A. F. Izmaylov, J. Bloino, G. Zheng, J. L. Sonnenberg, M. Hada, M. Ehara, K. Toyota, R. Fukuda, J. Hasegawa, M. Ishida, T. Nakajima, Y. Honda, O. Kitao, H. Nakai, T. Vreven, J. A. Montgomery, Jr., J. E. Peralta, F. Ogliaro, M. Bearpark, J. J. Heyd, E. Brothers, K. N. Kudin, V. N. Staroverov, R. Kobayashi, J. Normand, K. Raghavachari, A. Rendell, J. C. Burant, S. S. Iyengar, J. Tomasi, M. Cossi, N. Rega, J. M. Millam, M. Klene, J. E. Knox, J. B. Cross, V. Bakken, C. Adamo, J. Jaramillo, R. Gomperts, R. E. Stratmann, O. Yazyev, A. J. Austin, R. Cammi, C. Pomelli, J. W. Ochterski, R. L. Martin, K. Morokuma, V. G. Zakrzewski, G. A. Voth, P. Salvador, J. J. Dannenberg, S. Dapprich, A. D. Daniels, Ö. Farkas, J. B. Foresman, J. V. Ortiz, J. Cioslowski, and D. J. Fox, *Gaussian Inc*., Wallingford CT, **2009**.

2. Self-Aggregation in Pyrrole: Matrix Isolation, Solid State Infrared Spectroscopy, and DFT Study, A. Gomez-Zavaglia, R. Fausto, *J. Phys. Chem. A*, **2004**, 108, 6953-6967.

3. N-H Stretching Vibrations of Pyrrole Clusters Studied by Infrared Cavity Ringdown Spectroscopy, Y. Matsumoto, K. Honma, *J. Chem. Phys*., **2007**, 127**,** 184310(1-9).

4. The Self-Associating Behavior of Pyrrole in Liquid Xenon, L. I. De Beuckeleer, W. A. Herrebout, *J. Mol. Struct*., **2016**, 1108, 71-79.

5. Incremental NH stretching downshift through stepwise nitrogen complexation of pyrrole: a combined jet expansion and matrix isolation study, S. Oswald, M. A. Suhm, S. Coussan , *Phys. Chem. Chem. Phys*., **2019**, 21, 1277-1284.

---

6. N–H$\cdots\pi$ Interactions in Pyrroles: Systematic Trends from the Vibrational Spectroscopy of Clusters, I. Dauster, C. Rice, P. Zielke, M. Suhm, *Phys. Chem. Chem. Phys*., **2008**, 10, 2827-2835.

Chapter 4 H···π Interactions of Pyrrole

This chapter explores the N-H···π interactions of pyrrole with benzene, ethylene and acetylene. Apart from the primary N-H···π interaction the heterodimers are stabilized by C-H···π and π···π* interactions between the electron clouds of pyrrole and the π-electron system.

4.1 Experimental Conditions

The details of the matrix isolation set-up and the experimental methodology were described in Chapter 2. Acetylene (C_2H_2, Asiatic Oxygen Limited, India, Commercial grade) and ethylene (C_2H_4, Air Products Limited, London, 99%) were used without further purification, while benzene (C_6H_6, Merck, >99%) and pyrrole (C_4H_5N, Spectrochem, 99%) were frozen to ~100 K and subjected to several freeze-pump-thaw cycles before use. The sample to matrix ratio ranged 0.025(C_4H_5N)/0.5(C_2H_2/C_2H_4/C_6H_6)/1000 to 0.25/2.0/1000 for N_2 and 0.1/0.5/1000 to 0.25/2.0/1000 for Ar.

4.2 Experimental and Computational Results

4.2.1 Pyrrole···Benzene

Experimentally, the formation of pyrrole-benzene (PB) heterodimer at low temperatures in inert matrixes was evidenced in the N-H stretching, bending modes of C_4H_5N and C-H bending mode of C_6H_6. Figure 4.1 grids A and B, trace ‘a’ correspond to IR spectra of C_6H_6 alone in N_2 and Ar matrixes, which has no absorption in this region, while trace ‘b’ in all the grids show the IR spectra of N-H stretching mode of C_4H_5N, which has absorptions at 3519.3, 3513.8 and 3508.9 cm^{-1} in N_2 matrix and the corresponding features observed in Ar matrix at 3522.9, 3520.9 and 3519.7 cm^{-1} respectively [1]. As the concentration of C_6H_6 was varied, new spectral bands were observed at 3461.4/3457.6 cm^{-1} in N_2 and at 3460.9/3456.9 cm^{-1} in Ar matrixes. Figure 4.2 grids A and B show the N-H bending mode of

C_4H_5N; with variation in C_6H_6 concentration, new features appeared at 545.5 and 538.8 cm^{-1} in N_2 and Ar matrixes, respectively. Figure 4.3 shows the infrared spectra of C-H bending region of C_6H_6 spanning the region 670-700 cm^{-1} in N_2 matrix, where the intense feature observed at 678.1 cm^{-1} is due to the C_6H_6 monomer in N_2 matrix and the spectral bands observed at 679.3/680.3/681.9 cm^{-1} are due to C_6H_6 dimer [2]. As the concentration of C_4H_5N was varied, a sharp peak at 683.2 cm^{-1} picks up in intensity.

4.2.1.1 Computational details

Computations performed at MP2/aug-cc-pVDZ level of theory indicated that the global minimum corresponding to 1:1 $C_4H_5N\cdots C_6H_6$ PB-A heterodimer possesses a partially stacked geometry with N-H⋯π and cooperative π⋯π* interactions (NBO Analysis). Geometry optimization of C_4H_5N with C_6H_6 also resulted in another local minimum structure stabilized only by N-H⋯π interaction with a tilted T-shape (PB-B) geometry. In PB-A heterodimer, the bond distances between the hydrogen H22 of C_4H_5N with C_6H_6 carbons C1/C3, C2/C6 and C7/C10 are 2.619, 2.868 and 3.088 Å, respectively clearly show the presence of N-H⋯π interaction. Surprisingly, the donor-acceptor dihedral angle of ∠N15-H22-C1-C3 is 105.9° and as a result N-H of C_4H_5N sub-molecule is inclined towards the C_6H_6 (Figure 4.4).

Apart from this primary N-H⋯π interaction, NBO analysis (which will be discussed in section 4.4) revealed a secondary interaction between the π-electrons of the two aromatic moieties, which plays a crucial role in altering the geometry of the PB-A heterodimer. Unlike previous reports, a partially stacked geometry is preferred over the T-shaped structure as revealed through computations [3-4]. Pfaffen et al. used DFT-D, spin component scaled (SCS) MP2 and CC2 methods with aug-cc-pVTZ basis sets, which yielded a T-shaped geometry with an N-H⋯π interaction for the $C_4H_5N\cdots C_6H_6$ heterodimer. Experimentally, the

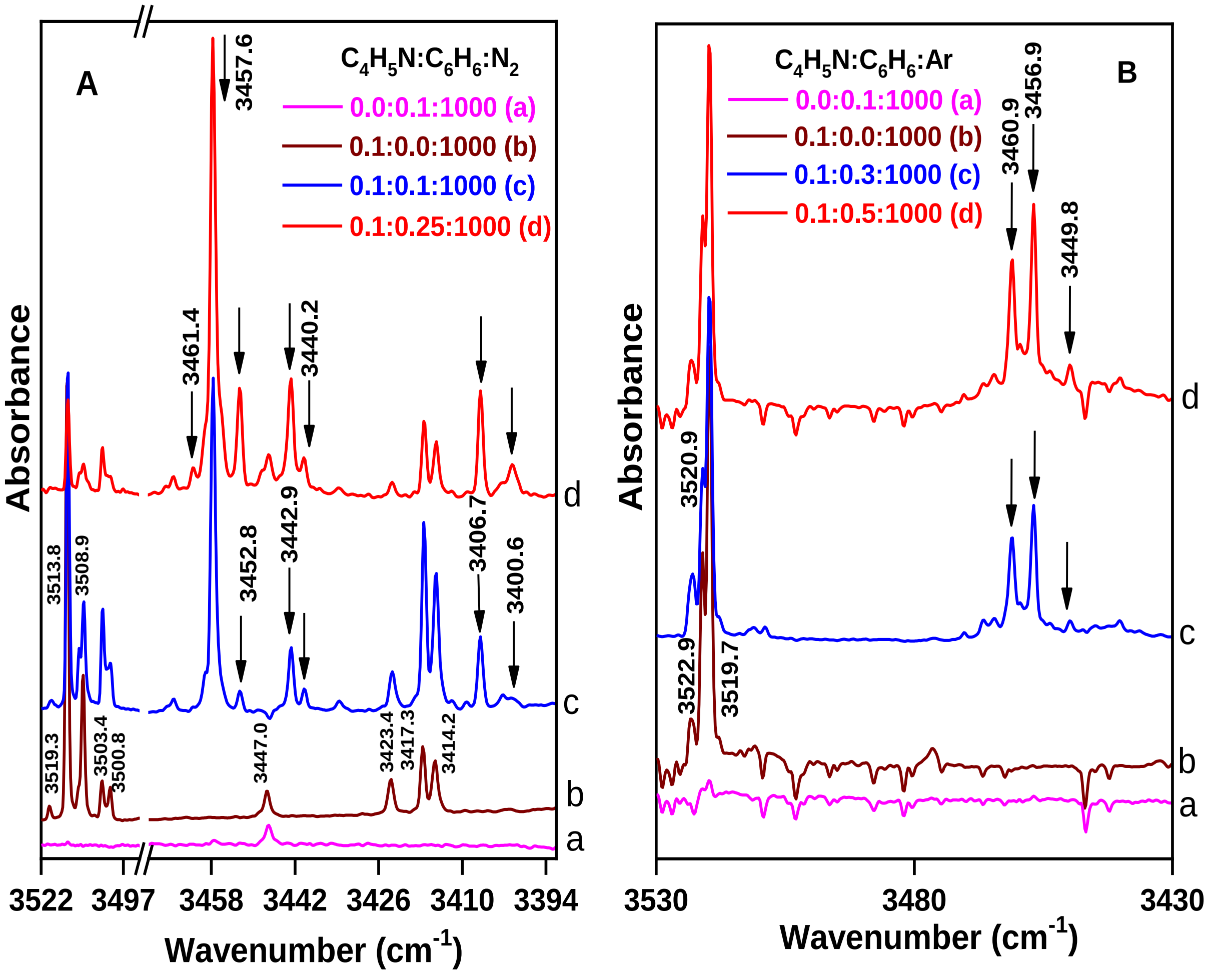

Figure 4.1 Grids A, B correspond to the infrared spectra of the N-H stretching region of C_4H_5N in N_2 and Ar matrixes, respectively. All spectra shown were annealed at 30 K (N_2) and 35 K (Ar)

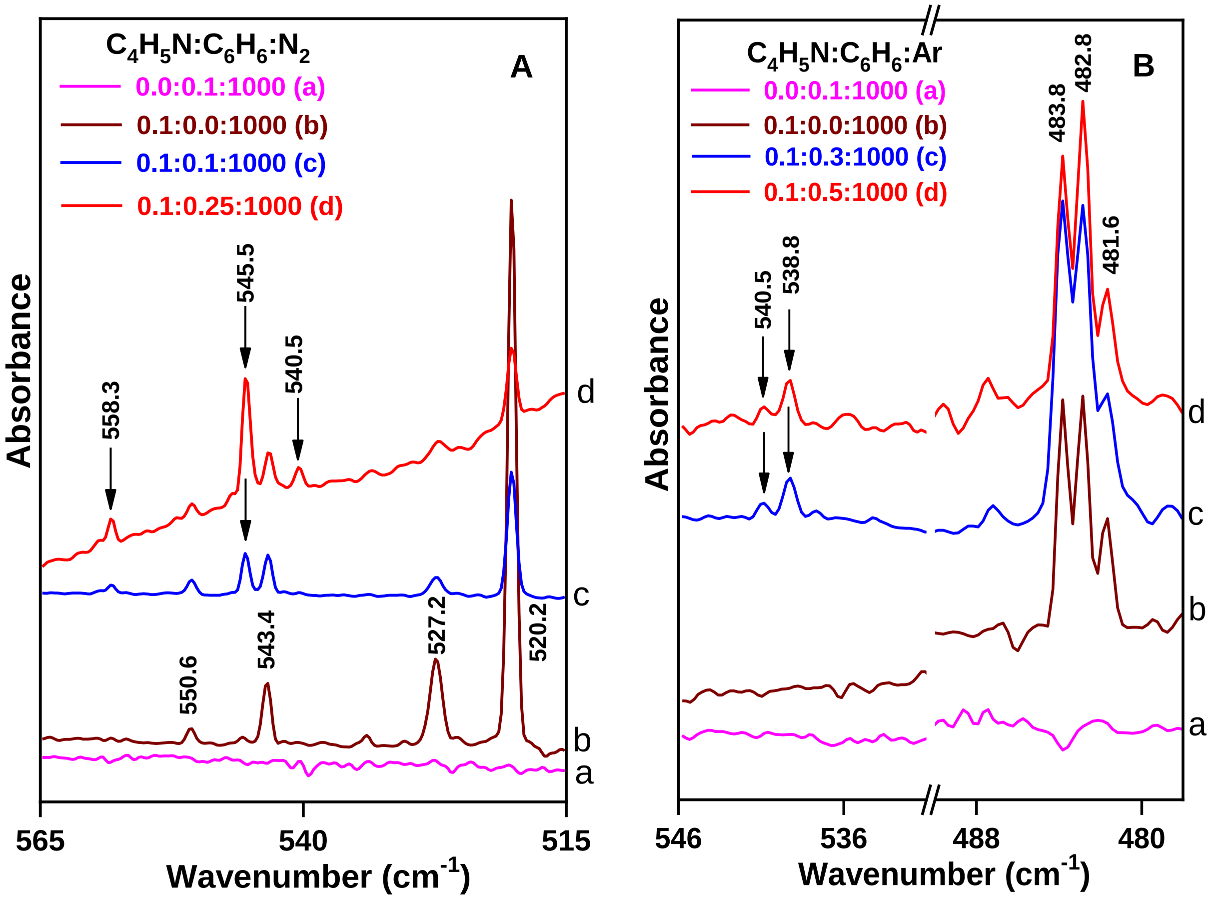

Figure 4.2 Grids A, B correspond to the infrared spectra of the N-H bending region of C_4H_5N in N_2 and Ar matrixes, respectively. All spectra shown were annealed at 30 K (N_2) and 35 K (Ar).

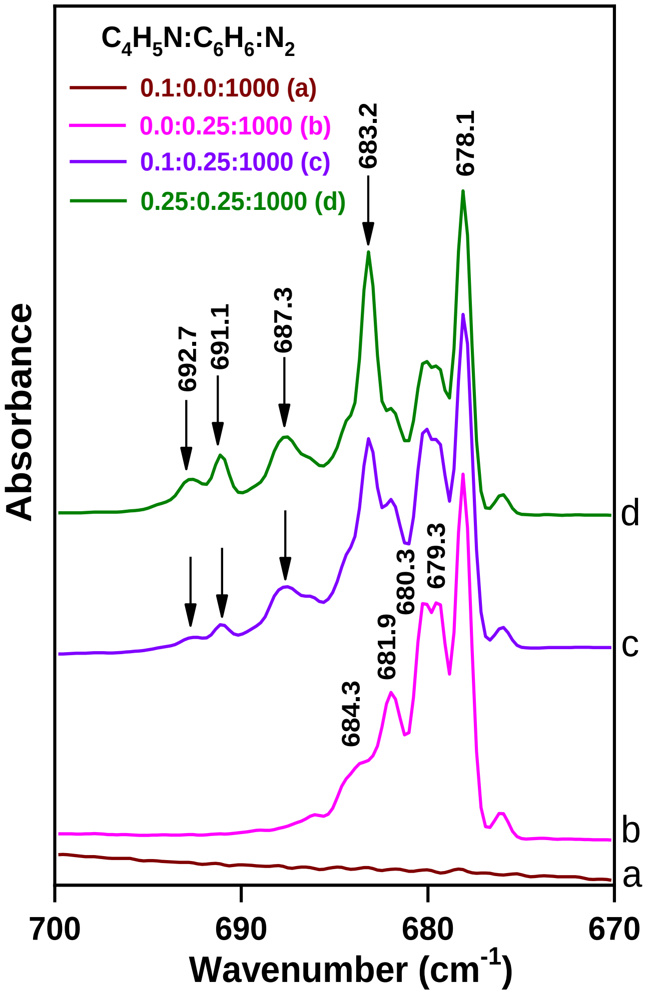

Figure 4.3 The infrared spectra of C-H bending region of C_6H_6 in N_2 matrix. All spectra shown were annealed at 30 K.

IR depletion spectra showed a red-shift of -59.0 cm^{-1} in the N-H stretch of C_4H_5N submolecule in the heterodimer from the bare C_4H_5N absorption and were assigned to the N-H$\cdots\pi$ stabilized $C_4H_5N\cdots C_6H_6$ heterodimer. Dauster et al. have reported a T-shaped structure for the $C_4H_5N\cdots C_6H_6$ heterodimer with a red-shift of ~-46 cm^{-1} in the N-H stretching mode of C_4H_5N in pulsed jet experiments [4]. However, none of the papers reported the computed vibrational wavenumber for the heterodimer. Our computations indicated a red-shift of -56.2 cm^{-1} for the partially stacked structure. Hence, it is interesting to study the $C_4H_5N\cdots C_6H_6$ heterodimer at low temperatures to predict whether the actual structure of $C_4H_5N\cdots C_6H_6$ heterodimer is T-shaped or partially stacked.

Computations were also carried out for the higher clusters of C_4H_5N and C_6H_6. Calculations performed at MP2/aug-cc-pVDZ level of theory indicated two types of higher clusters 2:1 $(C_4H_5N)_2\cdots C_6H_6$ (PDB) and 1:2 $C_4H_5N\cdots(C_6H_6)_2$ (PBD) and the structures of these clusters are illustrated in the Figure 4.4. The PDB and PBD clusters have N-H$\cdots\pi$ and C-H$\cdots\pi$ interactions of C_4H_5N with C_6H_6 thus forming a cyclic structure with multiple π-interactions. Table 4.1 gives the stabilization energies of the PB heterodimer and multimers (PDB, PBD). The comparison between the computed and experimental wavenumbers of $C_4H_5N\cdots C_6H_6$ heterodimers and multimers are given in Table 4.2.

4.2.1.2 Vibrational Assignment of ν_1 and ν_{16} Modes of C_4H_5N

Figure 4.1 blocks A and B correspond to the N-H stretching mode of C_4H_5N. The new spectral peaks at 3461.4/3457.6 cm^{-1} in N_2 and at 3460.9/3456.9 cm^{-1} in Ar matrix are red-shifted by -53.7 and -61.3 cm^{-1}, respectively, from the C_4H_5N monomer absorption, match well with the computed red-shift of -56.2 cm^{-1} for the PB-A heterodimer with an N-H$\cdots\pi$ interaction. Apart from the features due to 1:1 heterodimer, two new peaks were observed at 3406.7/3400.6 and 3442.9/3440.2 cm^{-1} in N_2 matrix which increases in intensity with the variation in the concentration of C_6H_6, amounts to a red-shift of -109.5 and -71.6 cm^{-1}, respectively. The experimental shifts compare well with the computed shifts -132.5 and -91.5 cm^{-1} for the proton donor and acceptor modes of C_4H_5N in the 2:1 PDB cluster. Experimentally, a new feature observed at 3452.8 (in N_2) and 3449.8 cm^{-1} (in Ar), with red-shifts of -60.4 cm^{-1} and -70.4 cm^{-1}, respectively, that matches well with the computed red-shift of -55.9 cm^{-1} for the 1:2 PBD cluster.

In the N-H bending region of C_4H_5N, new features appearing at 545.5 and 538.8 cm^{-1} in N_2 and Ar matrixes respectively, with a blue-shift of 56.1 cm^{-1} from C_4H_5N monomer absorption in Ar matrix correlate well with the computed blue-shift of 54.0 cm^{-1} while in N_2 matrix, a small blue-shift of 22.0 cm^{-1} was observed. Computations predicted blue-shifts of 79.2 and 86.8 cm^{-1} for the PDB cluster which is assigned to the experimental feature at 558.3 cm^{-1} with an observed blue-shift of 34.8 cm^{-1} in N_2 matrix. The feature at 540.5 cm^{-1} in N_2 matrix at a shift of 17.5 cm^{-1} is assigned to PBD heterotrimer (Table 4.2). It is observed that the N-H stretching mode of C_4H_5N submolecule in the heterotrimer agrees reasonably well with the computations whereas the N-H bending mode shows large variation. The reason for such deviations between the experimental and computed shift is likely due to the interaction of matrix on the vibrational modes of C_4H_5N submolecule in the aggregate. It is important to point out that the computations are performed for isolated gas phase molecules without taking into consideration the effect of matrix and it is indeed difficult to incorporate the matrix effect for different vibrational modes in the computations. Further, the levels of theory and the basis sets used for the calculation can give rise to such deviation between the calculated and observed vibrational wavenumber.

Table 4.1 [a]Raw/ZPE/BSSE Corrected Stabilization Energies (kcal mol^{-1}) of the C_4H_5N-C_6H_6 Heterodimers PB-A, PB-B and Higher Clusters PBD, PDB Computed at MP2/aug-cc-pVDZ Level of Theory.

Heterodimers	**Stabilization Energies**
PB-A	-9.3/-8.4/-5.1
PB-B[b]	-9.1/-8.3/-5.1
PDB	-27.9/-25.8/-17.3
PBD	-23.9/-21.8/-12.8

[a] Raw interaction energies refer to energies not corrected for either ZPE or BSSE.
[b] PB-B has a small negative frequency (10i).

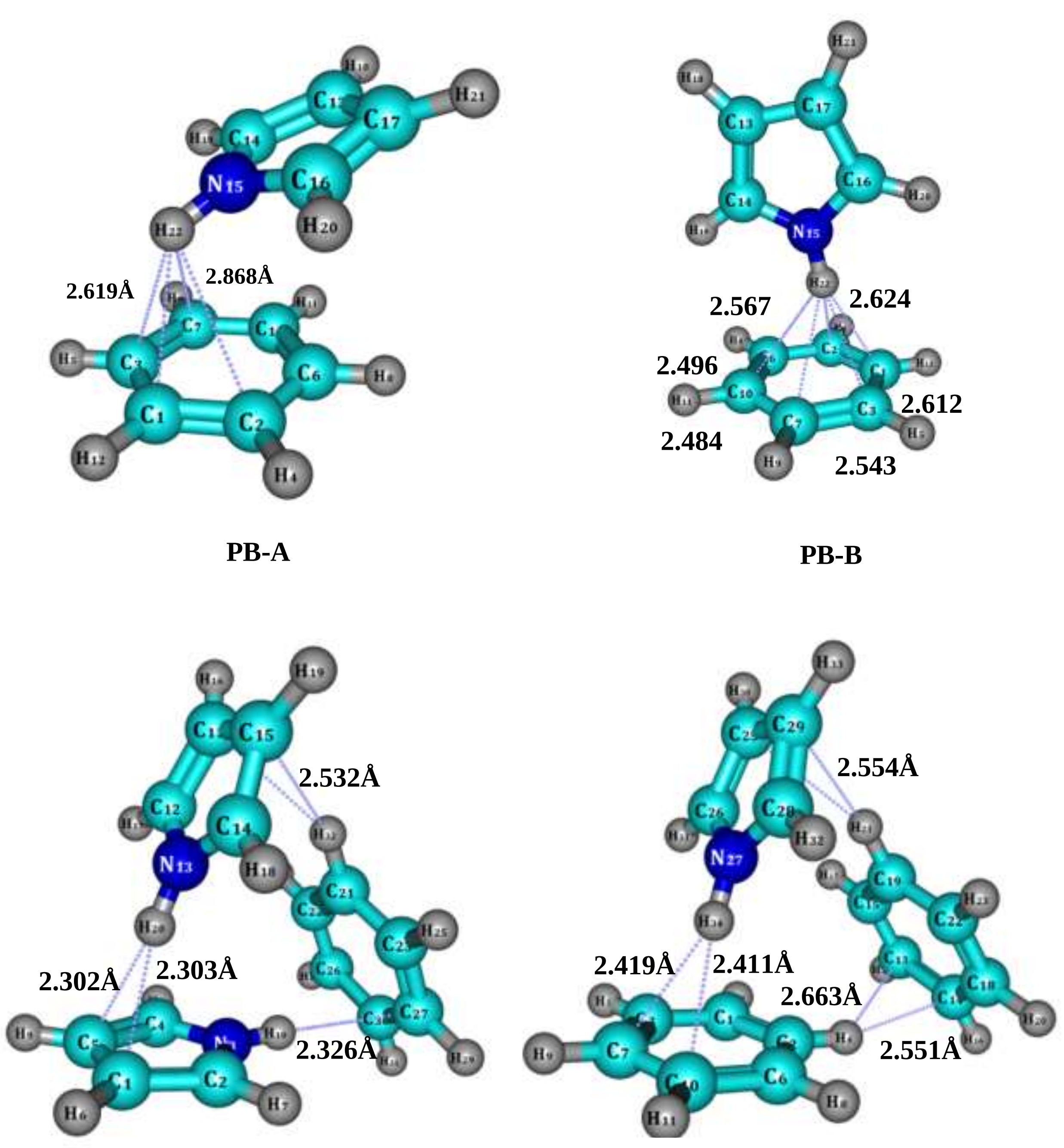

PB-A **PB-B**

PDB **PBD**

Figure 4.4 Computed structures of the 1:1, 2:1 and 1:2 C_4H_5N-C_6H_6 heterodimer PB-A/B, heterotrimers PDB and PBD optimized at MP2/aug-cc-pVDZ level of theory.

Table 4.2 Comparison of the Shift in the Experimental Vibrational Wavenumbers in N_2 and Ar Matrixes with the Computed Wavenumbers of 1:1 PB heterodimer, 2:1 PDB and 1:2 PBD Higher adducts Computed at MP2/aug-cc-pVDZ Level of Theory.

Computed (cm^{-1})		Experimental (cm^{-1})				Mode Assignment
ν	Δν[a]	N_2		Ar		
		ν	Δν[a]	ν	Δν[a]	
Pyrrole (C_4H_5N)						
514.9(59)[b]	-	527.2/520.2	-	483.8/482.8/481.6	-	N-H bending of C_4H_5N
3672.4(76)	-	3519.3/3513.8/ 3510.9/3508.9	-	3522.9/ 3520.9/3519.7	-	N-H stretching of C_4H_5N
Benzene (C_6H_6)						
678.3(116)	-	678.1	-	675.0	-	C-H bending of C_6H_6
3223.4(29)	-	3043.9	-	3046.8	-	C-H stretching of C_6H_6
PB-A						
685.3(156)	7.0	683.2	5.1	-[c]	-	C-H bending of C_6H_6
3222.4(16) 3222.8(17)	-1.0 -0.6	-[c]	-	-[c]	-	C-H stretching of C_6H_6
568.9(76)	54.0	545.5	22.0	538.8	56.1	N-H bending of C_4H_5N
3616.2 (118)	-56.2	3461.4/3457.6	-53.7[d]	3460.9/3456.9	-61.3[d]	N-H stretching of C_4H_5N
PB-B						
692.4(125)	-14.1	-[c]	-	-[c]	-	C-H bending of C_6H_6
542.7(20)	24.3	-[c]	-	-[c]	-	N-H bending of C_4H_5N
3642.4 (331)	-30.0	-[c]	-	-[c]	-	N-H stretching of C_4H_5N
PDB						
706.3(48)	28.0	692.7/691.1	13.8	-[c]	-	C-H bending of C_6H_6
3230.6(18)	7.2	-[c]	-	-[c]	-	C-H stretching of C_6H_6
594.1(22)	79.2	558.3	34.8	-[c]	-	N-H bending of C_4H_5N
601.7(10)	86.8					
3539.9 (424)	-132.5	3406.7/3400.6 3442.9/3440.2	-109.5[d] -71.6[d]	-[c]	-	N-H stretching of C_4H_5N
3580.9 (426)	-91.5					

PBD						
690.0(51)	11.7	687.3	9.2	-[c]	-	C-H bending of C_6H_6
696.9(161)	18.6					
3215.4(21)	-8.0	-[c]	-	-[c]	-	C-H stretching of C_6H_6
3220.7(16) 3233.2(16)	-2.7 9.8					
568.7(29)	53.8	540.5	17.5	540.5	57.5	N-H bending of C_4H_5N
3616.5 (327)	-55.9	3452.8	-60.4	3449.8	-70.4	N-H stretching of C_4H_5N

[a] $\Delta\nu = \nu_{heterodimer} - \nu_{monomer}$.

[b] Intensity in km mol^{-1} is given in parenthesis.

[c] Experimental features were not observed.

[d] Average of multiplet experimental wavenumbers of the monomers and multimers were taken to compute the experimental shift.

4.2.1.3 Vibrational Assignment of C-H bending mode of C_6H_6

Figure 4.3 shows the infrared spectra of C-H bending region of C_6H_6 spanning the region 670-700 cm^{-1} in N_2 matrix. The intense feature observed at 678.1 cm^{-1} is due to the C_6H_6 monomer in N_2 matrix [5]. For comparison, the infrared spectrum of C_4H_5N is also shown (trace 'a' of Figure 4.3), which has no absorption in this region. In C_6H_6, features due to C_6H_6 dimer were observed at 679.3/680.3/681.9 cm^{-1} [5]. As the concentration of C_4H_5N was varied, a sharp peak at 683.2 cm^{-1} picks up in intensity that amounts to a blue-shift of 5.1 cm^{-1}, which is in close agreement with the computed shift of 7.0 cm^{-1} for the PB-A heterodimer (Figure 4.3, Table 4.2). A doublet observed at 692.7/691.1 cm^{-1}, with a blue-shift of 13.8 cm^{-1} correlates with the computed blue-shift of 28.0 cm^{-1} for the 2:1 PDB cluster. For the 1:2 PBD cluster, computed shift of 11.7/18.6 cm^{-1} matches with the experimental shift of 9.2 cm^{-1} in N_2 matrix. The experimental features corresponding to the 1:1 $C_4H_5N\cdots C_6H_6$ PB-A, 1:2 $C_4H_5N\cdots C_6H_6$ PBD and 2:1 $C_4H_5N\cdots C_6H_6$ PDB complexes were not observed in Ar matrix.

It should be emphasized that apart from the shift in the vibrational wavenumbers of the heterodimers with respect to the monomers, the variation of intensity is also a clear manifestation of complexation. As seen from the Table 4.2, the infrared absorption intensities of the N-H stretching and bending modes of C_4H_5N monomer and the C-H bending mode of C_6H_6 were found to be 76, 59 and 116 km mol^{-1}, respectively. Upon complex formation, these modes displayed an increased infrared absorption intensity of 118, 76 and 156 km mol^{-1}, indicating distinctly that these modes are perturbed due to the formation of heterodimer, with a concomitant red- and blue-shift of vibrational wavenumbers from the monomer absorption band respectively. Experimentally, the corresponding red- and blue-shifts due to heterodimer formation are observed in N_2 and Ar matrixes.

4.2.2 Pyrrole···Ethylene

As discussed in Chapter 3 pyrrole homodimers $(C_4H_5N)_2$ were observed in N_2 matrix at 3503.4, 3500.8 and 3423.4, 3417.3, 3414.2 cm^{-1} (Figure 4.5a, grids A and B). It is obvious from the Figure 4.5 that the Ar matrix spectra were simpler and devoid of dimers and multimers when compared to N_2 matrix. New peaks were found at 3510.4, 3505.5, 3502.4, 3467.7, 3461.5, 3450.7, 3439.0, 3412.5 and 3400.4 cm^{-1} in N_2 and at 3520.9, 3484.8, 3480.9, 3470.6, 3469.4, 3463.6, 3388.9, 3384.1 and 3380.0 cm^{-1} in Ar matrix, which increases in intensity as the concentration of C_2H_4 was varied. Further, as the concentration of C_2H_4 was varied in N_2 matrix, the peaks corresponding to C_4H_5N monomer and dimer decreased remarkably in intensity and the new spectral features picked up intensity, clearly confirming the possibility of forming heterodimers and multimers involving C_4H_5N and C_2H_4.

Figure 4.6 shows the infrared spectra of N-H bending mode of C_4H_5N in N_2 matrix, where C_4H_5N monomer feature is observed as a doublet at 520.2/527.2 cm^{-1}. As the concentration of C_2H_4 was varied, new peaks were observed at 524.5, 526.0, 532.5, 534.7, 535.6 cm^{-1}. No new features were discerned in the N-H bending region of C_4H_5N in Ar matrix. Figure 4.7 grids A and B show the C-H bending region of C_2H_4 in N_2 and Ar matrixes, respectively. The feature observed at 950.0 cm^{-1} in N_2 matrix is due to C_2H_4 monomer and the corresponding feature in Ar matrix was observed at 947.6 cm^{-1} [6]. In the co-condensation experiments, new features start appearing and picked up in intensity in N_2 matrix at 959.7, 956.5, 940.4, 938.7, 936.0 and 933.6 cm^{-1} and in Ar matrix at 950.0 and 945.2 cm^{-1} respectively.

4.2.2.1 Computational details

Geometry optimization of C_4H_5N with C_2H_4 indicated four minima corresponding to 1:1 PE-A, PE-B, PE-C and PE-D heterodimers. Table 4.3 gives the stabilization energies of the C_4H_5N-C_2H_4 hetero dimers and trimers and Figure 4.8 illustrates the structures. The BSSE

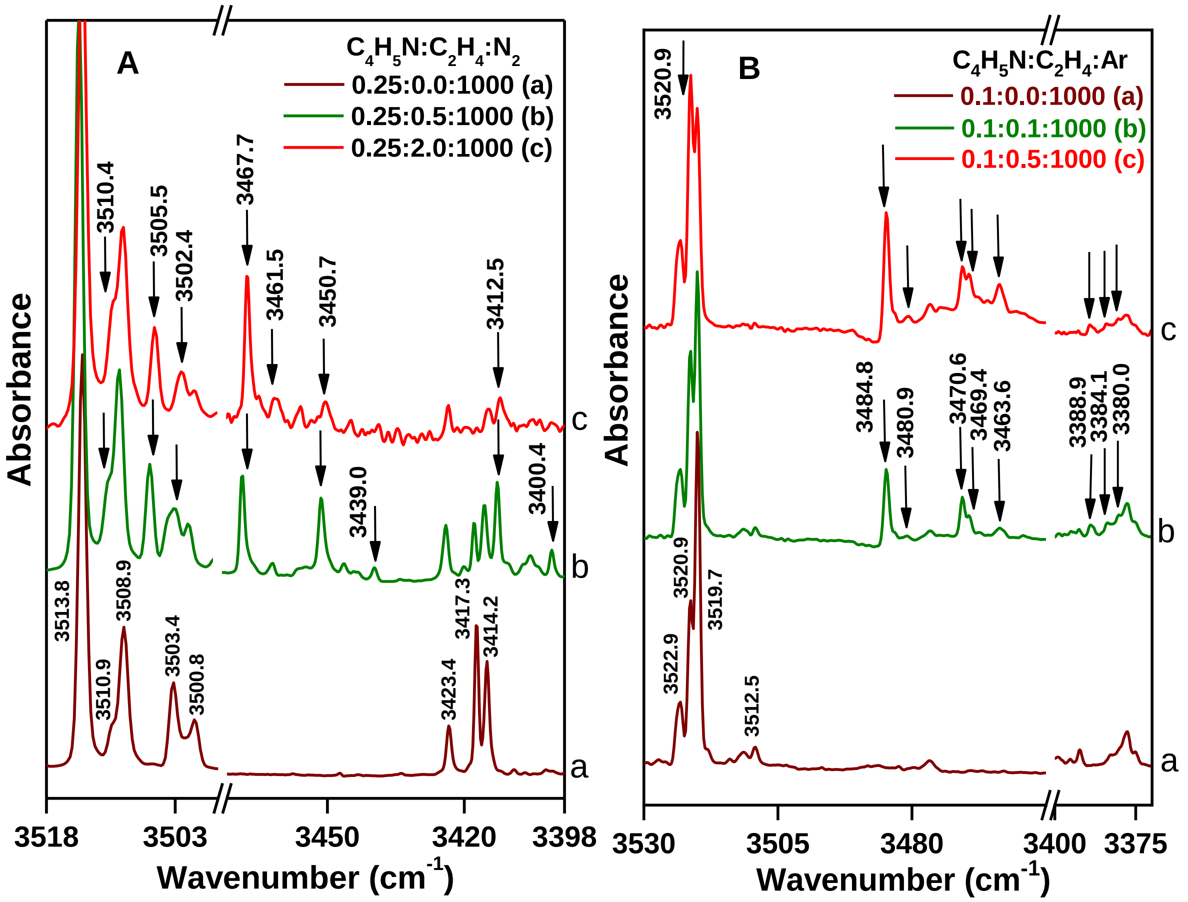

Figure 4.5 Grids A, B correspond to the infrared spectra of the N-H stretching region of C_4H_5N in N_2 and Ar matrixes. All the spectra shown were annealed at 30 K (N_2) and 35 K (Ar).

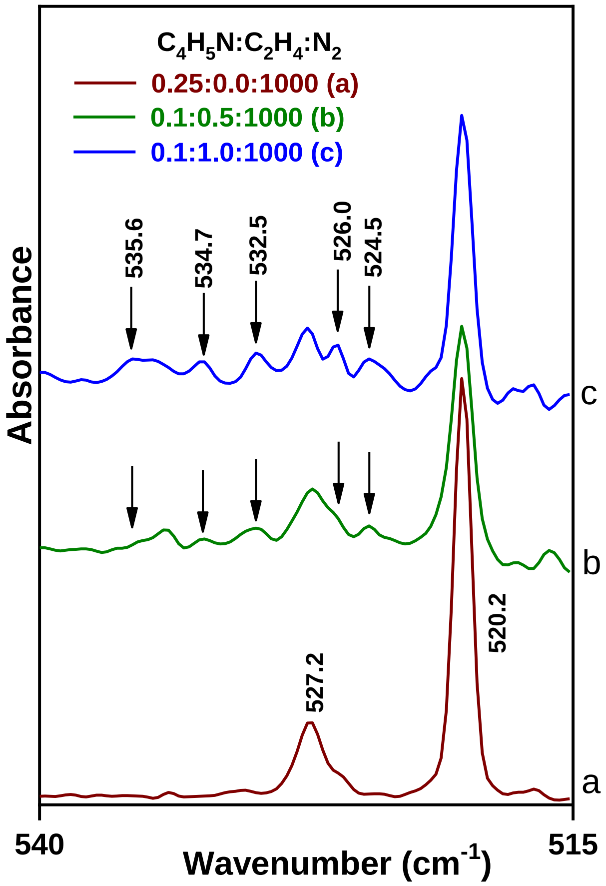

Figure 4.6 The infrared spectra of the N-H bending mode of C_4H_5N in N_2 matrix are depicted. All spectra shown were annealed at 30 K (N_2).

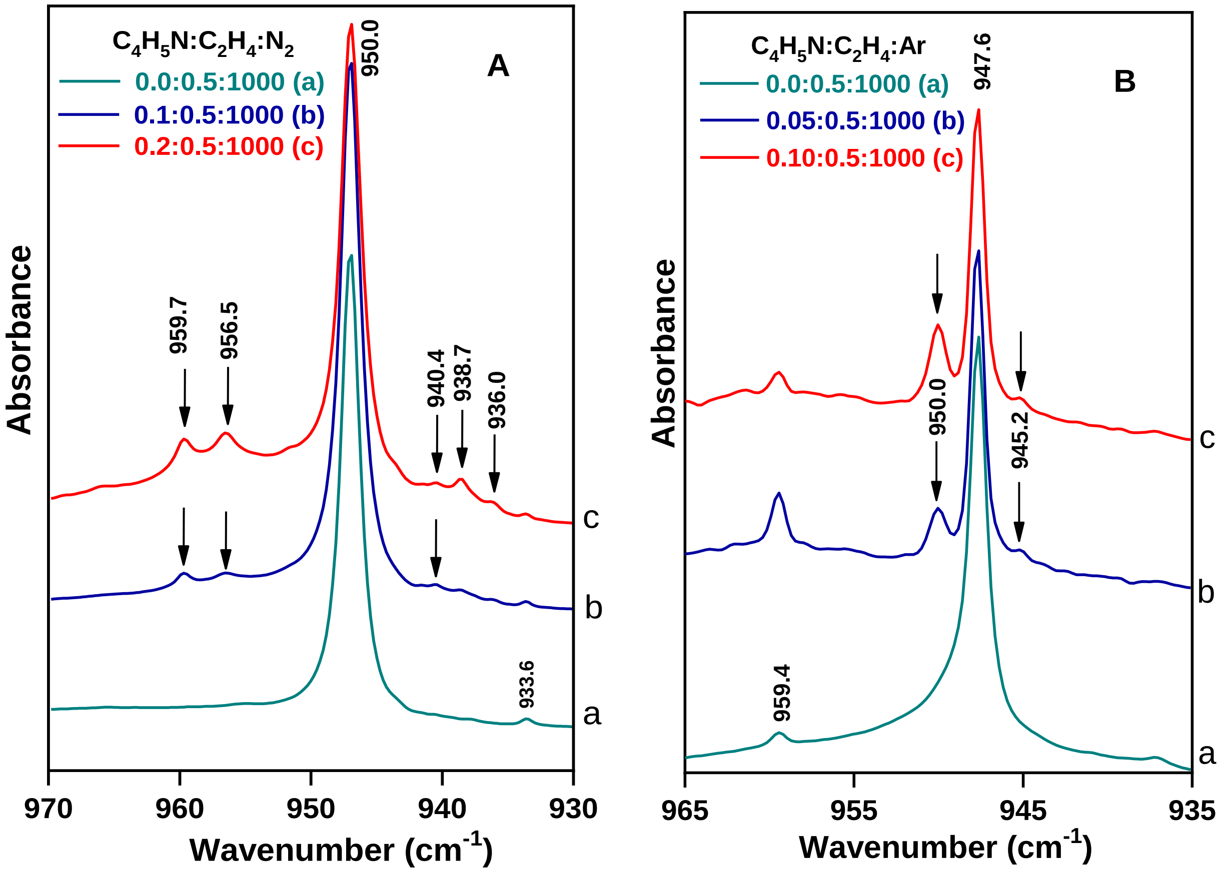

Figure 4.7 Grids A and B corresponds to the infrared spectra of the C-H bending region of C_2H_4 in N_2 and Ar matrixes. All spectra shown were annealed at 30 K (N_2) and 35 K (Ar).

corrected stabilization energy of the four heterodimers is in the order PE-A<PE-B<PE-C<PE-D, clearly showing the PE-A heterodimer is the global minimum. The PE-A is exothermic by ~0.21 kcal mol^{-1} with respect to PE-B rendering the heterodimers to be nearly isoenergetic. In PE-A heterodimer, the bond distances between the H16 of C_4H_5N and the carbons C1 and C2 are equidistant (2.462 and 2.467 Å, respectively), indicating an N-H$\cdots\pi$ interaction. The dihedral angle of 174° between N1-H9-C1-C2 clearly shows that the C_4H_5N molecule is perpendicular to the π-electron cloud of C_2H_4. In the PE-B heterodimer, the bond distance between the H5 of C_2H_4 with the ring carbon C7 is 2.689 Å, C8, C11 is 2.699 Å, C10 is 2.714 Å and N9 is 2.719 Å of C_4H_5N, clearly indicating a C-H$\cdots\pi$ interaction. PE-C heterodimer shows a $\pi\cdots\pi^*$ interaction, where the bond distance between the carbons C11 and C12 of C_2H_4 and carbons C2 and C4 of C_4H_5N are 3.269 and 3.264 Å, respectively. PE-D heterodimer is the least energetic, where the bond distance between the hydrogen atoms, H6 and H9 of C_4H_5N with carbon C11 of C_2H_4 are 2.819 and 3.028 Å, respectively.

Computations optimized two structures corresponding to $(C_4H_5N)_2\cdots C_2H_4$ (PDE-A and PDE-B) clusters and one geometry corresponding to $C_4H_5N\cdots(C_2H_4)_2$ (PED) cluster as shown in Figure 4.8. All the three clusters are stabilized by multiple N-H$\cdots\pi$ and C-H$\cdots\pi$ interactions between C_4H_5N and C_2H_4.

4.2.2.2 Vibrational Assignment of ν_1 and ν_{16} Modes of C_4H_5N

Figure 4.5 grids A and B illustrate the infrared spectra of N-H bending region of C_4H_5N in N_2 and Ar matrixes with variation in concentration of C_2H_4. Apart from the features due to C_4H_5N multimers and C_4H_5N-H_2O (will be discussed in Chapter 5) heterodimer, new features were observed as a doublet at 3467.7/3461.5 cm^{-1} in N_2 and the corresponding feature at 3484.8/3480.9 cm^{-1} in Ar, red-shifted by of -48.6 and -37.3 cm^{-1}, respectively that compares with the computed red-shift of -72.6 cm^{-1} for the global minimum PE-A heterodimer (Table 4.4).

Table 4.3 Raw/ZPE/BSSE-Corrected Stabilization Energies (kcal mol^{-1}) of C_4H_5N-C_2H_4 Heterodimers PE-A, PE-B, PE-C, PE-D and Higher Clusters PDE-A, PDE-B and PED Computed at MP2/aug-cc-pVDZ Level of Theory.

Heterodimers	**Raw[a]/ZPE/BSSE**
PE-A	-4.47/-3.85/-2.91
PE-B	-4.89/-4.10/-2.70
PE-C	-4.03/-3.48/-1.90
PE-D	-2.38/-1.77/-1.08
PDE-A	-19.87/-18.02/-13.11
PDE-B	-15.19/-16.48/-8.74
PED	-11.21/-9.54/-6.71

[a] Raw interaction energies refer to energies not corrected for either ZPE or BSSE.

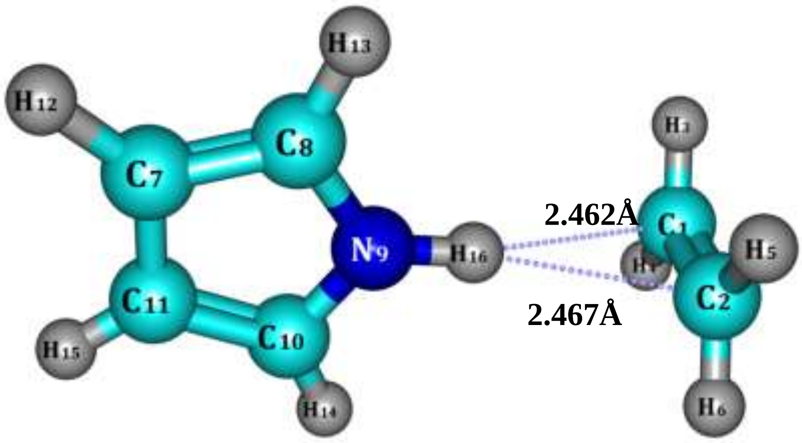

PE-A

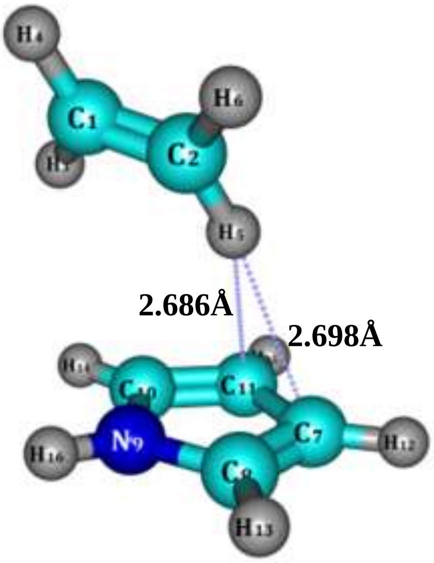

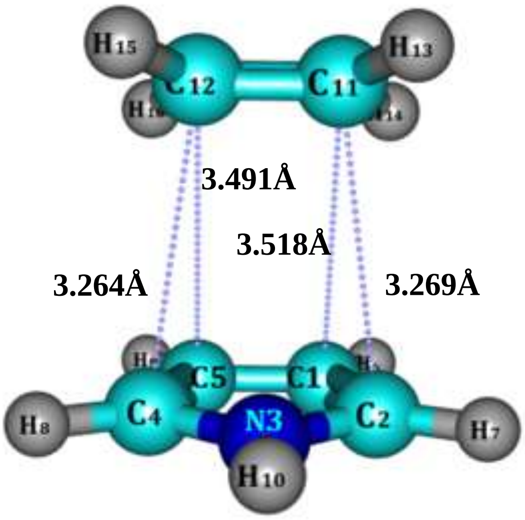

PE-B

PE-C

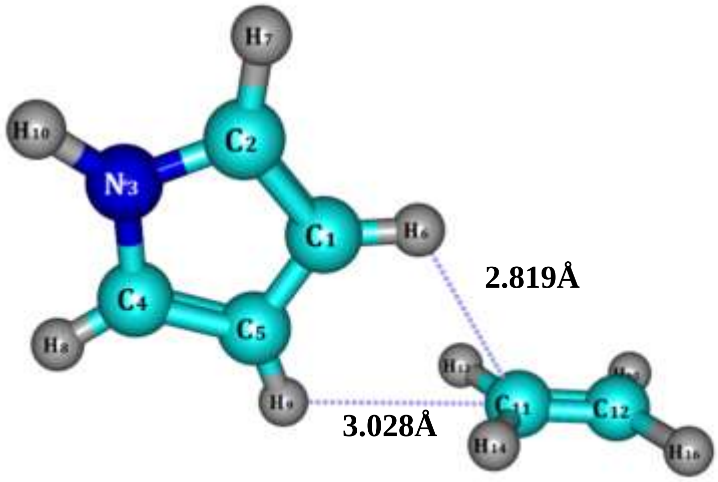

PE-D

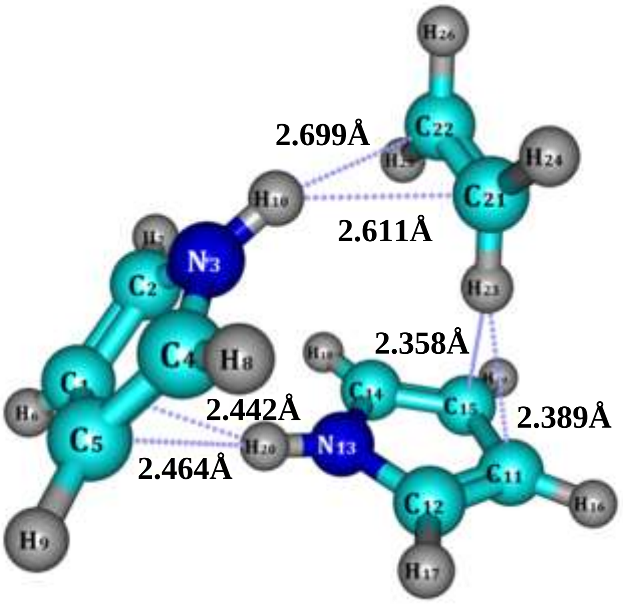

PDE-A

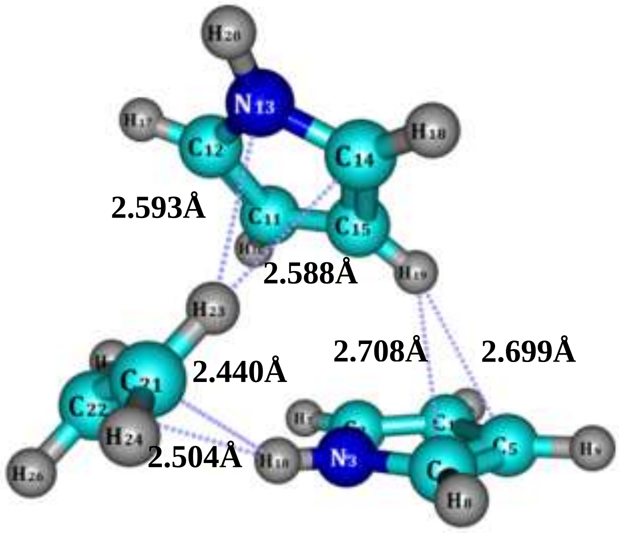

PDE-B

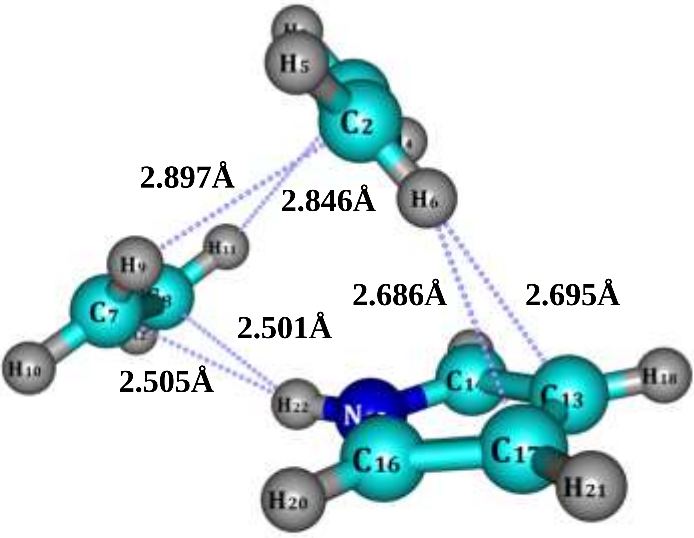

PED

Figure 4.8 Structures of the 1:1, 2:1 and 1:2 C_4H_5N-C_2H_4 PE-A, PE-B, PE-C, PE-D, PDE-A, PDE-B and PED complexes computed at MP2/aug-cc-pVDZ level of theory.

Computations predicted a red-shift of -4.5 cm^{-1} for the first local minimum PE-B heterodimer, which agrees well with the experimentally observed feature at 3502.4/3505.5 cm^{-1}, with a red-shift of -9.7 cm^{-1} in N_2 matrix. In Ar matrix, due to the presence of multiple site split $(C_4H_5N)_2$ features, PE-B heterodimer could not be clearly discerned. The stacked second local minimum (PE-C heterodimer) showed a very small red-shift of -1.4 cm^{-1}, which compares well with the experimental red-shifts of -2.8 and -0.7 cm^{-1} in N_2 and Ar matrixes, respectively. It should be mentioned that PE-C is structurally similar to the C_4H_5N-N_2 dimer, which is stabilized by $\pi\cdots\pi^*$ interaction (π stacking) with a red-shift of ~1.5 cm^{-1} and this dimer was experimentally observed in Ar matrix [7]. In the N-H stretching region of C_4H_5N, experimentally new features were observed at 3412.5/3400.4 and 3450.7 cm^{-1} with red-shifts of -106.7 and -62.5 cm^{-1} in N_2 matrix and the corresponding feature in Ar matrix at 3388.9/3384.1/3380.0 cm^{-1} and 3470.6 cm^{-1} with the red-shifts of -135.9 and -49.6 cm^{-1} respectively. These shifts agree well with the computed red-shifts -129.8 and -107.1 cm^{-1} of the PDE-A cluster (Table 4.4). With the increase in concentration of C_2H_4, these peaks decrease in intensity due to the predominance in the formation of 1:1 PE heterodimers (Figure 4.8).

For the PED cluster, computations indicated a red-shift ~-67.9 cm^{-1} that matches well with the experimental red-shifts of -73.8 and -53.7 cm^{-1} in N_2 and Ar matrixes, respectively (Table 4.4). No new features could be discerned for the PDE-A and PED cluster in the N-H bending of C_4H_5N and C-H stretching and bending modes of C_2H_4 in either N_2 or Ar matrixes. It is illustrative from the Table 4.4 that the infrared absorption intensity of the N-H bending mode of the PDE-A and PED higher clusters was computed to be 302/448 and 287 km mol^{-1}, respectively, which is higher than the C_4H_5N monomer absorption intensity. Experimentally, evidence for the formation of the higher clusters was observed only in the N-H stretching mode of C_4H_5N sub-molecule in N_2 and Ar matrixes.

In the N-H bending mode of C_4H_5N, although computation indicated a red-shift of -64.7 cm^{-1} for the PE-A heterodimer, experimentally new peaks were not observed for this heterodimer in N_2 and Ar matrixes. The probable reason for not observing the experimental feature could be the negligible infrared absorption intensity (~17 km mol^{-1}) of PE-A heterodimer. Experimentally, site split features observed at 532.5/534.7/535.6 cm^{-1}, with an average blue-shift of 7.6 cm^{-1} in N_2 matrix correlates well with the computed blue-shift of 5.7 cm^{-1} for the PE-B heterodimer. For the PE-C heterodimer with a $\pi\cdots\pi^*$ interaction, computations indicated a small red-shift of -0.2 cm^{-1} that agrees reasonably well with the experimental blue-shift of 1.7 cm^{-1} in N_2 matrix. No new feature was observed for the PE-C heterodimer in Ar matrix in this region (Table 4.4).

4.2.2.3 Vibrational Assignment of C-H bending mode of C_2H_4

Infrared spectra of C-H bending region of C_2H_4 in N_2 and Ar matrixes are shown in Figure 4.7 grids A and B, respectively. The feature observed at 950.0 cm^{-1} in N_2 matrix is due to C_2H_4 monomer absorption and the corresponding feature in Ar matrix was observed at 947.6 cm^{-1}. The peak at 959.4 cm^{-1} in Ar matrix corresponds to C_2H_4-H_2O heterodimer [6]. As the concentration of C_4H_5N varied, new feature at 959.7 in N_2 and at 950.0 cm^{-1} in Ar matrixes were blue-shifted by 9.7 and 2.4 cm^{-1} respectively from the monomer absorption, which is in agreement with the computed blue-shift of 14.4 cm^{-1} for the PE-A heterodimer. The computed blue-shift of 9.1 cm^{-1} for the PE-B heterodimer matches well with the experimental blue-shift of 6.5 cm^{-1} in N_2 matrix. Surprisingly, for the PE-C heterodimer with a $\pi\cdots\pi^*$ interaction, computations indicated a red-shift of -24.1 cm^{-1} that agrees with the experimental red-shifts of -11.6 and -2.4 cm^{-1} in N_2 and Ar matrixes, respectively. These peaks were tentatively assigned to the PE-C heterodimer, since the peaks intensified on increasing the concentration of C_4H_5N (Table 4.4).

Table 4.4 Comparison of Shift in the Experimental Vibrational Wavenumbers in N_2 and Ar Matrixes with the Computed Wavenumbers of the 1:1 PE-A, PE-B, PE-C Heterodimers and 2:1 PDE, 1:2 PDE Higher Adducts Computed at MP2/aug-cc-pVDZ Level of Theory.

Computed (cm^{-1})		Experimental (cm^{-1})				Mode Assignment
		N_2		Ar		
ν	$\Delta\nu^{a}$	ν	Δν	ν	Δν	
Pyrrole						
$514.9(59)^{b}$	-	527.2/520.2	-	483.8/482.8/481.6	-	N-H bending of C_4H_5N
718.4(176)	-	729.9	-	722.2	-	C-H bending of C_4H_5N
3672.4(76)	-	3519.3/3513.8/3510.9/3508.9	-	3522.9/3520.9/3519.7	-	N-H stretching of C_4H_5N
Ethylene						
979.4(95)	-	950.0	-	947.6	-	C-H bending of C_2H_4
PE-A						
993.8(125)	14.4	959.7	9.7	950.0	2.4	C-H bending of C_2H_4
579.6(17)	64.7	$-^{c}$	-	$-^{c}$	-	N-H bending of C_4H_5N
722.3(156)	3.9	731.1	1.2	723.5	1.3	C-H bending of C_4H_5N
3599.8 (430)	-72.6	3467.7/3461.5	-48.6^{d}	3484.8/3480.9	-37.3^{d}	N-H stretching of C_4H_5N
PE-B						
988.5(62)	9.1	956.5	6.5	$-^{c}$	-	C-H bending of C_2H_4
520.6(76)	5.7	535.6/534.7/532.5	7.6^{d}	$-^{c}$	-	N-H bending of C_4H_5N
724.3(181)	5.9	$-^{c}$	-	$-^{c}$	-	C-H bending of C_4H_5N
3667.9(76)	-4.5	3502.4/3505.5	-9.7^{d}	$-^{c}$	-	N-H stretching of C_4H_5N
PE-C						
955.3(97)	-24.1	940.4/938.7/936.0	-11.6^{d}	945.2	-2.4	C-H bending of C_2H_4
514.7(74)	-0.2	526.0/524.5	1.7^{d}	$-^{c}$	-	N-H bending of C_4H_5N
718.3(183)	-0.1	$-^{c}$	-	$-^{c}$	-	C-H bending of C_4H_5N
3671.0(72)	-1.4	3510.4	-2.8	3520.9	-0.7	N-H stretching of C_4H_5N
PDE-A						
1006.3(64)	26.9	$-^{c}$	-	$-^{c}$	-	C-H bending of C_2H_4
596.9(38) 604.2(17)	82.0 89.3	$-^{c}$	-	$-^{c}$	-	N-H bending of C_4H_5N
3542.6 (302)	-129.8	3412.5/3400.4	-106.7^{d} -62.5	3388.9/3384.1/ 3380.0	-135.9^{d}	N-H stretching of C_4H_5N

3565.3 (448)	-107.1	3450.7		3470.6	-49.6	
PED						
989.9(64) 995.6(99)	10.5 16.2	-[c]	-	-[c]	-	C-H bending of C_2H_4
582.6(42)	67.7	-[c]	-	-[c]	-	N-H bending of C_4H_5N
3604.5 (287)	-67.9	3439.4	-73.8	3469.4/3463.6	-53.7	N-H stretching of C_4H_5N

[a] $\Delta\nu = \nu_{heterodimer}-\nu_{monomer}$; [b] Intensity in km.mol^{-1} is given in parenthesis; [c] Experimental features were not observed; [d] Average of the multiplet experimental wavenumbers of the monomers and multimers were taken to compute the experimental shift.

4.2.3 Pyrrole···Acetylene

Experiments for $C_4H_5N\cdots C_2H_2$ heterodimer were performed in N_2 and Ar matrixes. The formation of 1:1, 1:2 and 2:1 $C_4H_5N\cdots C_2H_2$ heteroadducts were evidenced in the C-H stretching, bending modes of C_2H_2, N-H stretching, bending and C-H bending modes of C_4H_5N, respectively. Since both C_2H_2 and C_4H_5N are capable of self-association, the formation of dimers and trimers were found in all the matrixes.

Figure 4.9 grids A and B show the annealed spectra of the C-H stretching (ν_3) and grids C and D correspond to the bending (ν_5) region of C_2H_2 in N_2 and Ar matrixes. In N_2 and Ar matrixes, the ν_3 mode of C_2H_2 has strong absorptions at 3283.3 and 3288.5 cm^{-1}, respectively. The doubly degenerate ν_5 mode of C_2H_2 splits in N_2 matrix and appears as a doublet at 741.7 and 746.8 cm^{-1} whereas in the Ar matrix the same mode was observed as a single sharp peak at 736.8 cm^{-1} (not shown in the figure). The features due to C_2H_2 dimer were observed in N_2 at 3279.2, 3264.7, 3257.0, 752.3, 755.2, 760.3, 765.8 cm^{-1} and at 3285.2, 3262.8, 762.0 and 760.8 cm^{-1} in Ar matrix [8,9,10]. Since, water is an inevitable impurity in matrix isolation experiments, the features due to C_2H_2-H_2O heterodimer in N_2 and Ar matrixes were produced at 3218.5/3222.5 and 3240.1 cm^{-1}, respectively [8,9]. When C_4H_5N concentration was varied and the matrix was annealed, new features started appearing in the C-H stretching and bending regions of C_2H_2 in N_2 matrix at 3242.3, 3239.9 cm^{-1} and 763.7 cm^{-1}; and in Ar matrix at 3252.2, 3245.4, 3231.7 cm^{-1} and 764.2, 757.4 cm^{-1}.

Figure 4.10 grids A, B show the annealed spectra corresponding to the N-H stretching region of C_4H_5N in N_2 and Ar matrixes. Features due to the monomer and multimers of C_4H_5N were observed in N_2 and Ar matrixes (discussed in detail in Chapter 3). Co-deposition of precursors followed by annealing, new spectral bands were produced at 3504.6, 3497.6, 3491.3, 3479.7, 3474.4, 3463.6, 3450.8 and 3443.1 cm^{-1} in N_2, and in Ar at 3460.5, 3458.3 cm^{-1}. Figure 4.11 grids A, B show the N-H bending mode of C_4H_5N in N_2 and Ar matrixes.

Co-deposition experiments produced new features at 562.6, 560.4, 558.3, 556.8, 554.9, 553.9, 539.5 and 538.3 cm^{-1} in N_2, and 503.5, 502.6 cm^{-1} in Ar matrixes. The intensity of all these new bands increased as a function of C_2H_2 concentration, clearly showing that the new features could be due to the formation of C_4H_5N-C_2H_2 heterodimer and multimers.

Figure 4.12 blocks A and B illustrate the C-H bending mode of C_4H_5N in N_2 and Ar matrixes, respectively, where apart from C_4H_5N monomer absorption at 729.9 cm^{-1} in N_2 and 725.4/721.9/720.5 cm^{-1} in Ar, on addition of C_2H_2 new peaks appear at 736.4 and 728.7 cm^{-1} in N_2 and Ar matrixes, respectively.

4.2.3.1 Computational details

Geometry optimization performed at MP2 level of theory using aug-cc-pVDZ basis set yielded three minima corresponding to the 1:1 C_4H_5N-C_2H_2 heterodimers PA-A, PA-B and PA-C. Figure 4.13 shows the structures of the heterodimers optimized at MP2/aug-cc-pVDZ level of theory. Ozaki and co-workers [11] carried out the calculations on 1:1 C_4H_5N-C_2H_2 and C_4H_5N-C_2H_4 heterodimers at DFT//B3LYP/6-311++G (3df, 3pd) level of theory and optimized only the N-H•••π structure. Our calculations indicated C-H•••π and N-H•••π structures to be the global and local minima, respectively on the potential energy surface. For the heterodimer PA-A stabilized by C-H•••π interaction, the bond distance between the hydrogen H14 of C_2H_2 with carbons C1 and C5 of C_4H_5N is 2.545 Å. Further, the bond distance between H14 with C2, C4 and N3 of C_4H_5N is 2.587 Å and 2.601 Å, respectively and hence the hydrogen H14 of C_2H_2 is closer to the carbons C1 and C5 of C_4H_5N. Furthermore, the bond angle between the H14-C1-C2 and H14-C4-C5 is of the order of ~ 75° which directs the hydrogen H14 of C_2H_2 towards the carbons C1 and C5 of C_4H_5N. Due to this C-H•••π interaction, the C-H bond in C_2H_2 and N-H bond in C_4H_5N slightly gets elongated in the heterodimer PA-A with the order of 0.003 and 0.001 Å, respectively from the monomer.

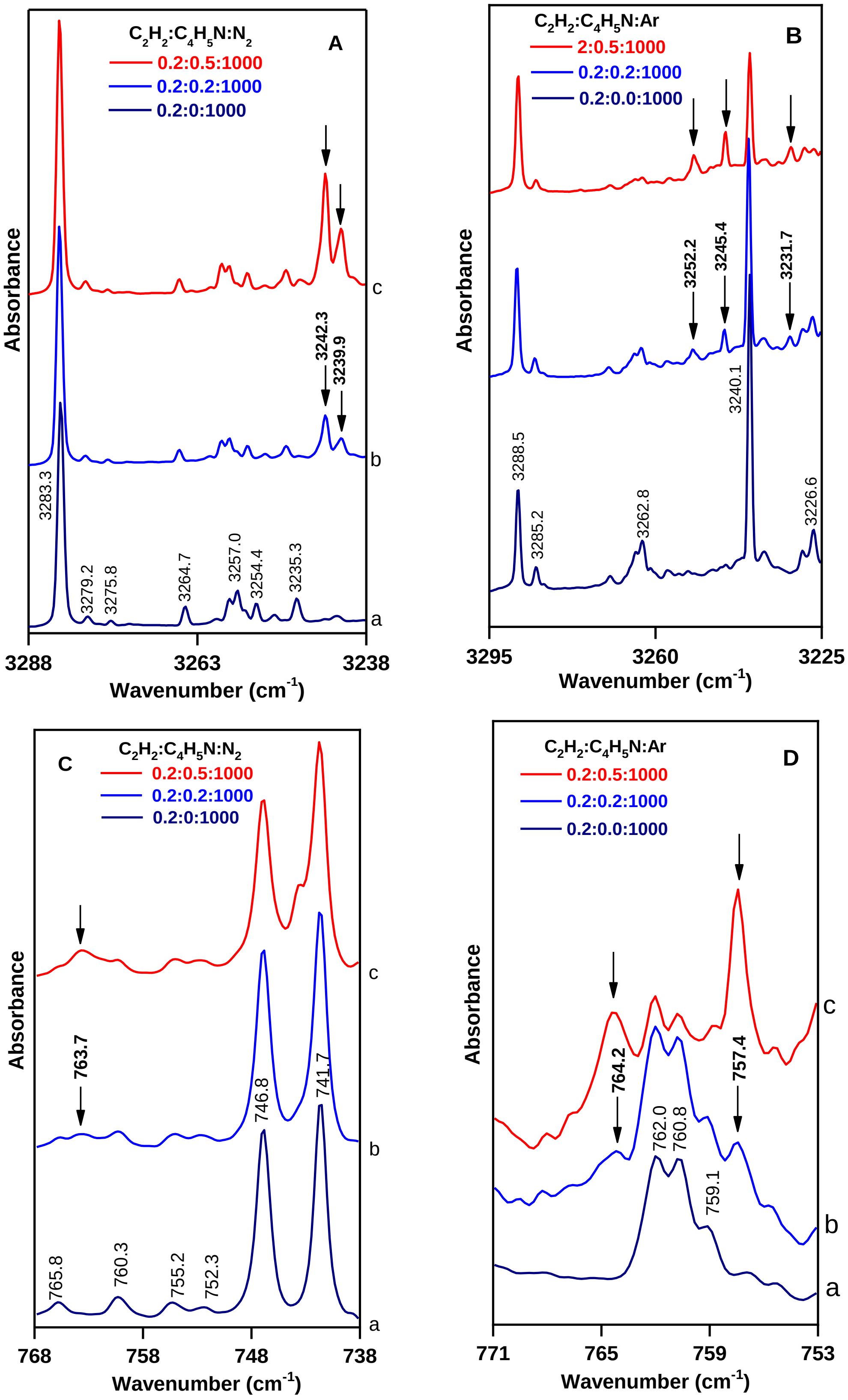

Figure 4.9 Matrix isolated infrared spectra of C-H stretching and bending regions of C_2H_2. Blocks A & C correspond to the 30 K annealed spectra in N_2, B & D to the 35 K annealed spectra in Ar matrixes, respectively.

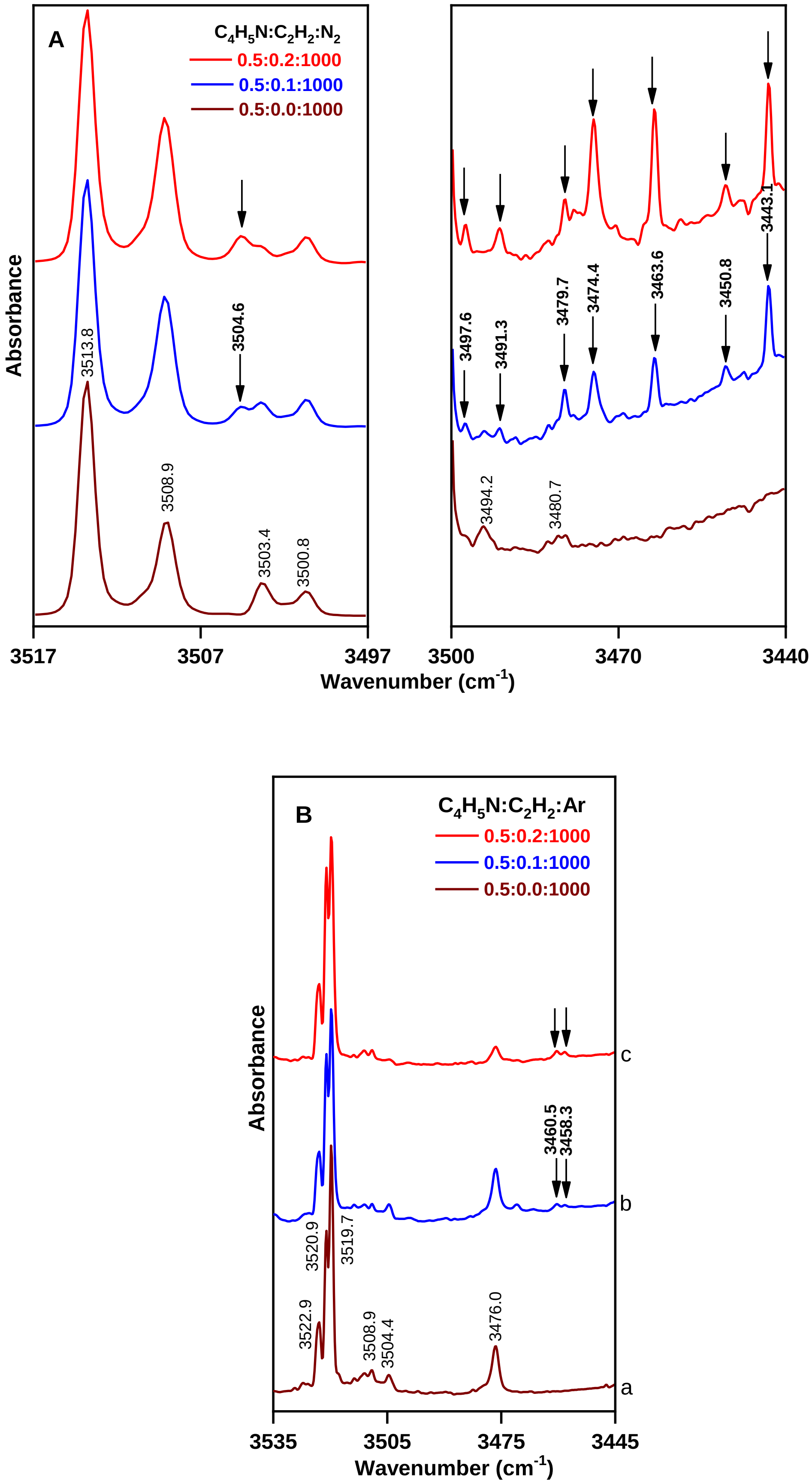

Figure 4.10 Matrix isolated infrared spectra of N-H stretching region of C_4H_5N in N_2 (block A) and Ar (block B) matrixes. All the spectra shown here were annealed at 30 K (for N_2) and 35 K (for Ar).

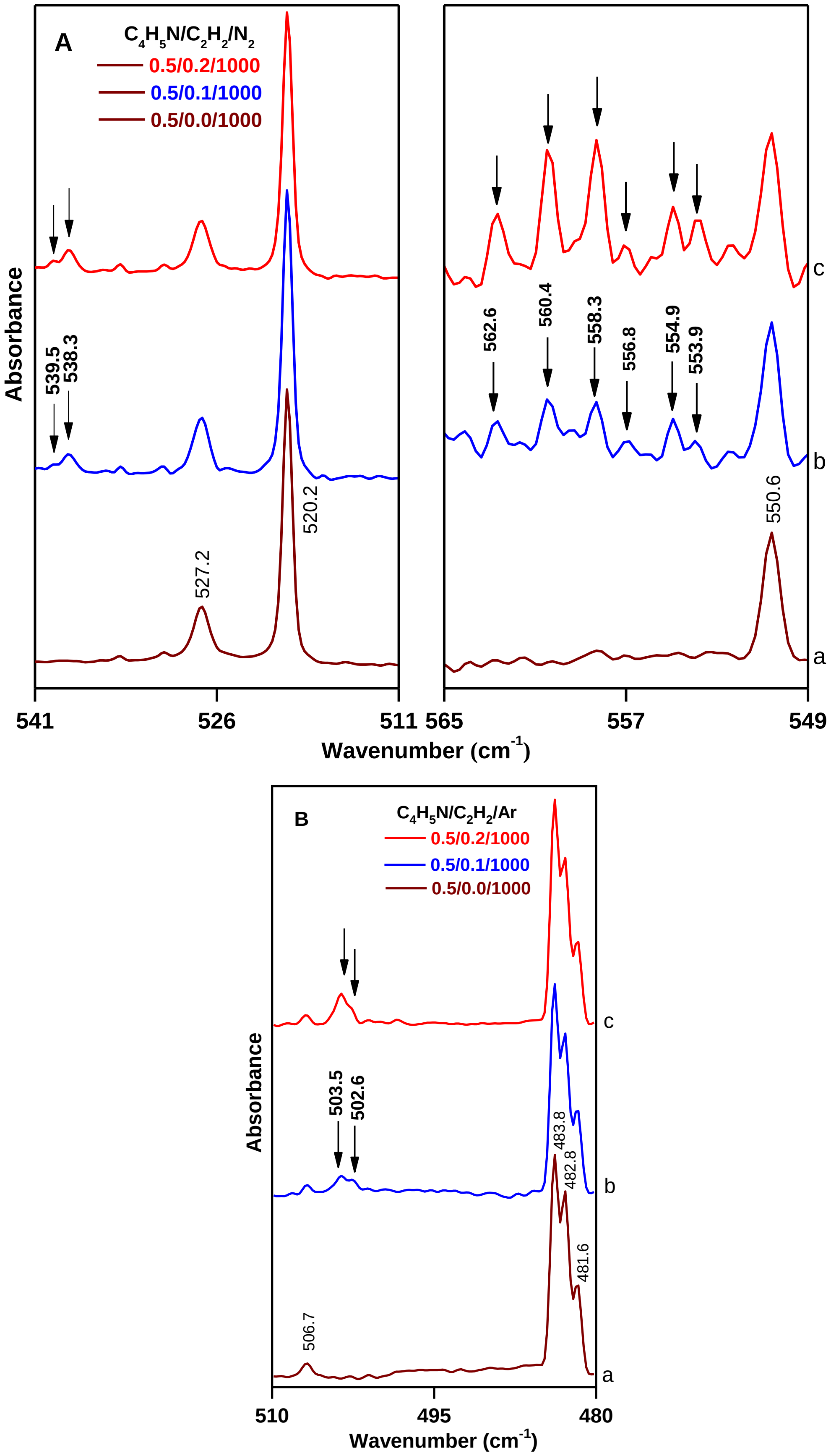

Figure 4.11 Matrix isolated infrared spectra of N-H bending region of C_4H_5N in N_2 (block A) and Ar (block B) matrixes. All the spectra shown here were annealed at 30 K (for N_2) and 35 K (for Ar).

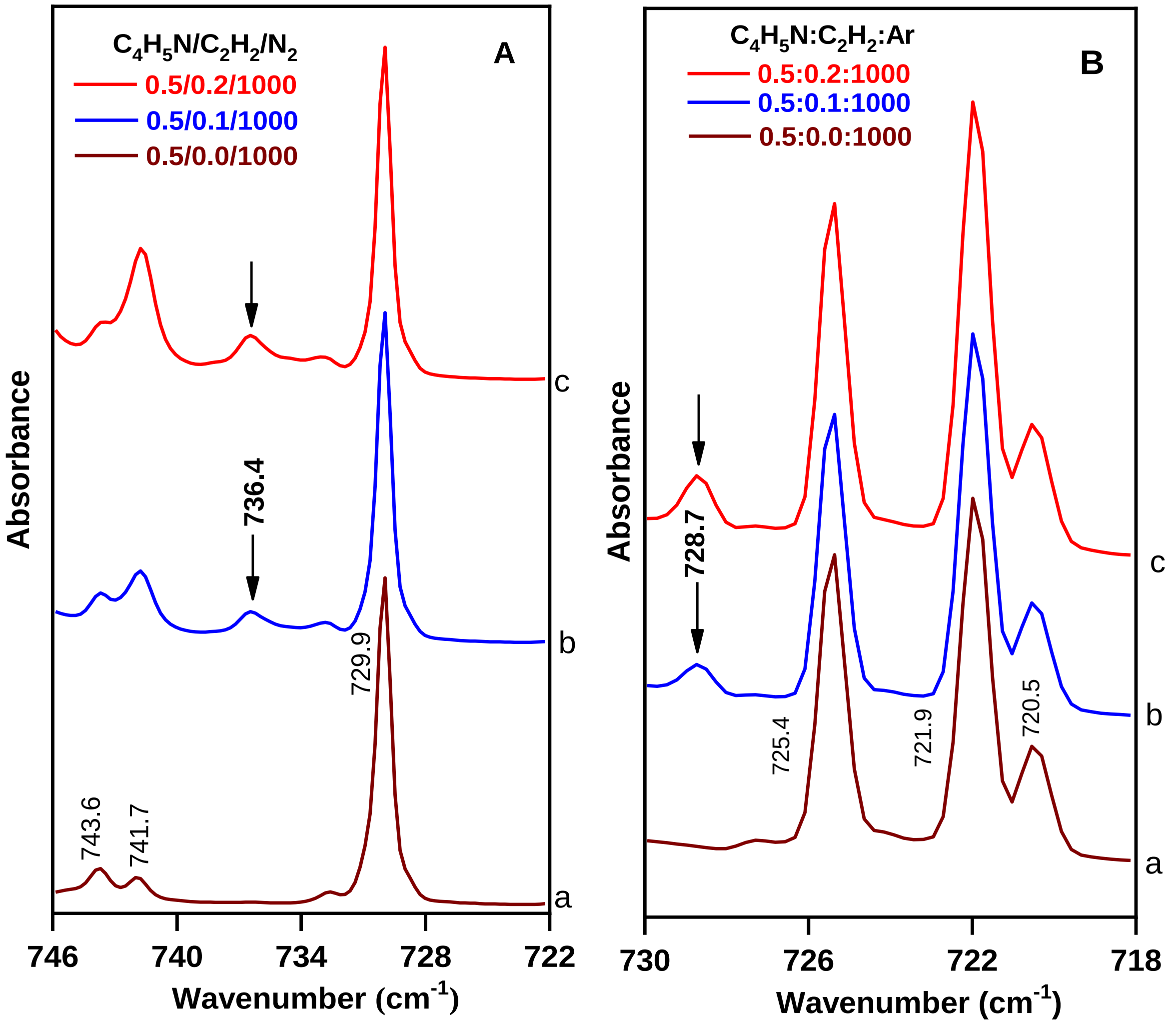

Figure 4.12 Matrix isolated infrared spectra of C-H bending region of C_4H_5N in N_2 (block A) and in Ar (block B) matrixes. All the spectra shown here were annealed at 30 K (for N_2) and 35 K (for Ar).

For the heterodimer PA-B, the bond distances between the hydrogen H10 of C_4H_5N and carbons C11 and C12 of C_2H_2 are equal (2.423Å), indicating an N-H•••π interaction. The bond angle between N3-H10-C11 and N3-H10-C12 is ~ 165° and the corresponding dihedral angles between C4-N3-H10-C12 and C4-N3-H10-C11 are ~ 92° and -92° clearly showing that the C_4H_5N is perpendicular to C_2H_2 and forms a T-shaped heterodimer. Due to the N-H•••π interaction in PA-B, the N-H and C-H bond length of C_4H_5N and C_2H_2 are elongated by 0.003 and 0.001Å, respectively. Heterodimer PA-C is stabilized by π•••π* interaction between the π-electron clouds of C_2H_2 and C_4H_5N. The bond distance between the C11 and C12 of C_2H_2 to the carbons C2 and C4 of C_4H_5N are 3.278 and 3.268 Å, respectively. Table 4.5 gives the Raw/ZPE/BSSE-corrected stabilization energies of the binary C_4H_5N-C_2H_2 heterodimers. At the MP2/aug-cc-pVDZ level, the ZPE corrected energies of the heterodimer PA-A is -5.46, for the heterodimer PA-B is -3.73 and for PA-C is -2.75 kcal.mol^{-1}, respectively. On the other hand, BSSE corrected values for PA-A, PA-B and PA-C were -3.75, -2.97 and -1.45 kcal mol^{-1}, respectively, suggesting a possibility of formation of all the three heterodimers in low temperature conditions, since the energy gap becomes 0.78 (PA-B) and 2.3 (PA-C) kcal mol^{-1} only, with respect to the most stable isomer.

In order to find out the next possible region of attack of C_2H_2 or C_4H_5N on the C_2H_2-C_4H_5N heterodimer, *ab initio* computations were performed for the higher clusters. Two minima corresponding to the 1:2 C_2H_2-C_4H_5N heterotrimers PPA-A and PPA-B and three minima for the 2:1 C_2H_2-C_4H_5N heterotrimers PAA-A, PAA-B and PAA-C were optimized in the potential energy surface. Figure 4.13 shows the structures of 2:1 and 1:2 C_2H_2-C_4H_5N heterotrimers computed at MP2/aug-cc-pVDZ level of theory. The higher aggregates are stabilized by the combination of both C-H•••π and N-H•••π interactions or C-H•••π interactions. Table 4.5 gives the stabilization energies of the 2:1 and 1:2 C_2H_2-C_4H_5N heterotrimers, computed at MP2/aug-cc-pVDZ level of theory. Among the 2:1 C_2H_2-C_4H_5N

heterotrimers, the ZPE corrected energy indicated that the heterotrimer PAA-A is exothermic by -11.44 kcal mol^{-1} and it is more stable than heterodimer PAA-B and PAA-C at MP2/aug-cc-pVDZ level of calculation. It should be noted from the Figure 4.13 that heterotrimer PAA-A forms a cyclic structure with two C-H⋯π and one N-H⋯π interactions between the C_2H_2 and C_4H_5N. The bond distance between the hydrogen H3 of C_2H_2 with carbons C9, C13 of C_4H_5N is 2.528 and 2.538 Å and hydrogen H18 of C_4H_5N with carbons C5, C6 of C_2H_2 is 2.361 and 2.592 Å and hydrogen H8 of C_2H_2 with carbons C1 and C2 of C_2H_2 is 2.642 and 2.613 Å making the heterotrimer cyclic. The other two heterotrimers PAA-B and PAA-C have the open structures and ZPE corrected stabilization energy for the heterotrimers are -7.25 and -5.21 kcal mol^{-1} respectively. The ZPE corrected stabilization energy for the 1:2 C_2H_2-C_4H_5N heterotrimers PPA-A and PPA-B are -19.84 and -15.54 kcal mol^{-1} respectively. Heterotrimer PPA-A forms a cyclic structure with two N-H⋯π and one C-H⋯π interactions with a bond distance between the H20 with carbons C1 and C2 of C_4H_5N is 2.355Å and between the H10 of C_4H_5N with carbons C21, C22 are 2.354 and 2.443Å and the hydrogen H24 of C_2H_2 with carbons C11 and C15 of C_4H_5N are 2.487 and 2.498 Å. Heterotrimer PPA-B has an open structure.

4.2.3.2 Vibrational Assignments in v_3 mode of C_2H_2

When C_4H_5N concentration was increased in the C_2H_2/inert gas mixture, new features started appearing in the v_3 C-H stretching region of C_2H_2 sub-molecule in N_2 matrix at 3242.3/3239.9 cm^{-1} and in Ar matrix at 3252.2/3245.4/3231.7 cm^{-1}. The experimental red-shifts of -42.2 (N_2) and -45.4 (Ar) matches well with the computed shift of -36.5 cm^{-1} for the C-H⋯π heterodimer PA-A. No feature was observed for the heterodimer PA-B in N_2 or Ar matrixes in this region. In our earlier studies on C_2H_2-CH_3OH and C_2H_2-C_6H_5OH system, both C-H⋯O and O-H⋯π heterodimers were observed in N_2 matrix [9,12].

Table 4.5 RAW[a]/ZPE/BSSE Corrected Stabilization Energies for the 1:1, 1:2 and 2:1 C_2H_2-C_4H_5N Complexes computed at MP2/aug-cc-pVDZ Level of Theory.

Complex	**Stabilization Energy (∆E)**
	MP2/aug-cc-pVDZ
PA-A	-6.26/-5.46/-3.75
PA-B	-4.36/-3.73/-2.97
PA-C	-3.01/-2.75/-1.45
PAA-A	-13.34/-11.44/-8.02
PAA-B	-8.63/-7.25/-4.65
PAA-C	-6.50/-5.21/-3.83
PPA-A	-21.89/-19.84/-13.62
PPA-B	-17.10/-15.54/-9.69

All energies are in kcal mol^{-1}.

[a] Raw interaction energies refer to energies not corrected for either ZPE or BSSE.

Table 4.6 Comparison of Shift in the Experimental Vibrational Wavenumbers in N_2 and Ar Matrixes with the Computed Wavenumbers for the C_2H_2-C_4H_5N complexes PA-A, PA-B, PPA-A and PAA-A. Computations were performed using MP2/aug-cc-pVDZ Level of Theory.

Computed ν (cm^{-1})		**Experimental ν (cm^{-1})**				**Mode Assignment**
ν	**$\Delta\nu^{a}$**	**N_2**		**Ar**		
		ν	**$\Delta\nu^{a}$**	**ν**	**$\Delta\nu^{a}$**	
Acetylene						
703.0(94)^{b}	-	741.7/746.8	-	736.8	-	C-H bending of C_2H_2
3431.7(93)	-	3283.3	-	3288.5	-	C-H antisym. str. of C_2H_2
Pyrrole						
514.9(59)	-	520.2/527.2	-	483.8/482.8/481.6	-	N-H bending of C_4H_5N
718.4(177)	-	729.9	-	725.4/721.9/720.5	-	C-H bending of C_4H_5N
3672.4(76)	-	3519.3/3513.8/3510.9/3508.9	-	3522.9/3520.9/3519.	-	N-H stretching of C_4H_5N
PA-A						
715.3(54) 739.4(164)	12.3 36.4	763.7	19.0	764.5/757.4	35.4^{d}	C-H bending of C_2H_2
3395.2 (260)	-36.5	3242.3/3239.9	-42.2^{d}	3252.5/3245.4/3231.7	-45.4^{d}	C-H antisym. str. of C_2H_2
534.4(71)	19.5	539.5/538.3	15.2^{d}	503.5/502.6	20.3^{d}	N-H bending of C_4H_5N
726.2(77)	7.8	736.4	6.5	728.7	6.5	C-H bending of C_4H_5N
3666.1(80)	-6.3	3504.6	-6.8	-^{c}	-	N-H stretching of C_4H_5N
PA-B						
705.6(81) 722.1(115)	2.6 19.1	-^{c}	-	-^{c}	-	C-H bending of C_2H_2
3420.3 (109)	-11.4	-^{c}	-	-^{c}	-	C-H antisym. str. of C_2H_2
584.8(16)	69.9	553.9/554.9	30.7^{b}	-^{c}	-	N-H bending of C_4H_5N
727.8(153)	9.4	-^{c}	-	-^{c}	-	C-H bending of C_4H_5N
3616.4 (399)	-56.0	3474.4/3479.7	-34.3^{d}	3460.5/3458.3	-60.8	N-H stretching of C_4H_5N
PAA-A						
712.0(34) 748.5(136) 754.3(75) 767.7(70)	9.0 45.5 51.3 64.7	-^{c}	-	-^{c}	-	C-H bending of C_2H_2

3377.0 (185) 3382.9 (316)	-54.6 -48.7	-[c]	-	-[c]	-	C-H antisym. str. of C_2H_2
588.6(36)	73.7	558.3/560.9/562.6	36.9[d]	-[c]	-	N-H bending of C_4H_5N
738.0(62) 752.0(191)	19.6 33.6	-[c]	-	-[c]	-	C-H bending of C_4H_5N
3607.3 (291)	-65.1	3463.6	-47.7	-[c]	-	N-H stretching of C_4H_5N
PPA-A						
727.2(41) 771.7(88)	24.2 68.7	-[c]	-	-[c]	-	C-H bending of C_2H_2
3356.5 (296)	-75.1	-[c]	-	-[c]	-	C-H antisym. str. of C_2H_2
600.3(37) 606.7(11)	85.4 91.8	566.3 568.4	42.6 44.7	-[c]	-	N-H bending of C_4H_5N
733.5(143)	15.1	-[c]	-	-[c]	-	C-H bending of C_4H_5N
3576.1 (394) 3533.2 (391)	-96.3 -139.2	3450.8/3443.1 3404.8/3401.4	-64.5[d] -110.3[d]	-[c]	-	N-H stretching of C_4H_5N

[a] $\Delta\nu = \nu_{heterodimer}-\nu_{monomer}$; [b] Intensity in km mol^{-1} is given in parenthesis; [c] Experimental features were not observed; [d] Average of multiplet experimental wavenumbers of the monomers and multimers were taken to compute the experimental shift.

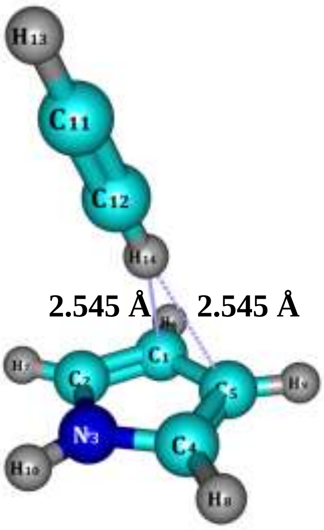

PA-A

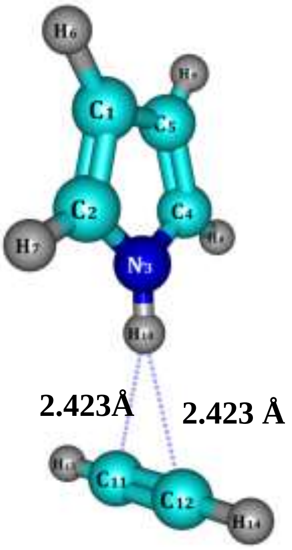

PA-B

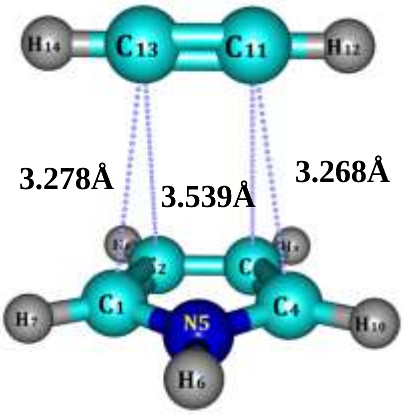

PA-C

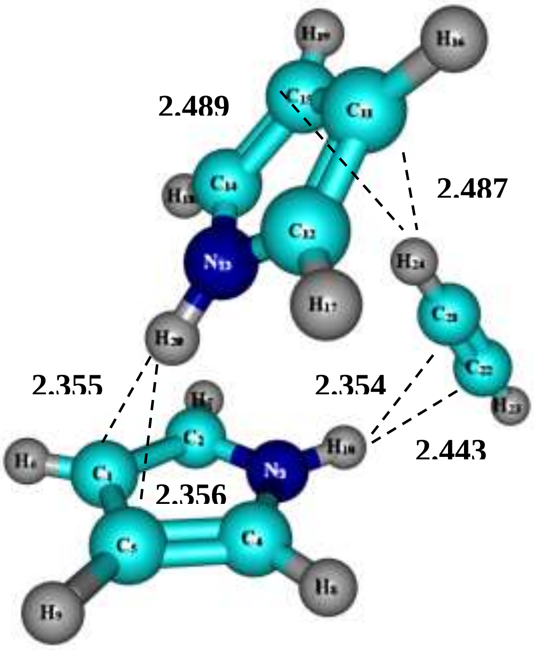

PPA-A

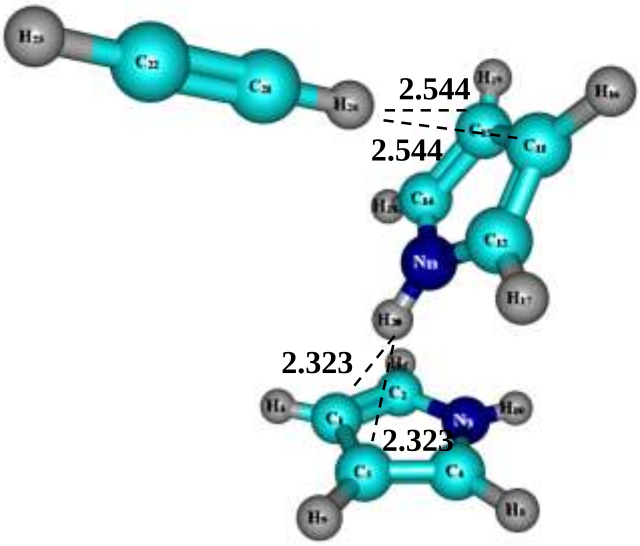

PPA-B

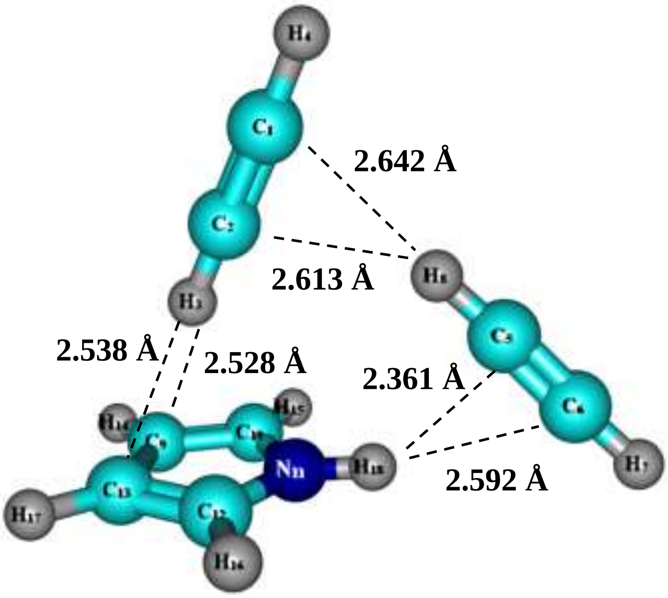

PAA-A

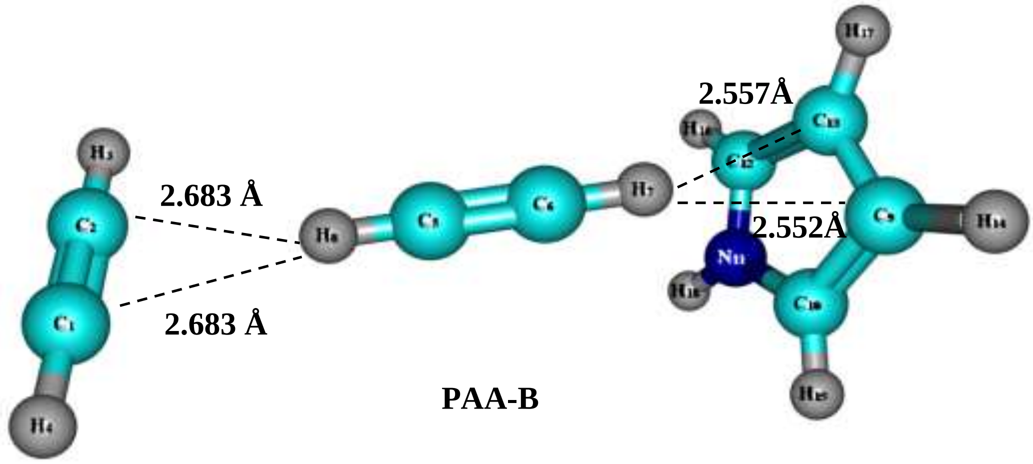

PAA-B

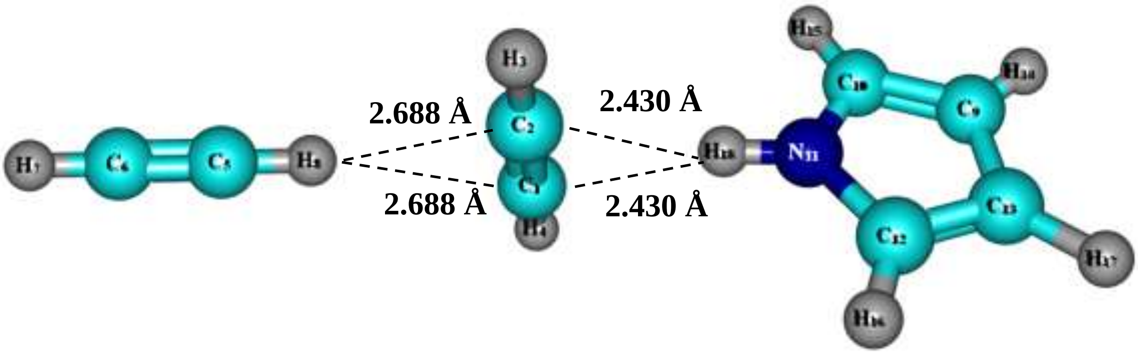

PAA-C

Figure 4.13 Structures of 1:1, 2:1 and 1:2 C_2H_2-C_4H_5N heterodimers PA-A, PA-B, PA-C, PPA-A, multimers PPA-B, PAA-A, PAA-B AND PAA-C computed at MP2/aug-cc-pVDZ level of theory.

4.2.3.3 Vibrational assignments in the ν_5 mode of C_2H_2

Computations showed that the doubly degenerate ν_5 C-H bending mode gets split on heterodimer formation and occurs at 715.3 and 739.4 cm^{-1}. Experimentally, new feature was observed at 763.7 and 764.2/757.4 cm^{-1} in N_2 and Ar matrixes, respectively (Figure 4.9 grids D, E). The experimental blue-shift of 19.0 (N_2) and 35.4 (Ar) cm^{-1} agrees well with computed blue-shift of 36.4 cm^{-1} for the heterodimer PA-A (Table 4.6). The other computed feature at 715.3 cm^{-1} with a blue-shift of 12.1 cm^{-1} could not be observed experimentally in the matrixes (Figure 4.9 grids D, E).

For the heterodimer B, the computations indicated a blue-shift of 2.6 and 19.1 cm^{-1}. Experimentally, we could not discern any new feature for the heterodimer PA-B in the matrixes.

4.2.3.4 Vibrational assignments in the ν_{N-H} stretching mode of C_4H_5N

When C_2H_2 concentration was varied in C_4H_5N/inert gas mixture, new feature was observed in the N-H stretching region of pyrrole sub-molecule in N_2 matrix at 3504.6 cm^{-1}. The experimental red-shift of -6.8 (N_2) from the C_4H_5N monomer absorption matches well with the computed red-shift of -6.3 cm^{-1} for the C-H•••π heterodimer PA-A where C_4H_5N acts as a proton acceptor. The corresponding feature was not observed in the Ar matrix. Furthermore, new features were observed experimentally at 3479.7/3474.4 cm^{-1} (N_2) and 3460.5/3458.3 (Ar) which were red-shifted by -34.3 cm^{-1} in N_2 and -60.8 cm^{-1} in Ar, compared well with the computed shift of -56.0 cm^{-1} for the heterodimer PA-B with N-H•••π interaction, where pyrrole acts as proton donor (Table 4.6).

In N_2 matrix, a new peak was observed in the N-H stretching region of C_4H_5N sub-molecule at 3463.6 cm^{-1}, with a red-shift of -47.7 cm^{-1}, comparing with the computed red-shift of -65.1 cm^{-1} for the cyclic heterotrimer PAA-A. Furthermore, new peaks were observed in N_2 matrix at 3450.8, 3443.1, 3404.8 and 3401.4 cm^{-1}, shifted by -64.5 and -110.3 cm^{-1}

matched well with the computed shifts of -96.3 and -139.2 cm^{-1} of the C_2H_2-C_4H_5N heterotrimer PPA-A. The corresponding bands were not seen in Ar matrix.

4.2.3.5 Vibrational assignments in the ν_{N-H} bending mode of C_4H_5N

On heterodimer formation, new features were observed in the N-H bending region at 539.5/538.3 cm^{-1} in N_2 and 503.5/502.6 cm^{-1} in Ar matrix. The experimental blue-shift of 15.2 (N_2) and 20.3 (Ar) cm^{-1} correlates well with the computed blue-shift of 19.5 cm^{-1} for the heterodimer PA-A. The experimental feature observed at 553.9/554.9, at a blue-shift of 30.7 cm^{-1} can be assigned to PA-B having a computed blue-shift of 69.9 cm^{-1}. No new feature could be observed for the heterodimer PA-B in Ar matrix.

New features were observed in N_2 matrix at 558.3, 560.9 and 562.6 cm^{-1}, which amounts to a blue-shift of ~ 36.9 cm^{-1}. The experimental shift agrees reasonably well with the computed shift of 73.7 cm^{-1} for the heterodimer PA-A. Furthermore, the experimental feature observed in N_2 matrix at 566.3, 568.4 with a blue-shift of 42.6 and 44.7 cm^{-1} matches well with the computed blue-shift of 85.4 and 91.8 cm^{-1} for the heterodimer PPA-A. The corresponding peaks for the higher aggregates were not seen in Ar matrix (Table 4.6). Experimentally, new features for the higher heterotrimers PAA-A, PAA-B, PAA-C and PPA-A, PPA-B in the ν_3, ν_5 modes of C_2H_2 and ν_{C-H} bending mode of C_4H_5N sub-molecule were not observed.

It should be mentioned that the computed shift in the N-H bending mode of C_4H_5N submolecule was larger when compared to the N-H stretching mode. This observation is likely due to the effect of Ar/N_2 matrix on the N-H bending and stretching vibrational modes of C_4H_5N monomer and C_2H_2-C_4H_5N heterodimers. Based on the experimental observation, it can be concluded that the interaction of Ar/N_2 matrix on the N-H bending and stretching modes of C_4H_5N in the C_2H_2-C_4H_5N heterodimer is very different, due to which there is a large deviation between the experiment and computation in the N-H bending mode. In fact, the experimental wavenumbers of N-H stretching mode of C_4H_5N are red-shifted by ~-9.0 (Ar) and -17.8 (N_2) cm^{-1}, respectively, in the matrixes with respect to the gas phase value [1, 13, 14]. Notably, the shift in the matrix with respect to the gas phase is an indicator of the effect of matrixes on the vibrational modes of C_4H_5N.

4.2.3.6 Vibrational assignments in the $\nu_{C\text{-}H}$ bending mode of C_4H_5N

The C-H bending mode of C_4H_5N shows a strong absorption at 722.2 and 729.9 cm^{-1} in Ar and N_2 matrixes, respectively (Figure 4.12). The experimental feature observed at 728.7 and 736.4 cm^{-1} in Ar and N_2 matrixes, with the blue-shift of 6.5 cm^{-1} in both Ar and N_2 matrixes compares well with the computed blue-shift of 7.8 cm^{-1} for the heterodimer PA-A. Experimentally, the feature corresponding to heterodimer PA-B could not be discerned in either in Ar or in N_2 matrix at this mode (Figure 4.9 grid E, Figure 4.12 grids A & B).

4.3 Atoms-in-Molecules Analysis

Atoms-in-molecules (AIM) analysis uses the gradient of electron density, $\nabla^2\rho(r_c)$ to partition the molecules into atoms and to show that they are chemically bonded by forming bond paths along the critical points (bond critical point, *bcp*) between the atoms. The formation of hydrogen bond between C_4H_5N and C_2H_2/C_2H_4/C_6H_6 was confirmed by the presence of (3, -1) *bcp*s, between the interacting atoms along the atomic interaction line. The (3, -1) *bcp* signifies the presence of electron density $\rho(r_c)$ between the pair of atoms and the nature of interaction is known by the value of the gradient of electron density, $\nabla^2\rho(r_c)$. Table 4.7(A-C) lists the values of electron density (ρ), Laplacian ($\nabla^2\rho(r_c)$) and the Eigen values (λ_1, λ_2, λ_3) for the intermolecular *bcps* of the 1:1 PB-A, PE-A, PE-B, PE-C, PE-D, PA-A and PA-B heterodimers, respectively. Figures 4.14 (I-VIII) illustrate the AIM plots showing the intermolecular *bcp,* ring critical point *(rcp)* and cage critical point *(ccp)* of the $C_4H_5N\cdots C_6H_6$, $C_4H_5N\cdots C_2H_2$ and $C_4H_5N\cdots C_2H_4$ heterodimers. From the table, it is clear that the magnitude of $\rho(r_c)$ and $\nabla^2\rho(r_c)$ at the *bcp* for all the heterodimers is of the order of 10^{-2} a.u., which is indicative of the weak nature of interaction of closed shell type. In PB-A heterodimer (Figure 4.14 IV), AIM analysis divulged two *bcp*'s between the nitrogen of C_4H_5N and the carbon of C_6H_6 and one *bcp* between the hydrogen of C_4H_5N with the π-electrons of C_6H_6 ring. One of the *bcps* had a higher magnitude of ρ, while the other two *bcps* have similar values and marginally less than the former explaining the angular distortion of the heterodimer, something between a pure T-shape and a pure π···π* stacking (Table 4.7A). In PE-A heterodimer (Figure 4.14 V), the only N-H···π interaction shows a *bcp* between the bridging H atom and the π-cloud of C_2H_4 (Table 4.7B). For the PE-B heterodimer (Figure 4.14 VI), three intermolecular *bcp*s, *rcp*s and one *ccp* between the C_2H_4 and C_4H_5N confirm the interaction is of C-H···π type. The presence of n···π*/π_N···π* bonding defines the angular distortion of C_2H_4 towards the C_4H_5N-ring, instead of a perpendicular structure. In PE-C heterodimer (Figure 4.14 VII), two intermolecular *bcp*s were found between the carbons of C_4H_5N and C_2H_4, confirms the π···π* interaction. Finally, the PE-D heterodimer showed two intermolecular *bcps* between the hydrogen of C_4H_5N with the carbon of C_2H_4 thus forming a C-H···C interaction. The magnitude of $\rho(r_c)$ and $\nabla^2\rho(r_c)$ at the intermolecular *bcp*s are the lowest and shows that PE-D (Figure 4.14 VIII) is the weakest among all the heterodimers. For the C-H•••π heterodimer PA-A (Figure 4.14 I), AIM analysis indicated two *bcps* between the hydrogen H14 of C_2H_2 and carbons C1 and C5 of C_4H_5N, two (3,+1) *rcp* and one (3,+3) *ccp* satisfying the Poincare-Hopf rule. For the heterodimer PA-B, AIM analysis showed one (3,-1) *bcp* between the hydrogen of C_4H_5N and carbons C11, C12 of C_2H_2. Table 4.7C gives the properties of the *bcp* between the heterodimers PA-A and PA-B computed at MP2/aug-cc-pVDZ level of theory.

4.4 Natural Bond Orbital Analysis

Natural bond orbital (NBO) analysis is a useful tool to understand the nature of the interaction in the hydrogen bonded heterodimers. In NBO analysis, the off-diagonal element in the NBO basis gives the measure of the delocalization effects and the second order perturbation energy (E_2) gives the magnitude of delocalization interactions [15]. The present work compares the N-H···π/C-H···π type of hydrogen bonding interactions and the presence of π···π* between the 1:1 heterodimer of C_4H_5N···C_2H_4, C_4H_5N···C_2H_2, and C_4H_5N···C_6H_6. Table 4.8A illustrates the NBO analysis of the PB-A heterodimer. The E_2 energy of the π(C1-C3) and π(C2-C6)→σ*(N15-H22) interaction is 1.76 kcal mol^{-1} and due to this interaction, the N-H bond length elongates and as a result, the red-shift in the N-H stretching mode of C_4H_5N sub-molecule in the PB-A heterodimer is observed. Apart from the π···σ*, there exists another stabilizing interaction between the bonding π-orbitals of C_6H_6 to the antibonding π*-orbitals of C_4H_5N (π···π*), which amounts to ~1.81 kcal mol^{-1}. Due to this π···π* interaction, the geometry of the C_4H_5N molecule is altered and the PB-A heterodimer has a π-stacked structure, which is in contrast from the earlier gas-phase report of T-shaped geometry [3,4]. In both the interactions, the electron occupancies vary in the corresponding donor and the acceptor π-orbitals, as evident from the Table 4.8A. Figure. 4.15A show the orbital picture of the π···σ* and π···π* interactions in the PB-A heterodimer.

In C_4H_5N···C_2H_4 system, NBO analysis indicated that the PE-A heterodimer stabilized by π(C1-C2)→σ*(N9-H16) interaction and the corresponding E_2 energy is 7.18 kcal mol^{-1} (Table 4.8B). The electron occupancies of the donor decreases, while that of the acceptor orbital increases due to this interaction. Surprisingly, there exists another interaction that apparently seems to be between the non-bonded electrons on nitrogen of C_4H_5N to the antibonding π*-orbital of C_2H_4 (n^1N9→π*(C1-C2)) with an E_2 energy of 0.37 kcal mol^{-1}. Even though the E_2 energy of n···π* is much smaller in magnitude than the π···σ* interaction, it synergistically favors and strengthens the N-H···π geometry and the corresponding red-shift in the N-H stretching wavenumber increases in the C_4H_5N sub-molecule of the PE-A heterodimer. Importantly, it is to be noted that the lone pair *p*-orbital of the N atom in C_4H_5N is parallel to those of the adjacent C atoms and hence participates in maintaining the aromaticity of the ring and hence, n···π* delocalization should be considered as $\pi_{(N)}$···π* delocalization. Figure 4.15B depicts the orbital overlap picture of the π···σ* and π···π* interactions prevailing in the PE-A heterodimer.

The PE-B heterodimer is stabilized by C-H···π interaction and the E_2 energy for the π(C7-C8)→σ*(C2-H5) and π(C10-C11)→σ*(C2-H5) is 1.16 and 0.85 kcal mol^{-1}, respectively. In this heterodimer, the magnitude of E_2 energy of the $\pi_{(N)}$···π* interaction is very small of the order ~0.08 kcal mol^{-1} (Figure 4.15C), and that of π···π* interaction is π(C7-C8)→π*(C1-C2) is 0.14 kcal mol^{-1}. To facilitate this interaction, the ethylene molecule bends towards the plane of the C_4H_5N ring.

The second local minimum corresponds to a purely π···π* stacked PE-C heterodimer, where bonding π-orbitals of C_4H_5N interacts with antibonding π*-orbitals of C_2H_4. The cumulative E_2 energy of the π(C1-C2)/π(C4-C5)→π*(C11-C12) interaction is 2.29 kcal mol^{-1}. Furthermore, back donation of π-electron cloud of C_2H_4 to the antibonding π-electron cloud of C_4H_5N is also observed and the E_2 energy of this π^1(C11-C12)→π*(C1-C2) and π*(C4-C5) interaction is 0.35 kcal mol^{-1}. The change in orbital occupancies is seen due to this interaction. As there is no direct participation of N-H group of C_4H_5N in the formation of PE-C heterodimer, the corresponding shift in this mode is negligible. Fig. 4.15D shows the orbital picture of the interaction.

The least energetic PE-D heterodimer is stabilized by π···σ* interaction with an overall E_2 energy of ~0.59 kcal mol^{-1} and the orbital overlap picture of this interaction is shown in Fig. 4.15E.

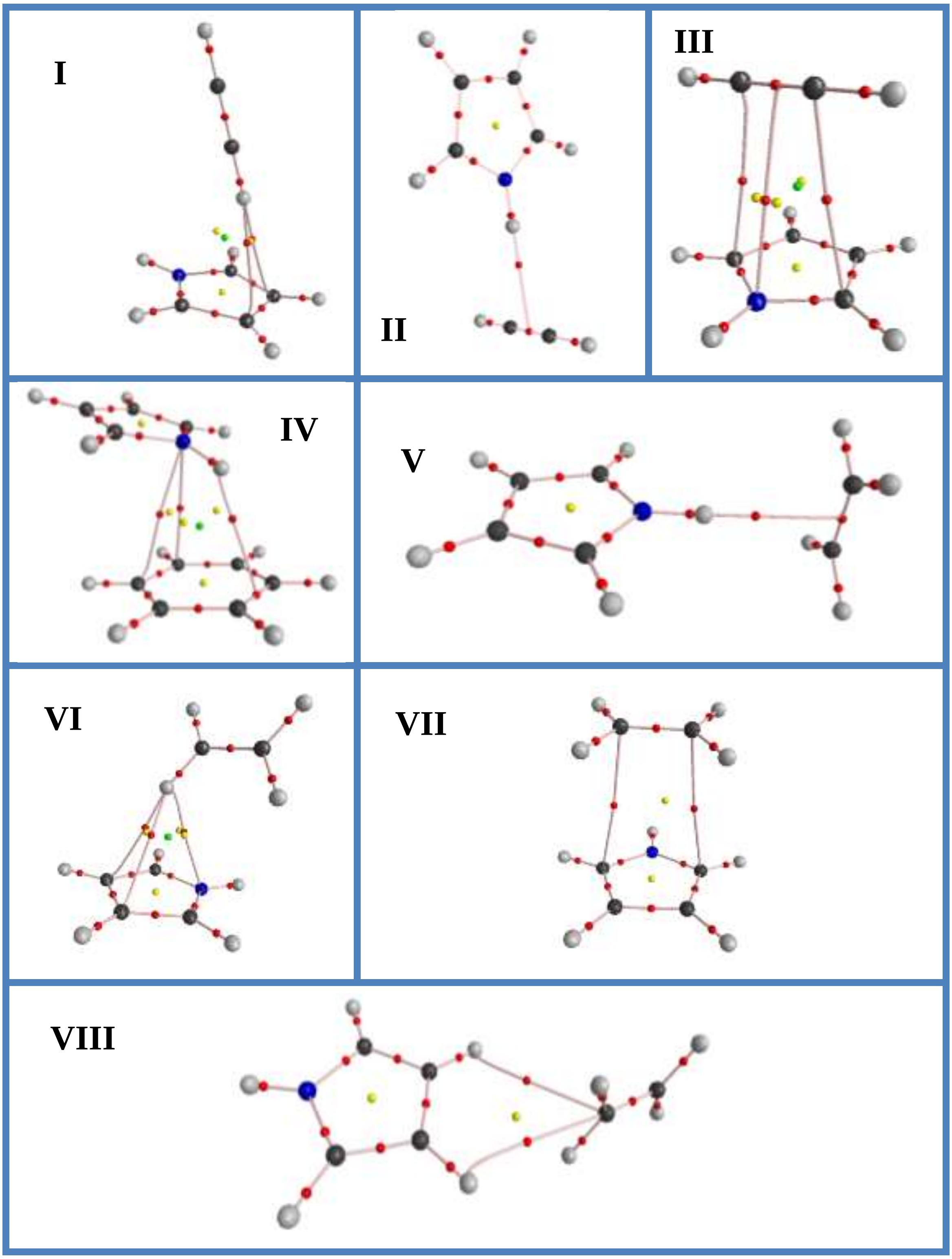

Figure 4.14 AIM plot showing the bond critical point (BCP in red), ring critical point (RCP, in yellow) and cage critical point (CCP, in green) obtained from topological AIM analysis computed at MP2/aug-cc-pVDZ level of theory for C_4H_5N-C_2H_2 heterodimer, (I) PA-A, (II) PA-B and (III) PA-C, C_4H_5N-C_6H_6 heterodimer, (IV) PB and C_4H_5N-C_2H_4 heterodimers (V) PE-A, (VI) PE-B, (VII) PE-C and (VIII) PE-D.

Table 4.7A Properties of (3,-1) bond critical point (BCP) of Pyrrole-Benzene Heterodimer PB-A computed at MP2/aug-cc-pVDZ Level of Theory.

Heterodimer	Interaction	$\rho(r_c)$	$\nabla^2\rho(r_c)$	λ_1	λ_2	λ_3
PB-A	N-H…π	0.0098	0.0287	-0.0074	-0.0019	0.0380
	N-H…π	0.0092	0.0271	-0.0048	-0.0009	0.0328
	N-H…π	0.0092	0.0271	-0.0048	-0.0009	0.0328

Table 4.7B Properties of (3,-1) bond critical point (BCP) of Pyrrole-Ethylene Heterodimers PE-A, PE-B, PE-C and PE-D computed at MP2/aug-cc-pVDZ Level of Theory.

Heterodimer	Interaction	$\rho(r_c)$	$\nabla^2\rho(r_c)$	λ_1	λ_2	λ_3
PE-A	N-H…π	0.0133	0.0312	-0.0126	-0.0076	0.0514
PE-B	C-H…π	0.0087	0.0287	-0.0052	-0.0005	0.0344
	C-H…π	0.0087	0.0285	-0.0052	-0.0007	0.0344
	π_N…π*	0.0080	0.0323	-0.0029	-0.0005	0.0357
PE-C	π…π*	0.0074	0.0206	-0.0038	-0.0012	0.0256
	π…π*	0.0073	0.0205	-0.0037	-0.0012	0.0254
PE-D	π…C-H	0.0055	0.0203	-0.0030	-0.0024	0.0257
	π…C-H	0.0045	0.0184	-0.0021	-0.0002	0.0207

Table 4.7C Properties of (3,-1) bond critical point (BCP) of Pyrrole-Acetylene Heterodimers PA-A and PA-B computed at MP2/aug-cc-pVDZ Level of Theory.

Heterodimer	Interaction	$\rho(r_c)$	$\nabla^2\rho(r_c)$	λ_1	λ_2	λ_3
PA-A	C-H…π	0.0105	0.03420	-0.00720	-0.00036	0.04176
PA-B	N-H…π	0.0133	0.03693	-0.01223	-0.00801	0.05717

Table 4.8C list the results of the NBO analysis of the $C_2H_2 \cdots C_4H_5N$ heterodimers A, B and C computed at MP2/aug-cc-pVDZ level of theory. From the Table 4.8C, it is clear that the electron occupancy in the antibonding orbital σ*(C12-H14) of C_2H_2 sub-molecule is increased while there is a reduction in the electron occupancies in the bonding π(C1-C2), π(C4-C5) orbital and in the nitrogen lone pair of n^1N3 of C_4H_5N sub-molecule in the C-H•••π heterodimer A. The second order perturbation energy E_2 for the delocalization interactions π(C1-C2)→σ*(C12-H14) and π(C4-C5)→σ*(C12-H14) is ~1.69 kcal mol^{-1}. Even though the E_2 energies are smaller in magnitude for the remote delocalization interactions π(C1-C2)→σ*(C11-H12), π(C4-C5)→σ*(C11-H12), n^1N3→σ*(C12-H14) and n^1N3→σ*(C11-C12), their contribution in stabilizing the C-H•••π heterodimer A cannot be neglected. For the heterodimer B stabilized by N-H•••π interaction, the E_2 energy for the delocalization interactions π(C11-C12)→σ*(N3-H10) is ~6.16 kcal mol^{-1}. The other remote delocalization interactions such as σ(C11-H13)→σ*(N3-H10), σ(C12-H14)→σ*(N3-H10) and n^1N3→σ*(C11-C12) also contribute in stabilizing the heterodimer B. In heterodimer PA-C, electron delocalization was observed from the bonding orbitals of C_4H_5N π(C1-C2)/π(C3-C4) to the antibonding π*(C11-C13) orbitals of C_2H_2. From the Table 4.8C it is observed that the change in the electron occupancies of the antibonding orbital of σ*(N3-H10) is larger than σ*(C12-H14) and the magnitude of E_2 energies for the delocalization interaction is higher for the N-H•••π heterodimer B than C-H•••π heterodimer A, which is reflected by a larger red-shift in the former than the latter. Apart from the conventional π···σ* hyperconjugative charge transfer interactions, NBO analysis revealed the heterodimers are further stabilized by n···π*/π···π* interactions. The E_2 energies of the n···π*/π···π* bonding in C-H···π (PA-A) and N-H···π (PA-B) heterodimers are 0.23 and 0.30 kcal mol^{-1}, respectively (Table 4.8C). Figure

4.15F and 4.15G show the orbital overlap picture of the PA-A and PA-B heterodimers, respectively.

4.4.1 n···π or π···π* interaction ?*

NBO is a useful method that enumerates the changes of donor-acceptor interactions and their corresponding occupancies due to subtle changes in molecular environments, as in the case of hydrogen bond formation between neutral species. Derived from variational, perturbative, or density functional theoretic (DFT) approximations, NBO plays a robust role in predicting novel bonding motifs. In the current report, a unique n···π* interaction was predicted by NBO analysis for the PE-A, PE-B, PA-A and PA-B heterodimers. In this type of interaction, non-bonding electrons on the nitrogen of C_4H_5N serves as electron donor and the π-electron cloud of C_2H_4/C_2H_2 acts as electron acceptor. It is a well-established fact that, C_4H_5N molecule is weakly basic as the lone pair electrons on nitrogen participate in the electron delocalization to maintain its aromaticity [16-17].

The n···π* interaction must proceed through the Bürgi–Dunitz trajectory of approach, where the lone-pair orbital must orient at 107° angle to the plane of the π-cloud, which does not occur in these 1:1 heterodimers [18-20]. Hence, pyrrole cannot act as a lone-pair donor to participate in n···π* bonding, rather the predicted phenomena is actually a π···π* interaction, since the electron pair on nitrogen in pyrrole is part of the π-electron cloud of the ring. Therefore, hereafter we shall refer the n···π* as π_N···π* to distinguish between the two different types of interactions involving π···π* and π_N···π*, although both are synonymous. In order to understand the presence and the concurrent influence of the π···π*/π_N···π* interaction, NBO analysis was carried out for the heterodimers involving C_4H_5N with π-electron systems such as propene, but-1-ene, *trans*-but-2-ene, propyne, but-2-yne, acetonitrile, benzonitrile, cyanoacetylene, phenol, toluene, *p*-xylene, mesitylene, hexafluorobenzene and pyrrole homodimers.

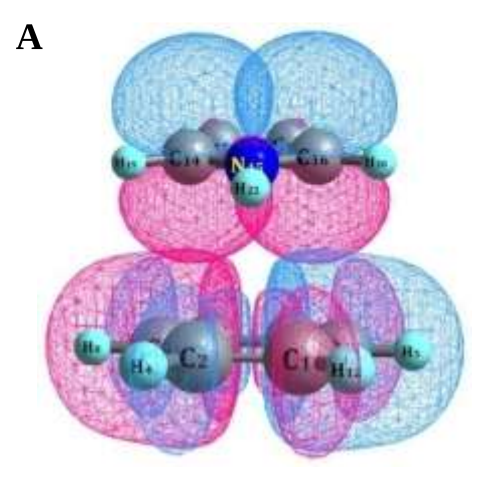

π(C13-C14)/π(C16-C17)→π*(C7-C10);
E2 = 1.32 kcal mol^{-1}

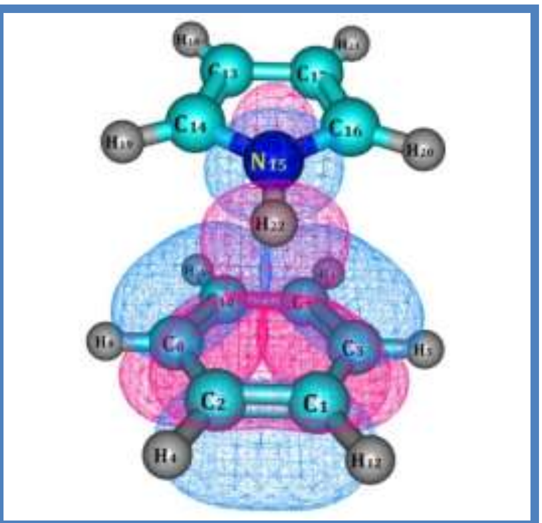

π(C1-C3)/π(C2-C6)→σ*(N15-H22);
E2=1.76 kcal mol^{-1}

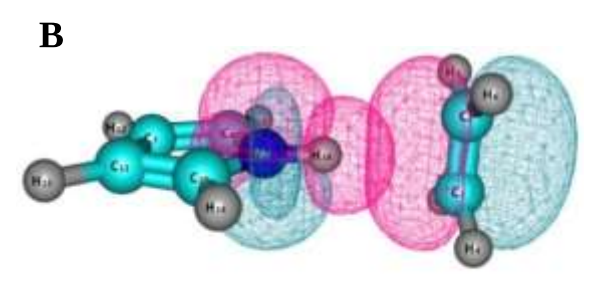

π(C1-C2)→σ*(N9-H16);
E2 = 7.18 kcal mol^{-1}

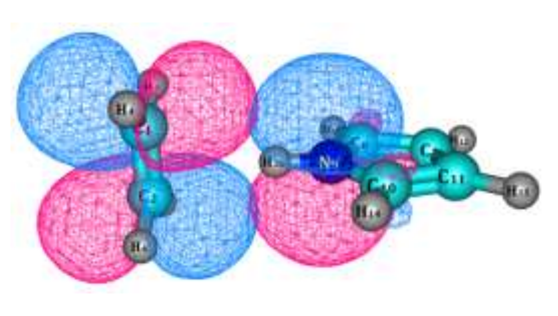

n^{1}N9→π*(C1-C2);
E2 = 0.37 kcal mol^{-1}

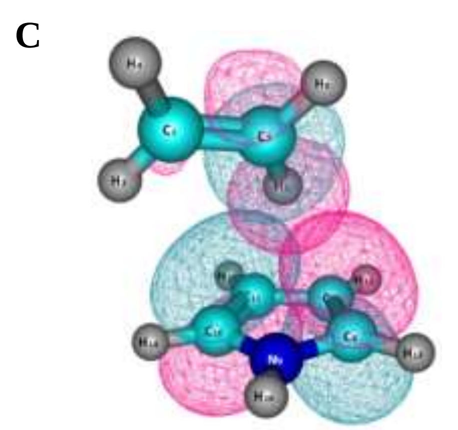

π(C7-C8)/π(C10-C11)→σ*(C2-H5);
E2 = 2.01 kcal mol^{-1}

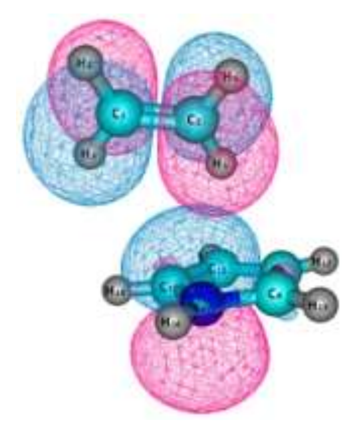

n^{1}N9→π*(C1-C2);
E2 = 0.08 kcal mol^{-1}

D 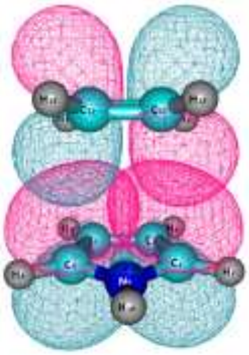	**π(C1-C2)/π(C4-C5)→π*(C11-C12); E2 = 2.29 kcal mol^{-1}** **π(C11-C12)→π*(C4-C5)/π*(C1-C2); E2 = 0.35 kcal mol^{-1}**
E 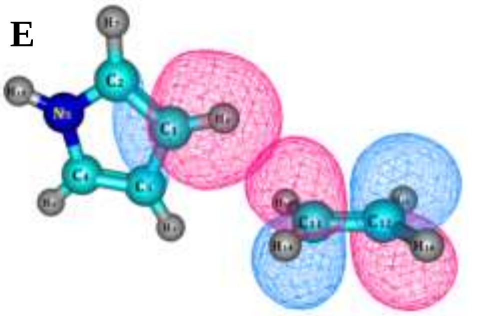	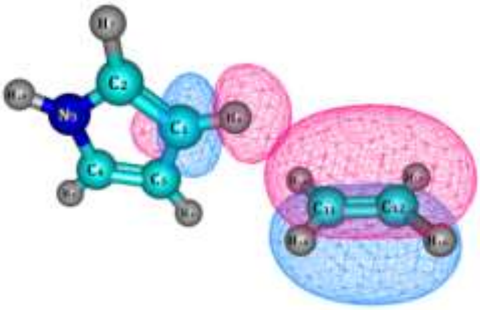
σ(C1-H6)→π^{1}*(C11-C12); E2= 0.25 kcal mol^{-1}	**π^{1}(C11-C12)→σ*(C1-H6); E2= 0.34 kcal mol^{-1}**
F 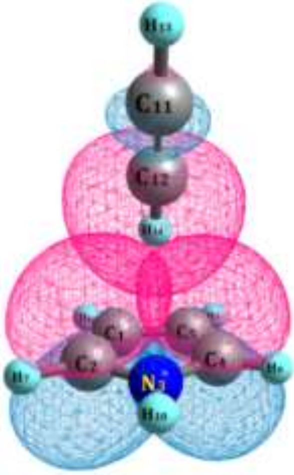	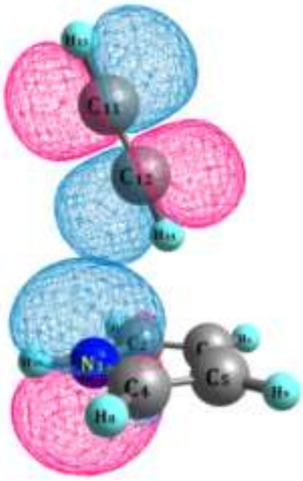
π(C1-C2)/π(C4-C5)→σ*(C12-H14); **E2 = 3.37 kcal mol-1**	**n1N3→π*(C11-C12);** **E2 = 0.23 kcal mol-1**

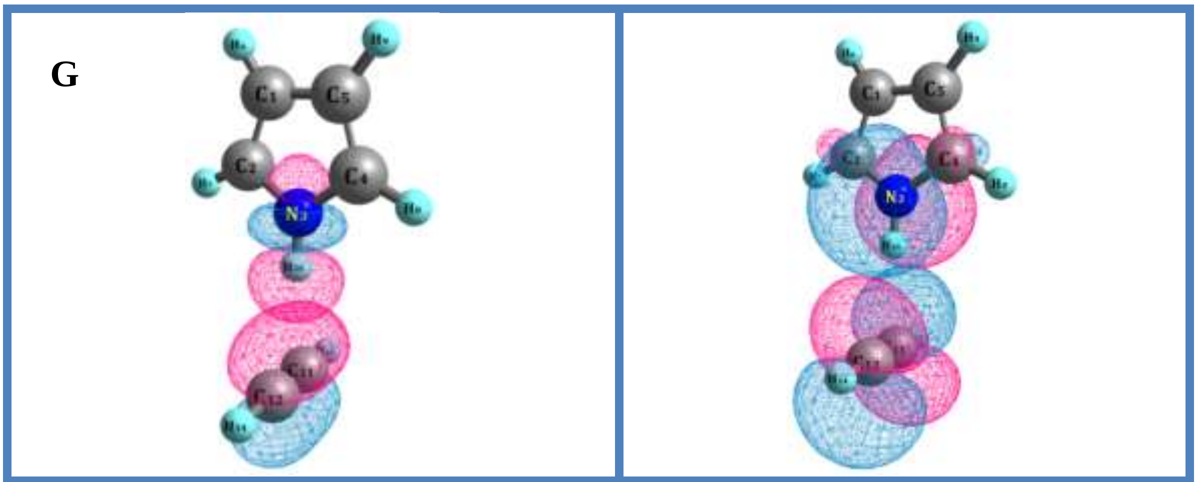

π(C11-C12)→σ*(N3-H10);
E2 = 6.16 kcal mol-1

n1N3→π*(C11-C12);
E2 = 0.30 kcal mol-1

Figure 4.15 NBO diagrams of the heterodimers of, C_4H_5N-C_6H_6 (PB) (A), and C_4H_5N-C_2H_4 (PE-A/B/C/D) (B, C, D, E) C_4H_5N-C_2H_2 (PA-A/B) (F & G) are shown. The delocalization energies in kcal mol^{-1} are given for the interaction.

Table 4.8A Electron occupancies of various NBOs of 1:1 Pyrrole-Benzene heterodimers computed at MP2/aug-cc-pVDZ level of theory. The donor-acceptor delocalization interaction and second order perturbation energies (E_2, kcal mol^{-1}) are also shown.

NBO	**Occupancy**	**Donor-acceptor delocalization interaction**	**E_2**
PB-A			
π(C1-C3) π(C2-C6)	1.67976(1.66397)[a]	π(C1-C3)→σ*(N15-H22)	0.88
π(C7-C10)	1.64562(1.66397)[a]	π(C2-C6)→σ*(N15-H22)	0.88
π*(C7-C10)	0.30734(0.33237)[a]	π(C7-C10)→π*(C13-C14)	0.24
σ*(N15-H22)	0.01903(0.01370)[a]	π(C7-C10)→π*(C16-C17)	0.25
π(C13-C14) π(C16-C17)	1.85835(1.86030)[a]	π(C13-C14)→π*(C7-C10)	0.66
π*(C13-C14) π*(C16-C17)	0.31428(0.31218)[a]	π(C16-C17)→π*(C7-C10)	0.66

[a] Electron occupancy of the monomer.

Table 4.8B Electron occupancies of various NBOs of 1:1 PE-A, PE-B and PE-C heterodimers computed at MP2/aug-cc-pVDZ level of theory. The donor-acceptor delocalization interaction and second order perturbation energies (E_2, kcal mol^{-1}) are also shown.

NBO	**Occupancy**	**Donor-acceptor delocalization interaction**	**E_2**
PE-A			
π(C1-C2)	1.98666(1.99235)[a]	π(C1-C2)→σ*(N9-H16)	7.18
σ*(N9-H16)	0.01256(0.01370)[a]	n^{1}N9→π*(C1-C2)	0.37
n^{1}N9	1.61641(1.63057)[a]		
PE-B			
π(C7-C8)	1.85771(1.86030)[a]	π(C7-C8)→σ*(C2-H5)	1.16
π(C10-C11)	1.85676(1.86030)[a]	π(C10-C11)→σ*(C2-H5)	0.85
σ*(C2-H5)	0.00967(0.00820)[a]	n^{1}N9→π*(C1-C2)	0.08
PE-C			
π(C1-C2)	1.85049(1.86030)[a]	π(C1-C2)→π^1*(C11-C12)	1.08
π(C4-C5)	1.85049(1.86030)[a]	π(C4-C5)→π^1*(C11-C12)	1.21
π^1*(C11-C12)	0.01097(0.00)[a]	π^1(C11-C12)→π*(C4-C5)	0.17
		π^1(C11-C12)→π*(C1-C2)	0.18
PE-D			
σ(C1-H6)	1.98597(1.98688)[a]	σ(C1-H6)→π^1*(C11-C12)	0.25
σ*(C1-H6)	0.00989(0.00936)[a]	π^1(C11-C12)→σ*(C1-H6)	0.34
π^1(C11-C12)	1.99778(1.99235)[a]		
π^1*(C11-C12)	0.00051(0.00)[a]		

[a] Electron occupancy of the monomer.

Table 4.8C Electron Occupancies of various NBOs of 1:1 PA-A, PA-B and PA-C Heterodimers computed at MP2/aug-cc-pVDZ Level of Theory. The Donor-Acceptor Delocalization Interaction and Second Order Perturbation Energies (E_2, kcal mol^{-1}) are also shown.

NBO	**Occupancy**	**Donor-acceptor delocalization interaction**	**E_2**
PA-A			
π(C1-C2)	1.85582(1.86030)[a]	π(C1-C2) → σ*(C12-H14)	1.69
		π(C1-C2) → σ*(C11-C12)	0.32
π(C4-C5)	1.85579 (1.86030)[a]	π(C4-C5) → σ*(C12-H14)	1.68
		π(C4-C5) → σ*(C11-C12)	0.32
σ*(C12-H14)	0.01040 (0.00521)[a]	n^1N3 → σ*(C12-H14)	0.06
n^1N3	1.62388(1.63057)[a]	n^1N3 → π*(C11-C12)	0.23
PA-B			
π(C11-C12)	1.99043(1.99224)[a]	π(C11-C12) → σ*(N3-H10)	6.16
σ(C11-H13)	1.99086(1.99137)[a]	σ(C11-H13) → σ*(N3-H10)	0.20
σ(C12-H14)	1.99086(1.99137)[a]	σ(C12-H14) → σ*(N3-H10	0.20
σ*(N3-H10)	0.02170 (0.01370)[a]	n^1N3 → π*(C11-C12)	0.30
n^1N3	1.61768(1.63057)[a]		
PA-C			
π(C1-C2)	1.85258(1.86030)[a]	π(C1-C2)→π^1*(C11-C13)	0.07
π(C3-C4)	1.85272(1.86030)[a]	π(C1-C2)→π^2*(C11-C13)	0.18
π^1*(C11-C13)	0.00031(0.00)[a]	π(C1-C2)→π^3*(C11-C13)	0.39
π^2*(C11-C13)	0.00941(0.00)[a]	π(C3-C4)→π^1*(C11-C13)	0.08
π^3*(C11-C13)	0.00894(0.00911)[a]	π(C3-C4)→π^2*(C11-C13)	0.20
		π(C3-C4)→π^3*(C11-C13)	0.44

[a] Electron occupancy of the monomer.

Table 4.9 lists E_2 energies of the $\pi\cdots\sigma^*$, $\pi\cdots\pi^*$ and $\pi_N\cdots\pi^*$ interactions prevailing in the C_4H_5N with the π-electron systems. Figures 4.16 and 4.17 illustrate the structure of all the heterodimers.

It is clear from the Table 4.9 that except for benzene and mesitylene, all the π-electron donors showed this $\pi_N\cdots\pi^*$ interaction. The magnitude of E_2 energy of the $\pi_N\cdots\pi^*$ of all the π-electron donors with C_4H_5N is lesser than $\pi\cdots\sigma^*$ except for hexafluorobenzene. The magnitude of E_2 energy of $\pi_N\cdots\pi^*$ interaction of the alkyne is more than that of alkene due to the increased π-electron density of the former than the latter. Furthermore, the alkyl group substitution on the alkene/alkyne chain increases the magnitude of the $\pi_N\cdots\pi^*$ interaction due to the +I effect of the alkyl group. Among the aromatic ring systems, the interaction follows the order of $\pi\cdots\sigma^* > \pi\cdots\pi^* > \pi_N\cdots\pi^*$ except for benzene, mesitylene, phenol, benzonitrile and hexafluorobenzene. For the C_4H_5N-C_6H_5OH system the E_2 energy follows the order, $\pi\cdots\sigma^* > \pi_N\cdots\pi^* > \pi\cdots\pi^*$, which is evident from the structure of the heterodimers where the O-H and C-H of phenol interacts with the π–cloud of C_4H_5N. The planes of both the molecules are not perpendicular to each other and phenol ring is inclined towards the N-atom of C_4H_5N. Similar observation was also found in $(C_4H_5N)_2$ and PB-A. The slanting geometry is probably a result of the influence of both $\pi\cdots\pi^*$ (as mentioned by Dauster et al.) and $\pi_N\cdots\pi^*$ interactions, since the donor-C_4H_5N aligns towards the N-side of the acceptor-C_4H_5N. In C_4H_5N-benzonitrile, the order is $\pi\cdots\pi^* > \pi_N\cdots\pi^* > \pi\cdots\sigma^*$ and the dominant interaction is due to the charge transfer between the two π-electron clouds of precursors, followed by $\pi_N\cdots\pi^*$ from C_4H_5N bonding orbital to the antibonding orbital of C≡N of benzonitrile. Hence, the final geometry is a stacked one, with the N-H of C_4H_5N is parallel to the C≡N of benzonitrile, instead of perpendicular structure. In case of C_4H_5N-hexafluorobenzene heterodimer, the interaction order is completely inverted ($\pi_N\cdots\pi^* > \pi\cdots\pi^* > \pi\cdots\sigma^*$) and the E_2 energy of the $\pi_N\cdots\pi^*$ is 1.2 kcal mol^{-1}. The $\pi_N\cdots\pi^*$

dominance is likely due to the electronegativity of fluorine, which siphons off all the π-electron from the benzene ring and the hexafluorobenzene acts as electron acceptor. Hence the final geometry is a parallel displaced, instead of pure stacking. (Figure 4.17 block G) The reason for not observing the $\pi_N\cdots\pi^*$ interaction in C_4H_5N with benzene and mesitylene is due to the uniform delocalization of π- electrons over the aromatic ring, for which $\pi\cdots\pi^*$ charge transfer interaction is preferred over the $\pi_N\cdots\pi^*$.

4.5 Energy Decomposition Analysis

EDA is a useful tool to dissect the physical origin of intra and intermolecular interactions of molecules. The most popular and well-known EDA methods are the one based on Morokuma and the Extended Transition State (ETS) of Ziegler and Rauk [21-22] implemented in the ADF program package [23] and Localized molecular orbital energy decomposition analysis (LMOEDA) developed by Su et al. [24]. In the ADF-EDA method the interaction energy is decomposed into three main components: electrostatic, Pauli repulsion and orbital interaction terms. Figure 4.18 depicts the various contributions from the electrostatic, dispersion and exchange interactions stabilizing, while the Pauli repulsion term (kinetic and coulomb) destabilizing the total binding energy for the various heterodimers. The dispersion corrected B3LYP level in combination with the triple zeta and doubly polarized basis set (B3LYP-D3/TZ2P) is similar to MP2/aug-cc-pVDZ in terms of computational quality. NBO analysis revealed that the PB-A heterodimer has both N-H$\cdots\pi$ and $\pi\cdots\pi^*$ interactions and the EDA also confirmed that the magnitude of electrostatic and dispersion contributions is nearly the same, indicating the *co-operative* stabilization of these two interactions in this heterodimer.

Table 4.9 Comparison of the Second Order Perturbation Energies (E_2, in kcal mol^{-1}) of the $\pi_n \rightarrow \pi^*$ Interaction in the various N-H···π heterodimers of Pyrrole with π-electron Systems computed at MP2/aug-cc-pVDZ Level of Theory.

Systems	**$\pi \rightarrow \sigma^*$**	**$\pi \rightarrow \pi^*$**	**$\pi_n \rightarrow \pi^*$**
Pyrrole-Ethylene	7.28	----[a]	0.37
Pyrrole-Propene	3.14	0.17	0.32
Pyrrole-But-1-ene	6.46	----[a]	0.16
Pyrrole-*t*-But-2-ene	8.67	----[a]	0.47
Pyrrole-Acetylene	6.46	----[a]	0.30
Pyrrole-Propyne	3.47	----[a]	0.54
Pyrrole-But-2-yne	3.65	----[a]	0.53
Pyrrole-Acetonitrile	3.25	----[a]	0.70
Pyrrole-Cyanoacetylene(a)	4.12	0.95	0.30
Pyrrole-Cyanoacetylene(b)	2.35	----[a]	0.36
Pyrrole-Benzene	1.76	1.81	----[a]
Pyrrole-Toluene	3.67	1.54	0.31
Pyrrole-p-Xylene	3.70	1.53	0.28
Pyrrole-Mesitylene	2.25	1.38	----[a]
Pyrrole Dimer	4.43	0.55	0.36
Pyrrole-Phenol	9.52	0.36	0.51
Pyrrole-Benzonitrile	0.59	3.41	0.86
Pyrrole-Hexafluorobenzene	0.4	1.08	1.20

[a] Energy contribution is absent for the interaction.

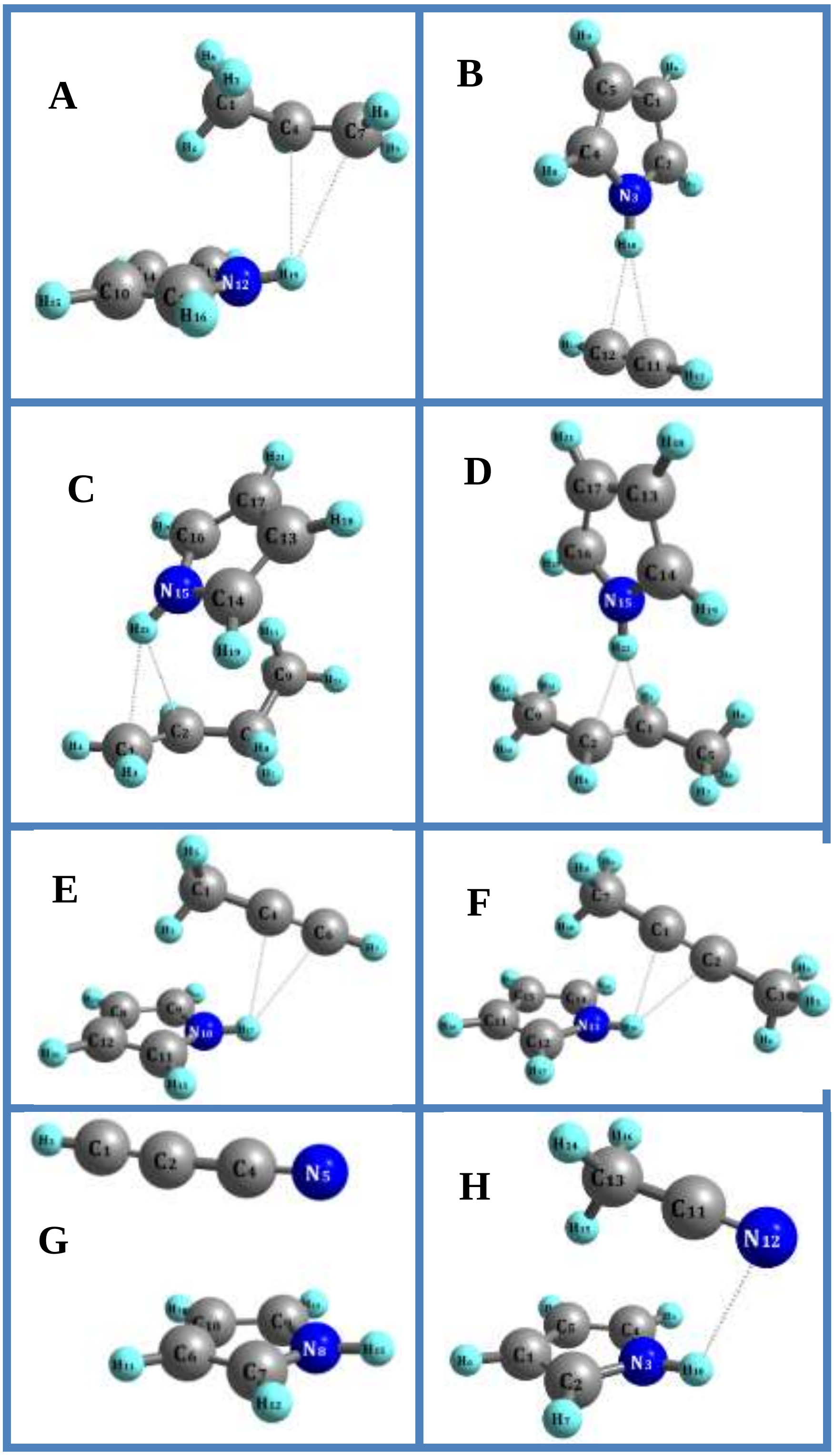

Figure 4.16 Computed structures of C₄H₅N with (A) propene, (B) acetylene, (C) but-1-ene, (D) *t*-but-2-ene, (E) propyne, (F) but-2-yne, (G) cyanoacetylene and (H) acetonitrile optimized at MP2/aug-cc-pVDZ level of theory.

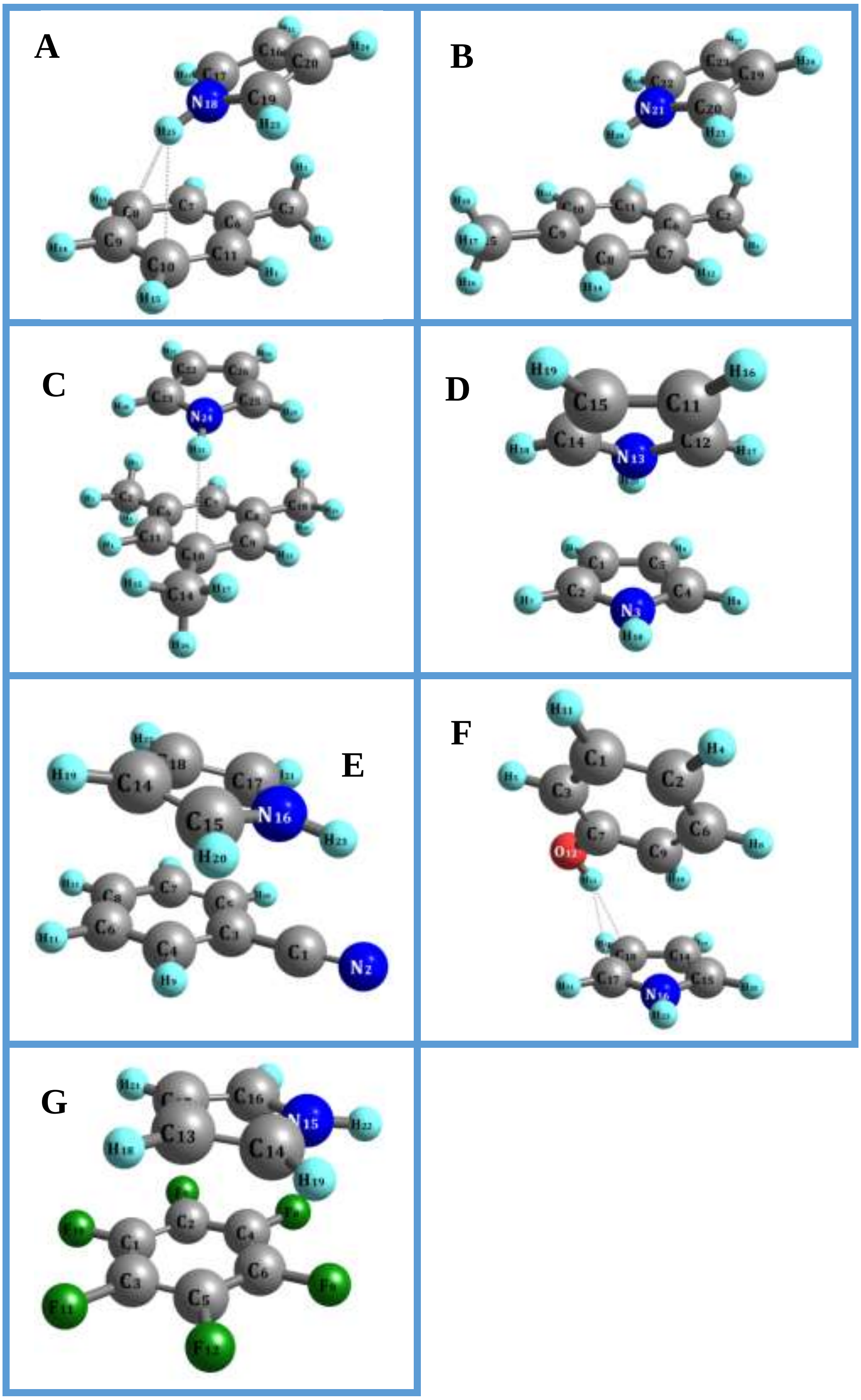

Figure 4.17 Computed structures of C_4H_5N with (A) toluene, (B) *p*-xylene, (C) mesitylene, (D) C_4H_5N, (E) benzonitrile, (F) phenol and (G) hexafluorobenzene heterodimer optimized at MP2/aug-cc-pVDZ level of theory.

Among the different heterodimers, probably due to the approach of two bulkier groups, the contribution of destabilizing Pauli repulsion contribution is highest for the PB-A. Overall the subtle balance between the combined contribution of stabilizing and the Pauli repulsion makes the PB-A heterodimer energetically more favorable than the PE heterodimers. On fragmenting the stabilizing energies of pyrrole-ethylene heterodimers PE-A, PE-B, PE-C and PE-D, it was found that the contribution from electrostatic forces decrease in the order PE-A>PE-C>PE-B>PE-D, while the dispersion contribution increases as PE-D<PE-A<PE-B<PE-C. In the PE-A and PE-B dimers, which is stabilized by N-H···π and C-H···π interactions, respectively, the contribution of electrostatic interaction decreases the energy of PE-A by 0.6 kcal mol^{-1} compared to PE-B while the dispersion contribution stabilizes PE-B by 1.52 kcal mol^{-1}. The sum total of destabilizing Pauli repulsion and the stabilizing interaction makes the PE-A heterodimer energetically more favorable than PE-B heterodimer. The PE-C heterodimer is stabilized by π···π* interaction, and as expected, the contribution of dispersion is increased while the contribution of exchange is decreased compared to the other two heterodimers. The destabilizing contribution from the Pauli repulsion term is highest for this heterodimer thus making the PE-C heterodimer least energetic than the other two PE-A and PE-B heterodimers. The PE-D conformer shows low stabilization energy compared to PE-C, and hence the ED analysis fails to show major contribution from any of the energy terms and infact. In PA-A and PA-B heterodimers, the strongest attractive interactions are electrostatic followed by charge transfer (orbital) and dispersion interactions. However for PA-C, the strongest interaction is the dispersion followed by electrostatic and charge transfer. The above trend clearly shows that due to the π•••π interaction in PA-C the contribution of dispersion interaction is higher than that in heterodimer A and B. The relatively large orbital interaction for the heterodimers PA-A, PA-B and PA-C, show that there is a significant charge transfer between the donor and acceptor sub-molecules.

4.6 Summary

In this chapter, the co-existence of co-operative $\pi_N\cdots\pi^*/\pi\cdots\pi^*$ interactions along with the predominant $\pi\cdots\sigma^*$ interactions in the heterodimers of pyrrole with benzene, ethylene and acetylene was highlighted through both experimental and computational methodologies. The PB, PE and PA heterodimers were synthesized and characterized at low temperatures using infrared spectroscopy. Computations indicated two geometries corresponding to PB-A (stabilized by N-H$\cdots\pi$ ($\pi\cdots\sigma^*$) and $\pi_N\cdots\pi^*$ interaction) and PB-B (stabilized by N-H$\cdots\pi$) heterodimers. Geometry optimization of C_4H_5N with C_2H_4 yielded four heterodimers PE-A, PE-B, PE-C and PE-D, which were stabilized by N-H$\cdots\pi$, C-H$\cdots\pi$, $\pi_N\cdots\pi^*$ and $\pi\cdots$H-C interactions, respectively; and that of C_4H_5N with C_2H_2 thrived three heterodimers PA-A, PA-B and PA-C, stabilized by C-H$\cdots\pi$, N-H$\cdots\pi$ and $\pi_N\cdots\pi^*$ interactions, respectively. Apart from the conventional $n\cdots\sigma^*/\pi\cdots\sigma^*$ interactions, NBO analysis revealed the presence of $\pi\cdots\pi^*$ interaction in the PB-A, PE-A, PE-B, PA-A and PA-B heterodimers. Through ED analysis, the contribution of dispersion was found to be equivalent to that of electrostatic in PB-A and PE-B heterodimers, while it was the primary stabilizing factor for PE-C and PA-C due to $\pi_N\cdots\pi^*$ bonding. Evidence for the formation of higher clusters of pyrrole$\cdots$benzene, pyrrole$\cdots$ethylene and pyrrole$\cdots$acetylene, stabilized co-operatively through dispersion was also found, in the cold matrixes. Furthermore, the geometries of heterodimers formed by pyrrole with acetylene, propene, *t*-but-2-ene, propyne, but-2-yne, acetonitrile, benzonitrile, cyanoacetylene, toluene, phenol, *p*-xylene, mesitylene, and hexafluorobenzene including the pyrrole-dimer are manifested through this weak $\pi_N\cdots\pi^*/\pi\cdots\pi^*$ interaction.

A comparison of various computed parameters with the experimental N-H vibrational shift of N-H$\cdots\pi$ and C-H$\cdots\pi$ heterodimers of pyrrole are listed in Table 4.10. Among the N-H$\cdots\pi$ heterodimers, PD shows the highest experimental and computed N-H vibrational shift for both proton donor (PD_{donor}) as well as acceptor ($PD_{acceptor}$), which correlates well with the change in the N-H bond length and BSSE corrected energy.

The magnitudes of electron density (ρ_{bcp}) at the BCP of the PD heterodimer and the E_2 energy are at variance with the experimental and computed N-H vibrational shift probably not considering the electrostatic and dispersion contributions. Based on the BSSE corrected energy, the next stronger heterodimer is PB-A, PE-A and PA-B are nearly isoenergetic. The experimental N-H vibrational shifts of PB-A, PE-A and PA-B correlate with the BSSE energies while the other parameters such as E_2, ρ_{bcp} and change in N-H bond length do not have linear correlation. A similar trend was observed in C-H$\cdots\pi$ heterodimers. The experimental shift in the Ar matrix does not correlate well with the BSSE corrected energies. The variation in the experimental shift is likely due to the difference in interaction of N_2 or Ar matrix to the different vibrational modes of C_4H_5N submolecule in the complex. Furthermore, the level of theory and basis sets used to compute the structures can give rise to such deviations. The deviation between the $\Delta\nu_{exp}$ and $\Delta\nu_{cal}$ is due to matrix effect is not taken into account while calculating the computed vibrational wavenumber of the heterodimers.

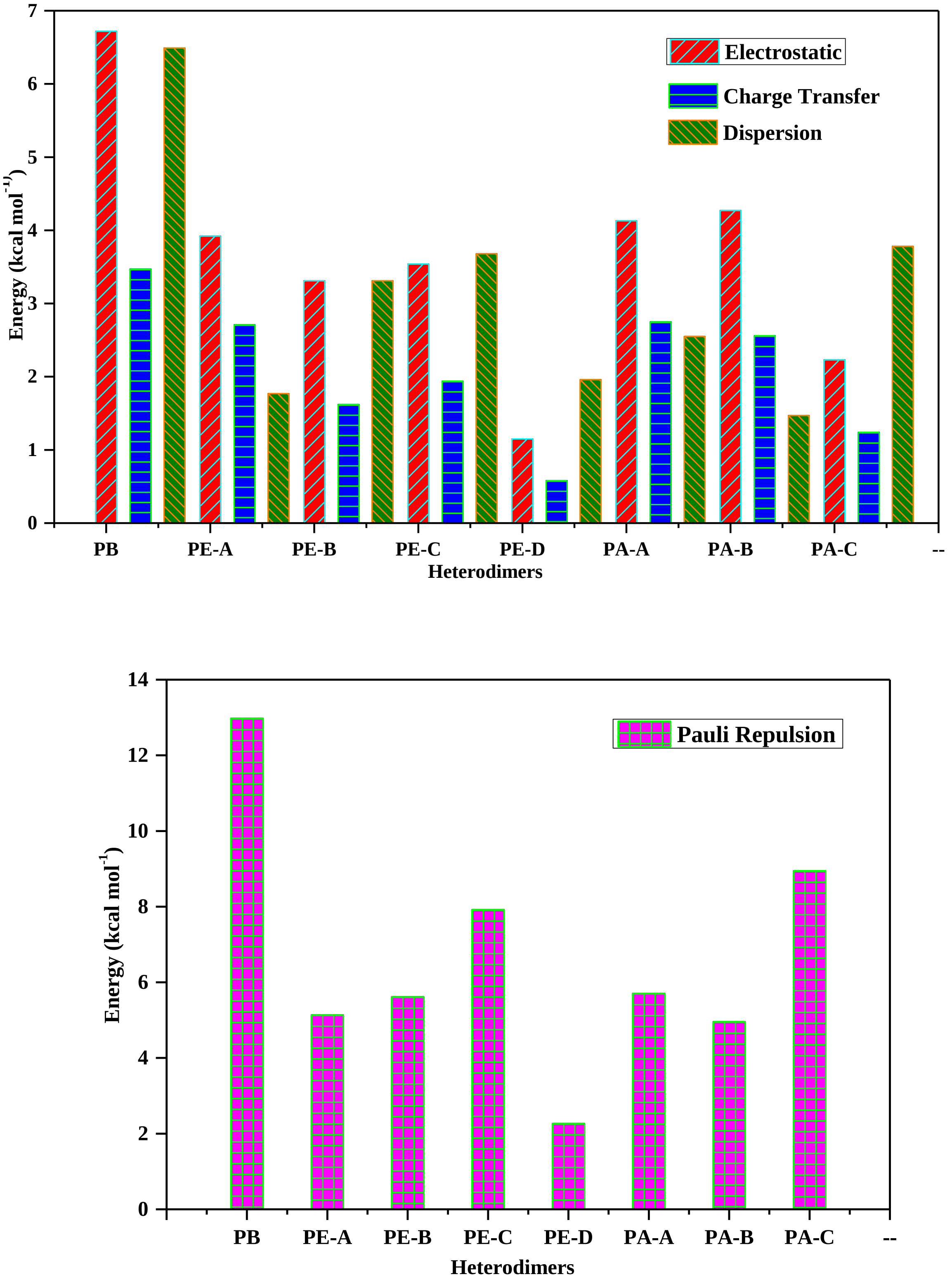

Figure 4.18 Bar graph showing the electrostatic, charge transfer, dispersion and Pauli repulsion contribution to the total binding energy of the C_4H_5N with C_6H_6, C_2H_4 and C_2H_2 heterodimers computed at B3LYP-D3/TZ2P level of theory.

Table 4.10 Table for comparing the Various Computed Parameters with the Experimental Shift in Wavenumbers for the N-H···π Heterodimers and C-H···π Heterodimers.

Heterodimers	$\Delta SE_{(BSSE)}$	$\Delta r_{(N-H)}$	ρ_{bcp}	E_2	$\Delta \nu_{calc}$	$\Delta \nu_{(N2)}$	$\Delta \nu_{(Ar)}$
N-H···π							
PA-B	-2.97	0.003	0.0133	-6.46	-56.0	-34.3	-60.8
PE-A	-2.91	0.004	0.0133	-7.28	-72.6	-48.6	-37.3
PB-A	-5.1	0.003	0.0282	-1.76	-56.2	-53.7	-61.3
PD_{donor}	-7.1	0.006	0.0138	-4.43	-109.0	-94.9	-106.7
H···π							
PE-B	-2.70	0.001	0.0147	-2.01	-4.5	-9.7	-
PA-A	-3.75	0.001	0.0105	-3.37	-6.3	-6.8	-
$PD_{acceptor}$	-7.1	0.001	0.0138	-4.43	-16.3	-11.1	-12.8

S.E. (BSSE) = Basis set superposition error corrected stabilisation energy in kcal mol^{-1};
$\Delta \nu_{N-H(calc)} = \nu_{N-H(complex)} - \nu_{N-H(monomer)}$ at MP2/aug-cc-pVDZ;
$\Delta r_{(N-H)} = r_{complex} - r_{monomer}$ (picometer);
E_2 = Second order perturbation energy in kcal mol^{-1} obtained from NBO Analysis;
$\Delta \nu_{N-H}$ (N_2) = $\nu_{N-H(complex)} - \nu_{N-H(monomer)}$ in N_2 matrix in cm^{-1};
$\Delta \nu_{N-H}$ (Ar)= $\nu_{N-H(complex)} - \nu_{N-H(monomer)}$ in Ar matrix in cm^{-1};

References

---

1. Self-Aggregation in Pyrrole: Matrix Isolation, Solid State Infrared Spectroscopy, and DFT Study, A. Gomez-Zavaglia, R. Fausto, *J. Phys. Chem. A*, **2004**, 108, 6953-6967.

2. PCl_3–C_6H_6 heterodimers: evidence for P···π phosphorus bonding at low temperatures, N. Ramanathan, K. Sankaran and K. Sundararajan, *Phys. Chem. Chem. Phys.*, **2016**, 18, 19350-19358.

3. N–H···π hydrogen-bonding and large-amplitude tipping vibrations in jet-cooled pyrrole–benzene, C. Pfaffen, D. Infanger, P. Ottiger, H. -M. Frey, S. Leutwyler, *Phys. Chem. Chem. Phys*., **2011**, 13, 14110-14118.

4. N–H···*π* Interactions in Pyrroles: Systematic Trends from the Vibrational Spectroscopy of Clusters, I. Dauster, C. Rice, P. Zielke, M. Suhm, *Phys. Chem. Chem. Phys*., **2008**, 10, 2827-2835.

5. PCl_3–C_6H_6 heterodimers: evidence for P···π phosphorus bonding at low temperatures, N. Ramanathan, K. Sankaran and K. Sundararajan, *Phys. Chem. Chem. Phys.*, **2016**, 18, 19350-19358.

6. H-*π* Heterodimers of Acetylene-Ethylene: A Matrix Isolation and Computational Study, K. Sundararajan, K. Sankaran, K. S. Viswanathan, A. D. Kulkarni, S. R. Gadre , *J. Phys. Chem. A*, **2002**, 106, 1504-1510.

7. Nitrogen: A New Class of π-Bonding Partner in Hetero π Stacking interaction, N. Ramanathan, K. Sankaran and K. Sundararajan, *J. Phys. Chem. A*, **2017**, 121(47), 9081-9091.

8. H···π heterodimers of acetylene–benzene: a matrix isolation and computational study, K. Sundararajan, K. S. Viswanathan, A. D. Kulkarni, S. R. Gadre, *J. Mol. Struct*., **2002**, 613, 209–222.

9. A matrix isolation and *ab initio* study of the C_2H_2-MeOH heterodimer, K. Sundararajan, K. S. Viswanathan, *J. Mol. Struct*., **2006**, 798, 109-116**.**

---

10. Production and characterization of para-hydrogen gas for matrix isolation infrared spectroscopy, K. Sundararajan, K. Sankaran, N. Ramanathan, R. Gopi, *J. Mol. Struct*., **2016**, 1117, 181-191.

11. Frequencies and absorption intensities of the fundamental and the first overtone of NH stretching vibrations of pyrrole···acetylene and pyrrole···ethylene complexes studied by density-functional-theory calculation, Y. Futami, Y. Ozaki, Y. Hamada, Y. Ozaki, *Vib. Spectrosc*., **2014**, 72, 124-127.

12. Acetylene–phenol heterodimers: A matrix isolation infrared and ab initio study, K. Sundararajan, N. Ramanathan, *J. Mol. Struct*., **2009**, 920, 369–376.

13. The N-H Stretch in Pyrrole: A Study of the Fundamental ($\Delta v=1$) and Third Overtone ($\Delta v=4$) Bands in the Bulk Gas and in a Molecular Beam, C. Douketis, J. P. Reilly, *J. Chem. Phys*. **1992**, 96, 3431–3440.

14. N-H Stretching Vibrations of Pyrrole Clusters Studied by Infrared Cavity Ringdown Spectroscopy, Y. Matsumoto, K. Honma, *J. Chem. Phys*., **2007**, 127**,** 184310(1-9).

15. Intermolecular interactions from a natural bond orbital, donor-acceptor viewpoint, A. E. Reed, L. A. Curtiss, F. Weinhold, *Chem. Rev*., **1988**, 88, 899-926.

16. Quantification of Aromaticity of Heterocyclic Systems Using Interaction Coordinates, S. Dey, D. Manogaran, S. Manogaran, H. F. Schaefer, *J. Phys. Chem. A*, **2018**, 122, 6953-6960.

17. Quantifying aromaticity with electron delocalisation measures, F. Feixas, E. Matito, J. Poater, M. Solà, *Chem. Soc. Revi*., **2015**, 44, 6434-6451.

18. Geometrical reaction coordinates. II. Nucleophilic addition to a carbonyl group, H. B. Burgi, J. D. Dunitz, E. Shefter, *J. Am. Chem. Soc*., **1973**, 95, 5065-5067.

19. Interplay between $n\rightarrow \pi^*$ Interactions and Dynamic Covalent Bonds: Quantification and Modulation by Solvent Effects, H. Zheng, H. Ye, X. Yu, L. You., *J. Am. Chem. Soc*., **2019**, 141, 8825-8833.

---

20. Substituted 2-(Dimethylamino)biphenyl-2′-carboxaldehydes as Substrates for Studying n→π* Interactions and as a Promising Framework for Tracing the Bürgi–Dunitz Trajectory, G. W. Breton, C. J. Crasto, *J. Org. Chem.*, **2015**, 80, 7375-7384.

21. A theoretical study of the ethylene-metal bond in complexes between copper(1+), silver(1+), gold(1+), platinum(0) or platinum(2+) and ethylene, based on the Hartree-Fock-Slater transition-state method, T. Ziegler, A. Rauk, *Inorg. Chem.*, **1979**, 18, 1558-1565.

22. Carbon monoxide, carbon monosulfide, molecular nitrogen, phosphorus trifluoride, and methyl isocyanide as σ donors and π acceptors. A theoretical study by the Hartree-Fock-Slater transition-state method, T. Ziegler, A. Rauk, *Inorg. Chem.*, **1979**, 18, 1755-1759.

23. F. M. Bickelhaupt, E. J. Baerends, K. B. Lipkowitz, D. B. Boyd, Rev.Comput. Chem. 15, Wiley-VCH, New York, **2000**.

24. Energy decomposition analysis of covalent bonds and intermolecular interactions, P. Su and H. Li, *J. Chem. Phys.*, **2009**, 131, 014102(1-2).

Chapter 5 Effect of Alkyl and Phenyl Substitutions on the N-H···O Interactions of Pyrrole

Pyrrole has a weakly acidic N-H bond and it is expected to interact with a Lewis base through this proton. Hence, the current chapter gives an elaborate account of the hydrogen bonded heterodimers of pyrrole with oxygen containing Lewis bases such as, water, methanol, diethyl ether and phenol. The effect of alkyl and phenyl substitution on the N-H···O hydrogen bond strength is probed through low temperature experiments and computational methods.

5.1 Experimental Conditions

Pyrrole (C_4H_5N, Spectrochem, 99%), Milli-Q deionized water (18MΩ), deuterated water (D_2O, 98%), methanol (CH_3OH, 99.8%, S. D. Fine Chemicals Ltd.), phenol (C_6H_5OH, >99%, Sigma-Aldrich) and diethyl ether ($C_2H_5OC_2H_5$, >99%, Merck) were used by chilling to ~100 K and then pumping off the volatile impurities by freeze-pump-thaw cycle. The typical sample to matrix ratio for $C_4H_5N/H_2O/N_2$ (or Ar) is varied from 0.25/0.5/1000 to 1.0/0.5/1000, $C_4H_5N/CH_3OH/N_2$ (or Ar) (0.25/0.1/1000 to 1.0/2.0/1000), $C_4H_5N/C_6H_5OH/N_2$ (or Ar) (0.25:0.25:1000 to 1.0:0.5:1000) and for $C_4H_5N/C_2H_5OC_2H_5/N_2$ (or Ar) (0.05/0.1/1000 to 0.5/1.0/1000). A triple jet nozzle assembly was used to co-deposit C_4H_5N and H_2O/C_6H_5OH by streaming them separately onto the cold KBr substrate. C_4H_5N/N_2 (or Ar) gas mixture in the required ratio is prepared in the mixing chamber, and this gas mixture was subsequently allowed to pass through a fine needle valve and deposited onto the substrate through the nozzle. A temperature range of 193 K to 198 K was kept for water in the sample bulb to control its concentration in the matrix and was deposited through a second nozzle. For the $C_4H_5N/C_6H_5OH/N_2$ (or Ar) experiments, the vapor pressure of C_6H_5OH was controlled by maintaining its temperature around 229 K to 248 K. Known concentrations of

CH_3OH or $C_2H_5OC_2H_5$ were pre-mixed in the mixing chamber along with C_4H_5N and matrix gases. This mixture C_4H_5N/CH_3OH or $C_2H_5OC_2H_5/N_2$ or Ar was streamed through a fine needle valve and deposited on to the cold substrate using a single jet nozzle. All the gas mixtures were deposited for ∼100 minutes at a deposition rate of ∼3 mmol.hr^{-1}. The infrared spectra of the deposited sample were recorded as described in detail in Chapter 2. All the spectra shown in this chapter were annealed spectra.

5.2 Experimental and Computational Results

5.2.1 Pyrrole···Water

In Figure 5.1b & Figure 5.2b, the blocks A & B show the N-H stretching and bending modes of C_4H_5N in N_2 and Ar matrixes, respectively. The features due to C_4H_5N multimers were observed and have been discussed in detail in Chapter 3. In the C_4H_5N alone spectrum (block A in Figure 5.1a, 5.2a), apart from the features due to C_4H_5N monomer and multimers, the peaks at 3385.3 and 3379.5 cm^{-1} in N_2 matrix and in Ar matrix at 3409.6 and 3407.9 cm^{-1} were observed. In N_2 matrix, the two peaks coalesce into a single sharp feature at 3385.3 cm^{-1} that increases in intensity on varying the concentration of H_2O, while in Ar matrix the features at 3409.6 and 3407.9 cm^{-1} increase in intensity with a new sharp peak at 3412.8 cm$^{-1.}$ Apart from this, other small peaks at 3493.8, 3402.2, 3335.9 and 3331.3 cm^{-1} were also observed in N_2 matrix while in Ar matrix, some features at 3476.7, 3432.8 and 3311.0 cm^{-1} were formed. On increasing the water concentration, additional features were seen in N_2 matrix at 3540.3 and 3409.1 cm^{-1}. Figure 5.1B and Figure 5.2B show the N-H bending region of C_4H_5N in N_2 matrix in the range 620-510 cm^{-1}. Apart from the C_4H_5N monomer and dimer features (trace b in Figure 5.1B, Figure 5.2B), addition of H_2O led to the formation of new spectral bands at 597.1, 603.4, 609.7 and 613.0 cm^{-1} in N_2, while 591.8 and 608.0 cm^{-1} in Ar matrixes, respectively. In the O-H stretching and bending modes of H_2O (Figure 5.1C, Figure 5.2C &

5.1D), with the variation of C_4H_5N concentration, new features were observed at 3720.1 and 1601.4 cm^{-1} in N_2 matrix and 3728.3 cm^{-1} in Ar matrix. In the O-H bending region of H_2O, no feature was observed in Ar matrix. To confirm that the new peaks observed in the O-H stretching and bending regions of H_2O are indeed due to C_4H_5N-H_2O heterodimer, experiments of C_4H_5N with D_2O were performed in N_2 matrix. The O-D stretching and bending modes of D_2O were observed at 2765.9 and 1178.6 cm^{-1} in N_2 matrix and are shown in Figure 5.3a grids A and B, respectively. The features observed at 2756.1/2758.3 cm^{-1} are due to $(D_2O)_2$ in N_2 matrix [1]. The addition of C_4H_5N leads to the formation of new peaks at 2761.1/2760.4 cm^{-1} and 1182.4/1181.2 cm^{-1} in the O-D stretching and O-D bending mode of D_2O. Since water is an inevitable impurity in the MI experiments, the C_4H_5N-H_2O heterodimers are readily formed and observed in the experiments where pyrrole alone was deposited and annealed (Figure 5.1a, 5.2a, block A and B).

5.2.1.1 Computational Details

Optimized geometries of the C_4H_5N-H_2O heterodimers were obtained using second order Møller-Plesset perturbation theory (MP2) with aug-cc-pVDZ basis set. Computations yielded two optimized structures for the 1:1 C_4H_5N-H_2O PW-A and PW-B heterodimers. Table 5.1 gives the stabilization energies for the 1:1, 2:1 and 1:2 C_4H_5N-H_2O heterodimers at MP2/aug-cc-pVDZ level of theory. Figure 5.4 illustrates the optimized structures of the 1:1, 2:1 and 1:2 C_4H_5N-H_2O multimers at MP2/aug-cc-pVDZ level of theory. The global minimum heterodimer (PW-A) is stabilized by N-H···O interaction between the C_4H_5N N-H and O of H_2O and the bond distance is 1.969 Å. The local minimum corresponds to the O-H···π heterodimer (PW-B) between the O-H of H_2O and the π-electron cloud of C_4H_5N-ring. Apart from the 1:1 heterodimers, higher clusters 2:1 and 1:2 were also optimized. Computations yielded two and one optimized structures corresponding to 2:1 PPW-A, PPW-B and 1:2 PWW C_4H_5N-H_2O clusters, respectively The global minimum cluster where the $(C_4H_5N)_2$ bonds with

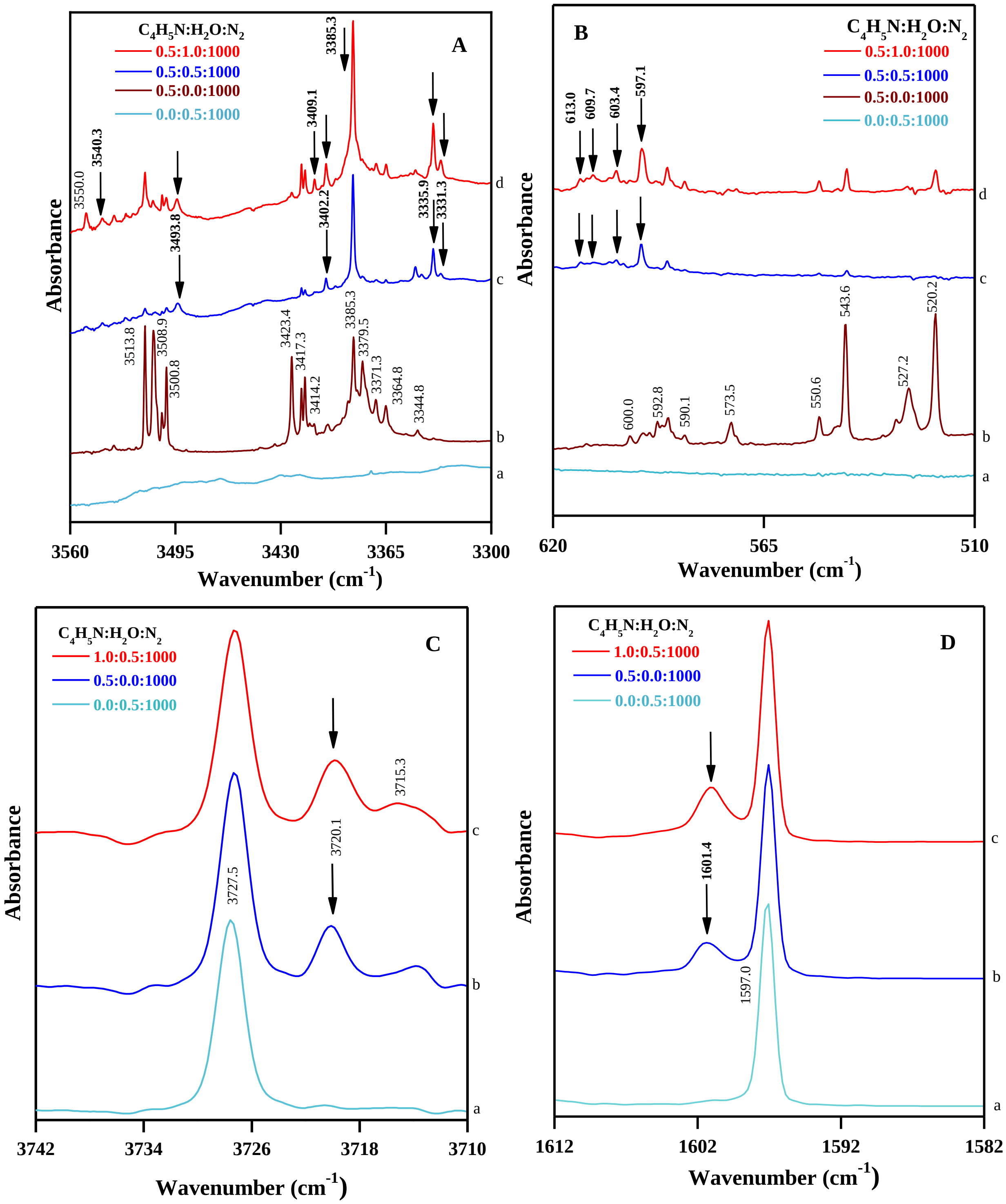

Figure 5.1 Matrix isolated IR spectra of (A) N-H stretching region of pyrrole, (B) N-H bending region of pyrrole, (C) O-H anti—symmetric stretching zone of water and (D) O-H bending mode of water in N_2 Matrix. All the spectra shown here were annealed at 30 K.

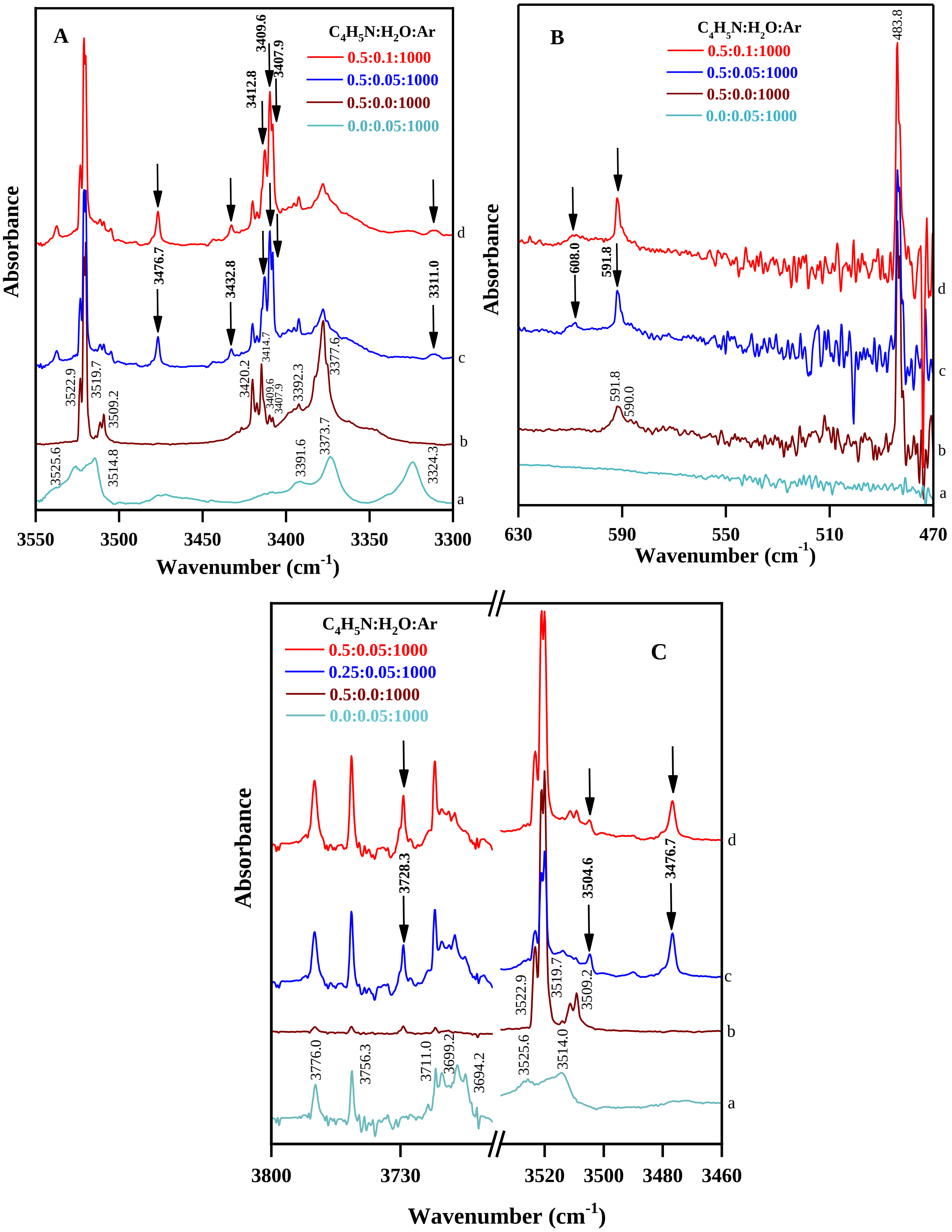

Figure 5.2 Matrix isolated IR spectra of (A) N-H stretching region of pyrrole, (B) N-H bending region of pyrrole, and (C) O-H anti-symmetric stretching zone of water in Ar matrix. All the spectra shown here were annealed at 35 K.

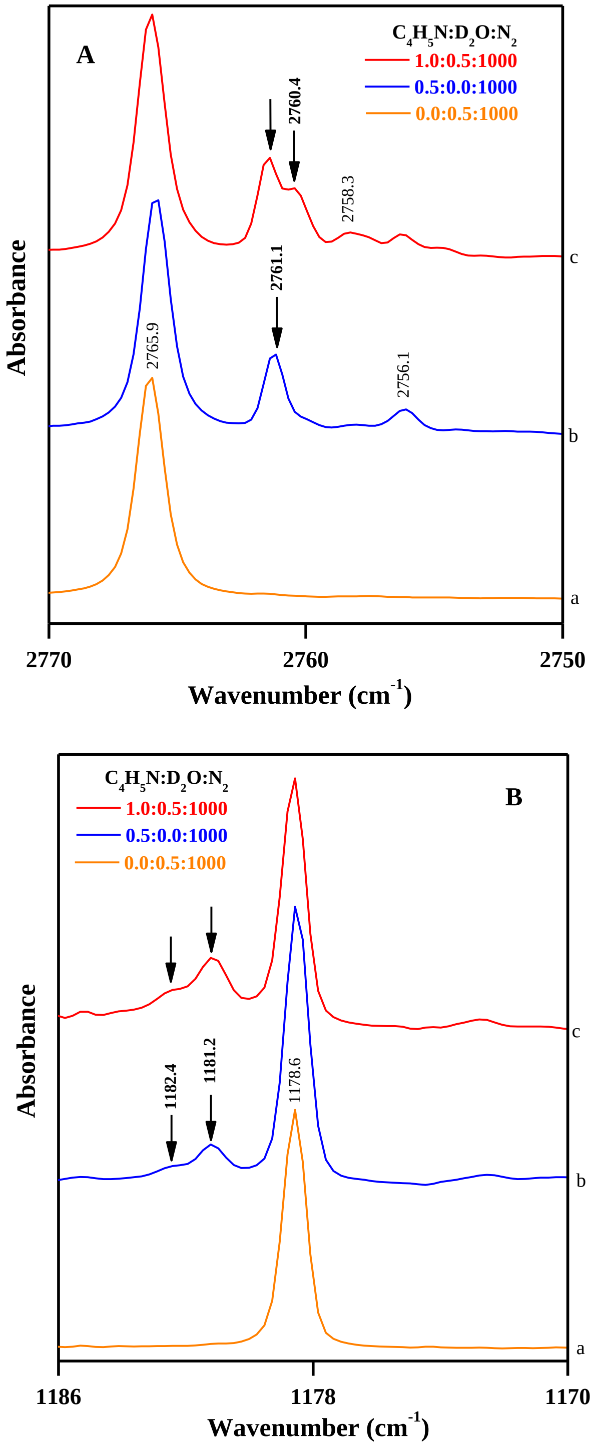

Figure 5.3 Matrix isolated IR spectra of (A) O-D stretching zone of water-D_2O in N_2 matrix and (B) O-D bending mode of water-D_2O in N_2 Matrix. All the spectra shown here were annealed at 30 K.

Table 5.1 Raw[a]/ZPE/BSSE corrected Stabilization Energies for the 1:1, 2:1 and 1:2 C_4H_5N-H_2O Complexes computed at MP2/aug-cc-pVDZ Level of Theory.

Complexes	**Stabilization Energies**
PW-A	-6.15/-4.95/-5.04
PW-B	-5.93/-4.65/-4.15
PPW-A	-23.74/-20.78/-18.05
PPW-B	-16.73/-14.63/-11.39
PWW	-17.97/-13.95/-14.84

All energies are in kcal mol^{-1}.

[a] Raw interaction energies refer to energies not corrected for either ZPE or BSSE.

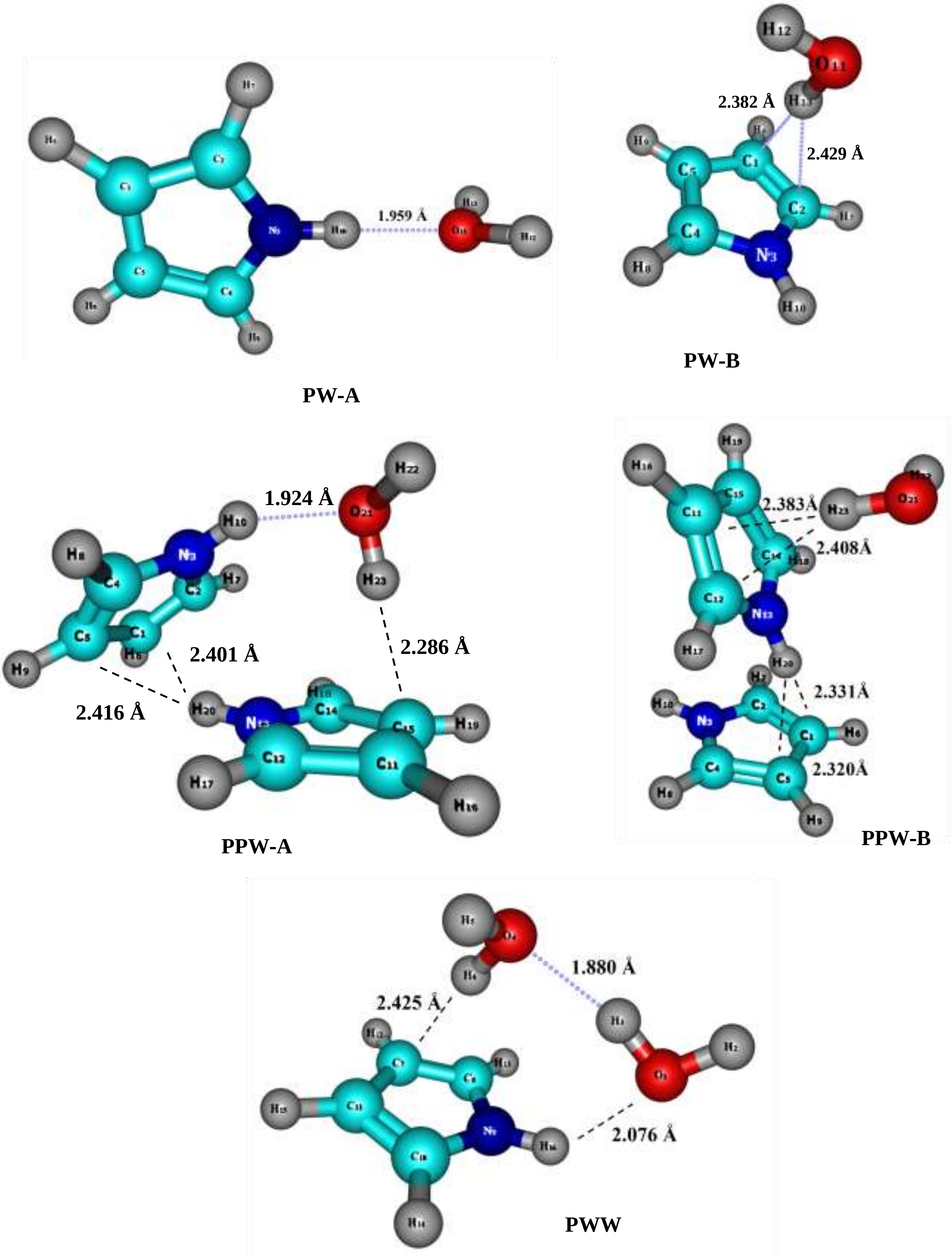

PW-A

PW-B

PPW-A

PPW-B

PWW

Figure 5.4 Structures of 1:1 C_4H_5N-H_2O PW-A, PW-B, 2:1 PPW-A, PPW-B and 1:2 PWW complexes computed at MP2/aug-cc-pVDZ level of theory.

H_2O through N-H···π (2.416 Å, 2.401 Å), N-H···O (1.924 Å) and O-H···π (2.286 Å) interactions. The first local minimum PPW-B heterodimer has N-H···π and O-H···π interaction. In the PWW cluster, $(H_2O)_2$ interacts with C_4H_5N through O-H···O (1.880 Å), N-H···O (2.076 Å), and O-H···π (2.425 Å) bonding.

5.2.1.2 Vibrational Assignment of ν_1 and ν_{16} Modes of C_4H_5N

Table 5.2 gives the comparison between the experimental and computed vibrational shifts of the 1:1, 1:2 and 2:1 C_4H_5N-H_2O heteroadducts. Computations showed a red-shift of -106.7 cm^{-1} and a blue-shift of 89.4 cm^{-1} in the ν_1 N-H stretching and ν_{16} N-H bending mode of C_4H_5N submolecule for the N-H···O (PW-A) heterodimer. For the PW-B heterodimer, computations indicated a red-shift of -5.3 cm^{-1} and a blue-shift of 23.7 cm^{-1} in the ν_1 and ν_{16} modes of C_4H_5N submolecule respectively. In N_2 matrix, when H_2O concentration was increased in C_4H_5N/N_2 mixture, a strong intense peak was observed at 3385.3 cm^{-1} in the N-H stretching region (ν_1 mode) with a red-shift of -127.9 cm^{-1} and at 597.1 cm^{-1} and a blue-shift of 73.6 cm^{-1} in the N-H bending region (ν_{16} mode) of C_4H_5N submolecule from the C_4H_5N monomer absorption band that which matches well with the computed shift (-106.7 and 89.4 cm^{-1}) of PW-A heterodimer. Similarly, in Figure 5.2 grid A in Ar matrix, on increasing the concentration of H_2O, the bands forming at 3412.8, 3409.6, 3407.9 cm^{-1}, at an average red-shift of -111.6 cm^{-1} show sharp increase in intensity.

In the N-H bending mode, a new broad peak was formed at a shift of 108.4 cm^{-1} at 591.8 cm^{-1}, overlapping with the peak at 590.0 cm^{-1} for the tetramer of C_4H_5N in Ar matrix, which has been assigned for the PW-A heterodimer (Figure 5.1B). No new features were identified for the PW-B heterodimer. It should be mentioned that the features due to PW-A heterodimer were observed in the C_4H_5N alone spectrum in N_2 matrix at 3385.3/3379.5 and 597.1 cm^{-1}, a small doublet at 3407.9, 3409.6 cm^{-1} in Ar matrix. As the water concentration was increased in the matrix, the peaks observed at 3385.3/597.1 cm^{-1} increased in intensity

Table 5.2 Comparison of Shift in the Experimental Vibrational Wavenumbers in Ar and N_2 Matrixes with the Computed Wavenumbers of the 1:1, 2:1 and 1:2 C_4H_5N-H_2O and 1:1 C_4H_5N-D_2O Complexes. Computations were performed using MP2/aug-cc-pVDZ Level of Theory.

Computed ν (cm^{-1})		**Experimental *v* (cm^{-1})**				**Mode Assignment**
		N_2		**Ar**		
v	**Δv[c]**	***v***	**Δv**	***v***	**Δv**	
H_2O						
1622.2(67)	-	1597.0	-	1589.6/ 1593.0	-	υ_2 O-H bending
3936.8(67)	-	3727.5	-	3737.0	-	υ_3 O-H antisym. str.
D_2O						
1187.0(36)	-	1178.5	-	1175.0	-	υ_2 O-D bending
2883.8 (41)	-	2765.9	-	2657.0	-	υ_3 O-D antisym. str.
C_4H_5N						
514.9(60)	-	520.2/527.2[b]	-	483.8/482.9[b]	-	υ_{16} N-H bending
3672.4 (76)	-	3519.3/3513.8 /3510.9/ 3508.9[b]	-	3523.3/ 3521.6/ 3520.2[b]	-	υ_1 N-H stretching
PW-A						
1621.7(64)	-0.5	1601.4	4.4	-[a]	-	υ_2 O-H bending
3931.1(91)	-5.7	3720.1	-7.4	3728.3	-8.3	υ_3 O-H antisym. str.
604.3(14)	89.4	597.1	73.6	591.8	108.4	υ_{16} N-H bending
3565.7 (544)	-106.7	3385.3	-127.9	3412.8/ 3409.6/ 3407.9[b]	-111.6	υ_1 N-H stretching
PW-B						
1618.0 (34)	-4.2	-[a]	-	-[a]	- -	υ_2 O-H bending
3899.2 (91)	-37.6	-[a]	-	-[a]	-	υ_3 O-H antisym. str.
538.6(49)	23.7	-[a]	-	-[a]	-	υ_{16} N-H bending
3667.1 (85)	-5.3	-[a]	-	-[a]	-	υ_1 N-H stretching
PDW-A						
1189.8 (26)	2.8	1182.4/1181.2	3.2[b]	-[d]	-	υ_2 O-D bending
2880.4 (52)	-3.4	2761.1/2760.4	-5.2[b]	-[d]	-	υ_3 O-D antisym. str.
604.0(14)	89.0	597.1	73.6	-[d]	-	υ_{16} N-H bending

3566.4 (537)	-106.0	3385.0	-128.2	-[d]	-	ν_1 N-H stretching
PDW-B						
1183.0(19)	-3.9	-[a]	-	-[a]	-	ν_2 O-D bending
2851.2(75)	-32.6	-[a]	-	-[a]	-	ν_3 O-D antisym. str.
537.2(57)	22.3	-[a]	-	-[a]	-	ν_{16} N-H bending
3667.1(85)	-5.3	-[a]	-	-[a]	-	ν_1 N-H stretching
PPW-A						
1623.6(28)	1.4	-[a]	-	-[a]	-	ν_2 O-H bending
3643.4(303	-159.0	3540.3	-94.3	3504.6	-133.7	ν_1 O-H sym. stretching
3879.8 (112)	-57	-[a]	-	-[a]		ν_3 O-H antisym. stretching
521.9(70)	7	-[a]	-	-[a]	-	ν_{16} N-H bending
609.4(22)	94.5	609.7/613.0	87.8[b]	608.0	125.3	
3471.0(343)	-201.4	3335.9/3331.3	-179.6[b]	3311.0	-210.0	ν_1 N-H stretching
3521.3(458	-151.1	-[a]	-	-[a]	-	
PPW-B						
1628.7(65)	6.5	-[a]	-	-[a]	-	ν_2 O-H bending
3894.6(85)	42.2	-[a]	-	-[a]	-	ν_3 O-H antisym. str.
547.2(86)	32.3	-[a]	-	-[a]	-	ν_{16} N-H bending
603.5(7)	88.6					
3546.1 (491)	-126.3	-[a]	-	-[a]	-	ν_1 N-H stretching
3660.0 (836)	-12.4					
PWW						
1620.1(55)	-2.0	-[a]	-	-[a]	-	ν_2 O-H bending
1653.1(47)	30.9					
3562.8 (115)	-239.6	3493.8	-140.8	3476.7	-256.3	ν_1 O-H sym. stretching
3670.5 (236)	-131.9	-[a]	-	-[a]	-	
3876.1(97)	-60.7	-[a]	-	-[a]	-	ν_3 O-H antisym. stretching
3892.7(83)	-44.1					
553.1(113)	38.2	-[a]	-	-[a]	-	ν_{16} N-H bending
3589.5 (504)	-82.9	3409.1/3402.2	-107.5[b]	3432.8	-88.9	ν_1 N-H stretching

[a] Experimental features were not observed;

[b] Average multiplet experimental wavenumbers of the monomers and multimers were taken to compute the experimental shift in the heterodimers;

[c] $\Delta\nu = \nu_{heterodimer} - \nu_{monomer}$;

[d] Experiments for Pyrrole-D_2O were not carried out in Ar matrix.

with clear concentration dependence, and hence these features are unambiguously assigned to the 1:1 C_4H_5N-H_2O PW-A heterodimer. As the water concentration was increased in the matrix, new peaks were observed at 3335.9/3331.3 cm^{-1} (N_2), 3311.0 cm^{-1} (Ar) and 609.7/613.0 cm^{-1} (N_2), 608.0 cm^{-1} (Ar) in the ν_1 N-H stretching and ν_{16} bending modes of C_4H_5N submolecule, respectively with a shift of -179.6/-210.0 cm^{-1} and 87.8/125.3 cm^{-1} that compares with the computed shift of -201.4 cm^{-1} and 94.5 cm^{-1} for the 2:1 PPW-A heterotrimer. For the PWW heterotrimer, computations predicted a shift of -82.9 cm^{-1} in the ν_1 mode of C_4H_5N submolecule in the heterotrimer, which correlates well with the experimental feature observed in N_2 matrix at 3409.1/3402.2 cm^{-1} and in Ar matrix at 3432.8 cm^{-1} with red-shifts of -107.5 and -89.0 cm^{-1}, respectively.

5.2.1.3 Vibrational Assignment of ν_3 and ν_2 Modes of H_2O and D_2O

Computations showed a red-shift of -5.7/-3.4 cm^{-1} in the ν_3 mode and a shift of -0.5/-2.8 cm^{-1} in the ν_2 mode of H_2O/D_2O submolecule from the monomer absorption band of H_2O/D_2O for the PW-A/PDW-A heterodimer, where C_4H_5N interacts with H_2O/D_2O through N-H···O interaction. For the O-H···π/O-D···π PW-B/PDW-B heterodimer/heterotrimer, computations showed a red-shift of -37.6/-32.6 cm^{-1} and -4.2/-3.9 cm^{-1} in the ν_3 and ν_2 modes of H_2O/D_2O submolecule, respectively. Experimentally, a red-shift of -7.4/-5.2 cm^{-1} in the ν_3 mode and a blue-shift of 4.4/3.2 cm^{-1} in the ν_2 mode of H_2O/D_2O was observed, which matches with the computed shift of the N-H···O PW-A/PDW-A heterodimer/trimer, where C_4H_5N acts as proton donor. No new feature was observed in the ν_3 and ν_2 modes of H_2O and D_2O submolecule for the O-H···π PW-B/PDW-B heterodimer/trimer in N_2 matrix (Figure 5.1C, 5.1D, 5.2C, 5.3A and 5.3B).

A new feature that was observed at 3540.3 cm^{-1} in N_2 matrix and 3504.6 cm^{-1} in Ar matrix in the ν_1 O-H stretching mode of H_2O submolecule and a shift of -94.3 and -133.7 cm^{-1} respectively, matching well with the computed shift of -159.0 cm^{-1} for the 2:1 PPW-A heterotrimer. For the PWW heterotrimer, computations predicted a shift of -239.6 cm^{-1} in the ν_1 mode of H_2O submolecule in the heterotrimer, which correlates with the experimental feature observed in N_2 matrix at 3493.8 cm^{-1}, at the shifts of -140.8 cm^{-1}, while that in Ar matrix at 3476.7 cm^{-1} at shift around -256.3 cm^{-1}, respectively. The experimental vibrational shifts in Ar matrix have a good correlation with the computed shifts.

5.2.2 Pyrrole···Methanol

Figure 5.5, blocks A and B show the infrared spectra of N-H stretching region of C_4H_5N in N_2 and Ar matrixes, blocks C and D, correspond to N-H bending of C_4H_5N and O-H bending region of CH_3OH in N_2 matrix, followed by Figure 5.6 blocks A and B showing the C-O stretching region of CH_3OH in N_2 and Ar matrixes. Traces 'a' and 'b' in all the blocks show the CH_3OH and C_4H_5N alone spectra in N_2 and Ar matrixes, respectively. The features due to $(CH_3OH)_2$ are observed at 3504.6, 3496.9, 3489.4 cm^{-1} in N_2 matrix. The CH_3OH-H_2O heterodimer is found at 3524.0 cm^{-1} in N_2 and at 3527.3 cm^{-1} in Ar matrix. When C_4H_5N and CH_3OH were co-deposited with Ar or N_2, new bands were found in the N-H stretching mode of C_4H_5N at 3458.8, 3366.7, 3349.6, 3300.9 and 3293.2 cm^{-1} in N_2 and at 3398.0, 3332.5 cm^{-1} in Ar matrixes, respectively. Similarly, in the N-H bending mode of C_4H_5N, apart from the monomer, dimer and C_4H_5N-H_2O heterodimer, new peaks were observed at 599.3 and 594.9 cm^{-1} on co-deposition of C_4H_5N with CH_3OH.

In the O-H stretching mode of CH_3OH, new peak is observed at 3661.5 cm^{-1}, which increases by varying the concentration of C_4H_5N in the matrix. No new spectral feature was found in the N-H bending mode of C_4H_5N as well as in the O-H stretching mode of CH_3OH in Ar matrix. In the C-O stretching region of CH_3OH, apart from the strong absorption peak of monomer at 1034.4 cm^{-1} in N_2 and the corresponding feature at 1034.2 cm^{-1} in Ar matrix, new spectral features were observed at 1027.9, 1022.3, 1019.7 cm^{-1} in N_2 and 1023.8 cm^{-1} in Ar, that showed concentration dependence on C_4H_5N. The peaks at 1051.0, 1047.9 cm^{-1} in N_2

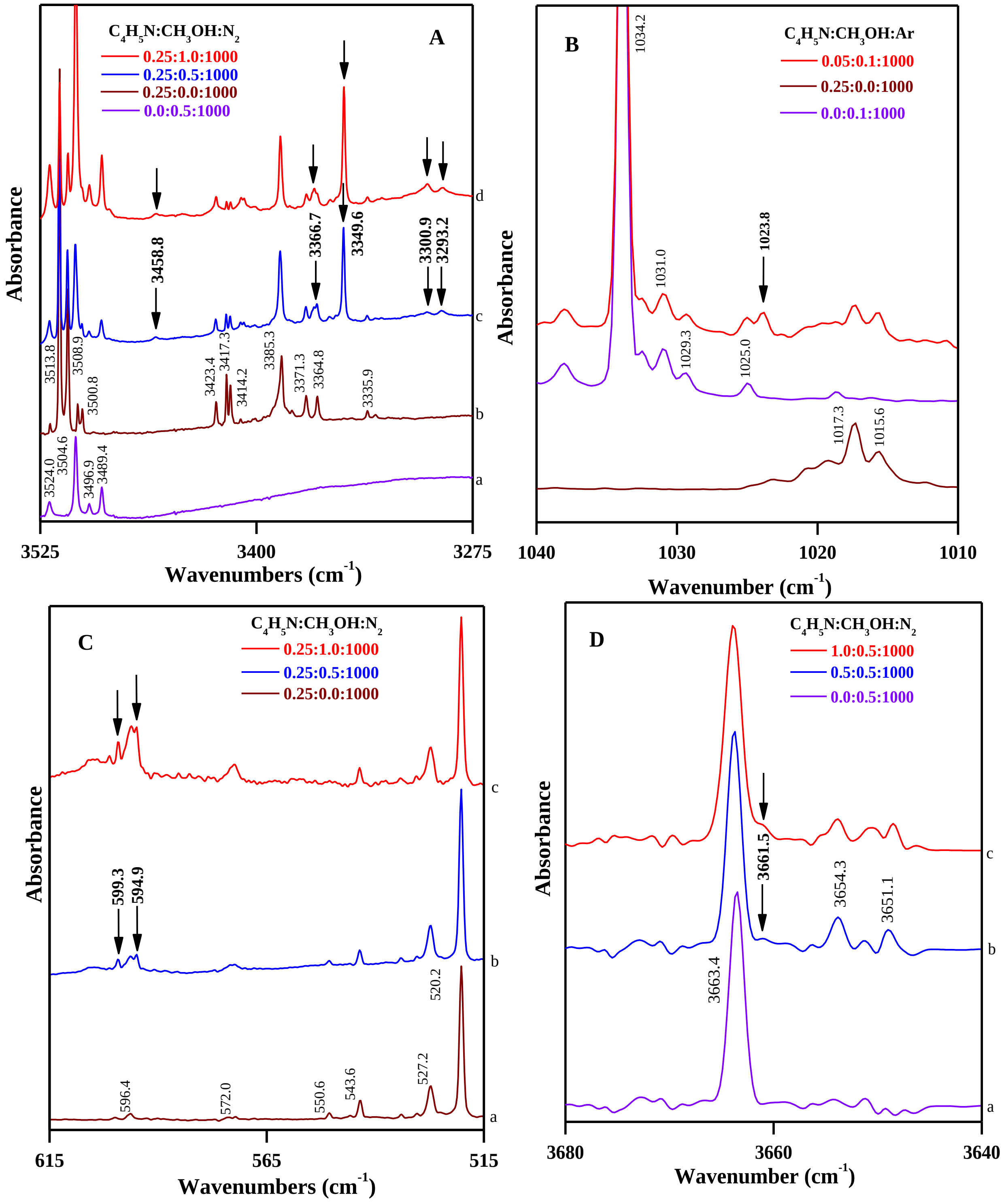

Figure 5.5 Matrix isolated IR spectra of (A) N-H stretching region of C_4H_5N in N_2 matrix, (B) N-H stretching region of C_4H_5N in Ar matrix, (C) N-H bending zone of C_4H_5N in N_2 matrix, (D) O-H stretching mode of CH_3OH in N_2 Matrix. All the spectra shown here were annealed at 30 K (for N_2) and 35 K (for Ar).

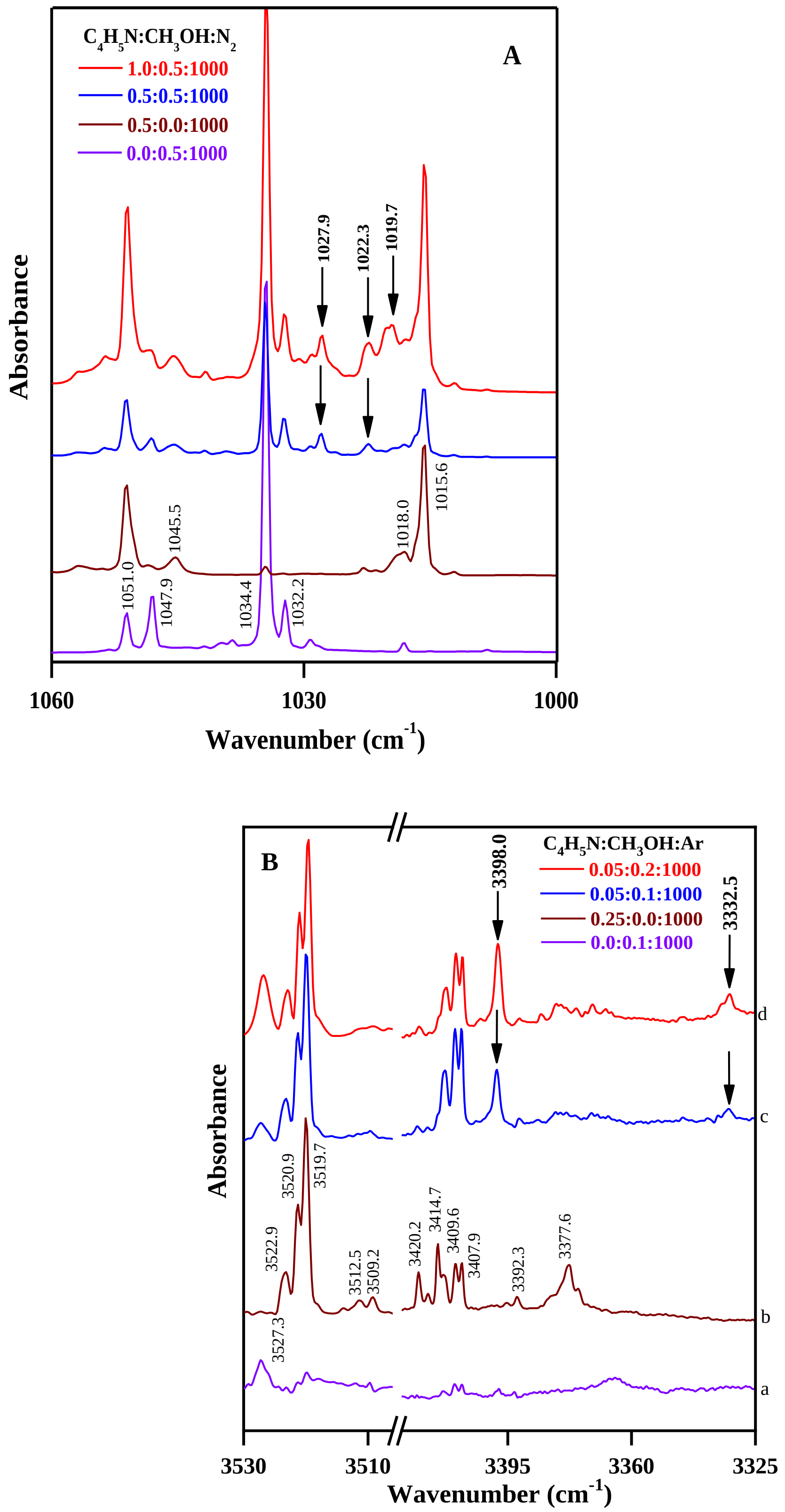

Figure 5.6 Matrix isolated IR spectra of (A) C-O stretching zone of CH_3OH in N_2 Matrix and (B) O-H stretching region of CH_3OH in Ar Matrix. All the spectra shown here were annealed at 30 K (for N_2) and 35 K (for Ar).

Table 5.3 Raw[a]/ZPE/BSSE Corrected Stabilization Energies for the 1:1, 2:1 and 1:2 C_4H_5N-CH_3OH Complexes computed at MP2/aug-cc-pVDZ Level of Theory.

Complex	Stabilization Energy
PM-A	-7.45/-6.62/-6.00
PM-B	-7.41/-6.45/-4.87
PPM-A	-26.17/-23.77/-19.56
PPM-B	-23.67/-21.69/-16.90
PMM-A	-21.09/-18.39/-16.75
PMM-B	-15.59/-13.40/-11.18

All energies are in kcal mol^{-1}.

[a] Raw interaction energies refer to energies not corrected for either ZPE or BSSE.

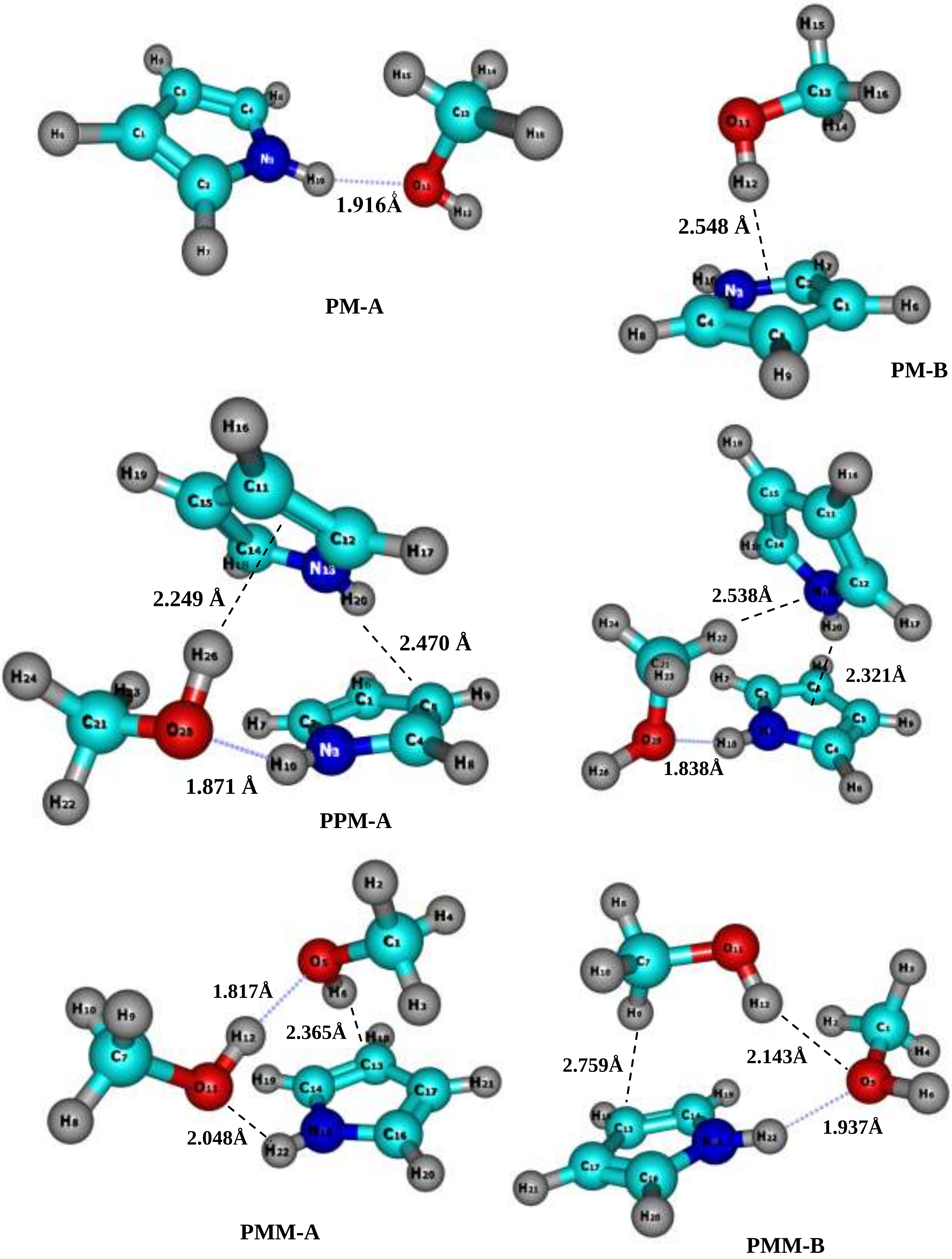

PM-A

PM-B

PPM-A

PMM-A

PMM-B

Figure 5.7 Structures of 1:1 C_4H_5N-CH_3OH PM-A, PM-B, 2:1 PPM-A, PPM-B and 1:2 PMM-A, PMM-B complexes computed at MP2/aug-cc-pVDZ level of theory.

and at 1031.0, 1029.3, 1025.0 cm^{-1} in Ar matrixes are due to the $(CH_3OH)_2$, whereas the C-H in-plane bending of C_4H_5N is observed in N_2 matrix at 1045.5, 1018.0, 1015.6 cm^{-1} and in Ar matrix at 1017.3, 1015.6 cm^{-1} respectively.

5.2.2.1 Computational details

At MP2/aug-cc-pVDZ level of theory, computation yielded two optimized structures for the 1:1 C_4H_5N-CH_3OH PM-A and PM-B heterodimers. PM-A heterodimer is the global minimum with an N-H···O interaction between N-H of C_4H_5N with O of CH_3OH with a bond distance of 1.916Å whereas the local minimum PM-B heterodimer stabilized by O-H···π interaction between OH of CH_3OH and π-electrons of C_4H_5N with a bond distance of 2.548Å. Table 5.3 lists the raw, ZPE and BSSE corrected stabilization energies of PM-A and PM-B computed at MP2 level of theory with aug-cc-pVDZ basis set. Figure 5.7 shows the structure of the PM-A and PM-B heterodimers computed at MP2/aug-cc-pVDZ level of theory. For the C_4H_5N-CH_3OH higher clusters, the PPM-A cluster is the global minimum, where the $(C_4H_5N)_2$ interacts with CH_3OH through N-H···π (2.470 Å), N-H···O (1.871 Å), and O-H···π (2.249 Å). At MP2 level, the BSSE corrected stabilization of the PPM-B and PMM-A heterotrimer shows that they are isoenergetic and the PMM-B is the second local minimum in the potential energy surface. Table 5.4 compares the shift in the experimental with the calculated vibrational wavenumbers of the PPM-A heterodimers computed at MP2/aug-cc-pVDZ level of theory. The structures of the higher clusters are illustrated in Figure 5.7.

5.2.2.2 Vibrational Assignments in the ν_1 and ν_{16} Modes of C_4H_5N

Experimentally, a red-shift of -163.6 and -122.2 cm^{-1} in N_2 and in Ar matrixes respectively, while a blue-shift of 73.5 cm^{-1} in N_2 matrix, were observed in the ν_1 and ν_{16} modes of C_4H_5N submolecule, which corroborates well with the computed red-shift of -125.6 cm^{-1} in the ν_1 mode and a blue-shift of 87.8 cm^{-1} in the ν_{16} mode of C_4H_5N submolecule for the PM-A heterodimer (Table 5.4, Figure 5.5A,B). It should be mentioned that Du et al. [2]

observed a red-shift of -149.0 cm^{-1} in Ar matrix for the C_4H_5N-CH_3OH N-H···O heterodimer. While the shift in the vibrational wavenumber for the N-H···O heterodimer in Ar matrix is reasonable, the corresponding shift in N_2 matrix is at variance from the computational predictions. The agreement between the experimental and computed vibrational wavenumbers depends upon (a) the level of theory and the basis sets used in the computations, (b) the effect of anharmonicity in the calculations, and (c) the influence of matrix on the vibrational wavenumbers of monomer and heterodimers (matrix effect). Among the different levels of theory with various basis sets used in the computations, harmonic vibrational wavenumber calculated using MP2/aug-cc-pVDZ level correlated reasonably well with the experimental wavenumbers of the C_4H_5N-CH_3OH heterodimer. It appears that both the anharmonicity and matrix effects (of N_2) together operate in the N-H···O heterodimer, which could be a possible reason for the difference in agreement between the experimental observation and computational predictions. For the O-H···π PM-B heterodimer, computations showed a red-shift of -6.2 cm^{-1} in the ν_1 N-H stretching mode and a blue-shift of 29.4 cm^{-1} in the ν_{16} N-H bending mode of C_4H_5N. Experimentally, new features could not be observed in these modes for the PM-B heterodimer in N_2 or in Ar matrixes. Furthermore, new features observed in the ν_1 mode of C_4H_5N at 3366.7, 3300.9/3293.2 cm^{-1}, a shift of -146.5 and -216.1 cm^{-1} matches with the computed shift of -153.2 and -286.2 cm^{-1} for the PPM-A heterotrimer in N_2 matrix. In Ar matrix, a red-shifted peak observed at 3332.5 cm^{-1} with a red-shift of -187.7 cm^{-1} was assigned to PPM-A heterotrimer. New feature was not discerned for the PPM-B, PMM-A and PMM-B heterotrimers in any of the modes of CH_3OH and C_4H_5N.

5.2.2.3 Vibrational Assignments in the ν_1 and ν_8 modes of CH_3OH

The ν_1 O-H and ν_8 C-O stretching mode of CH_3OH in N_2 matrix was observed at 3663.4 and 1034.4 cm^{-1}, and in Ar at 1034.2 cm^{-1}. When the concentration of C_4H_5N was varied in the matrixes, new features were observed in the ν_1 and ν_8 modes of CH_3OH

submolecule at 3661.5 and 1027.9 cm^{-1}, with a red-shift of -1.9 and -6.5 cm^{-1} in N_2, and at 1023.8 cm^{-1} with a red-shift of -10.4 cm^{-1} in Ar, that agree reasonably well with the computed red-shifts of -0.02 and -11.6 cm^{-1}, respectively, for the (N-H···O) PM-A heterodimer. No new spectral peaks were observed in Ar matrix in the v_1 mode. For the O-H···π (PM-B) heterodimer, computations indicated a red-shift of -101.0 cm^{-1} in the v_1 mode and a blue-shift of 13.3 cm^{-1} in the v_8 mode of CH_3OH submolecule. Experimentally, no new feature was observed for this heterodimer in both the matrixes. When the concentration of CH_3OH/C_4H_5N was increased, new features were observed in the O-H stretching region of CH_3OH at 3458.8 cm^{-1} in N_2 matrix with a shift of -204.6 cm^{-1} that agrees well with the computed shift of -213.1 cm^{-1} for the PPM-A heterotrimer (Refer Table 5.4, Figure 5.6A&B).

Du et al. studied the hydrogen-bonded heterodimers of CH_3OH with heterocyclic organic compounds using matrix isolation infrared spectroscopy [2]. In their work, they have performed computations on the C_4H_5N-CH_3OH system using B3LYP/aug-cc-pVTZ and found O-H···π and N-H···O heterodimers, which were found to be isoenergetic and their results agree with our computations performed at MP2/aug-cc-pVDZ level of theory. Experimentally, they observed red-shifts of ~-85-87 and -149 cm^{-1} in the O-H and N-H stretching modes of CH_3OH and C_4H_5N submolecule, respectively, for the O-H···π and N- H···O heterodimers in Ar matrix. Furthermore, in their experiments the features observed at 3581.0/3583.0 cm^{-1}, due to the formation of O-H···π adduct, do not show any intensity variation on annealing the matrix. The CH_3OH concentrations they have used to perform their experiments are high. In fact, we had also carried out experiments where CH_3OH concentration was varied in N_2 matrix from 1/2000 to 4/250 and in Ar matrix from 2/10000 to 5/700, and we did not observe any features corresponding to the O-H···π heterodimer in the O-H stretching mode of CH_3OH submolecule. The computed infrared intensity for the N-H···O heterodimer was 544 km mol^{-1} whereas for the O-H···π heterodimer it was 244 km

Table 5.4 Comparison of Shift in the Experimental and Computed Vibrational Wavenumbers of the 1:1, 2:1 and 1:2 C_4H_5N-CH_3OH Complexes in Ar and N_2 Matrixes. Computations were performed using MP2/aug-cc-pVDZ Level of Theory.

Computed ν(cm^{-1})		**Experimental ν (cm^{-1})**				**Mode Assignment**
		N_2		**Ar**		
ν	**$\Delta\nu$[c]**	***ν***	**$\Delta\nu$**	***ν***	**$\Delta\nu$**	
CH_3OH						
1044.1(112)	-	1034.4	-	1034.2	-	ν_8 C-O stretching
3841.5(35)	-	3663.4	-	3660.4	-	ν_3 O-H stretching
C_4H_5N						
514.9 (60)	-	520.2/527.2	-	483.8/482.8/481.6	-	ν_{16} N-H bending
3672.4 (76)	-	3519.3/3513.8/3510.9/3508.	-	3523.3/3521.6/3520.2	-	ν_1 N-H stretching
PM-A						
1032.4(101)	-11.6	1027.9	-6.5	1023.8	-10.4	ν_8 C-O stretching
3841.4(46)	-0.02	3661.5	-1.9	-[a]	-	ν_3 O-H stretching
602.7(15)	87.8	599.2/594.9	73.5[b]	-[a]	-	ν_{16} N-H bending
3546.8(501)	-125.6	3349.6	-163.6[b]	3398.0	-122.0	ν_1 N-H stretching
PM-B						
1057.3(72)	13.3	-[a]	-	-[a]	-	ν_8 C-O stretching
3740.8(256)	-101.0	-[a]	-	-[a]	-	ν_3 O-H stretching
544.4(42)	29.4	-[a]	-	-[a]	-	ν_{16} N-H bending
3666.3(85)	-6.2	-[a]	-	-[a]	-	ν_1 N-H stretching
PPM-A						
1043.9(46)	-0.2	-[a]	-	-[a]	-	ν_8 C-O stretching
3628.4(365)	-213.1	3458.8	-204.6	-[a]	-	ν_3 O-H stretching
599.7(93)	84.8	-[a]	-	-[a]	-	ν_{16} N-H bending
610.2(18)	95.3	-[a]	-	-[a]	-	
3386.3(547)	-286.2	3300.9/3293.2	-216.1[b]	3332.5	-187.7	ν_1 N-H stretching
PPM-B						
1016.0(107)	-28.1	-[a]	-	-[a]	-	ν_8 C-O stretching
3840.2(49)	1.3	-[a]	-	-[a]	-	ν_3 O-H antisym.str.
601.6(16)	86.7	-[a]	-	-[a]	-	ν_{16} N-H bending
616.8(12)	101.9					
3463.4(565)	-209.1	-[a]	-	-[a]	-	ν_1 N-H stretching
3526.5(554)	-146.0					
PMM-A						
1040.2(90)	-3.9	-[a]	-	-[a]	-	ν_8 C-O stretching
1064.5(99)	20.4					
3504.6(446)	-336.9	-[a]	-	-[a]	-	ν_3 O-H stretching
3664.8(321)	-176.7					

611.6(29)	96.7	-[a]	-	-[a]	-	υ_{16} N-H bending
3566.8(440)	-105.7	3366.7	-146.5	-[a]	-	υ_{1} N-H stretching
PMM-B						
1016.2(97)	-27.9	-[a]	-	-[a]	-	υ_{8} C-O stretching
1041.1(103)	-3					
3789.4(120)	-52.1	-[a]	-	-[a]	-	υ_{3} O-H stretching
3831.9(50)	-9.6					
599.5(12)	84.6	-[a]	-	-[a]	-	υ_{16} N-H bending
3545.0(468)	-127.5	-[a]	-	-[a]	-	υ_{1} N-H stretching

[a] Experimental features were not observed.

[b] Average multiplet experimental wavenumbers of the monomers and multimers were taken to compute the experimental shift in the heterodimers.

[c] $\Delta\nu = \nu_{heterodimer} - \nu_{monomer}$

mol^{-1}. The experimental feature observed in N_2 matrix at 3349.6 cm^{-1} and in Ar matrix at 3398.0 cm^{-1} for the N-H···O heterodimer is quite intense and one cannot miss the infrared feature of the O-H···π heterodimer if at all it is formed in the matrix. To conclude, in the C_4H_5N-CH_3OH heterodimers, PM-A and PM-B, only the former heterodimer was experimentally observed in the N_2 and Ar matrixes.

5.2.3 Pyrrole···Phenol

Figure 5.8 trace ‘a’ grids A-D and Figure 5.9 trace ‘a’ illustrate the IR spectra of phenol (C_6H_5OH) alone in N_2 and Ar matrixes, where the O-H stretching mode appears in N_2 matrix at 3622.0/3626.8 cm^{-1}, and at 3638.7/3634.3 cm^{-1} in Ar. The peaks at 3425.5 and 3417.1 cm^{-1} in N_2 matrix and 3460.8/3459.3 cm^{-1} in Ar matrixes respectively are due to C_6H_5OH-H_2O heterodimer as reported by Gor et al. [3] Evidence for the formation of heterodimer was found in the O-H stretching mode of C_6H_5OH in N_2 matrix, (Figure 5.8A) where apart from the C_6H_5OH vibrational absorption mode at 3622.0 cm^{-1}, new peaks were seen at 3619.8 and 3508.4/3506.5 cm^{-1} that increases in intensity with the increase of C_4H_5N. Similarly, in Ar matrix new peak was observed at 3500.0 cm^{-1} and shows concentration dependence. On varying C_6H_5OH concentration with constant C_4H_5N, new spectral bands were observed at 3497.0, 3441.4, 3436.4, 3433.9, 3412.5 and 3406.7 cm^{-1} in N_2 and at 3500.0, 3483.2 cm^{-1} in Ar matrixes respectively in the N-H stretching region of C_4H_5N. The N-H bending mode of C_4H_5N in N_2 matrix also showed the evidence of heterodimer formation at 587.9, 573.5, 551.6, 548.7, 546.2 and 526.0 cm^{-1}, with marked concentration dependence of C_6H_5OH.

5.2.3.1 Computational Details

Computations were performed to arrive at the optimized geometries of the C_4H_5N-C_6H_5OH heterodimers using different levels of theory such as B3LYP, B3LYP-GD3, MP2,

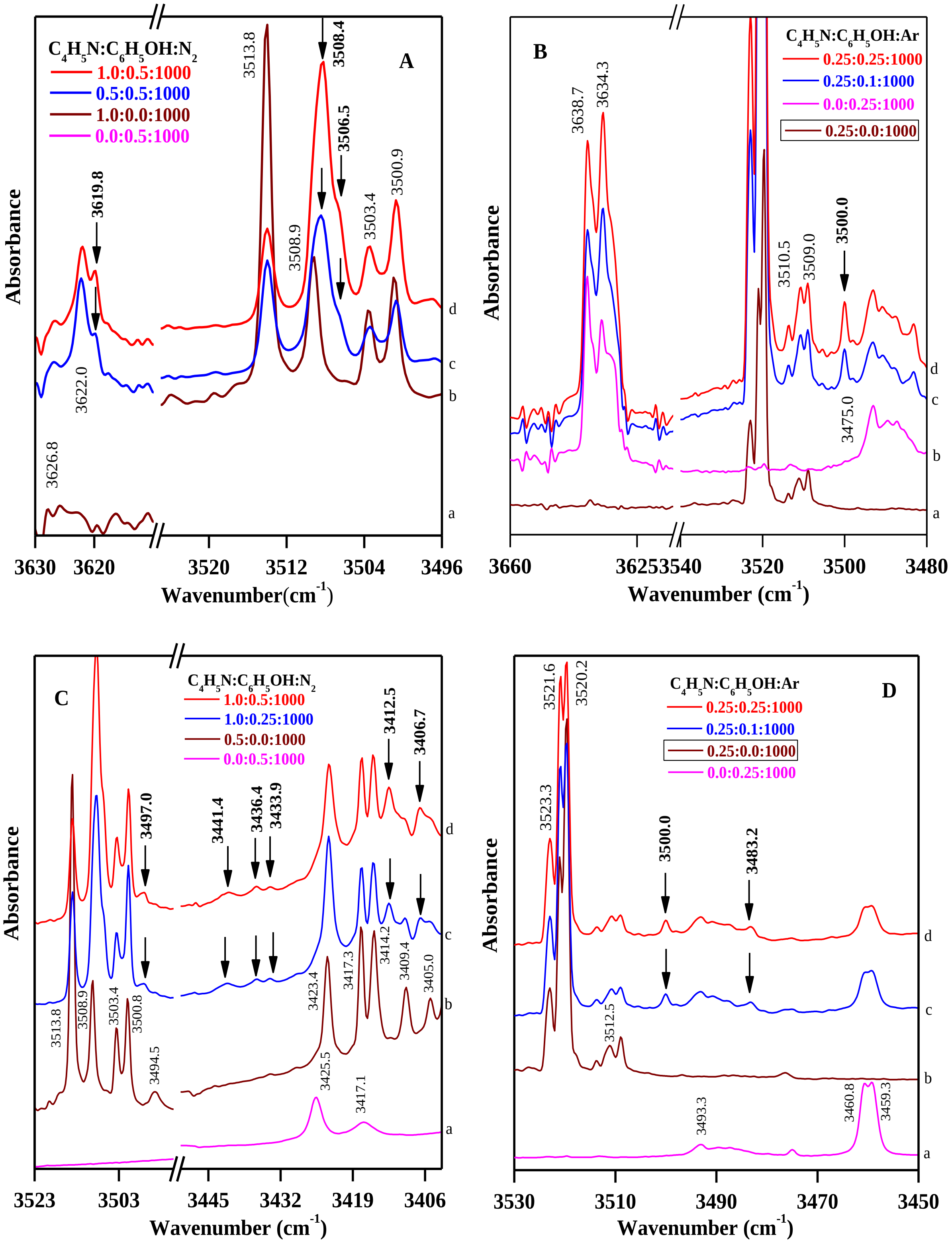

Figure 5.8 Matrix isolated IR spectra of (A) O-H stretching mode of C_6H_5OH in N_2 Matrix, (B) in Ar Matrix (C) N-H stretching region of C_4H_5N in N_2 matrix, (D) in Ar matrix. All the spectra shown here were annealed at 30 K (for N_2) and 35 K (for Ar).

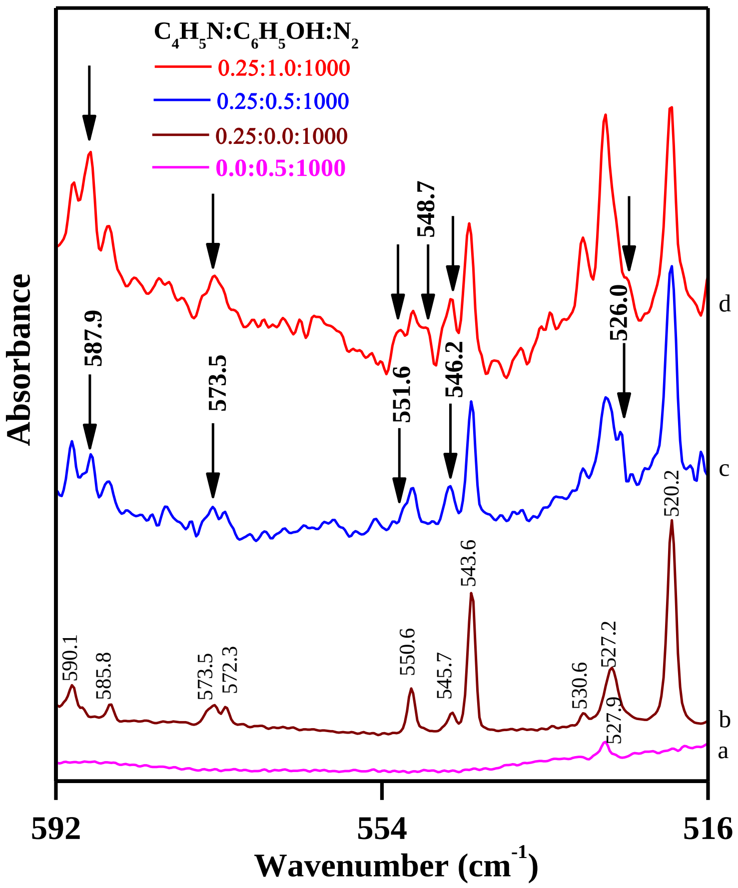

Figure 5.9 Matrix isolated IR spectra of N-H bending region of C_4H_5N in N_2 matrix. All the spectra shown here were annealed at 30 K.

and M06 with aug-cc-pVDZ basis set. Computations predicted three minima on the potential energy surface for the C_4H_5N-C_6H_5OH heterodimers, and the structures of the heterodimers computed at MP2/aug-cc-pVDZ level of theory are shown in Figure 5.10. The stabilization energies of the heterodimers along with their structures computed at different levels of theory using aug-cc-pVDZ basis set are illustrated in Table 5.4. Figure 5.11 shows the plot of BSSE corrected stabilization energies at different levels of theory using aug-cc-pVDZ basis set versus heterodimers PP-A, PP-B and PP-C. It is clear from the plot that at all level of theories, heterodimer PP-A (O-H···π) is lower in energy (global minimum) than the other two heterodimers PP-B (N-H···π) and PP-C (N-H···O) (local minima). Depending on the level of theory, the energies of heterodimers PP-B and PP-C fluctuate. At B3LYP/aug-cc-pVDZ level of theory, heterodimer PP-C is lower in energy than heterodimer PP-B, whereas with the inclusion of Grimme's dispersion correction at DFT level, the heterodimers become nearly isoenergetic. At M06 and MP2 levels of theory, heterodimer PP-B seems to be more stable than heterodimer PP-C, due to the incorporation of the hybrid functional and dispersion correction, respectively. Computations performed at B3LYP/aug-cc-pVDZ level of theory showed a decreasing order of stabilization energy, PP-A < PP-C < PP-B. Etter's rule is generally used to rationalize and predict the hydrogen-bonding interaction in the crystals which states that (1) all good proton donors and acceptors are used in hydrogen bonding, (2) six-membered ring intramolecular hydrogen bonds form in preference to intermolecular hydrogen bonds, and (3) the best proton donors and acceptors remaining after intramolecular hydrogen-bond formation form intermolecular hydrogen bonds to one another. Legon and Millen gave rules for the formation of X-H···B hydrogen bonds using the rotational spectra of several mixed dimers in the gas phase. These rules are as follows: (1) The axis of the HX molecule coincides with the supposed axis of a nonbonding electron pair on B. (2) If B has no nonbonding electron pairs and instead it has π-bonding electron pairs, then the axis of HX molecules intersects the internuclear axis of atoms forming the π bond in B. (3) If B has both nonbonding and π-bonding electron pairs, then rule (1) is definite. The first and second rules describe the structure of the complex, while the third rule indicates that the lone pair of electrons is preferred over π-bonding electron pairs in the hydrogen-bond formation. Both Etter's and Legon-Millen rules predict a definite order in the hydrogen bonding on the basis of these empirical rules. However, exceptions to these rules were noticed in the literature [4, 5].

The O-H of C_6H_5OH and π-electron of C_4H_5N are better proton donors and acceptors, respectively, and the non-bonded pair of electrons forms a stronger interaction (heterodimer PP-C) than the π-electron (heterodimer PP-B). It should be mentioned that at this level of theory, heterodimers PP-B and PP-C are devoid of any secondary interactions. As the dispersion correction is incorporated either through empirical (DFT-GD3 and M06) or by perturbation methods (MP2) to optimize the geometry of the heterodimers, the stabilization energy ordering is PP-A < PP-B < PP-C. Contrary to the DFT level, apart from the primary interaction in heterodimers PP-B and PP-C, they are further stabilized by secondary interactions. Because of this secondary interaction, the geometry of the heterodimers is altered, which makes heterodimer PP-B more stable than heterodimer PP-C. Clearly, a deviation from the Legon-Millen third rule was noticed as the π interactions are stronger than the nonbonding interaction. It should be mentioned that at all levels of theories with aug-cc-pVDZ basis sets, heterodimer PP-A was the global minimum structure (with both primary $\text{O-H}\cdots\pi$ and secondary $\text{C-H}\cdots\pi$ interactions), which therefore manifests that the O-H of phenol is more acidic than pyrrole N-H and forms a stronger heterodimer than heterodimers PP-B and PP-C (nonbonding and π-interaction), obeying Etter's first rule, according to which the best proton donor or the most acidic group will be used primarily for hydrogen bonding, followed by next acidic group [5]. Invariably, at all levels of theory the structures of heterodimers PP-A, PP-B, and PP-C violate the Legon-Millen's second rule [4]. In heterodimer A, there are synergistic (primary and secondary) interactions between the O-H and C-H of C_6H_5OH with π-cloud of C_4H_5N, respectively. The bond distances between the H13-C18, H13-C17, H10-C14, and H10-C15 are 2.339, 2.454, 2.671, and 2.527 Å. Furthermore, the bond angles ∠O12-H13-C18, ∠O12-H13-C17, ∠C9-H10-C15 and ∠C9-H10-C14 are 165.3°, 132.0°, 138.3° and 156.6° and the dihedral angles ∠O12-H13-C18-H22, ∠O12-H13-C17-H21, ∠C6-C9-H10-C15 and ∠C6-C9-H10-C14 are 111.5°, 38.4°, 76° and 125.7°, which make the C_6H_5OH moiety tilt towards the C_4H_5N molecule. At B3LYP/aug-cc-pVDZ level of theory, the C_6H_5OH molecule is perpendicular to the C_4H_5N (as shown in Figure 5.10). In heterodimer PP-B, the bond angle ∠N16-H23-C1 is 132.2° and the dihedral angles ∠C17-N16-H23-C1 and ∠C15-N16-H23-C1 are -76° and 89.3°, which make the C_4H_5N molecule displaced parallel to the plane of the C_6H_5OH molecule, favoring a $\pi\cdots\pi^*$ interaction between the aromatic π-electron clouds of these molecules. The bond distances between the H23-C1, H23-C2, C17-C7 and C17-C9 are 2.702, 2.831, 3.060 and 3.289 Å. At B3LYP/aug-cc-pVDZ level of theory, the N-H group of C_4H_5N is perpendicular to the C_6H_5OH and has only N-H⋯π interaction (Figure 5.10). Clearly, the incorporation of dispersion correction alters the geometry of the heterodimer and favors the synergistic interaction between the C_4H_5N and C_6H_5OH molecules. This is the likely cause for the violation of Legon-Millen rules, since these rules are based on electrostatic and charge transfer contributions, excluding any considerations from dispersion. At MP2/aug-cc-pVDZ level of theory, heterodimer C has both N-H⋯O and C-H⋯π interactions; the bond distance between the H23-O12 and H20 of C_4H_5N with all of the carbons of C_6H_5OH is 2.167 and 2.804 Å, respectively. The bond angles ∠N16-H23-O12 and ∠C15-H20-C1 are 157.6° and 141.7°, and the dihedral angles ∠C15-N16-H23-O12, ∠C17-N16-H23-O12, ∠C14-C15-H20-C1 and ∠C14-C15-H20-C2 are -32.1°, 147.0°, 134.4° and 162.5°, which orients the C_4H_5N

molecule perpendicular to the plane of the C_6H_5OH molecule. At B3LYP level, the geometry of the molecule is completely different, and there is only N-H···O interaction between the C_4H_5N and C_6H_5OH molecules (Figure 5.10). At MP2/aug-cc-pVDZ level of theory, invariably all of the heterodimers PP-A, PP-B, and PP-C demonstrate the synergistic ability of forming multiple hydrogen bonds (synergistic interactions), which increases the stability of the heterodimers.

5.2.3.2 Vibrational Assignments in the $\nu_{O\text{-}H}$ Stretching Region of C_6H_5OH

As discussed earlier, the ν_1 O-H stretching mode of bare C_6H_5OH was observed as a site-split feature at 3622.0/3626.8 cm^{-1} in N_2 matrix (Figure 5.8 Grid A) and in Ar matrix at 3638.7/3634.3 cm^{-1} (Figure 5.8 Grid B) [1]. As the concentration of C_4H_5N was varied, new peaks show up as site-split feature at 3508.4/3506.5 cm^{-1}, a red-shift of -117.0 cm^{-1} in N_2 matrix and at 3500.0 cm^{-1} with a red-shift of -136.0 cm^{-1} in Ar matrix from the C_6H_5OH monomer absorption, which compares well with the computed red-shift of -131.2 cm^{-1} for the O-H···π heterodimer (PP-A). It should be mentioned that the new feature observed at 3508.4/3506.5 cm^{-1} for heterodimer PP-A exactly falls on the site-split feature of $(C_4H_5N)_2$ at 3508.9 cm^{-1}, broadens, and picks up in intensity as the C_4H_5N concentration was varied, which clearly confirms the formation of O-H···π heterodimer (PP-A) at low temperatures. Computations predicted a red-shift of -17.8 and -16.2 cm^{-1}, for the N-H···π heterodimer (PP-B) and N-H···O heterodimer (PP-C), respectively, in the ν_1 O-H stretching mode of the C_6H_5OH submolecule. Experimentally, a red-shift of -2.2 cm^{-1} is observed in the ν_1 O-H stretching mode of C_6H_5OH, which is assigned for heterodimer PP-C. In heterodimer PP-A, where C_6H_5OH acts as a proton donor, the O-H vibrational shift was larger, whereas in heterodimers PP-B and PP-C, C_6H_5OH plays the role of proton acceptor, and the corresponding shifts are smaller in the ν_1 O-H stretching mode of C_6H_5OH submolecule. No new feature was discerned in Ar matrix for the PP-B and PP-C heterodimers in this mode.

5.2.3.3 Vibrational Assignments in the ν_1 and ν_{16} Mode of C_4H_5N

For the O-H⋯π heterodimer (PP-A), where C_4H_5N is a proton acceptor, the vibrational wavenumber shifts in the N-H stretching and bending mode in the C_4H_5N submolecule are smaller in comparison to those of the heterodimers PP-B and PP-C, where C_4H_5N is the proton donor. Experimentally, new features observed at 3497.0 and 546.2/548.7/551.6 cm^{-1} in the N-H stretching and bending modes of C_4H_5N in N_2 matrix, having shifts of -16.2 and 25.3 cm^{-1}, compare well with the computed shifts of -13.9 and 28.0 cm^{-1}, respectively, for heterodimer PP-A. In Ar matrix, new feature was seen at 3505.4 cm^{-1} with a shift of -16.2 cm^{-1}, that increased in intensity as a function of C_6H_5OH concentration. The site-split multiplets observed at 3441.4/3436.4/3433.9 cm^{-1} in the N-H stretching mode and at 573.5 cm^{-1} in the N-H bending mode, having a shift of -75.9 and 50.0 cm^{-1}, respectively, matches with the computed shifts of -51.5 and 40.0 cm^{-1} for heterodimer PP-B. A new feature at 3483.2 cm^{-1} at a shift of -38.5 cm^{-1} was observed in Ar matrix and has been tentatively assigned to PP-B. For the N-H⋯O heterodimer (PP-C), computations showed a shift of -56.7 and 64.8 cm^{-1}, but the experimental shifts are -103.6 and 64.4 cm^{-1} in the N-H stretching and bending modes of C_4H_5N submolecule, respectively. It is clear from the table that the experimental shift for heterodimer PP-A in the O-H stretching mode matches well with the computed shift at B3LYP, M06 and MP2 levels, whereas there is a deviation at the dispersion corrected B3LYP-GD3 level. In the N-H bending and stretching modes, the computed shift at the MP2 level of theory corroborates well with the experimental shift, whereas at the other levels of theory, there is a large deviation between the computed and experimental shifts for heterodimer PP-A. Interestingly, the synergistic O-H⋯π and C-H⋯π interactions were found to be present in heterodimer PP-A, at all levels of theory. In PP-B heterodimer, the experimental shift showed a deviation from the computed shift at B3LYP, B3LYP-GD3, and M06 levels of theory with aug-cc-pVDZ basis set in the N-H and O-H

Table 5.5 [a]Raw/ZPE/BSSE Corrected Stabilization Energies (kcal mol^{-1}) for the C_4H_5N-C_6H_5OH Heterodimers PP-A, PP-B and PP-C computed at different Level of Theories with aug-cc-pVDZ Basis Set.

Level of theory	**PP-A**	**PP-B**	**PP-C**
B3LYP/aug-cc-pVDZ	-4.04/-3.31/-3.40	-2.30/-1.93/-1.63	-3.75/-3.08/-3.31
B3LYP-GD3/aug-cc-pVDZ	-7.82/-6.90/-7.07	-6.48/-5.77/-5.62	-6.05/-5.26/-5.50
M06/aug-cc-pVDZ	-6.58/-5.78/-5.78	-5.85/-4.72/-5.28	-4.85/-4.10/-4.36
MP2/aug-cc-pVDZ	-11.04/-9.99/-7.27	-11.34/-10.61/-6.71	-9.62/-8.63/-5.55

All energies are in kcal mol^{-1}.

[a] Raw interaction energies refer to energies not corrected for either ZPE or BSSE

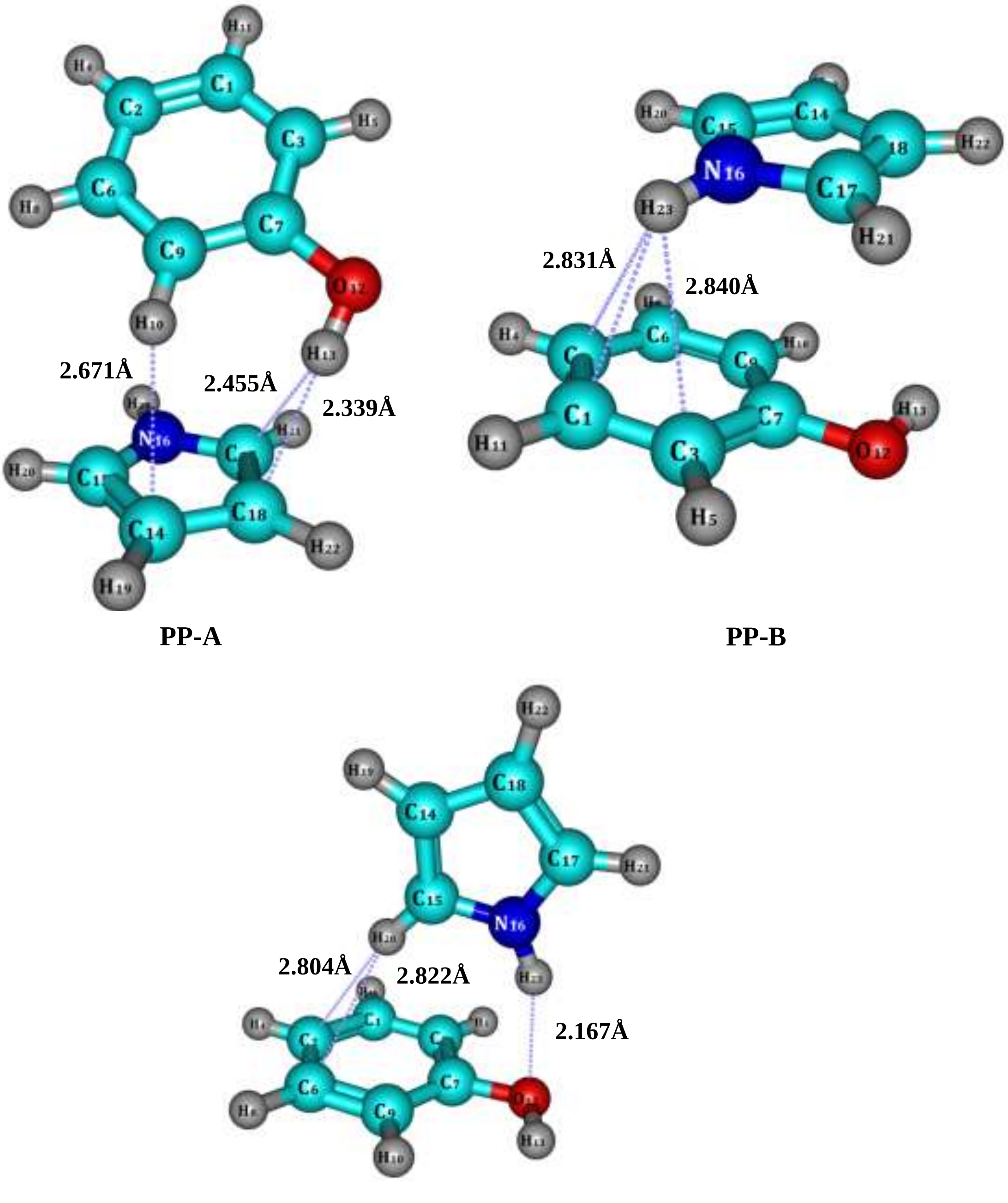

PP-A

PP-B

PP-C

Figure 5.10 Structures of 1:1 C_4H_5N-C_6H_5OH PP-A, PP-B, and PP-C computed at MP2/aug-cc-pVDZ level of theory.

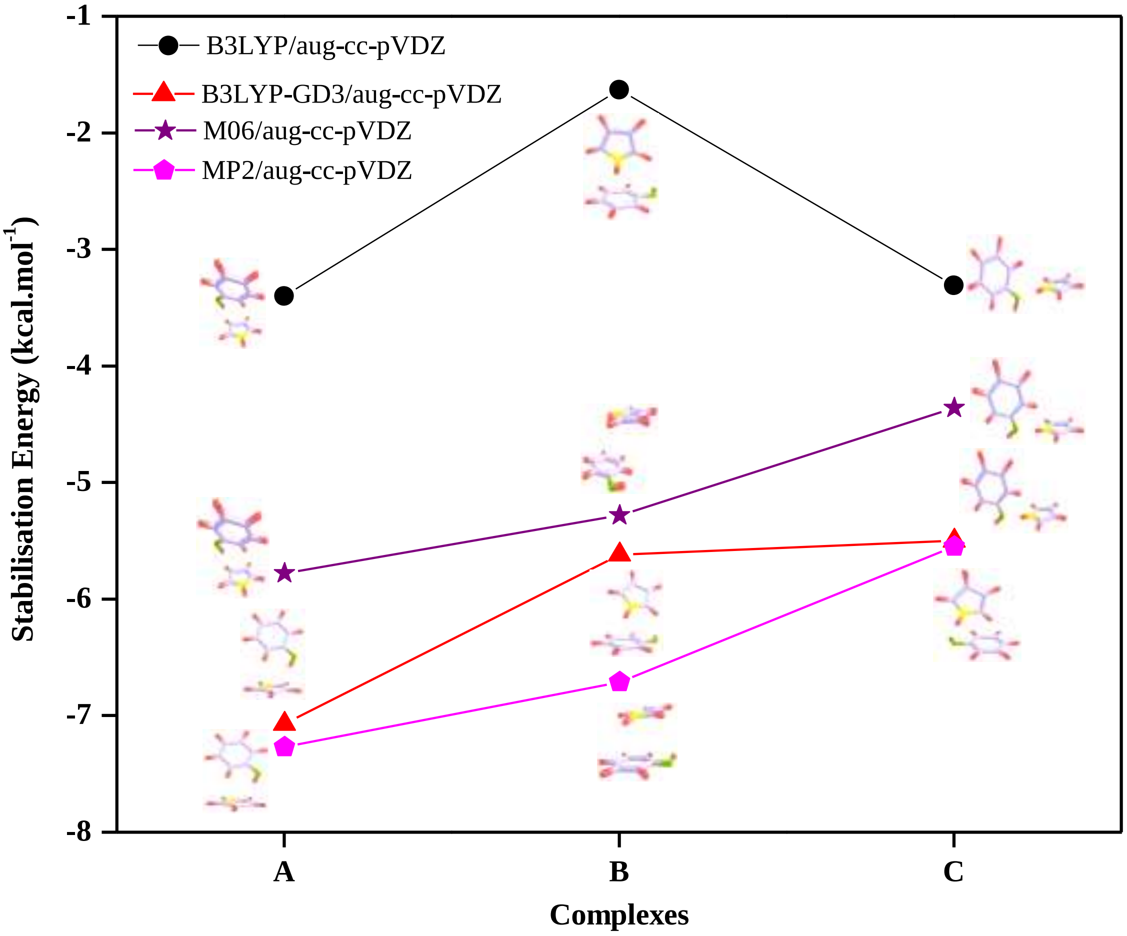

Figure 5.11 Plot of BSSE corrected stabilization energies versus heterodimers PP-A, PP-B and PP-C at different levels of theory with aug-cc-PVDZ basis sets.

stretching regions of C_4H_5N and C_6H_5OH submolecules. The geometry optimized at the B3LYP/aug-cc-pVDZ level shows only N-H···π interaction, whereas at MP2/aug-cc-pVDZ due to the dispersion correction, N-H···π and π···π* synergistic interactions, the C_4H_5N has a displaced parallel structure with the C_6H_5OH molecule, and the experimental wavenumber compares well with the computed shift. For heterodimer PP-C, the experimental and computed shifts are comparable in the O-H and N-H stretching regions at B3LYP, B3LYP-GD3, and M06 levels of theory, whereas at MP2 level of theory, there is a deviation. The experimental shift in the N-H bending mode for heterodimer PP-C matches reasonably well with the computed shift at other levels of theory, whereas there is a large difference in the N-H stretching wavenumbers at the MP2 level. Such discrepancies in the computed shift are probably due to the level of theory used to arrive at the optimized structures of the heterodimers. At B3LYP, B3LYP-GD3, and M06 levels of theory, heterodimer PP-C has only N-H···O interaction. There are no synergistic interactions for which the red-shift in the N-H stretching wavenumber of C_4H_5N submolecule was ca. 83-86 cm^{-1}, agreeing well with the experimental red-shift of 103.6 cm^{-1}. At MP2 level of theory, apart from the primary N-H···O interaction, a secondary C-H···π interaction was formed between C_4H_5N and C_6H_5OH, and these two interactions are acting opposite to each other. The incorporation of dispersion correction stabilizes the secondary C-H···π interaction, which probably weakens the N-H···O hydrogen bond, and the corresponding red-shift in the N-H stretching mode of C_4H_5N submolecule decreases in the heterodimer PP-C. This type of H-bond weakening due to secondary interaction has been reported by Mikami et al. in case of C_6H_5OH-C_6H_6 heterodimers [6]. Hence, for heterodimer C, a non-synergistic structure is favorable in the matrix, and it is stabilized by only N-H···O interaction as predicted by B3LYP/aug-cc-pVDZ level of theory.

In a nutshell, heterodimers PP-A (O-H···π, C-H···π) and PP-B (N-H···π, π···π*) have synergistic interactions on the π-electron cloud of C_4H_5N and C_6H_5OH, respectively. MP2/aug-cc-pVDZ level of theory was able to predict the structures, and the computed vibrational shifts agree reasonably with the experimental wavenumbers. Although the MP2 level of theory predicts the structure of heterodimer PP-C to have interactions on oxygen (N-H···O) and π-electron cloud (C-H···π) of C_6H_5OH with C_4H_5N, the experimental shift confirms that heterodimer PP-C may not possess a secondary interaction in the matrix. It is likely that the dispersion dominated heterodimer PP-C (as predicted by MP2 level of theory) is strongly destabilized due to the matrix surrounding, and further computational work is indeed essential to understand the role of the matrix on heterodimer PP-C. It is obvious from our matrix isolation experiments that the structures optimized in the isolated gas phase in a vacuum need not be generated at cold isolated conditions as the low temperature matrix plays a profound role in altering the geometry of the heterodimers.

5.2.4 Pyrrole···Diethyl ether

5.2.4.1 Conformations of DEE.

Since, the presence of rotational flexible ethyl groups are attached to oxygen on both the sides, at the outset, the conformational degrees of freedom were analyzed for DEE. The geometry optimization of different conformers of DEE was performed and was found that the energy of the conformers increases in the order $tt<tg^{\pm}<g^{\pm}g^{\pm}<g^{\pm}g^{\mp}$. The structures of the DEE conformers are illustrated in the Figure 5.12. Our results agree well with the earlier computational reports on the DEE conformers [7-17]. The energies, degeneracies and relative room temperature population of DEE conformers are given in Table 5.7. It is to be mentioned that the conformational studies were performed at B3LYP/aug-cc-pVDZ level of theory (since for probing conformations, DFT functional is superior), while the pyr-DEE

Table 5.6 Comparison of computed with the experimental shift in N_2 and Ar matrix, mode assignments for the C_4H_5N-C_6H_5OH heterodimers PP-A, PP-B and PP-C. Computations were performed at MP2/aug-cc-pVDZ Level of Theory.

Computed[a] v (cm^{-1})		**Experimental v (cm^{-1})**				**Mode Assignment**
		N_2		**Ar**		
v	**Δv[b]**	**v**	**Δv[b]**	**v**	**Δv[b]**	
Pyrrole						
514.9(58)	-	520.2/527.2[c]	-	483.8/482.8/ 481.6[c]	-	υ_{16} N-H bending
3672.4(76)	-	3519.3/3513.8 /3510.9/ 3508.9[c]	-	3523.3/3521.6/ 3520.2[c]	-	υ_1N-H stretching
Phenol						
329.5(95)	-	358.0	-	-[d]	-	O-H bending
3807.5(64)	-	3622.0/ 3626.8[c]	-	3638.7/3634.3[c]	-	υ_1 O-H stretching
PP-A						
542.9(68)	28.0	546.2/548.7/ 551.6	25.3[c]	-[d]	-	υ_{16} N-H bending
3658.5(72)	-13.9	3497.0	-16.2	3505.5	-16.2[c]	υ_1N-H stretching
492.5(98)	162.9	526.0	168.0	-[d]	-	O-H bending
3676.3(343)	-131.2	3508.4/ 3506.5[c]	-117.0[c]	3500.0	-136.5[c]	υ_1O-H stretching
PP-B						
554.9(104)	40.0	573.5	50.0	-[d]	-	υ_{16} N-H bending
3620.9(85)	-51.5	3441.4/3436.4 /3433.9	-75.9[c]	3483.2	-38.5	υ_1 N-H stretching
299.0(131)	-30.6	-[d]	-	-[d]	-	O-H bending
3789.7(55)	-17.8	-[d]	-	-[d]	-	υ_1 O-H stretching
PP-C						
579.7(15)	64.8	587.9	64.4	-[d]	-	υ_{16} N-H bending
3615.7(228)	-56.7	3412.5/3406.7	-103.6[c]	-[d]	-	υ_1 N-H stretching
365.2(106)	35.6	-[d]	-	-[d]	-	O-H bending
3791.3(60)	-16.2	3619.8	-2.2	-[d]	-	υ_1O-H stretching

[a] Intensity in km mol^{-1} is given in parenthesis.

[b] $\Delta\nu = \nu_{monomer}-\nu_{heterodimer}$.

[c] Average of multiplet experimental wavenumbers of the monomers and C_4H_5N-C_6H_5OH heterodimers PP-A, PP-B and PP-C were taken to compute the experimental shift.

[d] Experimental features were not observed.

heterodimers were analyzed at MP2/aug-cc-pVDZ level of theory, since the former is a superior method for conformational analysis. At B3LYP/aug-cc-pVDZ level of theory, the relative energies of $tg^{\pm}$ and $g^{\pm}g^{\pm}$ conformers with respect to ground state *tt* conformer were calculated to be 1.62 and 3.12 kcal mol^{-1}, respectively. From the relative energies and degeneracies, the room temperature populations of *tt*, $tg^{\pm}$ and $g^{\pm}g^{\pm}$ conformers were found to be 78%, 21% and 1%, respectively. Since, the $g^{\pm}g^{\pm}$ has a negligible population, this conformer is experimentally not important. Interestingly, upon optimization at the B3LYP/aug-cc-pVDZ level of theory, the $g^{\pm}g^{\mp}$ conformer is converted to $tg^{\pm}$ form and, therefore, the $g^{\pm}g^{\mp}$ conformer is not a minimum on the potential energy surface. As the populations of the *tt* and $tg^{\pm}$ conformers of DEE are appreciable at room temperature, it is possible to trap these two conformers at low temperatures under isolated condition. The computed wavenumber analysis of the different vibrational modes of *tt* and $tg^{\pm}$ conformers revealed that, only the C-O-C stretching mode has appreciable infrared absorption intensity and a significant vibrational wavenumber difference between the *tt* and $tg^{\pm}$ conformers. Hence, experimentally, only the C-O-C vibrational mode of DEE was probed for identifying the *tt* and $tg^{\pm}$ conformers.

5.2.4.2 Vibrational Assignments of DEE in C-O-C stretching region

Figure 5.13 grids A and B show the infrared spectra of the C-O-C stretching region of DEE in N_2 and Ar matrixes. Trace ‘a’ shows the simulated spectra of *tt* and $tg^{\pm}$ conformers, where the infrared intensities are weighted for their population. Traces ‘b’ and ‘c’ correspond to the as-deposited and annealed spectra of DEE, respectively. The site split features observed at 1127.8, 1126.1 cm^{-1} in N_2 and the corresponding features at 1133.4, 1131.9 cm^{-1} in Ar matrix compared well with the computed value of 1143.8 cm^{-1} of *tt*-conformer. Furthermore, in the as-deposited spectra adjacent to the intense peak, a weak feature was observed at 1119.9 cm^{-1} in N_2 and site split features at 1127.1 and 1124.9 cm^{-1} in Ar matrix.

Table 5.7 Relative Energies, Degeneracy and % Contributions of the Different Conformers of DEE Computed at B3LYP/aug-cc-pVDZ Level of Theory.

Conformers	**Relative Energy (Hartree a. u.)**	**Relative Energy (kcal mol^{-1})**	**Degeneracy**	**Relative Contribution (%)**
tt	-233.555531	0.0	2	78
tg$^{\pm}$	-233.552957	1.62	4	21
g$^{\pm}$*g*$^{\pm}$	-233.550577	3.11	2	1

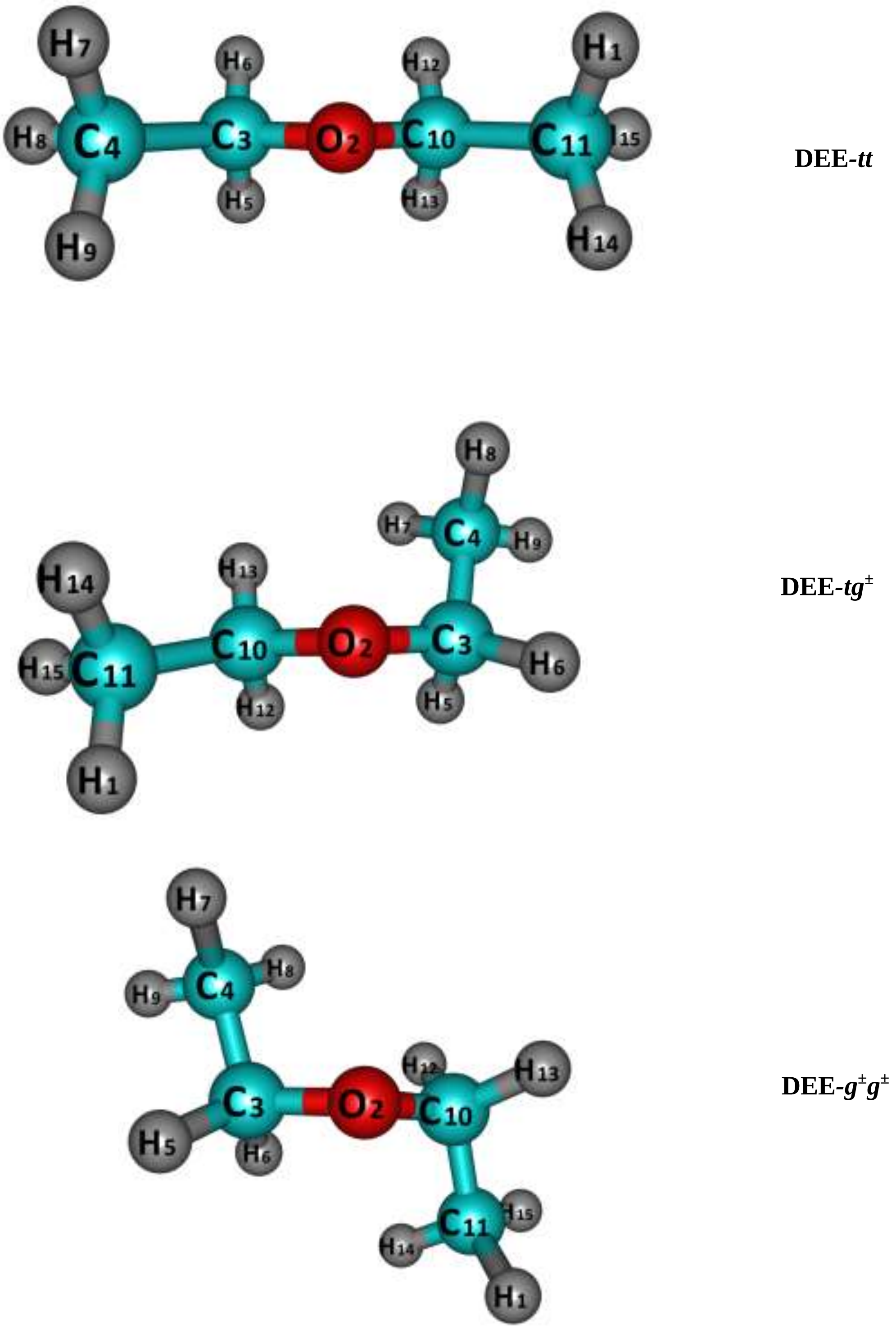

Figure 5.12 Structures of the different conformers of diethyl ether (DEE) have been computed at B3LYP/aug-cc-pVDZ level of theory.

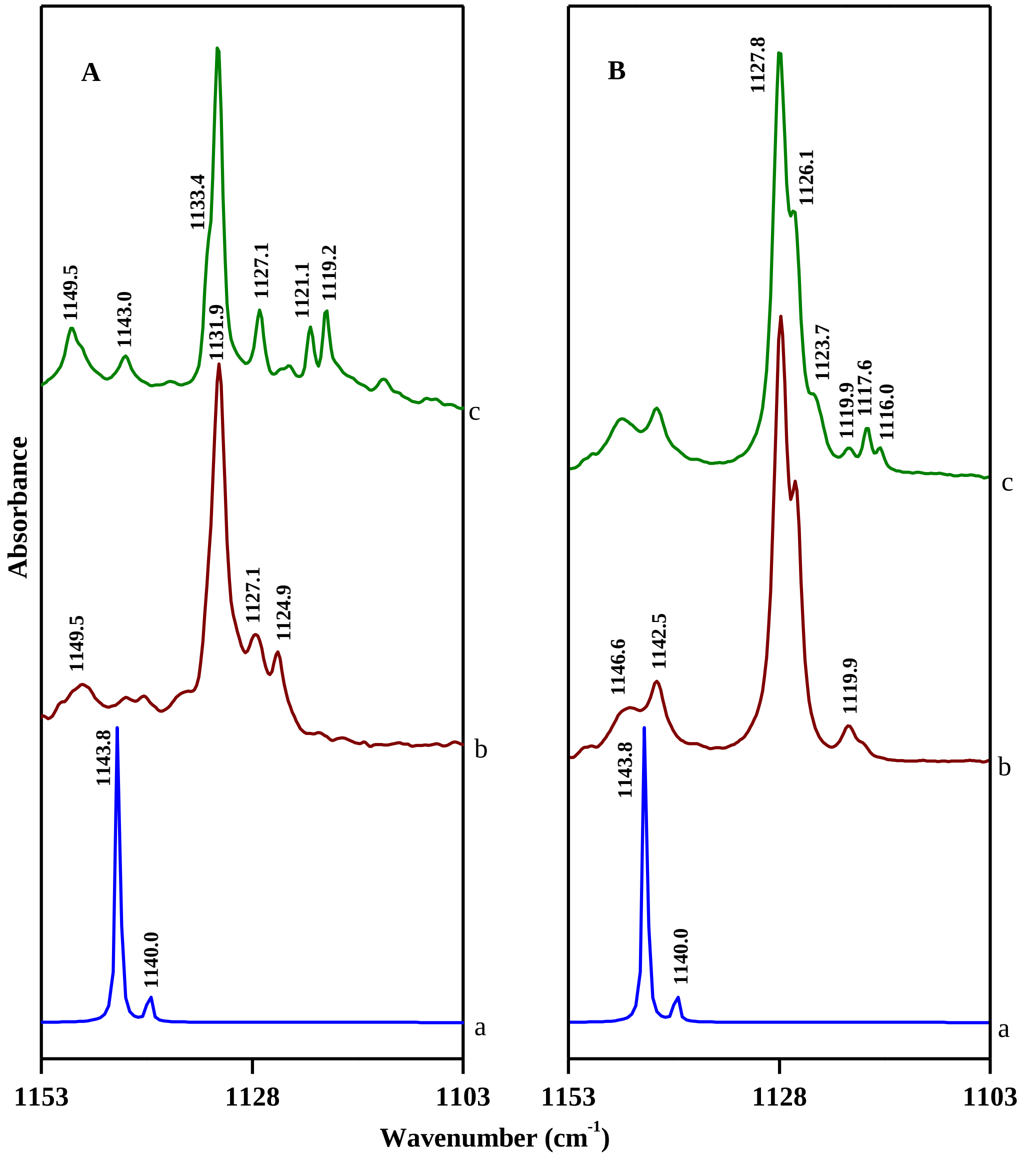

Figure 5.13 Infrared spectra of C-O-C stretching region of DEE in Ar (grid A) and N_2 (grid B) (a) Simulated spectra of DEE, (b) as deposited spectra and (c) Annealed spectra.

On annealing, the 1119.9 and 1124.9 cm^{-1} feature in N_2 and Ar matrixes, respectively, decrease in intensity and a new peak appears at 1123.7 cm^{-1} in N_2 matrix, whereas the intensity of the feature at 1127.1 cm^{-1} increases in Ar matrix. The behavior of the peaks (1119.9 cm^{-1} in N_2 and 1127.1 cm^{-1} in Ar) is identical in both matrixes and agree well with the computed value of 1140.0 cm^{-1} for *tg*$^{\pm}$ conformer of DEE. The features observed at 1117.6, 1116.0 and 1121.1, 1119.2 cm^{-1} in annealed N_2 and Ar matrixes, respectively, are likely due to DEE-H_2O heterodimer. Therefore, through matrix isolation infrared spectroscopy, both *tt* and *tg*$^{\pm}$ conformers of DEE were clearly discerned at low temperatures experimentally, which correlated well with the computational predictions.

5.2.4.3 Natural Bond Orbital (NBO) Analysis of the conformers of DEE

Geminal and vicinal hyperconjugative interactions are the two types of donor-acceptor interactions that stabilize the conformations of phosphates, phosphites, acetals and ketals [18-29]. Table 5.8 lists the NBO analysis of some of the important vicinal interactions in *tt*, *tg*$^{\pm}$ and *g*$^{\pm}$*g*$^{\pm}$ conformers of DEE together with E_2 energies. In order to estimate quantitatively the relative contribution of vicinal and geminal interactions to the conformational stability in DEE conformers, hyperconjugative interactions on the *tt*, *tg*$^{\pm}$ and *g*$^{\pm}$*g*$^{\pm}$ conformers of DEE were sequentially deleted. The energies of the three conformers of DEE after deleting either vicinal or geminal or all the acceptor orbital interactions are listed in table 5.9. The contribution due to steric interactions to the conformational ordering is obtained by deleting all the acceptor orbital hyperconjugative interactions. Figure 5.14 shows the picture of conformational ordering of DEE when all the hyperconjugative interactions were present and also by systematically deleting the geminal, vicinal and all the interactions. When the vicinal interaction is deleted, the energy of the *tt*, *tg*$^{\pm}$ and *g*$^{\pm}$*g*$^{\pm}$ conformer increases by 153, 152 and 153 kcal mol^{-1}, respectively, indicating that the relative contribution of ~90% from this interaction in stabilizing the conformers. The energy ordering after deleting the vicinal interactions is $g^{\pm}g^{\pm}<tt<tg^{\pm}$. However, when the geminal interactions were deleted the energy increase of all the three conformers is only 17(*tt*), 16($tg^{\pm}$), 16($g^{\pm}g^{\pm}$) kcal mol^{-1} and the relative contribution to the overall stability of the conformers is only ~ 9.0%, which clearly showed that the geminal interaction hardly contributes to the overall energetics of the conformers. The energy ordering after deleting the geminal interactions is $g^{\pm}g^{\pm}<tg^{\pm}<tt$. When both vicinal and geminal interactions were removed, the energy ordering becomes $tt<g^{\pm}g^{\pm}<tg^{\pm}$. It is clear from the NBO analysis that, of the two interactions, vicinal interactions completely dominate the geminal interactions in deciding the stability of the conformers. Invoking of geminal interactions indeed require a vacant ‘d’ orbital (as in the case of second row elements like phosphorus and silicon) and the absence of ‘d’ orbital clearly precludes the geminal interactions to overall energetics of the conformers of DEE.

5.2.4.4 Interaction of pyrrole with tt and tg± conformers of DEE

It is clear from the previous section that only *tt* and *tg*± conformers of DEE exist at low temperatures under isolated conditions. Using the optimized geometry of the *tt* and $tg^{\pm}$ conformers of DEE and pyrrole (C_4H_5N), the geometries of the C_4H_5N-DEE-*tt* and C_4H_5N-DEE-$tg^{\pm}$ heterodimers were computed at MP2/aug-cc-pVDZ level of theory and they are shown in Figure 5.15. Geometry optimization indicated that only N-H···O interaction exists between C_4H_5N with tt and $tg^{\pm}$ conformers of DEE.

Table 5.10 gives the stabilization energy of the heterodimers corrected separately for ZPE and BSSE. Interestingly, the energy profile of the C_4H_5N-DEE heterodimers is completely different with respect to the conformational equilibrium of bare DEE. Although, the *tt* conformer of DEE was the global minimum, on complexation, the reversal in energy trend was noticed. The C_4H_5N-DEE-$tg^{\pm}$ heterodimer was calculated to be to be more exothermic than C_4H_5N-DEE-*tt* heterodimer by ~0.16 kcal mol^{-1}. The small energy difference enabled the generation of both the heterodimers at low temperatures. Table 5.11 compares the

Table 5.8 NBO Analysis of some of the Important Vicinal Hyperconjugative Interactions, showing the Donor and Acceptor Orbitals and the Second Order Perturbation Energies, E2(kcal mol^{-1}), in *tt*, *tg*$^{\pm}$ and *g*$^{\pm}$*g*$^{\pm}$ conformers of DEE, calculated at the B3LYP/aug-cc-pVDZ Level of Theory.

Interaction	*tt*	*tg*$^{\pm}$	*g*$^{\pm}$*g*$^{\pm}$
n^2(O2)→σ*C3-H5	6.26	4.75	1.03
n^2(O2)→σ*C3-H6	6.26	-	3.19
n^2(O2)→σ*C10-H12	6.26	5.38	3.19
n^2(O2)→σ*C10-H13	6.26	7.19	1.03
n^2(O2)→σ*C4-H9	-	0.82	1.01
n^2(O2)→σ*C3-C4	-	6.95	7.26
n^2(O2)→σ*C10-C11	-	-	7.26
n^2(O2)→σ*C11-H15	-	-	1.01
n^1(O2)→σ*C3-C4	0.97	0.94	-
n^1(O2)→σ*C10-H13	1.01	0.78	1.71
n^1(O2)→σ*C10-H12	1.01	1.37	2.70
n^1(O2)→σ*C3-H5	1.01	1.74	1.71
n^1(O2)→σ*C3-H6	1.01	1.94	2.71
σC4-H8→σ*O2-C3	4.48	-	-
σC4-H9→σ*O2-C3	-	5.13	4.99
σC4-H9→σ*C3-H6	2.91	-	-
σC4-H7→σ*C3-H5	2.91	-	-
σC4-H7→σ*C3-H6	-	2.45	2.85
σC3-H5→σ*C4-H8	-	2.88	3.10
σC3-H6→σ*C4-H7	-	3.15	2.80
σC3-H6→σ*O2-C10	-	3.13	-
σC4-H8→σ*C3-H5	-	2.79	2.49
σC3-H5→σ*C4-H7	2.86	-	-
σC3-H6→σ*C4-H9	2.86	-	-
σC11-H15→σ*O2-C10	4.48	4.52	4.99
σC11-H14→σ*C10-H12	2.91	2.94	
σH1-C11→σ*C10-H13	2.91	2.79	-
σO2-C3→σ*C4-C8	1.23	-	-
σO2-C3→σ*C10-C11	1.62	1.47	-
σO2-C3→ σ*C4-H9	-	0.94	1.04
σC10-H12→σ*C11-H14	2.86	2.85	-
σC10-H13→σ* H1-C11	2.86	2.89	2.80
σC3-H5→σ*O2-C10	-	-	2.95
σC3-C4→σ*O2-C10	2.24	-	
σC10-C11→σ*O2-C3	2.24	2.40	0.57
σC10-H13→σ*C11-H14	-	-	3.10
σC11-H14→σ*C10-H13	-	-	2.49
σO2-C10→ σ*C11-H15	1.04	1.23	1.04
σH1-C11→σ*C10-H12	-	-	2.85

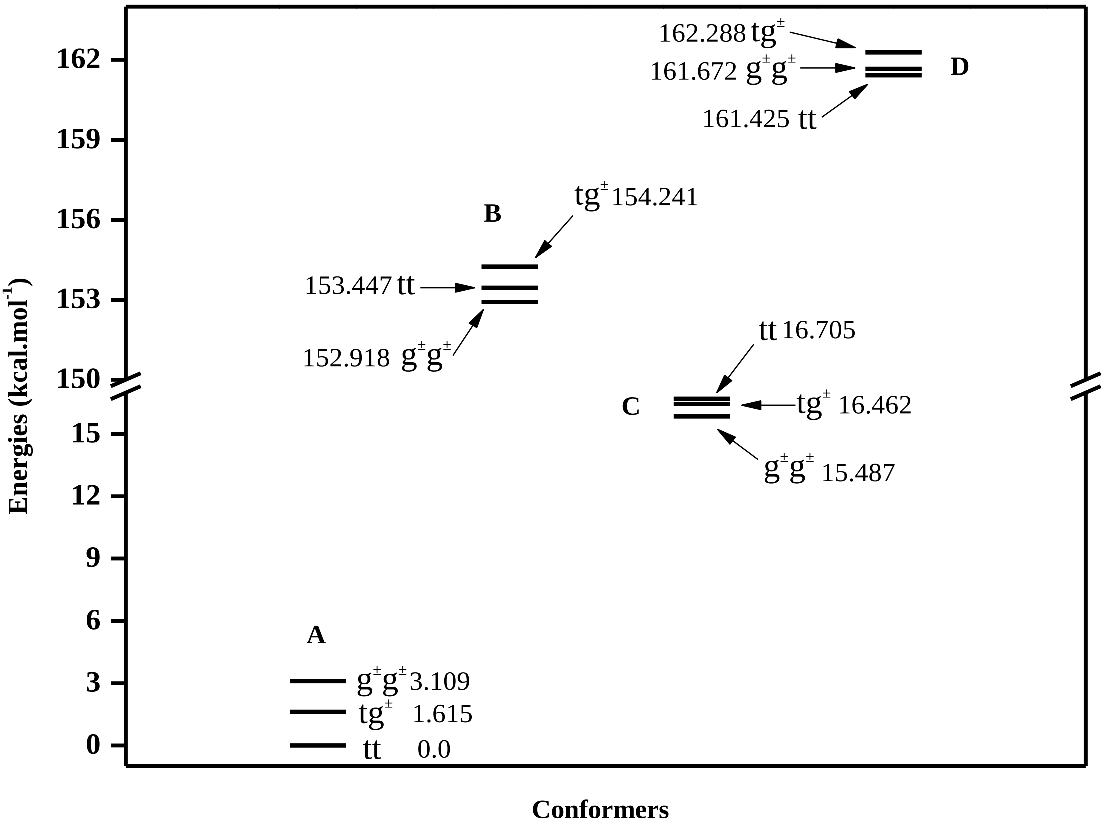

Figure 5.14 Diagram showing the correlation between the various conformers of DEE (A) with all hyperconjugative interactions present, (B) with vicinal interactions deleted, (C) with geminal interactions deleted, and (D) with all hyperconjugative interactions deleted.

Table 5.9 NBO Analysis showing the Energies obtained after deletion of various Hyperconjugative Interactions in *tt*, $tg^{\pm}$ and $g^{\pm}g^{\pm}$ Conformers of DEE, computed at the B3LYP/aug-cc-pVDZ Level of theory.

Conformers	**Energy** (hartrees)	**Interactions deleted** (hartrees)		**Change in energy**		**Relative contribution (%)**
				(hartrees)	(kcal mol^{-1})	
tt	-233.690926608	vicinal	-233.446393878	0.244533	153.447	90.2
		geminal	-233.664305630	0.026621	16.705	9.8
		all	-233.433679025	0.257248	161.425	-
$tg^{\pm}$	-233.688456860	vicinal	-233.442657612	0.245799	154.241	90.4
		geminal	-233.662223641	0.026233	16.462	9.6
		all	-233.429834271	0.258623	162.288	-
$g^{\pm}g^{\pm}$	-233.686108775	vicinal	-233.442419208	0.243690	152.918	90.6
		geminal	-233.442419208	0.025254	15.847	9.4
		all	-233.428467720	0.257641	161.672	-

shift in the computed wavenumbers with experimental values of the C_4H_5N-DEE-*tt* and C_4H_5N-DEE-*tg*$^\pm$ heterodimers computed at MP2/aug-cc-pVDZ level of theory.

5.2.4.5 Vibrational Assignments in the ν_1 and ν_{16} Mode of C_4H_5N

Figure 5.15 (grid A and B) correspond to the N-H stretching region of C_4H_5N in N_2 and Ar matrixes, respectively. The features observed at 3513.8, 3508.9 cm^{-1} in N_2 and the corresponding features at 3523.3, 3521.6, 3520.2 cm^{-1} in Ar matrix are due to the N-H stretching mode of C_4H_5N monomer. The site-split doublet features observed at 3503.4, 3500.8 cm^{-1} in N_2 and at 3512.5 cm^{-1} in Ar are those of proton accepting $(C_4H_5N)_2$, as mentioned in Chapter 3. When the precursors were deposited and annealed, new features appear with a high intensity at 3355.8 cm^{-1} and a small peak at 3361.0 cm^{-1} in N_2 and the corresponding feature is observed as multiple site split features at 3359.4, 3355.0, 3353.6 cm^{-1} in Ar matrix. These features are red-shifted by -154.0 and -165.7 cm^{-1} in N_2 and Ar matrixes, respectively from the bare monomer absorption of C_4H_5N that compares with the computed shift of -249.6 cm^{-1} for the C_4H_5N-DEE-*tt* heterodimer. Apart from the intense sharp feature due to C_4H_5N-DEE-*tt* heterodimer, another set of site split features that were observed at 3331.4, 3329.0 cm^{-1} in N_2 matrix and in Ar matrix at 3350.2 cm^{-1} with a shift of -181.8 and -171.5 cm^{-1} correlate with the computed shift of -236.5 cm^{-1} for the C_4H_5N-DEE-*tg*$^\pm$ heterodimer.

Figure 5.15 grids A and B show the N-H bending region of C_4H_5N in N_2 and Ar matrixes, respectively. The features observed at 520.2, 527.2 cm^{-1} in N_2 and at 483.8, 482.9 cm^{-1} in Ar matrix are due to N-H bending mode of C_4H_5N monomer absorption. In addition to these peaks new features were observed at 595.5, 599.8 in N_2 and at 594.3 cm^{-1} in Ar matrixes, respectively with a blue-shifts of 72.0 and 111.0 cm^{-1} that agree well with the computed blue-shift of 90.0/92.4 cm^{-1} for both C_4H_5N-DEE-*tt* and C_4H_5N-DEE-*tg*$^\pm$ heterodimers. As the computed blue-shift of the N-H bending mode is nearly the same for both heterodimers,

Table 5.10 [a]Raw/ZPE/BSSE Corrected Stabilization Energies of C_4H_5N-DEE-*tt* and C_4H_5N-DEE-*tg*$^{\pm}$ Heterodimers at various Levels of Theory.

Heterodimers	**Stabilization Energy (kcal mol^{-1})**		
	B3LYP/aug-cc-pVDZ	**B3LYP-D3/6-311++G (d p)**	**MP2/aug-cc-pVDZ**
C_4H_5N-DEE-*tt*	-4.95/-3.99/-4.31	-8.54/-7.49/-8.16	-10.13/-9.30/-7.12
C_4H_5N-DEE-*tg*$^{\pm}$	-5.31/-4.48/-4.72	-8.66/-7.58/-8.28	-10.31/-9.34/-7.28

All energies are in kcal mol^{-1}.
[a]Raw interaction energies refer to energies not corrected for either ZPE or BSSE.

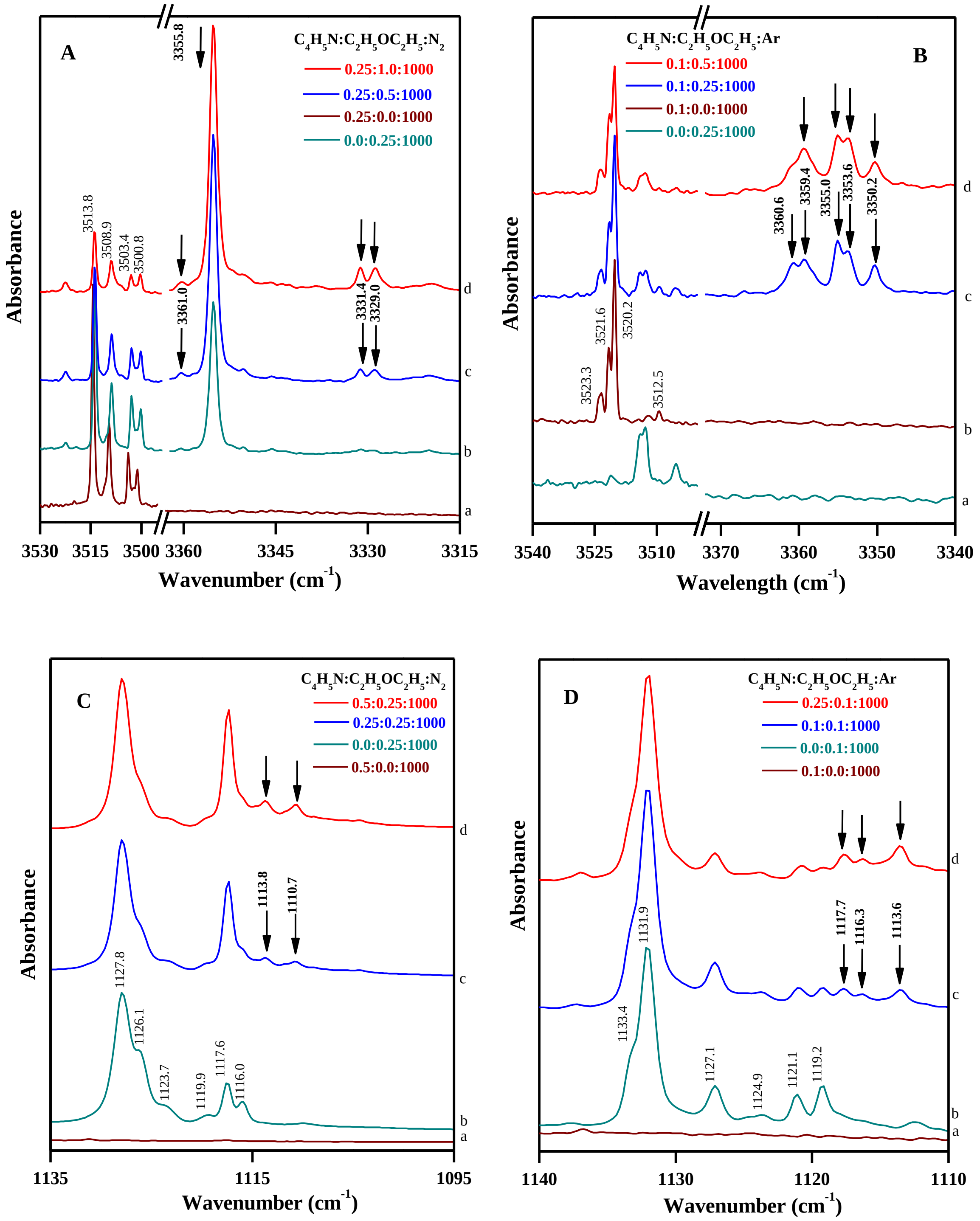

Figure 5.15 Infrared spectra of the (A) N-H stretching region of C_4H_5N in N_2, (B) N-H stretching region of C_4H_5N in Ar matrixes, (C) C-O-C stretching region of DEE in N_2 and (D) C-O-C stretching region of DEE in Ar matrixes. All the spectra shown here were annealed at 30 K (N_2) and 35 K (Ar).

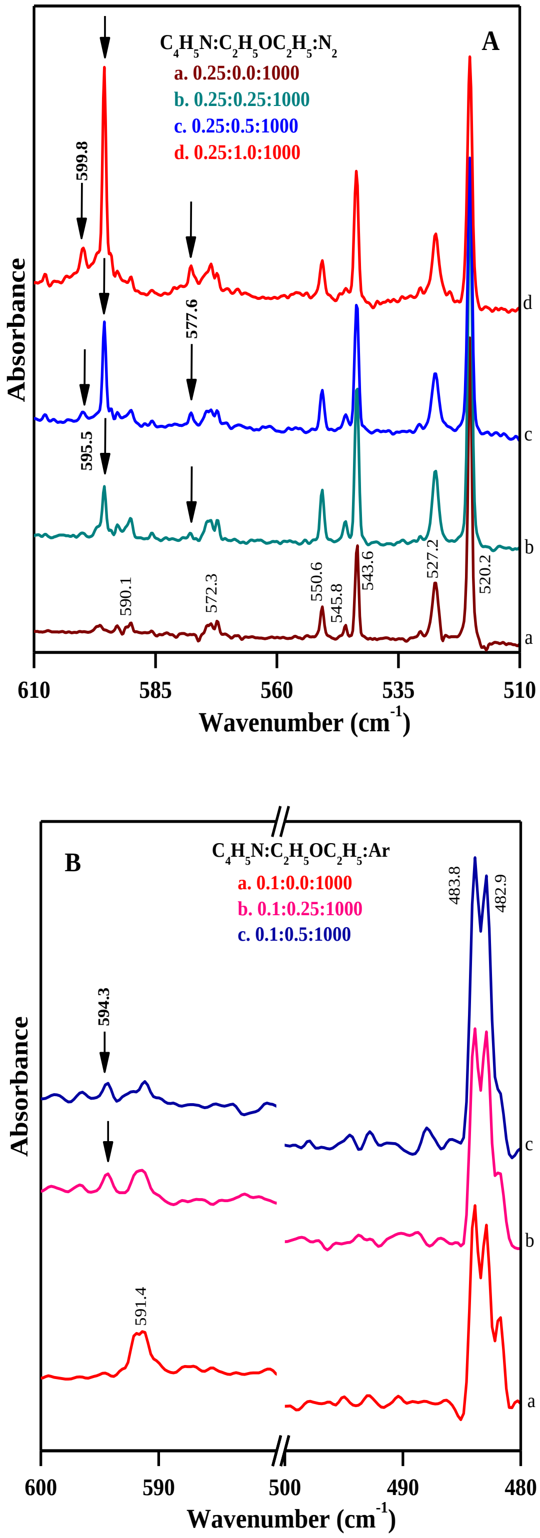

Figure 5.16 Infrared spectra of the (A) N-H bending region of C_4H_5N in N_2 and (B) N-H bending region of C_4H_5N in Ar matrixes. All the spectra shown here were annealed at 30 K (N_2) and 35 K (Ar).

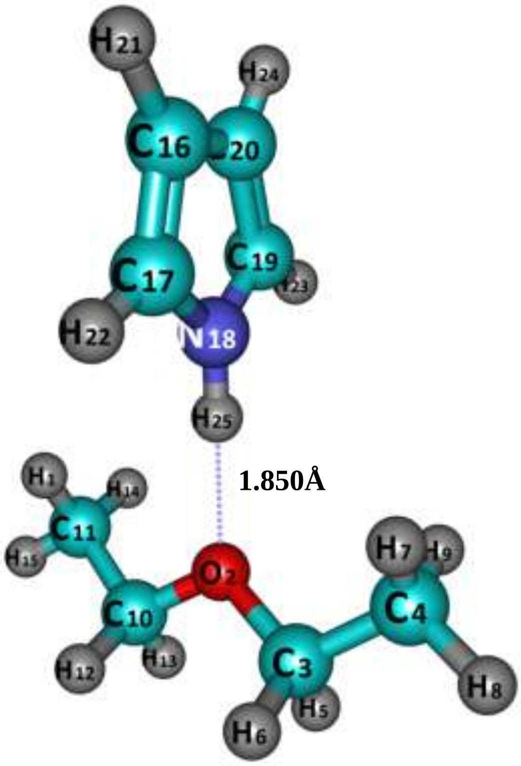

C$_4$H$_5$N-DEE-*tt*

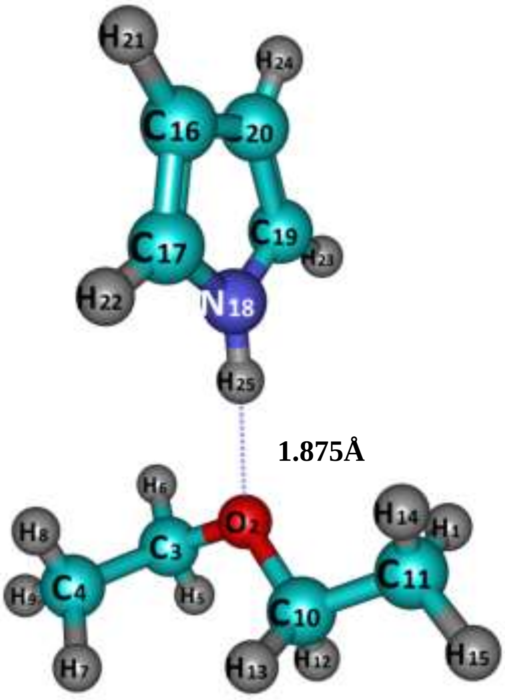

C$_4$H$_5$N-DEE-*tg*$^\pm$

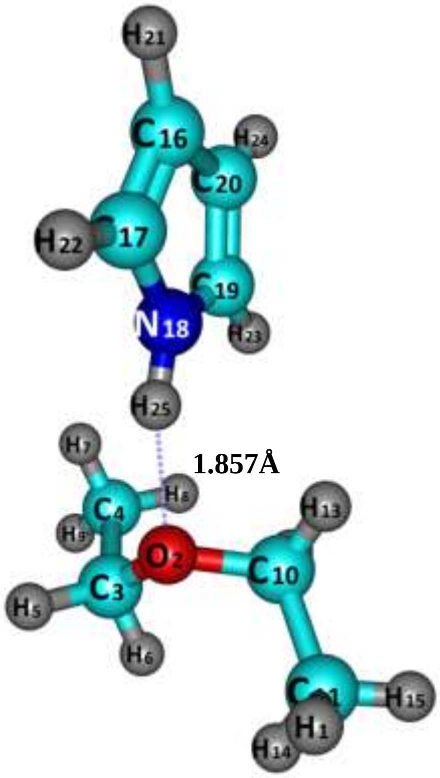

C$_4$H$_5$N-DEE-*g*$^\pm$*g*$^\pm$

Figure 5.17 Structures of the C$_4$H$_5$N-DEE-*tt*, C$_4$H$_5$N-DEE-*tg*$^\pm$ and C$_4$H$_5$N-DEE-*g*$^\pm$*g*$^\pm$ heterodimers computed at MP2/aug-cc-pVDZ level of theory.

the new features observed experimentally in both matrixes are assigned to C_4H_5N-DEE-*tt* and C_4H_5N-DEE-*tg*$^{\pm}$ heterodimers.

5.2.4.6 Vibrational Assignments in C-O-C stretching region of DEE

Figure 5.16 grids C and D show the C-O-C stretching region of DEE in N_2 and Ar matrixes, respectively, covering the region 1140 to 1110 cm^{-1}. Figure 5.16 trace 'a' represents the C_4H_5N alone spectrum in these matrixes. As discussed earlier, the *tt* and *tg*$^{\pm}$ conformers of DEE appear as site split features at 1127.8, 1126.1 cm^{-1} and 1119.9, 1123.7 cm^{-1} in N_2 and the corresponding features in Ar matrix are observed at 1133.4, 1131.9 and 1127.1, 1124.9 cm^{-1} respectively. The features observed at 1117.6, 1116.0 cm^{-1} in N_2 matrix, and 1121.1, 1119.2 cm^{-1} in Ar matrix, are probably due to DEE-H_2O heterodimer, since water is an inevitable impurity in matrix isolation experiments. Computations were performed at MP2/aug-cc-pVDZ level of theory for the DEE-H_2O heterodimers. A computed red-shift of -23.0 cm^{-1} compares with the experimental red-shift of -10.2 and -12.5 cm^{-1} in N_2 and Ar matrixes, respectively for the DEE-*tt*-H_2O heterodimer. We could not observe any new experimental feature for the DEE-*tg*$^{\pm}$-H_2O heterodimer in both Ar and N_2 matrixes, for which the computations showed a red-shift of -13.2 cm^{-1}. When the concentration of C_4H_5N was varied and the matrix was annealed, new features started appearing at 1113.8 and 1110.7 cm^{-1} in N_2 matrix, and at 1117.7, 1116.3 and 1113.6 cm^{-1} in Ar matrix. Experimentally, a red-shift of -14.9 and -18.3 cm^{-1} in N_2 and Ar matrixes, respectively, from the monomer absorption compares well with the computed red-shift of -24.3 cm^{-1} of the C_4H_5N-DEE-*tt* heterodimer. In Ar matrix, additional features were observed at 1117.7 and 1116.3 cm^{-1} with a shift of -10.1 cm^{-1}, which correlates well with the computed red-shift of -13.6 cm^{-1} of the C_4H_5N-DEE-*tg*$^{\pm}$ heterodimer. The C_4H_5N-DEE-*tg*$^{\pm}$ heterodimer feature could not be discerned in N_2 matrix.

5.2.5 Atoms-in-Molecules Analysis

AIM analysis [30-33] was performed on the 1:1 C_4H_5N-H_2O (PW-A and PW-B), C_4H_5N-CH_3OH (PM-A and PM-B), C_4H_5N-C_6H_5OH (PP-A, PP-B and PP-C) and C_4H_5N-$C_2H_5OC_2H_5$ (C_4H_5N-DEE-*tt* and C_4H_5N-DEE-$tg^{\pm}$) to understand the hydrogen bond properties in these heterodimers. According to AIM theory, a (3,-1) BCP is considered to be an essential criterion for the existence of a bond between two molecules. In fact, BCPs were found between the heterodimers of C_4H_5N with H_2O, CH_3OH, C_6H_5OH and $C_2H_5OC_2H_5$ indicating the formation of hydrogen bond between these precursors. The molecular graphs shown in Figure 5.18 illustrate the presence of BCPs in these heterodimers. The electron densities $\rho(r_c)$, and their Laplacian $\nabla^2\rho(r_c)$ at the BCP computed at MP2/aug-cc-pVDZ level of theory for the heterodimers are listed in Table 5.12. The magnitudes of the values of $\rho(r_c)$, and $\nabla^2\rho(r_c)$ at the BCP are used to distinguish between the shared and closed-shell (non-covalent) interactions. As can be seen from the table, the values of the $\rho(r_c)$ at the bond critical points for all the heterodimers are of the order of 10^{-2} au and $\nabla^2\rho(r_c)$ are positive, which are typical of closed shell interactions. In contrast, the BCP's of the neighboring bonds (which do not involve in hydrogen bonding) exhibit characteristic covalent interactions. The high positive and negative values of $\rho(r_c)$ and $\nabla^2\rho(r_c)$, respectively, clearly confirm the shared nature of the interactions in the neighboring bonds.

Interestingly, the magnitude of $\rho(r_c)$ values at the BCP increases in the order PP-C<PW-A<PM-A<C_4H_5N-DEE-*tt*≈C_4H_5N-DEE-$tg^{\pm}$ for the N-H···O heterodimers, which is consistent with the increase of N-H bond length and the corresponding increase in the red-shift of the N-H stretching wavenumber of C_4H_5N submolecule. In the C_4H_5N-C_6H_5OH PP-A heterodimers, the primary interaction being O-H···π, the electron density (ρ) was more than that at the secondary interaction C-H···π. For the heterodimer PP-B,

Table 5.11 Comparison of Shift in the Experimental Vibrational Wavenumbers in N_2 and Ar Matrixes with the Computed Wavenumbers of the 1:1 C_4H_5N-DEE (*tt* and *tg*$^{\pm}$) Heterodimers at MP2/aug-cc-pVDZ Level of Theory.

Computed[a] ν (cm^{-1})		**Experimental ν (cm^{-1})**				**Mode Assignment**
ν	**$\Delta\nu$[b]**	**N_2**		**Ar**		
		ν	**$\Delta\nu$[b]**	**ν**	**$\Delta\nu$[b]**	
C_4H_5N						
514.9(58)	-	527.2/520.2	-	483.8/482.9	-	N-H bending
3672.4(76)	-	3513.8/3508.9	-	3523.3/3521.6/ 3520.2	-	N-H stretching
DEE-*tt*						
1151.6(199)	-	1127.8/1126.1	-	1133.4/1131.9	-	C-O-C stretching
C_4H_5N-DEE-*tt*						
1127.3(172)	-24.3	1113.8/1110.7	-14.9[c]	1113.6	-18.3	C-O-C stretching
604.9(8)	90.0	595.5/599.8	72.0[c]	594.3	111.0	N-H bending
3424.6(800)	-249.6	3361.0/3355.8	-154.0[c]	3359.4/3355.0/ 3353.6	-165.7[c]	N-H stretching
DEE-*tg*$^{\pm}$						
1149.8(134)	-	1119.9/1123.7	-	1127.1/1124.9	-	C-O-C stretching
C_4H_5N-DEE-*tg*$^{\pm}$						
1136.2(112)	-13.6	-[d]	-	1117.7/1116.3	-10.1[c]	C-O-C stretching
607.3(9)	92.4	595.5/599.8	72.0[c]	594.3	111.0	N-H bending
3437.7(727)	-236.5	3331.4/3329.0	-181.8[c]	3350.2	-171.5	N-H stretching

[a] Intensity in km mol^{-1} is given in parenthesis.

[b] $\Delta\nu = \nu_{heterodimer} - \nu_{monomer}$

[c] Average of multiplet experimental wavenumbers of the monomers and Py-DEE heterodimers were taken to compute the experimental shift.

[d] Experimental features were not observed.

primary interaction was π···π* stacking apart from the N-H···π bonding, where the ρ-value of former was higher than the later. Similarly, the heterodimer PP-C has two types of hydrogen bonding, the N-H···O type of H-bond being stronger than the C-H···π as reflected from the ρ-value.

5.2.6 Natural Bond Orbital Analysis

NBO is a useful theoretical method to characterize the nature of interactions existing in the heterodimers. In the hydrogen bonded heterodimers, the contribution of charge transfer hyperconjugative interaction is substantial, which induces a bond elongation with a concomitant red-shift in the vibrational wavenumber of the proton donor. Table 5.13 lists the electron occupancies of the important molecular orbitals, donor-acceptor delocalization interactions and the second order perturbation E_2 energies of pyrrole with water, methanol, diethyl ether and phenol heterodimers computed at MP2/aug-cc-pVDZ level of theory. As can be seen from the table that the electron occupancies of the donor orbitals decrease with a concomitant increase in the acceptor antibonding orbitals of the N-H···O heterodimers (PW-A, PM-A and PDME) and O-H···π heterodimers (PW-B, PM-B), but the magnitude of change in electron occupancies of the donor and acceptor orbitals is lesser in the latter than in the former heterodimers. Furthermore, the second order perturbation E_2 energies for the hyperconjugative interaction of the N-H···O heterodimers increase in the order PW-A<PM-A<PDME, which correlates well with the shift in the N-H stretching and bending mode of C_4H_5N submolecule in the heterodimers. The magnitude of E_2 energies of the N-H···O heterodimers (PW-A, PM-A, PDME) are significantly larger than the O-H···π heterodimers (PW-B, PM-B), clearly showing that the hyperconjugative interactions are stronger in the former than the latter. It was also observed that, if %Δs decreases with the associated increase in %Δp character for

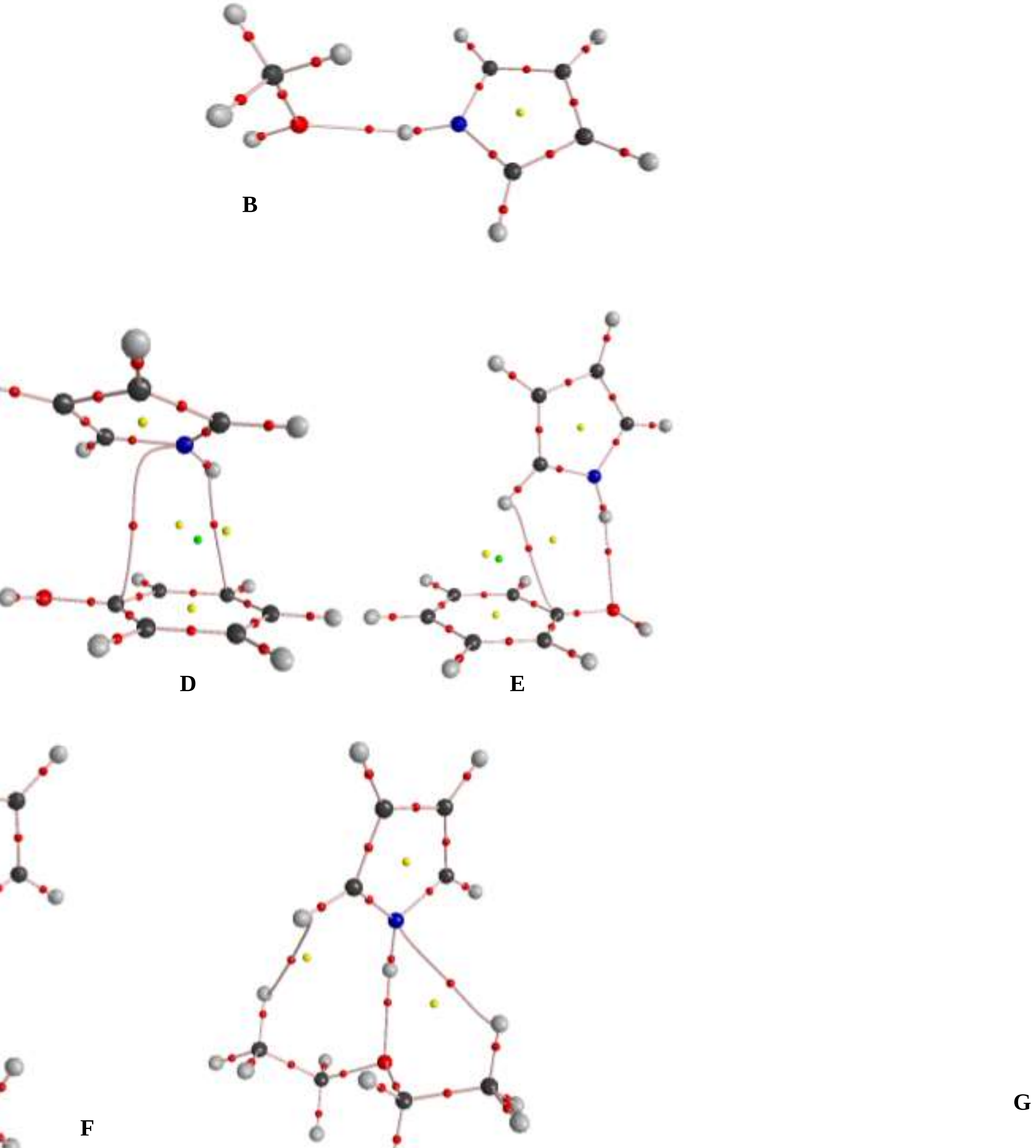

Figure 4.18 Structures showing the bond critical points (BCP in red), ring critical points (RCP, in yellow) and cage critical points (CCP, in green) obtained from topological AIM analysis. (A) PW-A, (B) PM-A, (C) PP-A, (D) PP-B, (E) PP-C, (F) C_4H_5N-DEE-*tt* and (G) C_4H_5N-DEE-*tq*$^{\pm}$.

Table 5.12 Properties of (3,-1) bond critical points (BCPs) of heterodimers of C_4H_5N with H_2O, CH_3OH, C_6H_5OH and $(C_2H_5)_2O$ computed at MP2/aug-cc-pVDZ Level of Theory.

Heterodimer		**$\rho(r_c)$**	**$\nabla^2\rho(r_c)$**	**λ_1**	**λ_2**	**λ_3**
#PW-A		0.0228	0.0834	-0.0293	-0.0285	0.1413
#PM-A		0.0259	0.0952	-0.0372	-0.0347	0.1722
***PP-A**	O-H···π	0.0151	0.0366	-0.0143	-0.0071	0.0581
	C-H···π	0.0112	0.0355	-0.0089	-0.0041	0.0486
PP-B	N-H···π	0.0082	0.0251	-0.0052	-0.0018	0.0322
	π···π*	0.0106	0.0306	-0.0042	-0.0015	0.0364
PP-C	N-H···O	0.0166	0.0517	-0.0186	-0.0166	0.0870
	C-H···π	0.0078	0.0270	-0.0040	-0.0007	0.0318
#C_4H_5N-DEE-*tt*		0.0337	0.1092	-0.0481	-0.0476	0.2049
#C_4H_5N-DEE-*tg*$^{\pm}$		0.0317	0.1023	-0.0438	-0.0433	0.1894

These heterodimers are purely N-H···O only.

* These heterodimers have multiple interactions which are specified in the adjacent column.

the non-bonding orbital as a result of complexation, the hyperconjugative delocalization increases. As the %p character increases, which makes the non-bonding orbital of oxygen atom more diffuse, thereby facilitating a facile overlap with antibonding N-H orbital of pyrrole sub-molecule with the corresponding increase in E_2 energy in the N-H···O heterodimers.

For C_4H_5N-C_6H_5OH heterodimer PP-A, the hyperconjugative interaction was between the π-electron cloud of C_4H_5N [π(C17-C18)] to the antibonding orbital [σ*(O12-H13)] of C_6H_5OH. The E_2 energy of this interaction is 6.33 kcal mol^{-1}. Furthermore, due to this interaction, there is a reduction in the occupancies of electrons in the donor π-orbital of C_4H_5N and a marginal increase in the occupancies of electrons in the acceptor σ*(O12-H13) orbital of C_6H_5OH. The increase in electron density at the antibonding orbital elongates the O-H bond with an associated red-shift in the vibrational wavenumber of C_6H_5OH sub-molecule in the O-H···π heterodimer PP-A. Furthermore, in the same heterodimer there is another hyperconjugative interaction between π(C14-C15) electron cloud of C_4H_5N with the antibonding orbital of σ*(C9-H10) of C_6H_5OH and the E_2 energy is 2.82 kcal mol^{-1}. This interaction also exhibits a change in the electron occupancies of the donor and acceptor orbitals. Due to these hyperconjugative interactions between the C_6H_5OH with C_4H_5N molecules, the geometry of the C_6H_5OH molecule is tilted and favors the synergistic interaction and the experimental shift supports the formation of the heterodimer in the matrix (Figure 5.19).

For the C_4H_5N-C_6H_5OH PP-B heterodimer, the maximum delocalization E_2 energy (2.55 kcal mol^{-1}) was observed for a unique π···π* interaction between π(C2-C6) and π(C7-C9) of C_6H_5OH to the antibonding orbitals of π*(C14-C15) and π*(C17-C18) of C_4H_5N, respectively; similarly, there is an interaction between the π-electrons π(C14-C15) and π(C17-C18) of C_4H_5N to the π*(C2-C6) and π*(C7-C9) antibonding orbital of C_6H_5OH,which makes the C_4H_5N parallel displaced to the plane of the C_6H_5OH molecule.

Table 5.13 Electron occupancies of various NBOs of C_4H_5N-H_2O (PW-A, PW-B), C_4H_5N-CH_3OH (PM-A, PM-B), C_4H_5N-CH_3OCH_3 (PDME), C_4H_5N-$C_2H_5OC_2H_5$ and C_4H_5N-C_6H_5OH (PP-A, PP-B, PP-C) heterodimers computed at MP2/aug-cc-pVDZ Level of Theory. The donor-acceptor delocalization interaction and second order perturbation energies (E_2, kcal mol^{-1}) are also shown.

Hetero dimers	NBO	Occupancy	Donor-acceptor delocalization interaction	E_2
PW-A	σ*(N3-H10)	0.02559(0.01370)	n1O11→σ*(N3-H10)	13.04
	σ(O11-H12)	1.99787(1.99918)		
	n2O11	1.99595(1.99748)	n2O11→σ*(N3-H10)	0.09
	n1O11	1.98359(1.99591)		
PW-B	π(C1-C2)	1.85770(1.86030)	π(C1-C2)→σ* (O11-H13)	3.71
	σ(O11-H13)	1.99854(1.99918)		
	n2O11	1.99569(1.99748)		
PM-A	σ*(N3-H10)	0.02686(0.01370)	n1O11→σ*(N3-H10)	9.15
	σ(O11-H12)	1.99132(1.99138)		
	n1O11	1.97415(1.98834)	n2O11→σ*(N3-H10)	4.60
	n2O11	1.97299(1.97244)		
PM-B	σ(O11-H12)	1.99148(1.99138)	π(C4-C5)→σ*(O11-H12)	4.73
	π(C4-C5)	1.85597(1.86030)		
	n2O11	1.96980(1.97244)		
PDME	σ*(N11-H19)	0.03393(0.01370)	n1O1→σ*(N12-H19)	4.15
	σ(O1-C2)	1.99388(1.99413)		
	n1O1	1.97058 (1.97606)	n2O1→σ*(N12-H19)	11.54
	n2O11	1.93637(1.94389)		
PP-A	σ*(O12-H13)	0.01711(0.00554)	π(C17-C18)→σ*(O12-H13)	6.33
	π(C17-C18)	1.85196(1.86030)		
	σ*(C9-H10)	0.01388(0.01034)	π(C14-C15)→σ*(C9-H10)	2.82
	π(C14-C15)	1.85420(1.86030)		
PP-B	π(C1-C3)	1.70123(1.69101)	π(C1-C3)→σ*(N16-H23)	1.22
	σ*(N16-H23)	0.01797(0.01370)	π(C2-C6)→σ*(N16-H23)	0.16
	π(C2-C6)	1.67498(1.68104)	π(C2-C6)→π*(C14-C15)	0.59
	π(C7-C9)	1.63539(1.66061)	π(C7-C9)→π*(C17-C18)	0.95
	π*(C14-C15)	0.31197(0.31218)	π(C14-C15)→π*(C2-C6)	0.49
	π*(C17-C18)	0.31526(0.31218)	π(C14-C15)→π*(C7-C9)	0.38
	π(C14-C15)	1.86030(1.85953)	π(C17-C18)→π*(C7-C9)	0.08
	π(C17-C18)	1.86030(1.85828)	π(C17-C18)→π*(C2-C6)	0.06
	π*(C2-C6)	0.34766(0.33769)		

	π*(C7-C9)	0.34996(0.36275)		
PP-C	n1(O12)	1.98277(1.98413)	n1(O12)→σ*(N16-H23) n2(O12)→σ*(N16-H23)	1.01 3.91
	n2(O12)	1.92157(1.92043)		
	σ*(N16-H23)	0.02005(0.01370)		
	π(C2-C6)	1.67351(1.68104)	π(C2-C6)→σ*(C15-H20)	1.00
	π(C1-C3)	1.68011(1.69101)	π(C1-C3)→σ*(C15-H20)	0.44
	σ*(C15-H20)	0.01145(0.00996)	π(C7-C9)→σ*(C15-H20)	0.17
	π(C7-C9)	1.66490(1.66065)	π(C1-C3)→ π*(C14-C15)	0.23
	π*(C14-C15)	0.31247(0.31218)	π(C7-C9)→ π*(C14-C15)	0.20
C_4H_5N-DEE-*tt*	n1O2	1.97039(1.97578)	n1O2→ σ*(N18-H25)	3.82
	n2O2	1.93342(1.94357)		
	σ*(N18-H25)	0.03854(0.01370)	n2O2→ σ*(N18-H25)	13.90
C_4H_5N-DEE-*tg*±	n1O2	1.96806(1.97379)	n1O2→ σ*(N18-H25)	3.99
	n2O2	1.93577(1.94476)		
	σ*(N18-H25)	0.03715(0.01370)	n2O2→ σ*(N18-H25)	12.89

The charge transfer hyperconjugative interaction between the π(C1-C3) of C_6H_5OH to the σ*(N16-H23) of C_4H_5N is 1.22 kcal mol^{-1}, inducing a red-shift in the N-H stretching vibrational wavenumber of C_4H_5N submolecule in the N-H···π PP-B heterodimer. In this heterodimer, the synergistic interaction between the two molecules changes the geometry and the experimental shift supports the formation in the matrix.

In C_4H_5N-C_6H_5OH PP-C heterodimer, the delocalization interaction is between the non-bonding orbitals of oxygen of C_6H_5OH to the N-H antibonding orbitals of C_4H_5N [n^2(O12)→σ*(N16-H23) and n^1(O12)→σ*(N16-H23)], the E_2 energy of these interactions are 1.01 and 3.91 kcal mol^{-1}, respectively. In addition to this interaction, there is another charge transfer interaction between π(C2-C6), π(C1-C3) and π(C7-C9) of C_6H_5OH to the antibonding orbital of σ*(C15-H20) of C_4H_5N submolecule. The increase in the electron occupancy of the σ*(N16-H23) orbital, causes the N-H bond to elongate with a corresponding red-shift of the N-H stretching wavenumber of C_4H_5N sub-molecule in the PP-C heterodimer. The difference in contribution of delocalization energy of the lone pairs of oxygen atom in C_6H_5OH is probably due to the different spatial orientations of the lone pair orbitals. The n^1(O12)→σ*(N16-H23) is an axial overlap whereas, n^2(O12)→σ*(N16-H23) is a lateral overlap; the former giving the highest interaction due to more facile interaction between the orbitals are observed in the previous systems (Figure 5.19).

Table 5.13 lists the electron occupancies of the important molecular orbital, donor-acceptor delocalization interactions and second order E_2 energies of C_4H_5N-DEE-*tt* and C_4H_5N-DEE-$tg^{\pm}$ heterodimers, computed at MP2/aug-cc-pVDZ level of theory. In both heterodimers, there is a charge transfer interaction from the non-bonded electrons on oxygen [n^1O2 and n^2O2] to the antibonding acceptor orbital of σ*(N18-H25) of C_4H_5N. Consequently, the electron occupancies of the donor orbital decrease while that of the acceptor orbital increase. Due to this hyperconjugative interaction, the N-H bond length increases and the corresponding red-shift in the N-H stretching vibrational wavenumber increases. It is clear from the table that the E_2 energy of the C_4H_5N-DEE-*tg*$^\pm$ is marginally higher than that of C_4H_5N-DEE-*tt* and the corresponding N-H shift is higher for the former heterodimer than the latter.

Figure 5.19 shows the natural bond orbital diagram using NBO 6.0 [35-38] for the overlap between the non-bonded electrons of oxygen [n^1O2 and n^2O2] of H_2O, CH_3OH, CH_3OCH_3, C_6H_5OH and DEE (*tt and tg*$^\pm$) with σ*(N18-H25) of C_4H_5N in the respective heterodimers and the corresponding E_2 energies.

5.2.7 Energy Decomposition Analysis

The ED analysis was performed to identify the dominant interactions in stabilizing the C_4H_5N-H_2O, C_4H_5N-CH_3OH, C_4H_5N-CH_3OCH_3, C_4H_5N-$C_2H_5OC_2H_5$ and C_4H_5N-C_6H_5OH dimers (Figure 5.20). Table 5.14 5.14 tabulates the results of the ED analysis for the above heterodimers performed using B3LYP-D3/TZ2P level of theory using ADF2016. On analyzing the dissected stabilization energies, it was found that the major energy contribution in stabilizing the N-H···O heterodimers is from the electrostatic forces of attraction which increases in the order PP-C<PW-A<PP-B<PM-A<PDME<PP-A<PDEE-tt<PDEE-tg. In each of these heterodimers, the contribution due to charge transfer interaction energies was also substantial, but the magnitude was nearly half of the electrostatic contribution and even less as in case of PP-B heterodimer. Although the contribution from dispersion interaction was minimal, yet it was higher in case of PP-B dimer owing to the partially stacked geometry resulting from the interaction of the π-electron clouds of both pyrrole and phenol. The contribution of Pauli repulsion term to the total binding energy destabilizes the heterodimer and follows the order PP-B> PDEE-tt >PDEE-tg > PP-A> PDME>PP-C>PM-A>PW-A. In case of PP-B heterodimers, which have a partially stacked geometry, the Pauli repulsion contribution is immense due to the approach of bulkier π-electron clouds of pyrrole and phenol.

5.3 Summary

The heterodimers of C_4H_5N with H_2O, CH_3OH, C_6H_5OH and $C_2H_5OC_2H_5$ (DEE) were trapped in N_2 and Ar matrixes and the spectral features were identified using infrared spectroscopy. To arrive at the optimized geometries of the heterodimers of the aforementioned systems and to correlate with the experimental vibrational wavenumber, MP2/aug-cc-pVDZ level of theory was used, which predicted two, two, three and one (for each conformer of DEE) minima for the C_4H_5N-H_2O (PW-A, PW-B), C_4H_5N-CH_3OH (PM-A, PM-B), C_4H_5N-C_6H_5OH (PP-A, PP-B, PP-C) and C_4H_5N-$C_2H_5OC_2H_5$ (py-DEE-*tt*, py-DEE-$tg^{\pm}$), respectively. Apart from C_4H_5N-C_6H_5OH heterodimer, the global and local minimum heterodimer of all other systems was stabilized by N-H···O and O-H···π interaction. Experimentally, only the global minimum structure was trapped and identified in each of these systems. In C_4H_5N-C_6H_5OH PP-A global minimum structure is stabilized by dual O-H···π and C-H···π interactions, the first local minimum PP-B with a partially stacked N-H···$\pi/\pi_N\cdots\pi^*$ interaction and then the second local minimum PP-C is strengthened by N-H···O interaction. Evidence for the formation of all the three heterodimers was found in N_2 matrix, while only PP-A heterodimer was identified in Ar matrix.

In case of C_4H_5N-$C_2H_5OC_2H_5$, computations performed at B3LYP/aug-cc-pVDZ level of theory predicted *tt*, $tg^{\pm}$ and $g^{\pm}g^{\pm}$ conformers. Experimentally, the ground state (*tt*) and higher energy ($tg^{\pm}$) conformers of DEE were trapped and identified in Ar and N_2 matrixes. Geometry optimization of C_4H_5N with *tt* and $tg^{\pm}$ conformers of DEE indicated structures with an N-H···O interaction corresponding to the py-DEE-*tt* and py-DEE-$tg^{\pm}$ heterodimers. NBO analysis of the DEE conformers showed that among the vicinal and geminal hyperconjugative interactions, the former interaction is controlling in stabilizing the conformers. In the py-DEE-*tt* and py-DEE-$tg^{\pm}$ heterodimers, the hyperconjugative interaction between the non-bonded electrons of oxygen from the bonding orbital to the antibonding orbital of the acceptor orbital (N-H) is dominant. Comparing the various computed parameters with experimental vibrational wavenumbers of the N-H···O heterodimers of C_4H_5N with C_6H_5OH, H_2O, CH_3OH, and $C_2H_5OC_2H_5$, revealed that by successively replacing the hydrogen atoms of H_2O with an alkyl group leads to the strengthening of the N-H···O hydrogen bond whereas the substitution of phenyl group weakens the interaction. Table 5.15 compares the stabilization energies, calculated and experimental vibrational shift in the N-H stretching mode of C_4H_5N, hydrogen bond distance, change in the N-H bond length, electron density at the bond critical point of N-H···O hydrogen bond and the second order perturbation energy (E_2) of the N-H···O hydrogen bonded heterodimers of C_4H_5N with H_2O, CH_3OH, $C_2H_5OC_2H_5$, and C_6H_5OH. Computations performed at the MP2/aug-cc-pVDZ level of theory predict the shifts of the $\Delta r_{\text{N-H}}$, N-H stretching wavenumber, stabilization energy and the E_2 energy increase in the order PP-C < PW-A < PM-A < py-DEE-*tt* ≈ py-DEE-*tg*$^{\pm}$. Stabilization and E_2 energies of the N-H···O heterodimers of C_4H_5N increase in the order PP-C < PW-A < PM-A < py-DEE-*tt* ≈ py-DEE-*tg*$^{\pm}$. The stronger the interaction between the oxygen of Lewis base and the acidic proton of C_4H_5N, the shorter will be the hydrogen bond distance, which correlates well with the computed results. Among the N-H···O heterodimers, PP-C shows the smallest red-shift in the N-H stretching of C_4H_5N, probably due to the participation of non-bonded lone pair of electrons of oxygen in resonance with the benzene ring. Furthermore, the hydrogen bond distance, stabilization and the E_2 energies for this heterodimer are the least, which agrees with the experimental results. The shift in the experimental vibrational wavenumbers for the N-H stretching mode follows the order PP-C < PW-A < PM-A < py-DEE-*tt* ≈ py-DEE-*tg*$^{\pm}$ in Ar matrix while the trend in the N_2 matrix is PP-C < PW-A < py-DEE-*tt* ≈ py-DEE-*tg*$^{\pm}$ < PM-A. In each of the cases, a good agreement was observed between the experimental wavenumber with computed shift in Ar matrix, whereas a small deviation is observed for the PM-A heterodimer in N_2 matrix, which could probably due to perturbations of the matrix on the different modes in the heterodimers are different.

Table 5.14 Energy Decomposition Analysis of the 1:1 heterodimers of Pyrrole with Water, Methanol, Dimethyl ether and Diethyl ether, computed using B3LYP-D3/TZ2P Level of Theory.

Systems	Electrostatics	Pauli Repulsion	Charge Transfer	Dispersion	Total
PW-A	-7.65	6.5	-3.37	-0.99	-5.51
PM-A	-9.23	8.76	-4.04	-2.07	-6.57
PDME	-9.65	10.81	-5.18	-2.84	-6.86
PP-A	-9.71	13.05	-5.20	-5.27	-7.13
PP-B	-9.15	15.48	-3.73	-7.49	-4.88
PP-C	-6.16	9.5	-3.42	-5.17	-5.25
Py-DEE-*tt*	-11.58	14.26	-6.32	-4.56	-8.2
Py-DEE-*tg*$^{\pm}$	-11.93	14.71	-6.19	-4.94	-8.35

Table 5.15 Comparison of some selected computed parameters of C_4H_5N with H_2O, CH_3OH, $C_2H_5OC_2H_5$ and C_6H_5OH with Experimental Shift in N_2 and Ar Matrixes. Computations were performed at MP2/aug-cc-pVDZ Level of Theory.

Heterodimers	$^{a}\Delta\nu_{N\text{-}Hstr}$	$^{b}\Delta\nu_{N\text{-}Hstr(N_2)}$	$^{c}\Delta\nu_{N\text{-}Hstr(Ar)}$	$^{d}d_{N\text{-}H\cdots O}$	$^{e}\Delta r_{N\text{-}H}$	$^{f}\Delta S.E.$	$^{g}E_2$	$^{h}\rho_{bcp}$
PP-C	-56.7	-103.6	-	2.166	0.328	-5.55	7.19	0.0167
PW-A	-106.7	-128.2	-111.6	1.959	0.601	-5.04	13.13	0.0228
PM-A	-125.6	-163.6	-122.0	1.916	0.723	-6.00	13.75	0.0256
Py-DEE-*tt*	-249.6	-154.0	-165.7	1.850	1.269	-7.12	19.41	0.0337
Py-DEE-*tg*±	-236.5	-181.8	-171.5	1.875	1.233	-7.28	17.71	0.0316

[a] $\Delta\nu_{N\text{-}H(calc)} = \nu_{N\text{-}H(heterodimer)} - \nu_{N\text{-}H(monomer)}$ at MP2/aug-cc-pVDZ.
[b] $\Delta\nu_{N\text{-}H}$ (N_2) = $\nu_{N\text{-}H(heterodimer)} - \nu_{N\text{-}H(monomer)}$ in N_2 matrix in cm^{-1}.
[c] $\Delta\nu_{N\text{-}H}$ (Ar) = $\nu_{N\text{-}H(heterodimer)} - \nu_{N\text{-}H(monomer)}$ in Ar matrix cm^{-1}.
[d] Hydrogen Bond distance (Å).
[e] $\Delta r_{(N\text{-}H)} = r_{heterodimer} - r_{monomer}$ (picometer)
[f,] S.E. (BSSE) = Basis set superposition error corrected stabilisation energy in kcal mol^{-1}.
[g] E_2 = Second order perturbation energy in kcal mol^{-1} obtained from NBO Analysis.
[h] Electron Density in a. u. obtained from AIM Analysis.

A 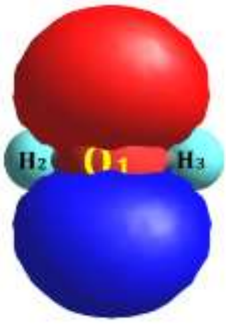	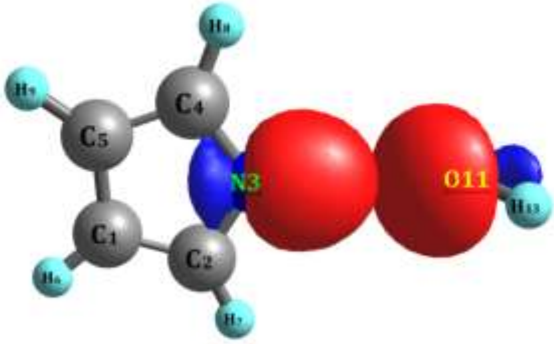
n^{1}O11	**n^{1}O11→σ*(N3-H10); E^2=13.04**
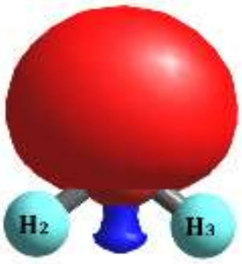	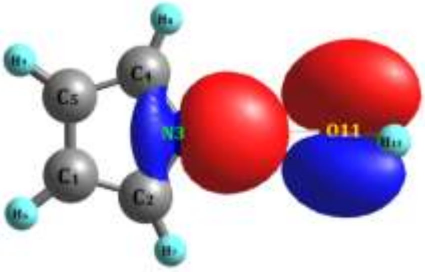
n^{2}O11	**n^{2}O11→σ*(N3-H10); E^2=0.09**
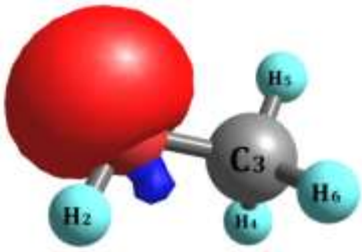 **B**	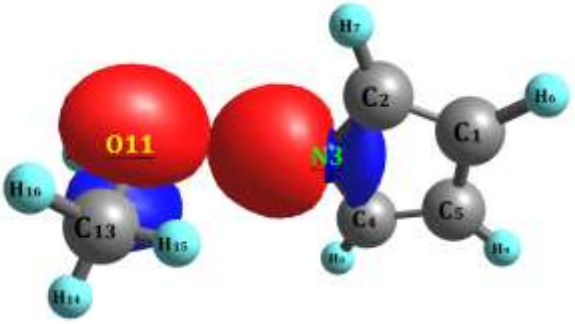
n^{1}O11	**n^{1}O11→σ*(N3-H10); E^2=9.15**
	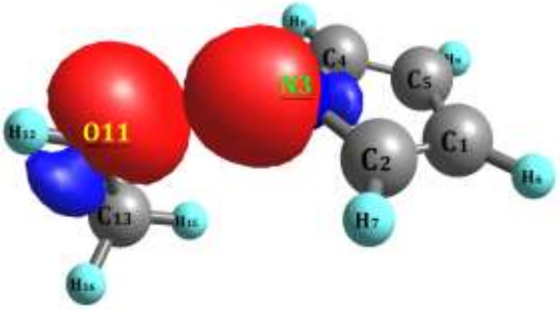
n^{2}O11	**n^{2}O11→σ*(N3-H10); E^2=4.60**

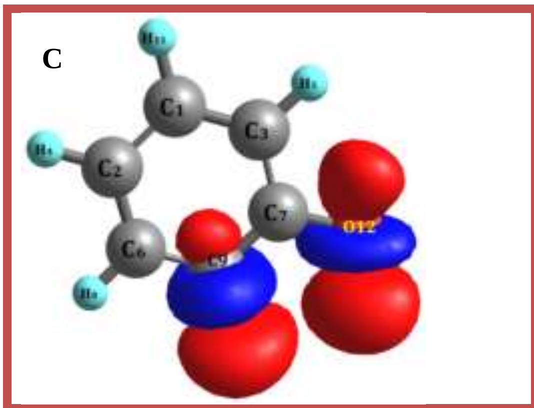	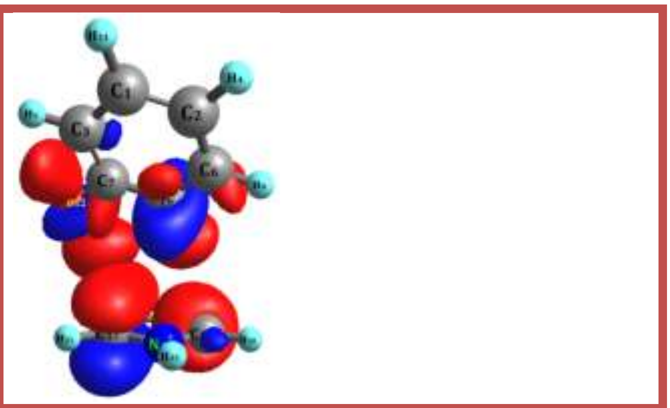
σ*(O12-H13) and σ*(C9-H10)	**π(C17-C18)→σ*(O12-H13); E^2=6.33** **π(C14-C15)→σ*(C9-H10); E^2=2.82**
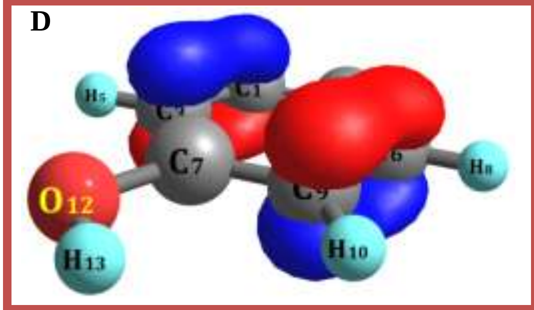	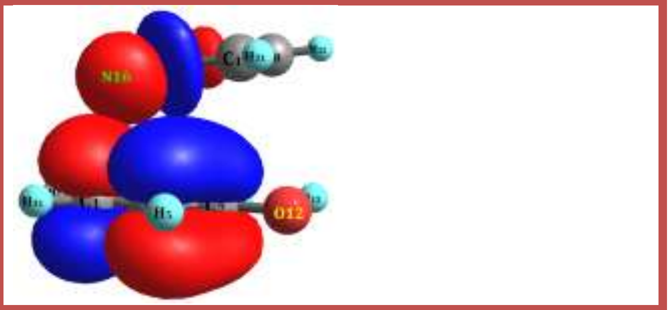
π(C1-C3) and π(C2-C6)	**π(C1-C3)/π(C2-C6)→σ*(N16-H23); E^2=1.38**
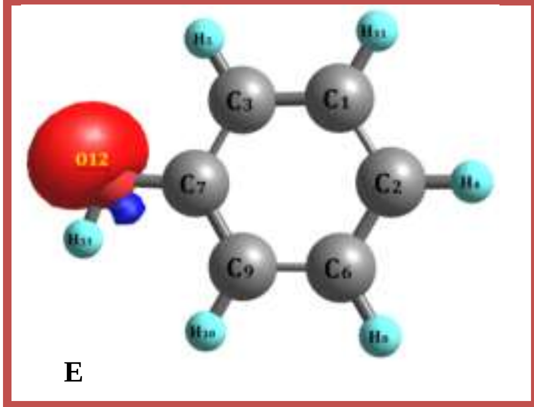	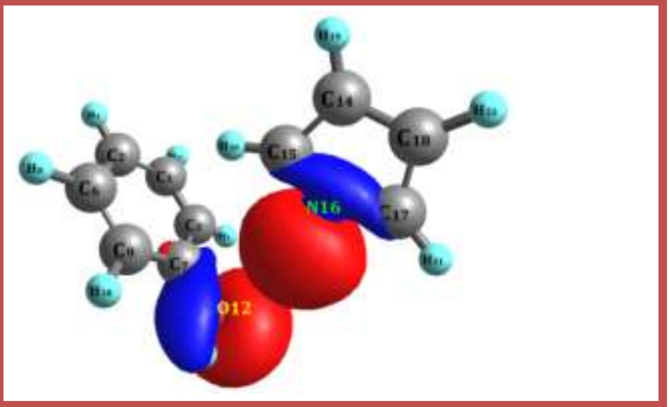
n^1O11	**n^1(O12)→σ*(N16-H23); E^2=1.01**
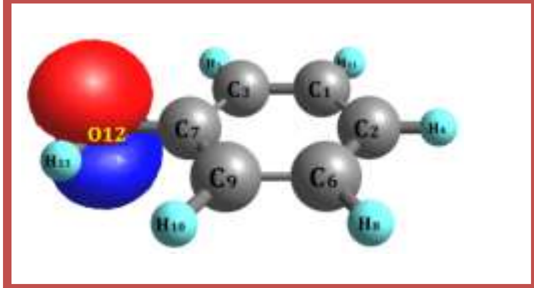	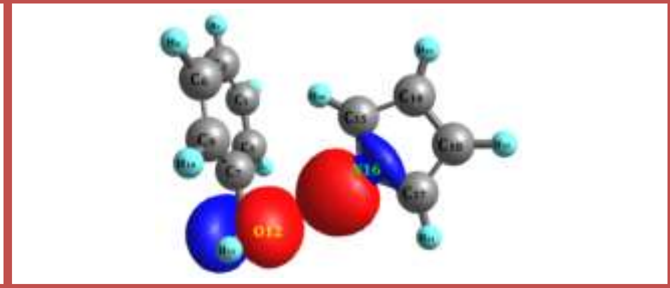
n^2O11	**n^2(O12)→σ*(N16-H23); E^2=3.91**

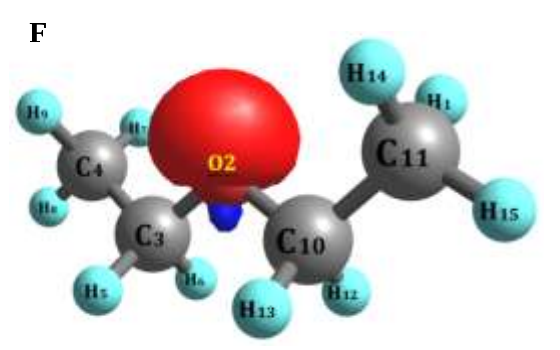

n^{1}O11

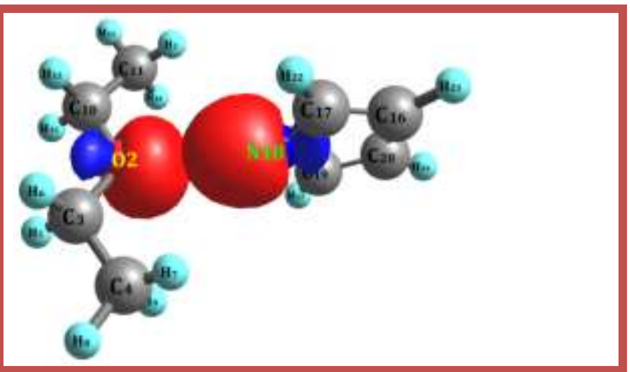

n^{1}O2→σ*(N18-H25); E^2=3.82

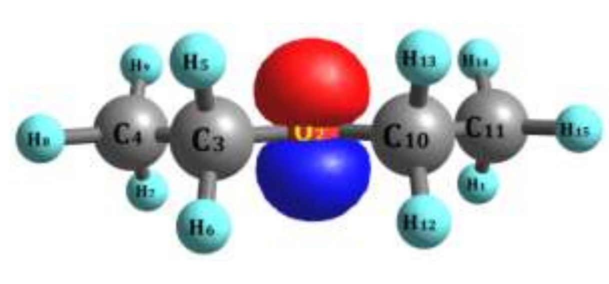

n^{2}O11

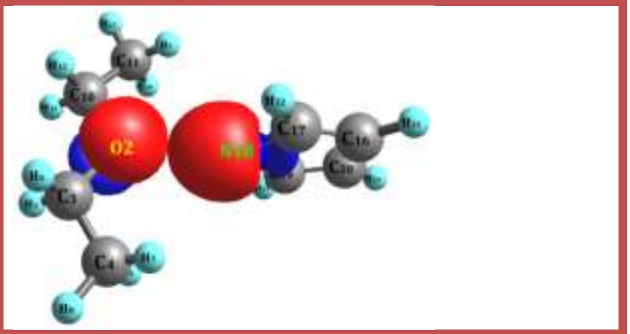

n^{2}O2→σ*(N18-H25); E^2=13.90

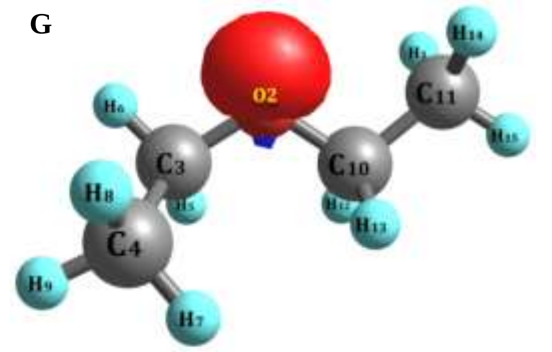

n^{1}O11

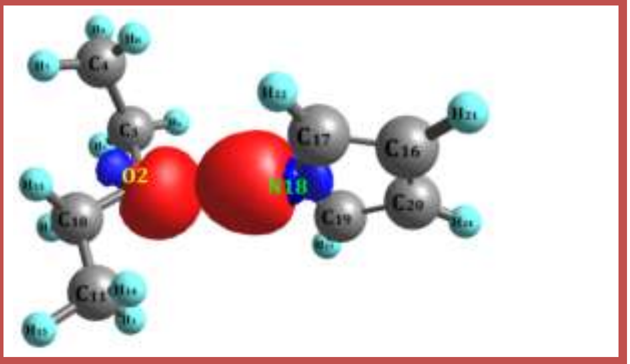

n^{1}O2→ σ*(N18-H25); E^2=3.99

n^{2}O11

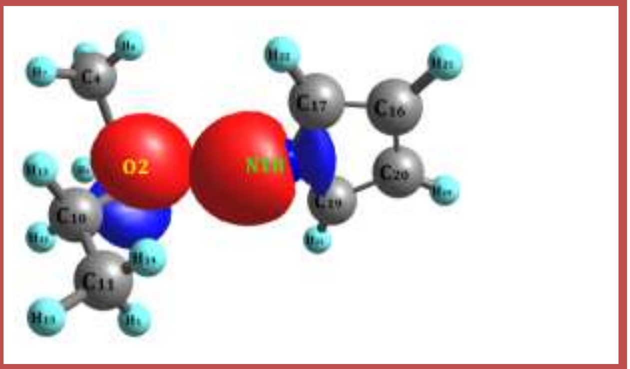

n^{2}O2→ σ*(N18-H25); E^2= 12.89

Figure 5.19 NBO diagrams of water, methanol, phenol and diethyl ether (*tt* and *tg*$^{\pm}$) along with the corresponding heterodimers with pyrrole: (A) PW-A, (B) PM-A (C) PP-A, (D) PP-B, (E) PP-C, (F) C_4H_5N-DEE-*tt* and (G) C_4H_5N-DEE-*tg*$^{\pm}$. The delocalization energies for the interactions are given in kcal mol^{-1}.

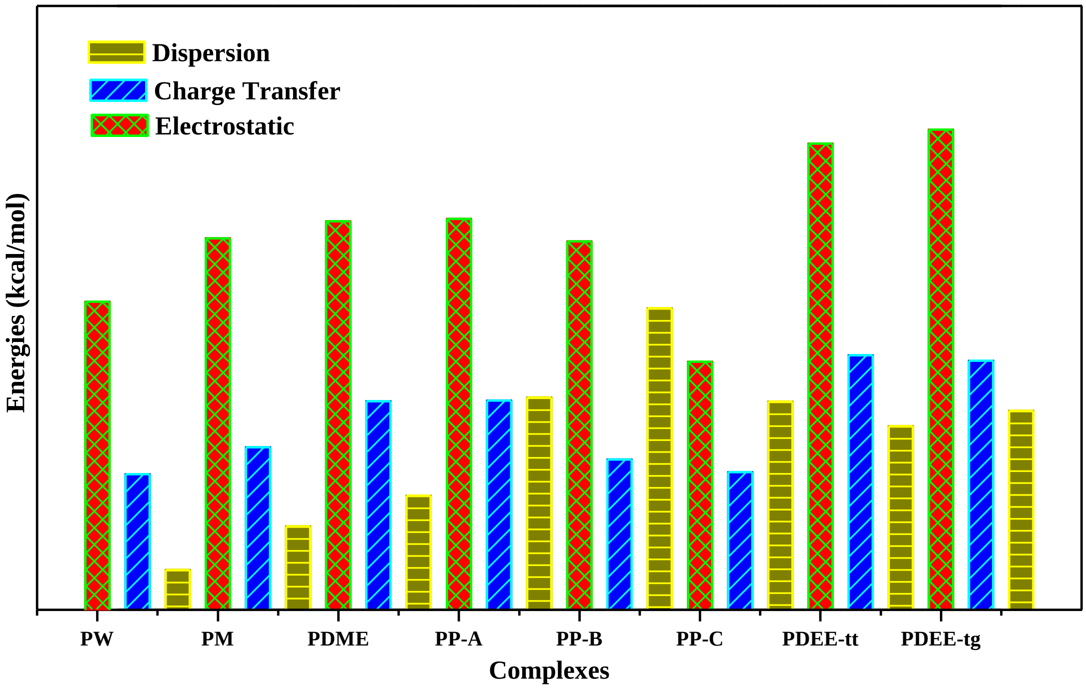

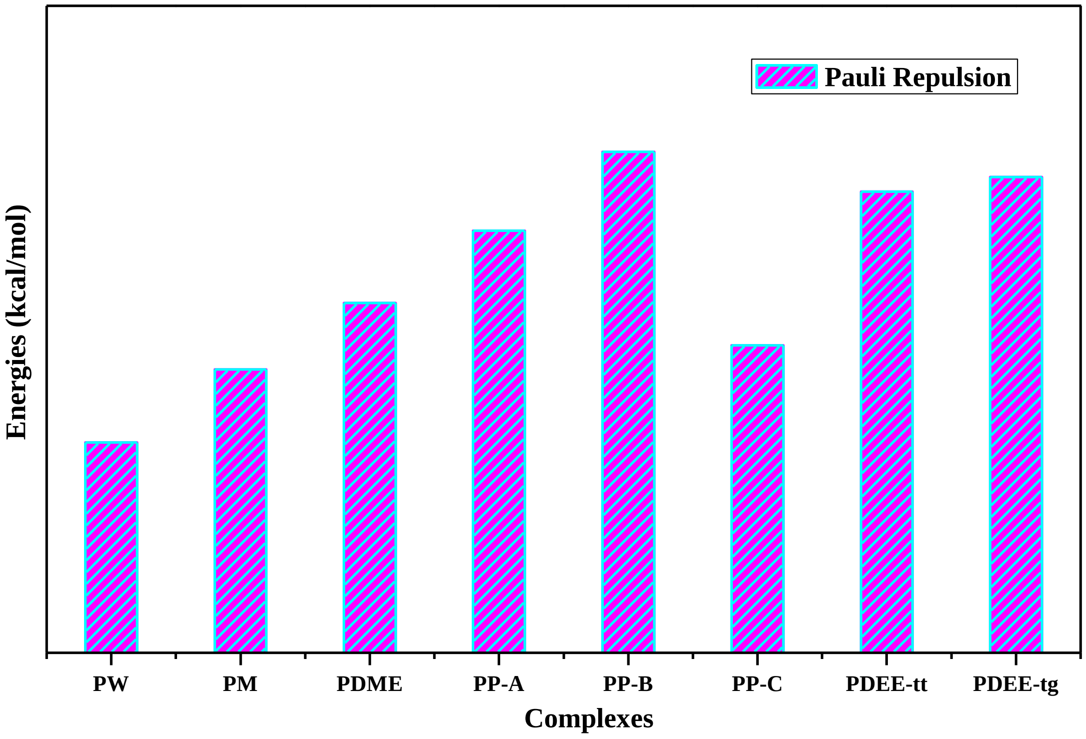

Figure 5.20 Bar graph showing the electrostatic, charge transfer, dispersion and Pauli repulsion contribution to the total binding energy of the C_4H_5N with water (PW), methanol (PM), dimethyl ether (PDME), phenol (PP-A, PP-B, PP-C), and diethyl ether (PDEE-*tt*, PDEE-*tg*$^{\pm}$) heterodimers computed at B3LYP-D3/TZ2P level of theory.

References

---

1. Studies of intermolecular interactions by matrix isolation vibrational spectroscopy: Self-association of water, R.M. Bentwood A. J. Barnes, W. J. Orville-Thomas, *J. Mol. Spec.*, **1980**, 84, 391-404.

2. Matrix Isolation FTIR Study of Hydrogen-bonded Heterodimers of Methanol with Heterocyclic Organic Compounds. X. Jiang, S. Liu, N. T. Tsona, S. Tang, L. Ding, H. Zhao, L. Du, *RSC Adv.*, **2017,** 7, 2503–2512.

3. Matrix-isolation Study of the Phenol–Water Heterodimer and Phenol Dimer. G. Y. Gor, S. Tapio, A. V. Domanskaya, M. Räsänen, A. V. Nemukhin, L. Khriachtchev, *Chem. Phys. Lett*. **2011**, 517, 9-15.

4. Angular Geometries and other Properties of Hydrogen-bonded Dimers: A Simple Electrostatic Interpretation of the Success of the Electron-pair Model. A. C. Legon, D. J. Millen, *Chem. Soc. Rev.*, **1987**, 16, 467-498.

5. Encoding and Decoding Hydrogen-Bond Patterns of Organic Compounds. M. C. Etter, *Acc. Chem. Res*., **1990**, 23, 120-126.

6. OH Stretching Vibrations of Phenol-(H_2O)^1 and Phenol-(H_2O)^3 in the S1 State. T. Ebata, N. Mizuochi, T. Watanabe, N. Mikami, *J. Phys. Chem*., **1996**, 100, 546-550.

7. Vibrational spectra and a valence force field for conformers of diethyl ether and deuterated analogues , H. Wieser, W. G. Laidlaw, P. J. Krueger, H. Fuhrer, *Spectrochim. Acta*, **1973**, 24, 1055-1089.

8. Molecular complexes of the hydrogen halides studied by matrix isolation infrared spectroscopy, A. J. Barnes, *J. Mol. Struct*., **1983**, 100, 259-280.

9. Low frequency infrared and Raman spectra of certain aliphatic ethers, A. D. H. Clague, A. Danti, *Spectrochim. Acta*, **1968**, 24, 439-441.

---

10 Vibrational analysis of ten simple aliphatic ethers: Spectra, assignments, valence force field and molecular conformations, R. G. Snyder, G. Zerbi, *Spectrochim. Acta.*, **1967**, 23, 391-437.

11. Interpretation and prediction of vibrational absorption intensities: methylethyl ether and diethyl ether, B. Galabov, S. Ilieva, T. Duoev, H. V. Phan, J. R. Durig, *Spectrochim. Acta,* **1993**, 49, 2093-2103.

12. Experimental determination of the *trans–gauche* energy difference of gaseous *n*-pentane and diethyl ether, I. Kanesaka, R. G. Snyder, H. L. Strauss, *J. Chem. Phys*., **1986**, 84, 395-397.

13. L. Schriver, A. Loutellier, A. Burneau, *Chem. Phys. Lett*., **1979**, 60, 471-475.

14. The Millimeter- And Submillimeter-Wave Spectrum Of Methyl Carbamate $[CH_3OC(:O)NH_2]$, I. Medvedev, M. Winnewisser, F.C. De Lucia, E. Herbst, E. Yi, L. P. Leong, R. P. A. Bettens, E. Biankowska-Jaworska, O. Desyatnyk, L. Pszczo´nkowski, Z. Kisiel, *Astrophys. J. Suppl. S*., **2003**, 148, 593-597.

15. Submillimeter-wave spectrum of *anti–anti* and *anti–gauche* diethyl ether, A. Walters, H. S. P. Muller, F. Lewen, S. Schlemmer, *J. Mol. Spectr*., **2009**, 257, 24-28.

16. The millimeter- and submillimeter-wave spectrum of the *trans–gauche* conformer of diethyl ether, I. Medvedev, M. Winnewissera, F. C. De Lucia, E. Herbst, E. Białkowska-Jaworsk, L. Pszczo´łkowski, Z. Kisiel, *J. Mol. Spect*., **2004**, 228, 314–328.

17. Raman spectra and conformational analyses for a series of diethyl ether and its organosilicon derivatives, $CH_3MH_2OM'H_2CH_3$ (M, M'=C and Si), by density functional theory, K. Taga, K. Kawasaki, Y. Yamamoto , T. Yoshida, K. Ohno, H. Matsuura, *J. Mol. Struct*., **2006**, 788, 159-175.

18. Conformations of dimethoxymethane: matrix isolation infrared and ab initio studies, V. Venkatesan, K. Sundararajan, K. Sankaran, K. S. Viswanathan, *Spectrochim. Acta Part A*, **2002**, 58, 467-478.

---

19. Conformations of 1, 1-diethoxyethane: A matrix isolation infrared and ab initio study, V. Venkatesan, K. S. Viswanathan, *J. Mol. Struct*., **2011**, 988, 79-86.

20. Conformations of trimethoxymethane: Matrix isolation infrared and *ab initio* studies, V. Venkatesan, K. S. Viswanathan, *J. Mol. Struct*., **2010**, 973, 89-95.

21. Conformations of diethoxymethane: matrix isolation infrared and ab Initio studies, V. Venkatesan, K. Sundararajan, K. S. Viswanathan, *J. Phys. Chem. A*, **2003**, 107, 7727-7732.

22. Matrix isolation infrared and ab initio study of the conformations of 2, 2-dimethoxypropane, V. Venkatesan, K. Sundararajan, K. Sankaran, K. S. Viswanathan, *Spectrochim. Acta A*, **2003**, 59, 1497-1507.

23. Matrix-Isolation Infrared Spectroscopy of Organic Phosphates, L. George, K. Sankaran, K. S. Viswanathan, C. K. Matthews, *Appl. Spectrosc*., **1994**, 48**,** 801-807.

24. Matrix isolation-supersonic jet infrared spectroscopy: conformational cooling in trimethyl phosphate, V. Vidya, K. Sankaran, K.S. Viswanathan, *Chem. Phys. Lett*., **1996**, 258, 113-117.

25. Conformations of triethyl phosphate: a supersonic jet-matrix isolation and semi-empirical (AM1) study, V. Vidya, K. Sankaran, K. Sundararajan, K. S. Viswanathan, *J. Mol. Struct*., **1999**, 476, 97-104.

26. Conformations of Trimethyl Phosphite: A Matrix Isolation Infrared and ab Initio Study, N. Ramanathan, K. Sundararajan, B. P. Kar, K. S. Viswanathan, *J. Phys. Chem. A*, **2011**, 115, 10059-10068.

27. Conformations of triethylphosphate: A reanalysis of the matrix isolation spectra, K. Sankaran, V. Venkatesan, K. Sundararajan, K. S. Viswanathan, *J. Indian Inst. Sci.*, **2005**, 85, 403-418.

28. *Ab initio* study of trimethyl phosphate: conformational analysis, dipole moments, vibrational frequencies, and barriers for conformer interconversion, L. George, K. S. Viswanathan, S. Singh, *J. Phys. Chem. A*, **1997**, 101, 2459-2464.

---

29. Conformational Landscape of Tri-*n*-butyl Phosphate: Matrix Isolation Infrared Spectroscopy and Systematic Computational Analysis, N. Ramanathan, K. Sundararajan, K. S. Viswanathan, *J. Phys. Chem. A*, **2017**, 121, 6108-6121.

30. Atoms in Molecules: A Quantum Theory; R. F. W. Bader, *Oxford Univ. Press*: Oxford, U.K., **1990**.

31. Identifying and Analyzing Intermolecular Bonding in van der Waals Molecules. R. G. A. Bone, R. F. W. Bader, *J. Phys. Chem*., **1996**, 100, 10892-10911.

32. Aim 2000, Version 1.0, F. Biegle-Koning, R. F. W. Bader, W. H. Tang, *J. Comput. Chem*. **2000**, 96, 6796.

33. The Quantum Theory of Atoms in Molecules, C. F. Matta, R. J. Boyd, *WILEY-VCH Verlag GmbH & Co. KGaA*, Weinheim, **2007**

34. Identifying and Analyzing Intermolecular Bonding in van der Waals Molecules. R. G. A. Bone, R. F. W. Bader, *J. Phys. Chem.* **1996**, 100, 10892–10911.

35. Valency and Bonding: A Natural Bond Orbital Donor-Acceptor Perspective, F. Weinhold, C. Landis, *Cambridge University Press*: Cambridge, U.K., **2005**.

36. Intermolecular Interactions From A Natural Bond Orbital, Donor-Acceptor Viewpoint, A. E. Reed , L. A. Curtiss , F. Weinhold, *Chem. Rev.*, **1988**, 88, 899-926.

37. Natural orbitals in the quantum theory of two-electron systems, P. O. Lowdin, H. Shull, *Phys. Rev.*, **1956**, 101, 1730

38. NBO 6.0, E. D. Glendening, J. K. Badenhoop, A. E. Reed, J. E. Carpenter, J. A. Bohmann, C. M. Morales, C. R. Landis, F. Weinhold, Theoretical Chemistry Institute, University of Wisconsin: Madison, **2013**.

Chapter 6 N-H···N Interactions of Pyrrole

The present chapter explores the N-H···N hydrogen bonded interaction between the weak proton donor pyrrole (C_4H_5N) and strong proton acceptors, such as ammonia (NH_3), pyridine (C_5H_5N) and quinoline (C_9H_7N). The formation of these N-H···N hydrogen bonded heterodimers was probed using matrix isolation infrared spectroscopy in N_2 and Ar matrixes and the experimental results were corroborated with computations. Higher aggregates of NH_3 with C_4H_5N and vice versa were also investigated.

6.1 Experimental Conditions

Pyrrole (C_4H_5N, Spectrochem, 99%), pyridine (C_5H_5N, Merck, 99.5%) and quinoline (C_9H_7N, Sigma-Aldrich, 98%) were used after removing the volatile impurities by performing several freeze-pump-thaw cycles. Ammonia gas (NH_3, INOX, 99%) was used without further purification. The vapor pressure of C_4H_5N in the mixing chamber was controlled, as mentioned in the previous chapters, by maintaining the temperature at -38 °C to -8 °C into which NH_3, C_5H_5N and inert gases were mixed in the ratio C_4H_5N/NH_3/Ar or N_2 ranging between 0.1:1.0:1000 to 0.5:4.0:1000 and C_4H_5N/C_5H_5N/Ar or N_2 in the range 0.05:0.5:1000 to 0.25:1.0:1000. The mixture was co-deposited onto the cold KBr substrate through a single jet nozzle. A double-jet nozzle system was used to co-condensate C_4H_5N and C_9H_7N by streaming them separately onto the cold KBr window. While C_4H_5N/Ar or N_2 was prepared in the mixing chamber C_9H_7N was expanded dynamically, through a double-jet nozzle. A temperature range of -25 °C to -10 °C was kept for C_9H_7N to control its concentration, while allowing dynamic expansion via one of the nozzles. The concentration of C_4H_5N/C_9H_7N/Ar or N_2 ranged from 0.05:0.05:1000 to 0.5:0.25:1000.

6.2 Experimental and Computational Results on Pyrrole

6.2.1 Pyrrole···Ammonia

6.2.1.1 Experimental Details

Figure 6.1 grids A and B illustrate the infrared spectra of the N-H stretching region of C_4H_5N in N_2 and Ar matrixes respectively. The traces 'a' and 'b' in the grids correspond to bare C_4H_5N and NH_3 infrared spectra, respectively. As mentioned in the previous chapters, the peaks observed at 3519.3, 3513.8, 3510.9, 3508.9 cm^{-1} in N_2 and at 3522.9, 3520.9, 3519.7 cm^{-1} in Ar matrix correspond to the N-H stretching mode of C_4H_5N monomer (marked as 'M') [1]. The ν_3 and ν_1 mode of NH_3 monomer was observed in N_2 matrix at 3440.7 and 3330.6 cm^{-1} and the corresponding feature in Ar matrix was observed at 3447.3/3436.4 and 3345.5 cm^{-1} [2,3]. The peaks due to NH_3 dimers and trimers in N_2 matrix are observed at 3414.9, 3402.4, 3395.9, 3312.1, 3310.0, 3244.7, 3234.8 cm^{-1} and 3374.5, 3216.0, 3210.7 cm^{-1}, respectively [4-7]. In Ar matrix, the dimer peak is observed at 3400.7, 3310.8, 3242.4 cm^{-1}, and the trimer peak at 3391.2-3377.6, 3306.0, 3236.0 cm^{-1} [8,9]. The features due to C-H stretching mode of C_4H_5N were found at 3127.6 and 3109.0 cm^{-1} in N_2 matrix, and in Ar matrix, a singlet was observed at 3109.9 cm^{-1} (not shown in the figure). On increasing the concentration of NH_3 (traces 'c' and 'd'), new peaks were observed at 3222.0 cm^{-1} in N_2, and at 3262.6 and 3249.8 cm^{-1} in Ar matrix. Figure 6.2 illustrates the infrared spectra of the N-H bending mode of C_4H_5N in N_2 and Ar matrixes. The C_4H_5N monomer absorption peaks were observed at 520.2/527.2 cm^{-1} in N_2 and in Ar matrix at 483.8/482.8/481.6 cm^{-1} (denoted as 'M'). Figure 6.3 grids A and B show the C-H bending region of C_4H_5N in N_2 and Ar matrixes, respectively. The C-H bending mode of C_4H_5N has a sharp peak at 729.9 cm^{-1} with a small shoulder at 732.2 cm^{-1} in N_2 matrix and the corresponding peak appeared as a multiple site split feature at 725.4, 722.0 and 720.5 cm^{-1} in Ar matrix.

New peaks picked up in intensity at 722.2, 720.5 and 718.6 cm^{-1} in N_2 and in Ar matrix at 718.6, 715.7, 714.0 and 712.8 cm^{-1}.

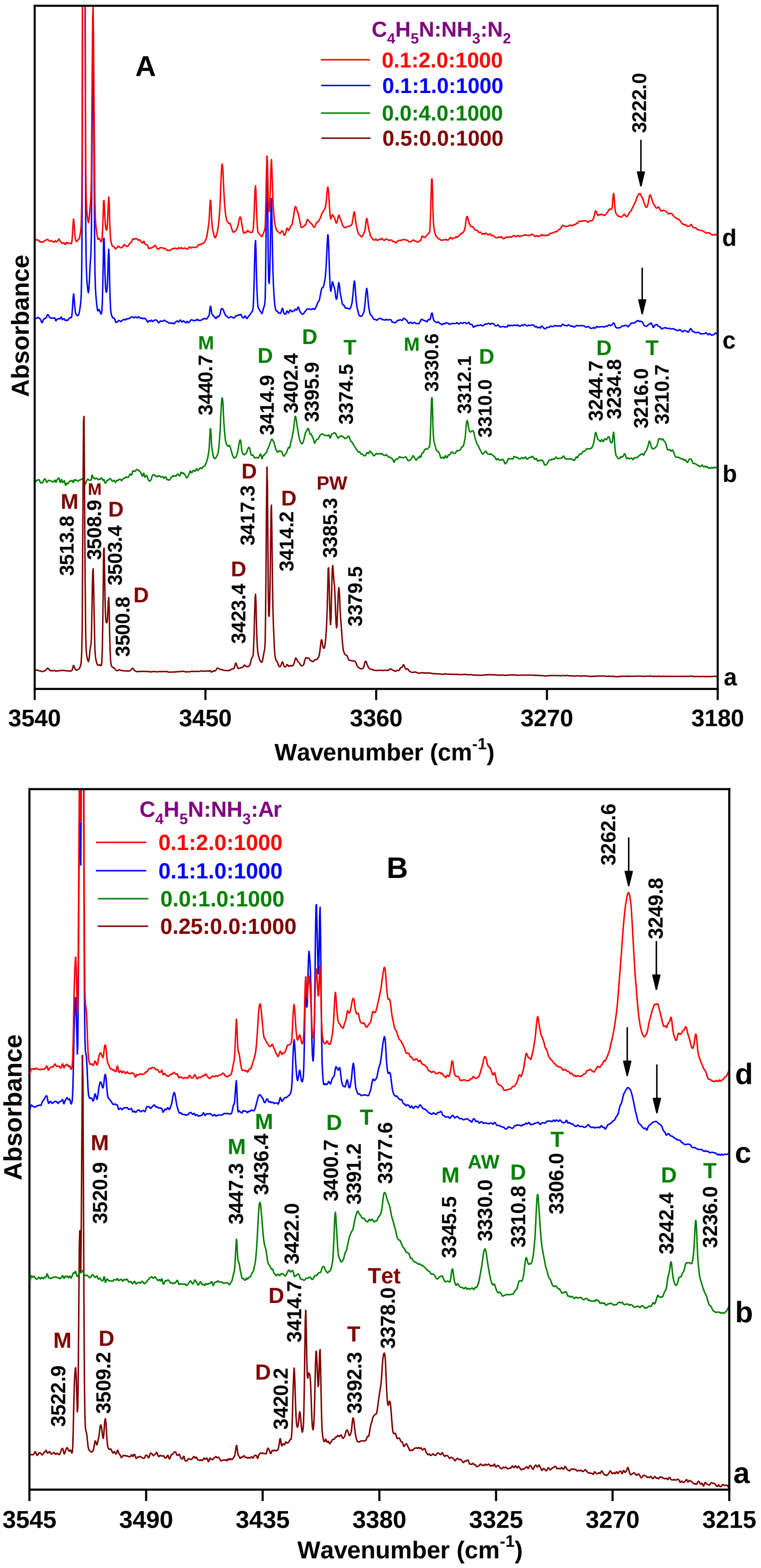

Figure 6.1 Infrared spectra corresponding to the N-H stretching region of C_4H_5N in the heterodimers of C_4H_5N-NH_3 in N_2 (A) and in Ar matrixes (B). All the spectra shown above were annealed at 30 K (N_2) and 35 K (Ar).

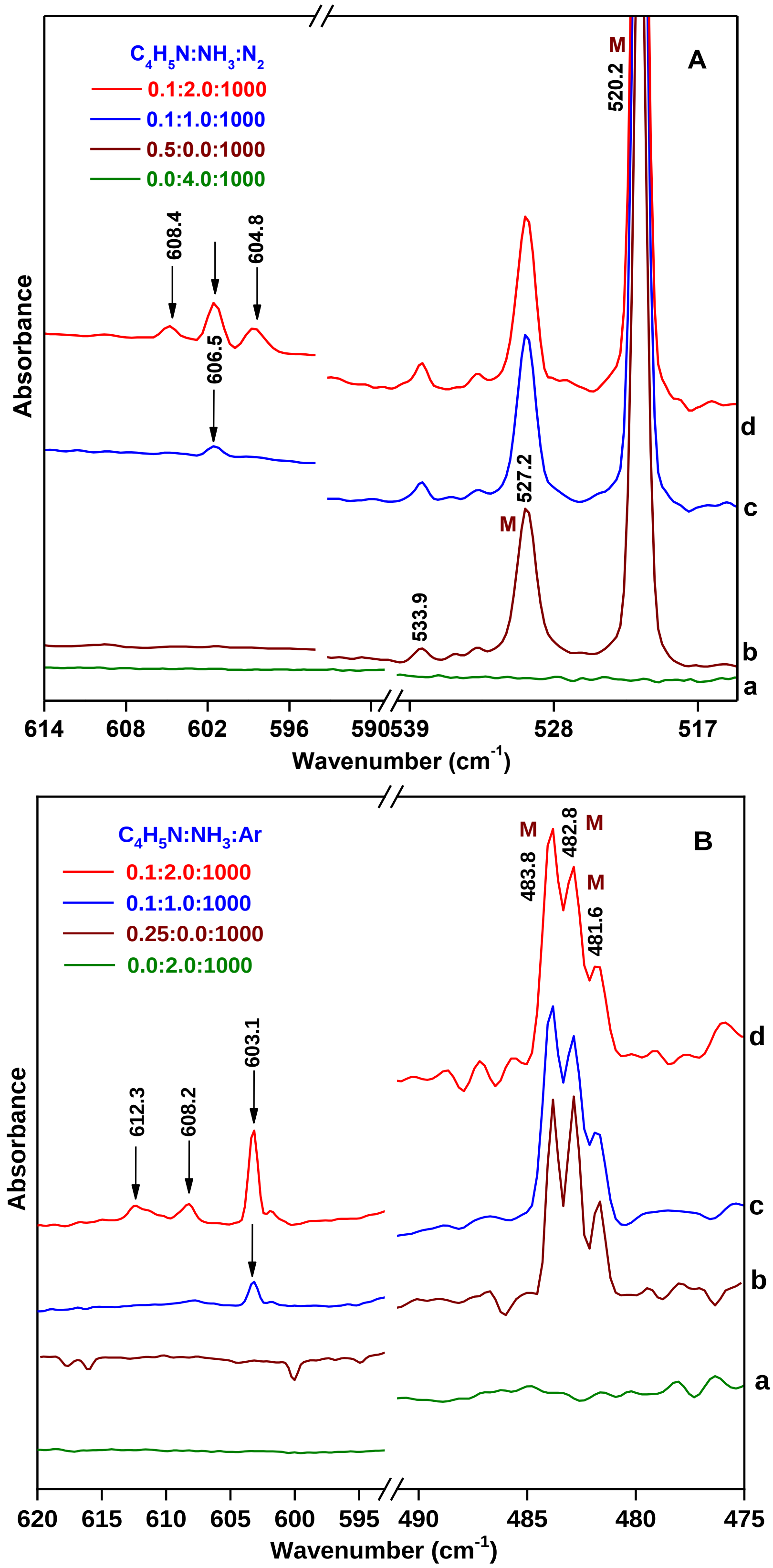

Figure 6.2 Infrared spectra corresponding to the N-H bending region of C_4H_5N in the heterodimers of C_4H_5N-NH_3 in N_2 (A) and in Ar matrixes (B). All the spectra shown above were annealed at 30 K (N_2) and 35 K (Ar).

Figure 6.4 blocks A and B depict the N-H bending mode of NH_3, which appear at 969.0 cm^{-1} and 974.3 cm^{-1} in N_2 and Ar matrixes, respectively. The C-H in-plane bending mode of C_4H_5N appeared in this region at 1015.6, 1051.3 cm^{-1} in N_2 and at 975.8, 1017.3, 1048.4 cm^{-1} in Ar matrixes, respectively. In N_2 matrix, the features in NH_3 alone, 1013.4, and 1003.3/985.8 cm^{-1} were assigned to higher aggregates (H) and $(NH_3)_2$ dimer (D), respectively [10]. In Ar matrix, due to rotational motion of NH_3, many peaks were observed, which are as follows: 999.8/989.8 (dimer, denoted as 'D'), 1018.0 (trimer, T), 1028.1 (higher aggregates, H), and 1035.1 ($NH_3\cdots H_2O$, AW) [4].

6.2.1.2 Computational Details

Since C_4H_5N can exhibit dual behavior as an electron acceptor and donor, to NH_3 molecule, through its acidic hydrogen and π-electron cloud, respectively, one can expect a large number of possibilities for the structure of the 1:1 heterodimer constituting these precursors. Computations performed using MP2/aug-cc-pVDZ level of theory yielded five different structures for the 1:1 C_4H_5N-NH_3 heterodimers and all were proper minima on the potential energy surface as indicated by positive vibrational wavenumbers. The Raw, ZPE, BSSE corrected and reorganization stabilization energies of the 1:1 C_4H_5N-NH_3 heterodimers are listed in Table 6.1. The structure of the lowest energy PAm-A heterodimer, followed by PAm-B, PAm-C, PAm-D, and PAm-E heterodimers are shown in Figure 6.5. It is clear from the figure that the global minimum structure, PAm-A is stabilized by an N-H···N interaction with the ZPE corrected stabilization energy -6.67 kcal mol^{-1}, where the hydrogen H14 interacts with the non- bonded electrons of nitrogen N1 of NH_3 with a bond distance of 1.999 Å and the bond angle between ∠N1-H14-N7 is 179.6°, indicating a near linear geometry. Due to this interaction, the change in the N-H bond length of C_4H_5N was 0.014 Å and the corresponding N-H stretching mode showed a red-shift of 265.5 cm^{-1} from the C_4H_5N monomer absorption, indicating a strong hydrogen bond. The first and second local minima,

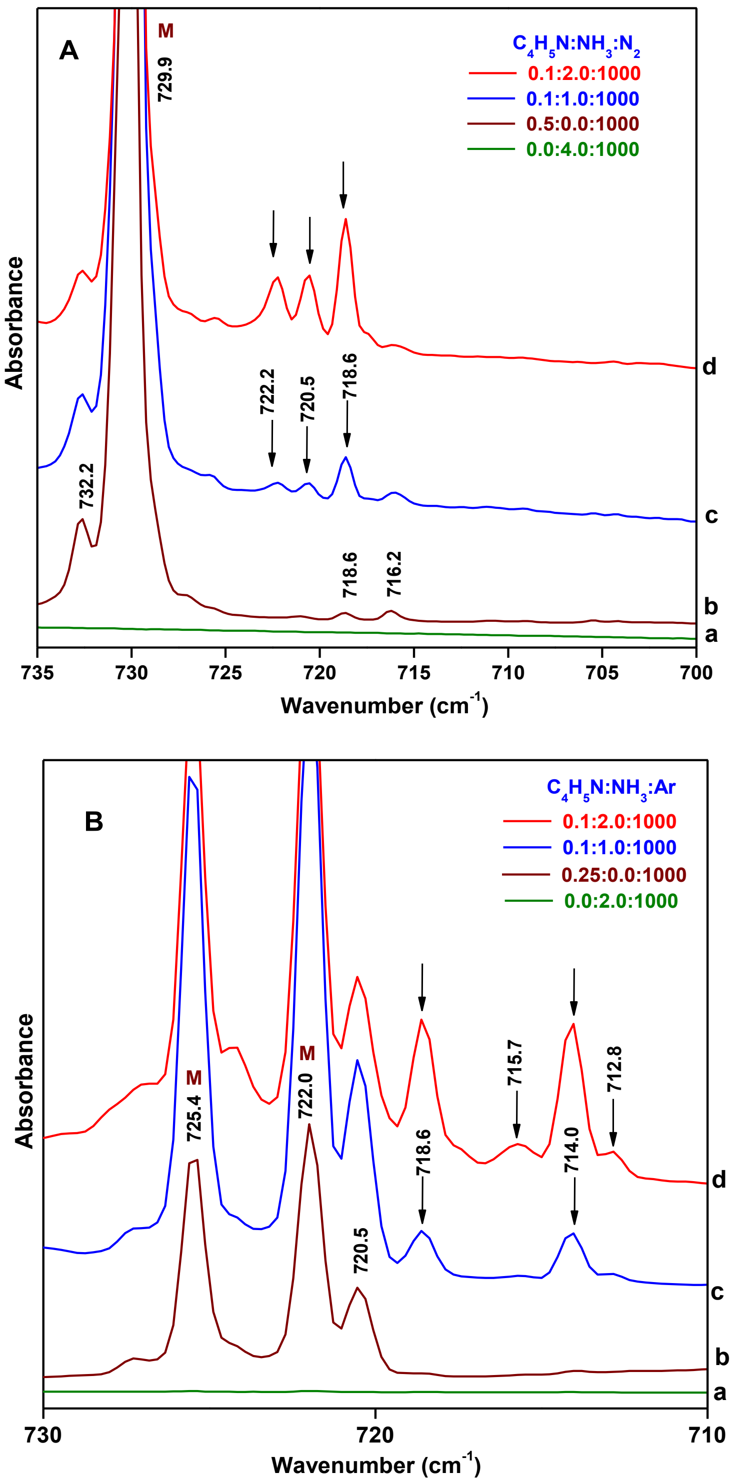

Figure 6.3 Infrared spectra correspond to the C-H bending region of C_4H_5N in the heterodimers of (A) C_4H_5N-NH_3 in N_2 matrix, (B) C_4H_5N-NH_3 in Ar matrix. All the spectra shown above were annealed at 30 K (N_2) and 35 K (Ar).

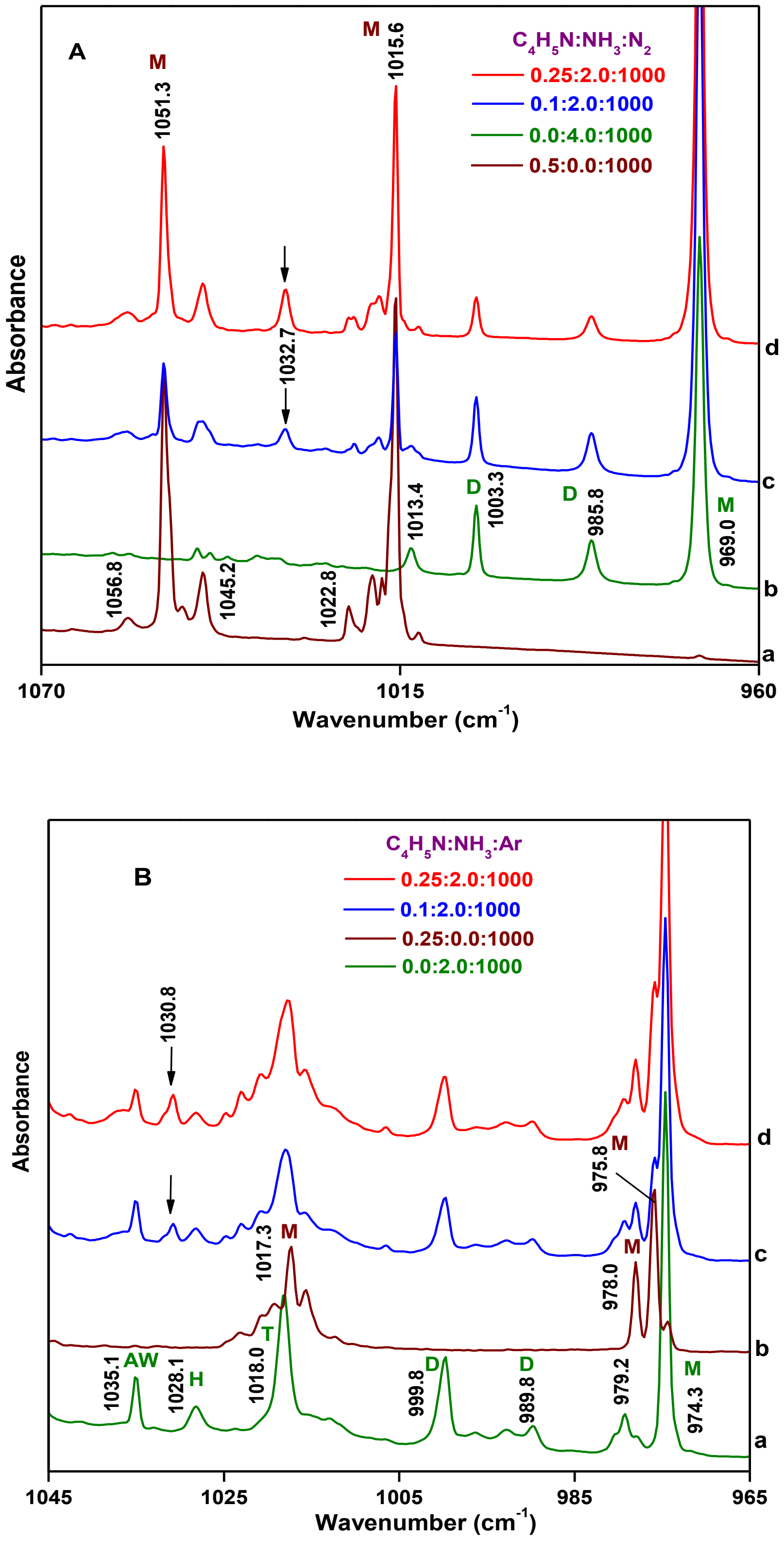

Figure 6.4 **Infrared spectra correspond to the N-H bending region of NH_3 in the heterodimers of (A) C_4H_5N-NH_3 in N_2 matrix, (B) C_4H_5N-NH_3 in Ar matrix. All the spectra shown above were annealed at 30 K (N_2) and 35 K (Ar).**

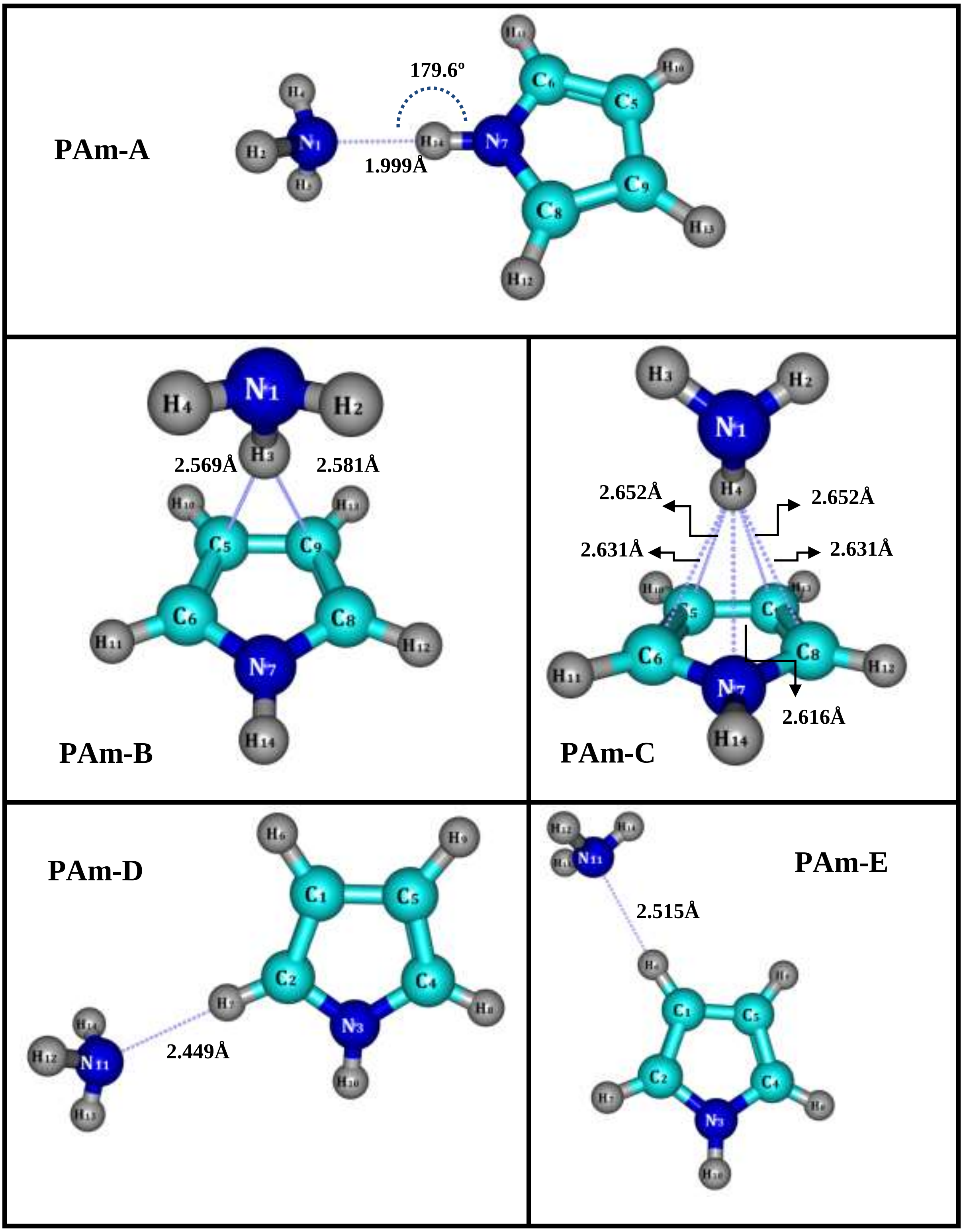

Figure 6.5 Structures of C_4H_5N-NH_3 heterodimers, PAm-A, PAm-B, PAm-C, PAm-D and PAm-E optimized at MP2/aug-cc-pVDZ level of theory.

Table 6.1 Stabilization Energies ([a]Raw/[b]ZPE/[c]BSSE/[d]Reorg) and Gibbs free energy (ΔG) at 10 K of 1:1 C_4H_5N-NH_3 Heterodimers and Higher C_4H_5N-NH_3 Clusters computed at MP2/aug-cc-pVDZ Level of Theory.

Complexes	Stabilization energies	ΔG
PAm-A	-8.07/-6.67/-6.71/-6.72	-6.61
PAm-B	-5.07/-3.98/-3.27/-3.44	-3.92
PAm-C	-4.11/-3.12/-2.65/-2.50	-3.14
PAm-D	-3.00/-2.12/-1.94/-[e]	-2.07
PAm-E	-2.00/-1.34/-0.98/-1.06	-1.29
PAm_2-A	-16.94/-13.58/-13.57	-
PAm_2-B	-9.66/-7.16/-6.41	-
P_2Am-A	-24.49/-21.67/-18.70	-
P_2Am-B	-15.43/-13.72/-10.00	-
P_2Am_2-A	-32.43/-28.08/-24.26	-
P_2Am_2-B	-34.23/-29.77/-26.30	-
PAm_3-A	-25.35/-20.27/-19.75	-
PAm_3-B	-17.97/-14.19/-13.14	-
PAm_4	-25.62/-20.25/-20.12	-

[a] Raw interaction energies refer to energies not corrected for either ZPE or BSSE.
[b] ZPE -Zero point energy
[c] BSSE-Basis set superposition error
[d] Reorg– BSSE with Geometry optimization
[e] Converts to PAm-A heterodimer
All energies are in kcal mol^{-1}.

PAm-B and PAm-C are stabilized by N-H···*π* interaction with the ZPE corrected binding energies of -3.98 and -3.12 kcal mol^{-1}, respectively. The two heterodimers differ in their energies only by ~0.86 kcal mol^{-1} and it is mainly due to the orientation of hydrogens of the NH_3 molecule with respect to the C_4H_5N ring. In PAm-B, the trigonal face of NH_3 containing the three H atoms at the vertices is oriented downwards whereas in PAm-C heterodimer, it is pointing upwards. The PAm-D and PAm-E heterodimers are stabilized by C-H···N interaction where the hydrogen H7 and H6 attached to the *α*- and *β*-carbon of C_4H_5N interacts with the nitrogen N11 of NH_3 with a bond distance of 2.449 and 2.515 Å, respectively. The magnitude of change in the counterpoise corrected reorganization energy of all the heterodimers is negligible compared to BSSE corrected energies. In case of PAm-D (Figure 6.5) heterodimer, the BSSE optimization (reorganization) converts to the global minimum PAm-A structure. The probable reason for this conversion could be the fact that nitrogen N11 of NH_3 molecule is in close proximity to hydrogen H10 of C_4H_5N in the PAm-D structure, which can make a facile transformation to the PAm-A heterodimer. In the PAm-E geometry, the N11 of NH_3 molecule is away from the hydrogen H10 of C_4H_5N. Hence, it a conversion to global minimum PAm-A is not possible, as confirmed by BSSE optimization. A comparison of the Gibbs free energies computed at 10 K and the ZPE corrected energies shows that the entropy and temperature factors do not alter the energy ordering of all the 1:1 C_4H_5N-NH_3 heterodimers.

6.2.1.3 Vibrational Assignment of ν_1 and ν_{16} Modes of C_4H_5N

An experimental red-shift of -291.2 and -263.8 cm^{-1}, respectively in N_2 and Ar matrixes, from the bare C_4H_5N monomer absorption (ν_1), matches well with the computed red-shift of -265.5 cm^{-1} for the 1:1 PAm-A C_4H_5N-NH_3 heterodimer as shown in Table 6.2, and such a large shift signifies a strong hydrogen bond formation. In the N-H bending mode (ν_{16}), as the concentration of NH_3 was varied and the matrix was annealed, new features at

608.4, 606.5 and 604.8 cm^{-1} in N_2 and at 612.3, 608.2 and 603.1 cm^{-1} in Ar matrix showed concentration dependence. These peaks that were observed in N_2 and Ar matrixes amount to an average blue-shift of 83.0 and 120.4 cm^{-1}, respectively and the experimental shift agreeing with the computed shift of 96.0 cm^{-1} for the PAm-A heterodimer.

6.2.1.4 Vibrational Assignments in the C-H bending region of C_4H_5N

Figure 6.3 grids A and B show the C-H bending region of C_4H_5N in N_2 and Ar matrixes respectively. The set of features at 722.2, 720.5 and 718.6 cm^{-1} in N_2 and in Ar matrix at 718.6, 715.7, 714.0 and 712.8 cm^{-1}, showed an average red-shift of -8.5 and -6.9 cm^{-1}, respectively that compares well with the computed red-shift of -7.5 cm^{-1} and has been assigned to the PAm-A heterodimer.

6.2.1.5 Vibrational Assignment of v_2 Mode of NH_3

The features formed at 1032.7 cm^{-1} and 1030.8 cm^{-1} in N_2 and Ar matrixes, at blue-shifts of 63.7 and 56.5 cm^{-1}, respectively, in close agreement to the computed blue-shift of 68.1 cm^{-1}, were assigned to PAm-A heterodimer. None of the local minima were trapped in any of the low temperature matrixes.

6.2.1.6 Higher Clusters of C_4H_5N-NH_3: computations and vibrational assignments

Computations were performed to optimize the higher clusters of C_4H_5N-NH_3 at MP2 level of theory with aug-cc-pVDZ basis set. Calculations indicated 1:2, 2:1, 1:3, 2:2 and 1:4 C_4H_5N-NH_3 clusters and all were minima on the potential energy surface. Figure 6.7 shows the structures of 1:2 C_4H_5N-$(NH_3)_2$ (PAm$_2$-A, PAm$_2$-B) and 2:1 $(C_4H_5N)_2$-NH_3 (P$_2$Am-A, P$_2$Am-B) clusters. Figure 6.8 shows the 1:3 C_4H_5N-$(NH_3)_3$ (PAm$_3$-A, PAm$_3$-B), 2:2 $(C_4H_5N)_2$-$(NH_3)_2$ (P$_2$Am$_2$-A, P$_2$Am$_2$-B) and 1:4 C_4H_5N-$(NH_3)_4$ (PAm$_4$) higher clusters.

In 1:2 PAm$_2$-A, there are co-operative N-H$\cdots$N interaction between the NH_3 molecules and C_4H_5N, thus forming a more stable cyclic dimer than acyclic PAm$_2$-B dimer, which is stabilized by cooperative N-H$\cdots$N and N-H$\cdots\pi$ interactions. Table 6.1 lists the

Table 6.2 Comparison of experimental vibrational wavenumbers of the 1:1, 1:2, 2:1, 2:2, 1:3 and 1:4 Aggregates of C_4H_5N-NH_3, with computed wavenumbers at MP2/aug-cc-pVDZ Level of Theory.

Calculated		**Experimental**				**Mode Assignment**
		N$_2$ Matrix		Ar Matrix		
ν (cm^{-1})	**Δν^{a}**	**ν (cm^{-1})**	**Δν**	**ν (cm^{-1})**	**Δν**	
C_4H_5N						
514.9 (59)^{a}	-	527.2/ 520.2	-	483.8/482.8/481.6	-	N-H bending-C_4H_5N
718.4 (176)	-	729.9/ 732.2	-	722.0/720.5/725.4	-	C-H bending-C_4H_5N
3672.4 (76)	-	3513.2	-	3520.2	-	N-H stretching-C_4H_5N
NH_3						
1048.4 (130)	-	969.0	-	974.3	-	N-H bending-NH_3
PAm-A						
610.9 (10)	96.0	606.5	83.0^{c}	603.1	120.4^{c}	N-H bending-C_4H_5N
710.9 (119)	-7.5	720.5/722.2/ 718.6	-8.5^{b}	712.8/714.0/ 715.7/718.6	-6.9^{c}	C-H bending-C_4H_5N
3406.9 (922)	-265.5	3222.0	-291.2^{b}	3262.6/ 3249.8	-263.8^{c}	N-H stretching-C_4H_5N
1116.5 (147)	68.1	1032.7	63.7	1030.8	56.5	N-H bending-NH_3
PAm$_2$-A						
621.8(8)	106.9	-^{b}	-	-^{b}	-	N-H bending-C_4H_5N
725.8 (116)	7.4	-^{b}	-	-^{b}	-	C-H bending-C_4H_5N
3354.7 (570)	-317.7	-^{b}	-	3189.8	-330.4	N-H stretching-C_4H_5N
1129.1 (99)	80.7	-^{b}	-	1053.0	78.7	N-H bending-NH_3
1144.5 (110)	96.0	-^{b}	-	-^{b}	-	
P$_2$Am-A						
606.7(16)	91.8	-^{b}	-	-^{b}	-	N-H bending-C_4H_5N
625.3(9)	110.4	-^{b}	-	-^{b}	-	
735.9(54)	17.5	-^{b}	-	-^{b}	-	C-H bending-C_4H_5N
751.7 (224)	33.2	-^{b}	-	-^{b}	-	
3271.0 (762)	-401.5	3092.4/3087.8	-423.0^{c}	3085.1	-435.1	N-H stretching-C_4H_5N
3524.9 (402)	-147.6	-^{b}	-	-^{b}	-	
1154.0 (80)	105.6	-^{a}	-	1063.8/ 1066.7	91.0^{c}	N-H bending-NH_3

P_2Am_2-A						
513.0(57) 603.5(13)	-1.9 88.6	-[b]	-	-[b]	-	N-H bending-C_4H_5N
730.5 (103) 751.2 (176)	12.1 32.8	-[b]	-	-[b]	-	C-H bending-C_4H_5N
3169.7 (1171) 3510.0 (556)	-502.8 -162.5	2983.2/ 2978.6 -[b]	-532.3[c] -	2977.9/ 2967.5 -	-547.5[c] -	N-H stretching-C_4H_5N
1150.0 (73) 1164.4 (57)	101.6 116.0	-[b]	-	-[b]	-	N-H bending-NH_3
PAm_3-A						
524.6(55)	9.7	-[b]	-	-[b]	-	N-H bending-C_4H_5N
727.8 (137)	9.4	-[b]	-	-[b]	-	C-H bending-C_4H_5N
3234.1 (1128)	438.3	-	-	3058.1	462.1	N-H stretching-C_4H_5N
1127.6 (88) 1156.4 (137) 1167.0 (60)	79.2 108.0 118.6	-[b]	-	-[b]	-	N-H bending-NH_3
PAm_4						
724.3 (129)	5.9	-[b]	-	-[b]	-	C-H bending-C_4H_5N
3044.7 (1656)	-627.7	2892.3/2885.3	-624.4[c]	2890.6/ 2878.5	-635.6[c]	N-H stretching-C_4H_5N
1105.3 (115) 1136.7 (117)	56.9 88.3	-[b]	-	-[b]	-	N-H bending-NH_3

[a] $\Delta\nu = \nu_{heterodimer} - \nu_{monomer}$

[b] Intensities (in km mol^{-1}) are given in parenthesis.

[c] Average multiplet experimental wavenumbers of the monomers and multimers were taken to compute the experimental shift in the heterodimers.

[d] Experimental features were not observed.

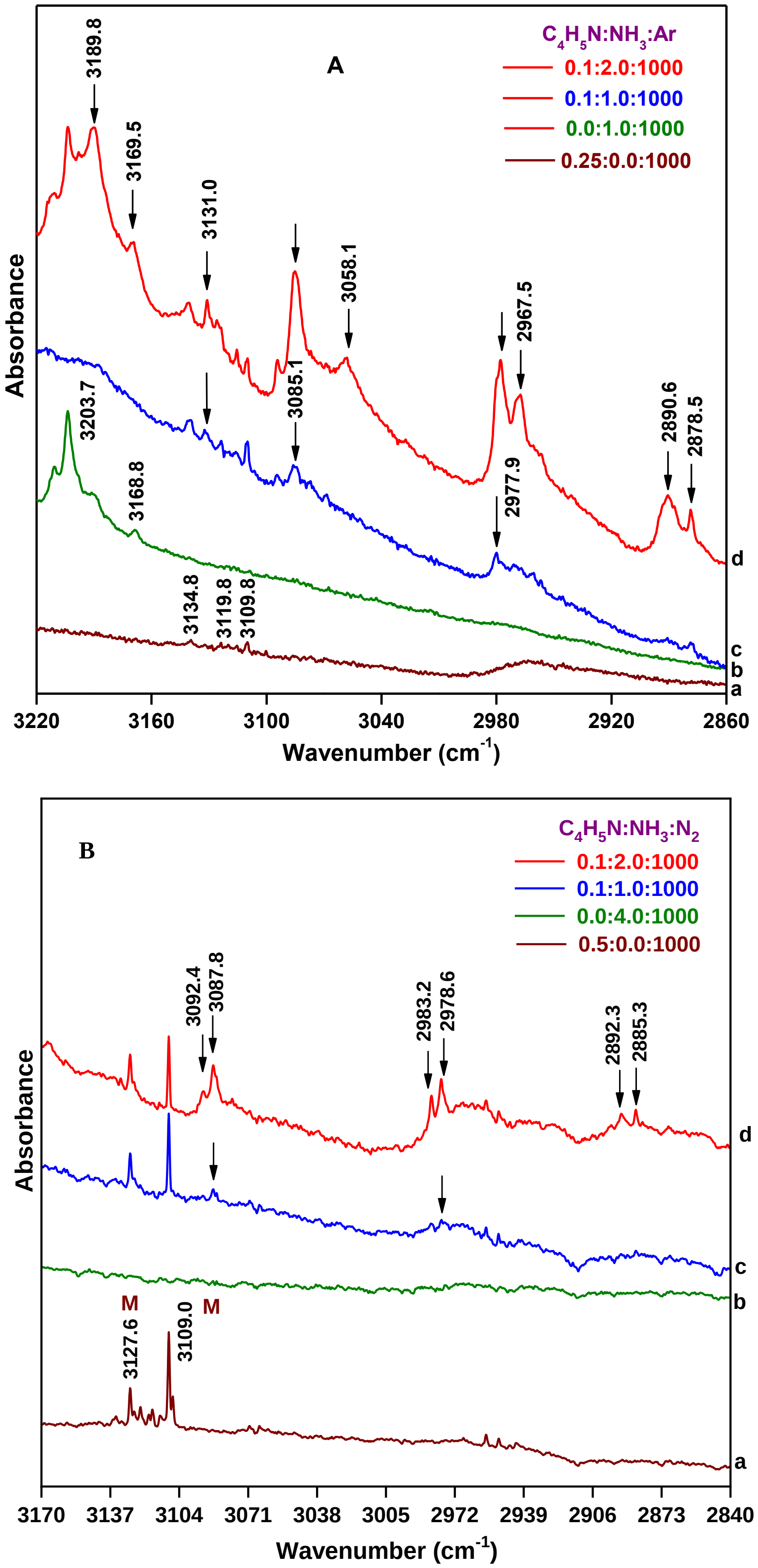

Figure 6.6 Infrared spectra correspond to the N-H stretching region of C_4H_5N in the heterodimers of (A) C_4H_5N-NH_3 in Ar matrix, (B) C_4H_5N-NH_3 in N_2 matrix. All the spectra shown above were annealed at 30 K (N_2) and 35 K (Ar).

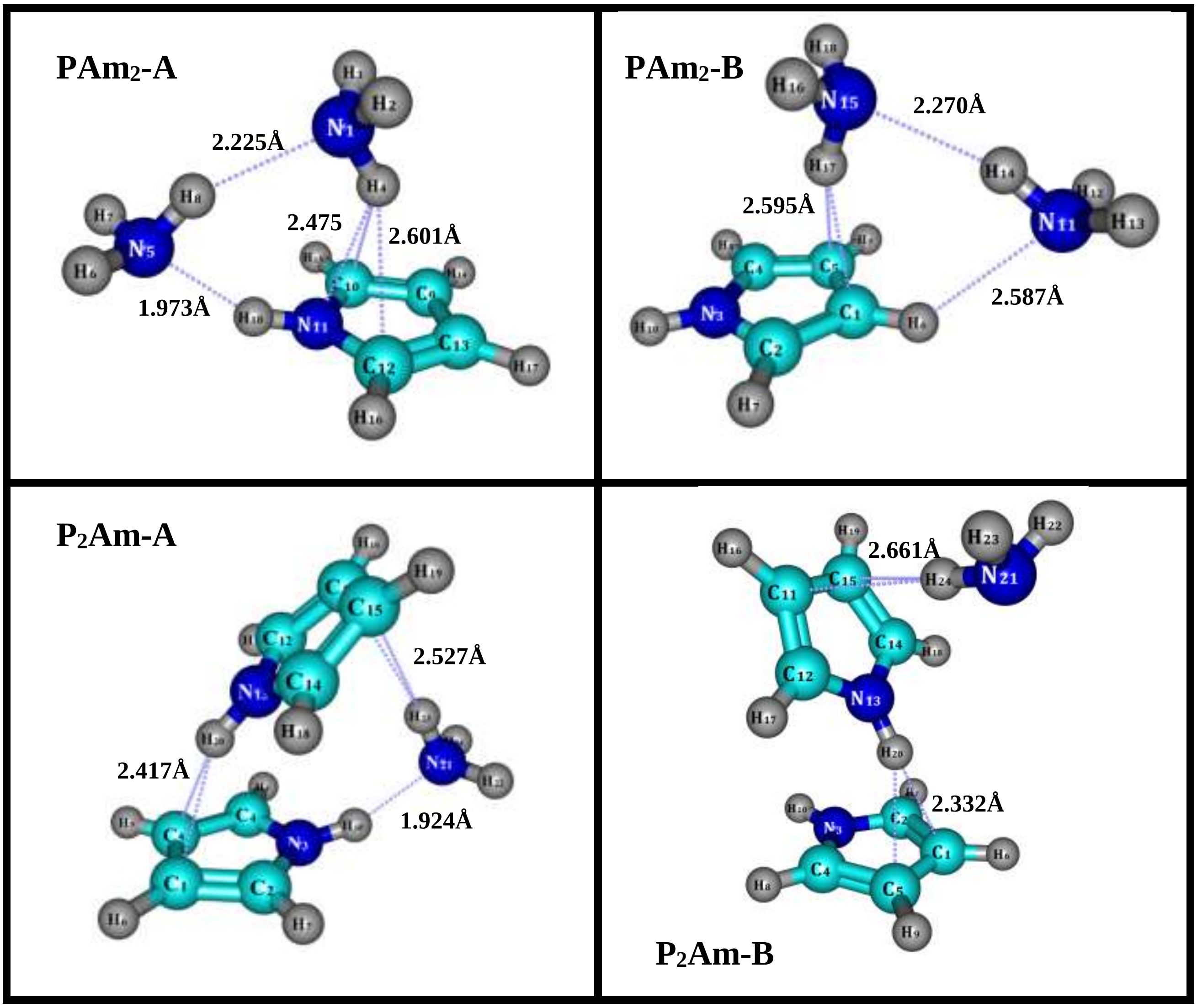
PAm$_2$-A

PAm$_2$-B

P$_2$Am-A

P$_2$Am-B

Figure 6.7 Structures of C_4H_5N-NH_3 1:2 (PAm$_2$-A/B) and 2:1 (P$_2$Am-A/B) heterodimers optimized at MP2/aug-cc-pVDZ level of theory.

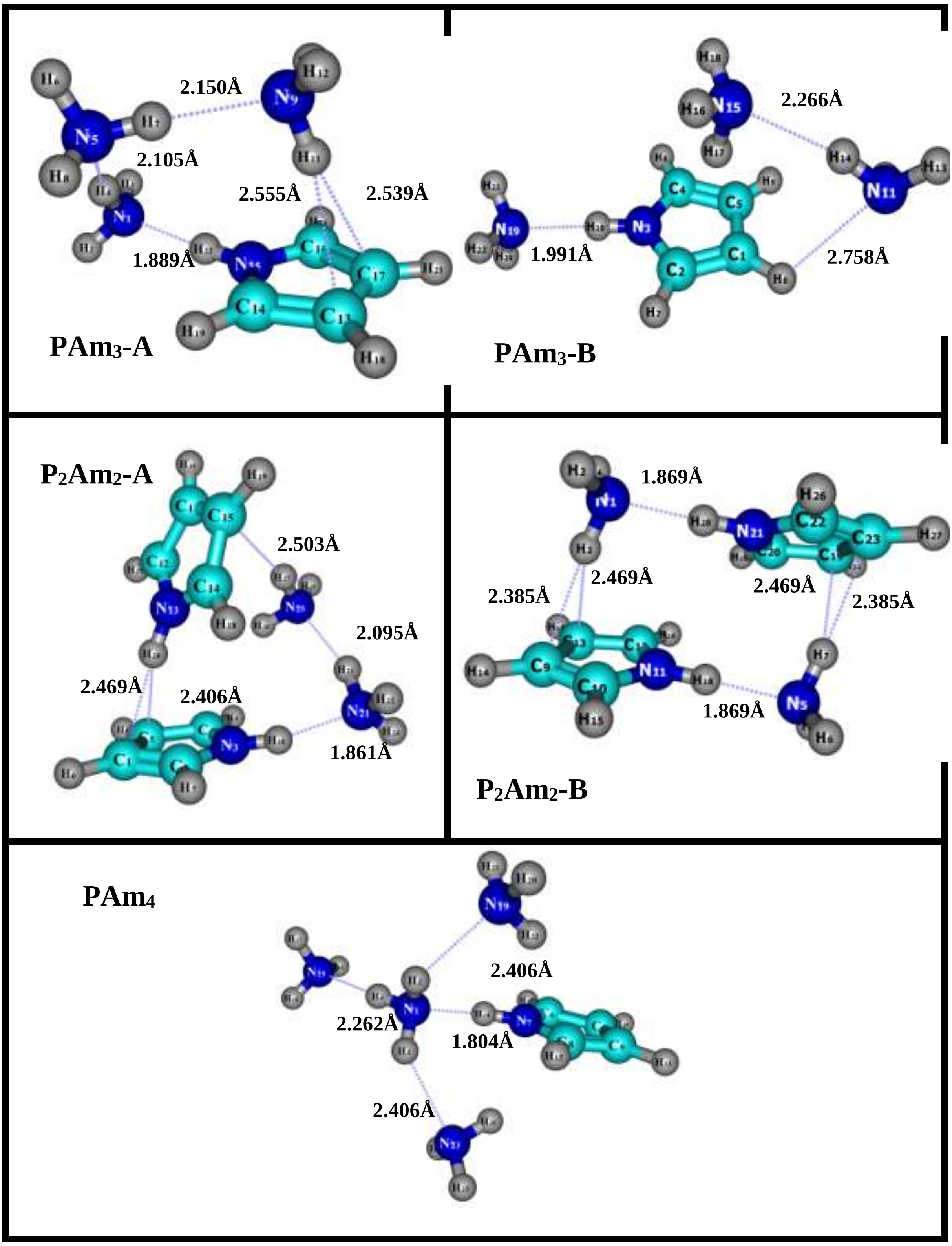

Figure 6.8 Structures of C_4H_5N-NH_3 1:3 (PAm$_3$-A/B), 2:2 (P$_2$Am$_2$-A/B) and 1:4 (PAm$_4$) heterodimers optimized at MP2/aug-cc-pVDZ level of theory.

stabilization energies of the C_4H_5N-NH_3 higher clusters.

C_4H_5N dimer interacts with NH_3 to form two types of 2:1 P_2Am-A and P_2Am-B higher clusters. The P_2Am-A cluster has a cyclic structure with a co-operative N-H$\cdots$N interaction which is more stable than the relatively ‘open’ P_2Am-B cluster. In P_2Am-B cluster, the N-H group of one of the C_4H_5N molecule is facing away from the NH_3 thus favoring an open cluster.

Computations indicated that NH_3 trimer forms 1:3 PAm_3-A and PAm_3-B higher clusters. In PAm_3-A, there are multiple N-H$\cdots$N and N-H$\cdots\pi$ interactions between ammonia and C_4H_5N making it more stable than PAm_3-B as shown in Figure 6.8. The cyclic dimer is more stable than the open structure.

NH_3 dimer and C_4H_5N dimer interact to form 2:2 P_2Am_2-A and P_2Am_2-B cyclic higher clusters with multiple N-H$\cdots$N and N-H$\cdots\pi$ interactions. In P_2Am_2-B cluster, two molecules of NH_3 and C_4H_5N interact to form cyclic structure which is more stable than P_2Am_2-A cluster. Figure 6.8 shows the optimized structure of C_4H_5N-$(NH_3)_4$ tetramer (PAm_4), which has multiple co-operative N-H$\cdots$N interactions.

It is well known that C_4H_5N and NH_3 form dimers, trimers, and tetramers at low temperatures and it is also possible that NH_3 and C_4H_5N can form higher clusters in the matrixes as the concentration of the precursors are increased [2]. Table 6.2 lists the comparison of computed with experimental wavenumbers for the C_4H_5N-NH_3 higher clusters. Figure 6.6, grids A and B show the infrared region of N-H stretching region of C_4H_5N in Ar and N_2 matrixes, respectively. Apart from the features due to 1:1 C_4H_5N-NH_3 heterodimers, experiments performed using higher concentration of NH_3 in Ar matrix revealed new features at 3189.8 cm^{-1} with a red-shift of -330.4 cm^{-1} that matches well with the computed red-shift of -317.7 cm^{-1} for the 1:2 PAm_2-A higher cluster. Surprisingly, the vibrational features due to this higher cluster are not observed in N_2 matrix.

Like NH_3 dimer, C_4H_5N undergoes self-aggregation in the matrix to form dimers which can interact with NH_3 to form 2:1 $(C_4H_5N)_2$-NH_3 higher clusters. Experimentally, new features were observed in N-H stretching mode of pyrrole at 3085.1 cm^{-1} in Ar matrix with a red-shift of -435.1 cm^{-1} and in N_2 matrix at 3092.4, 3087.8 with a red-shift of -423.0 cm^{-1} that matches well with the computed red-shift of -401.5 cm^{-1} for the P_2Am-A heterotrimer. The other computed red-shifted feature at -147.6 cm^{-1} could not be clearly discerned in the experiment. The feature for P_2Am-A was also found in the N-H bending mode of NH_3 at 1063.8/1066.7 cm^{-1} at a shift of 91.0 cm^{-1}, corroborating nicely with the computed shift of 105.6 cm^{-1}.

In the N-H stretching region of C_4H_5N in N_2 matrix, new features were observed as a doublet at 2983.2/2978.6 with a red-shift of -532.3 cm^{-1} and in Ar matrix at 2977.9/2967.5 with a red-shift of -547.5 cm^{-1} that compares well with the computed red-shift of -502.8 cm^{-1} for the P_2Am_2-A higher cluster. Computations indicated that the N-H stretching mode of C_4H_5N is red-shifted by -438.3 cm^{-1} for the 1:3 PAm_3 higher clusters. Experimentally, in Ar matrix, new features were observed at 3058.1 cm^{-1} with a red-shift of -462.1 cm^{-1} that matches well with the computed shift for the PAm_3 higher cluster. Features due to this higher cluster could not be observed in N_2 matrix.

Finally, computations gave only one minimum for the 1:4 PAm_4 heteropentamer and the formation of this aggregate is evidenced from the red-shifts of -624.4 and -635.6 cm^{-1} in N_2 and Ar matrixes, respectively. The computed red-shift of -627.7 cm^{-1} correlates well with the experimental shift in both matrixes.

6.2.2 Pyrrole···Pyridine

6.2.2.1 Experimental Details

Figure 6.9 grids A and B, traces ‘a’ and ‘b’ shows the infrared spectra of C_5H_5N and C_4H_5N alone in N_2 and Ar matrixes, respectively. Figure 6.10 grids A and B shows the infrared spectra of the N-H bending region of C_4H_5N. Upon increasing the concentration of C_5H_5N, new features were observed as site split multiplets at 3264.7, 3251.7 and 3242.6 cm^{-1}. The features observed at 590.1 and 591.0 cm^{-1} in N_2 and Ar matrixes respectively, are due to $(C_4H_5N)_3$(T) while the peak at 596.9 cm^{-1} in N_2 matrix is due to C_4H_5N-H_2O heterodimer (PW) [Chapter 5]. The ring deformation modes of C_5H_5N monomer have absorptions at 605.5 cm^{-1} in N_2 [11], and at 605.8 and 601.9 cm^{-1} in Ar matrix [12], while the peak at 611.6 cm^{-1} is due to C_4H_5N-H_2O heterodimer [13]. New spectral bands at 611.8, 610.8 and 602.6 cm^{-1} in N_2 and at 611.6, 599.3 cm^{-1} in Ar matrix were found to increase in intensity on co-depositing the precursors followed by annealing. Figure 6.11, grids A and B show the C-H bending mode of C_4H_5N in N_2 and Ar matrixes respectively. Co-deposition precursors and their subsequent annealing indicated the formation of new spectral bands at 725.6, 724.1 cm^{-1} in N_2 and at 716.7, 715.0 cm^{-1} in Ar matrixes.

6.2.2.2 Computational Details

Computations performed at MP2 level of theory with aug-cc-pVDZ basis set indicated three minima corresponding to PPy-A, PPy-B and PPy-C heterodimers. Computations also gave a geometry PPy-D where the ZPE corrected energies show the two heterodimers PPy-A and PPy-D to be isoenergetic and both are stabilized by N-H···N interaction. The vibrational wavenumber calculation of PPy-D heterodimer gave one imaginary vibrational wavenumber (*17i*), which demonstrates that it is only a saddle point on the potential energy surface. The stabilization energies of the heterodimers are listed in Table 6.3. Interestingly, a closer look at the geometries of these two heterodimers revealed a subtle difference in the orientation of the C_4H_5N moiety towards C_5H_5N. (Figure 6.12) In PPy-A heterodimer, the hydrogen bond distance between the N4 of C_5H_5N and H21 of C_4H_5N is 1.934 Å, with the change in N-H bond length of C_4H_5N to be 0.015 Å, and the bond angle between ∠N4-H21-N14 is 158.5° indicating a slightly tilted geometry of C_4H_5N towards

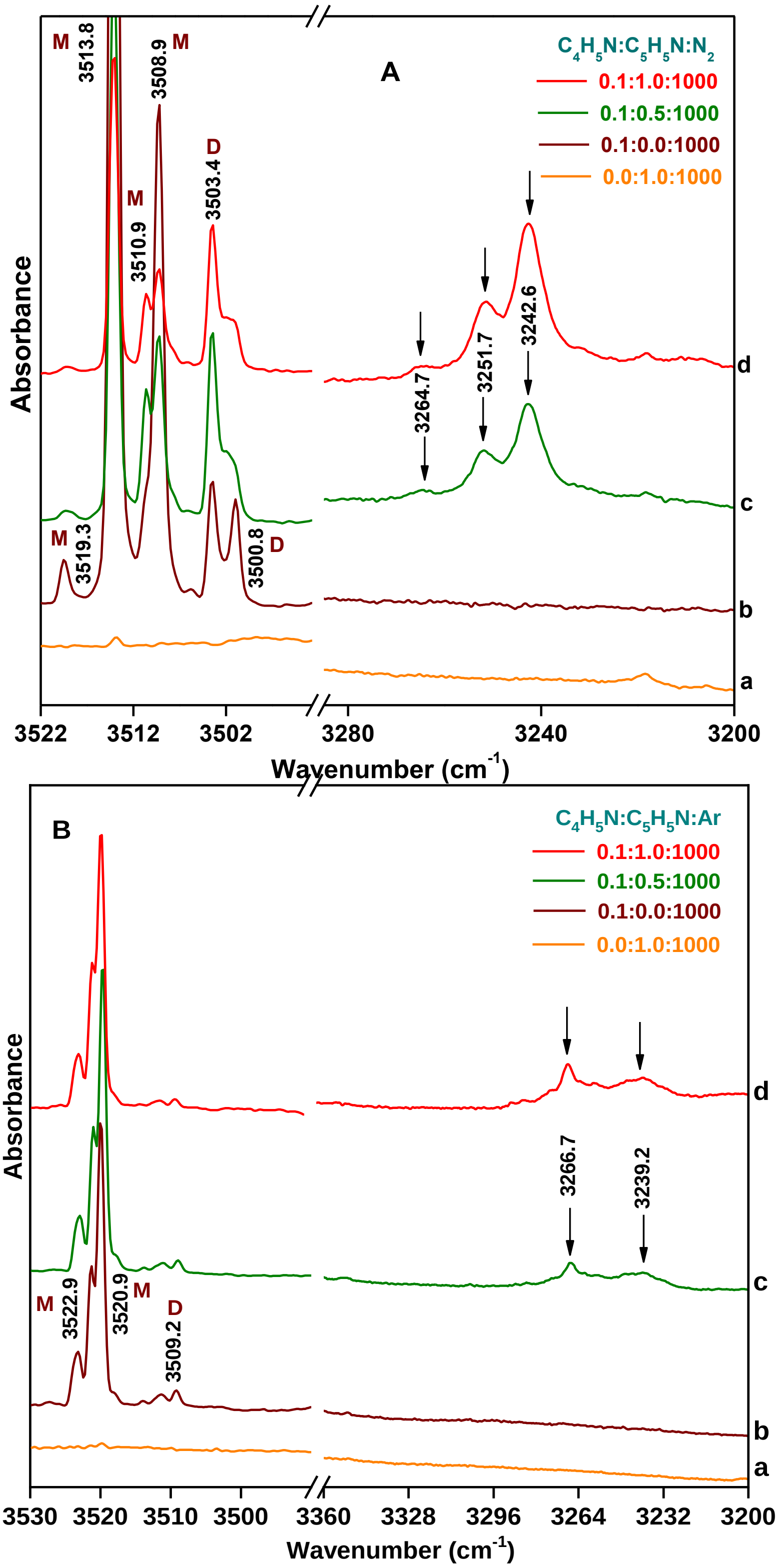

Figure 6.9 Infrared spectra correspond to the N-H stretching region of C_4H_5N in the heterodimers of (A) C_4H_5N-C_5H_5N in N_2 matrix, (B) C_4H_5N-C_5H_5N in Ar matrix. All the spectra shown above were annealed at 30 K (N_2) and 35 K (Ar).

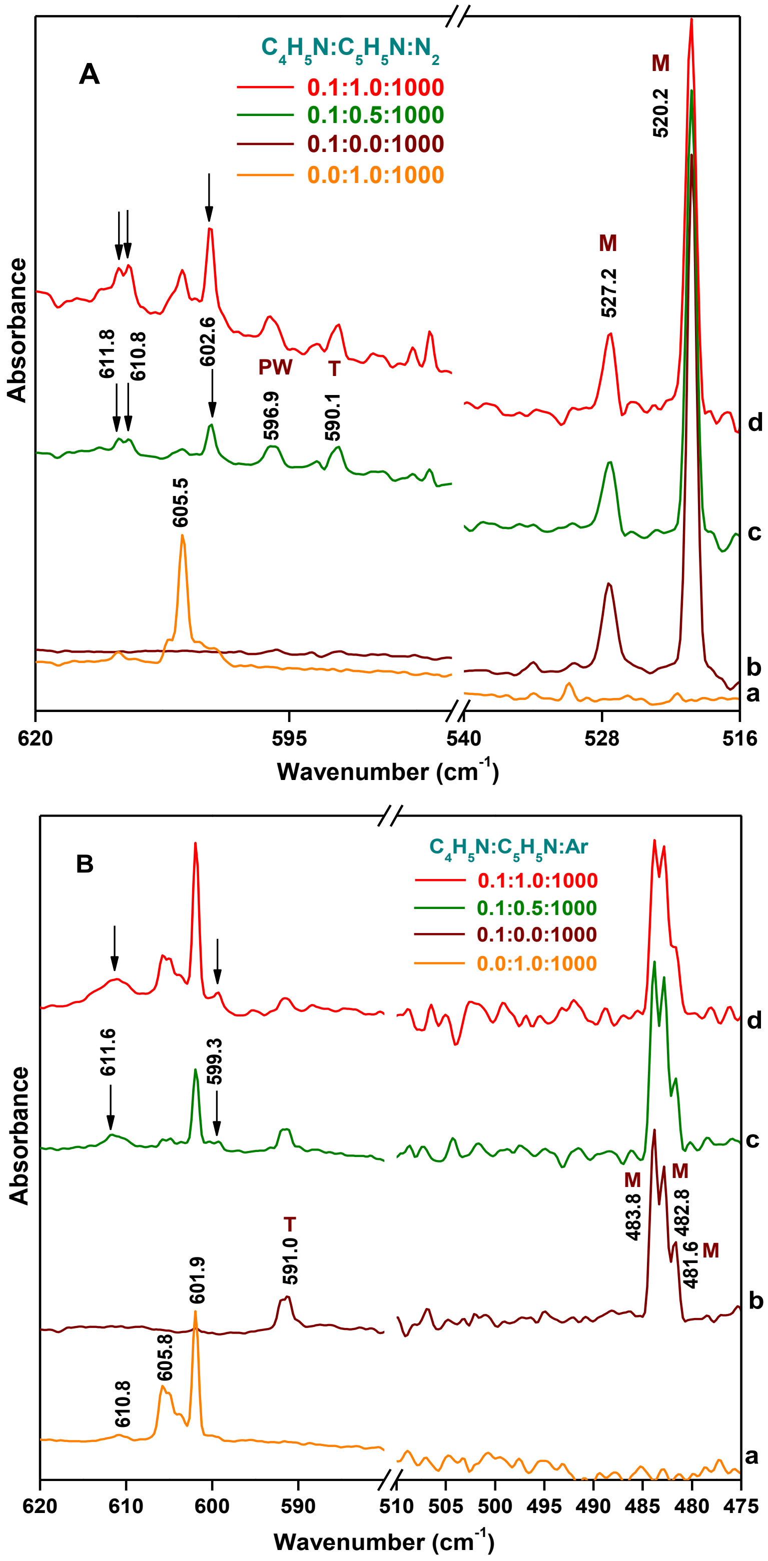

Figure 6.10 Infrared spectra correspond to the N-H bending region of C_4H_5N in the heterodimers of (A) C_4H_5N-C_5H_5N in N_2 matrix, (B) C_4H_5N-C_5H_5N in Ar matrix. All the spectra shown above were annealed at 30 K (N_2) and 35 K (Ar).

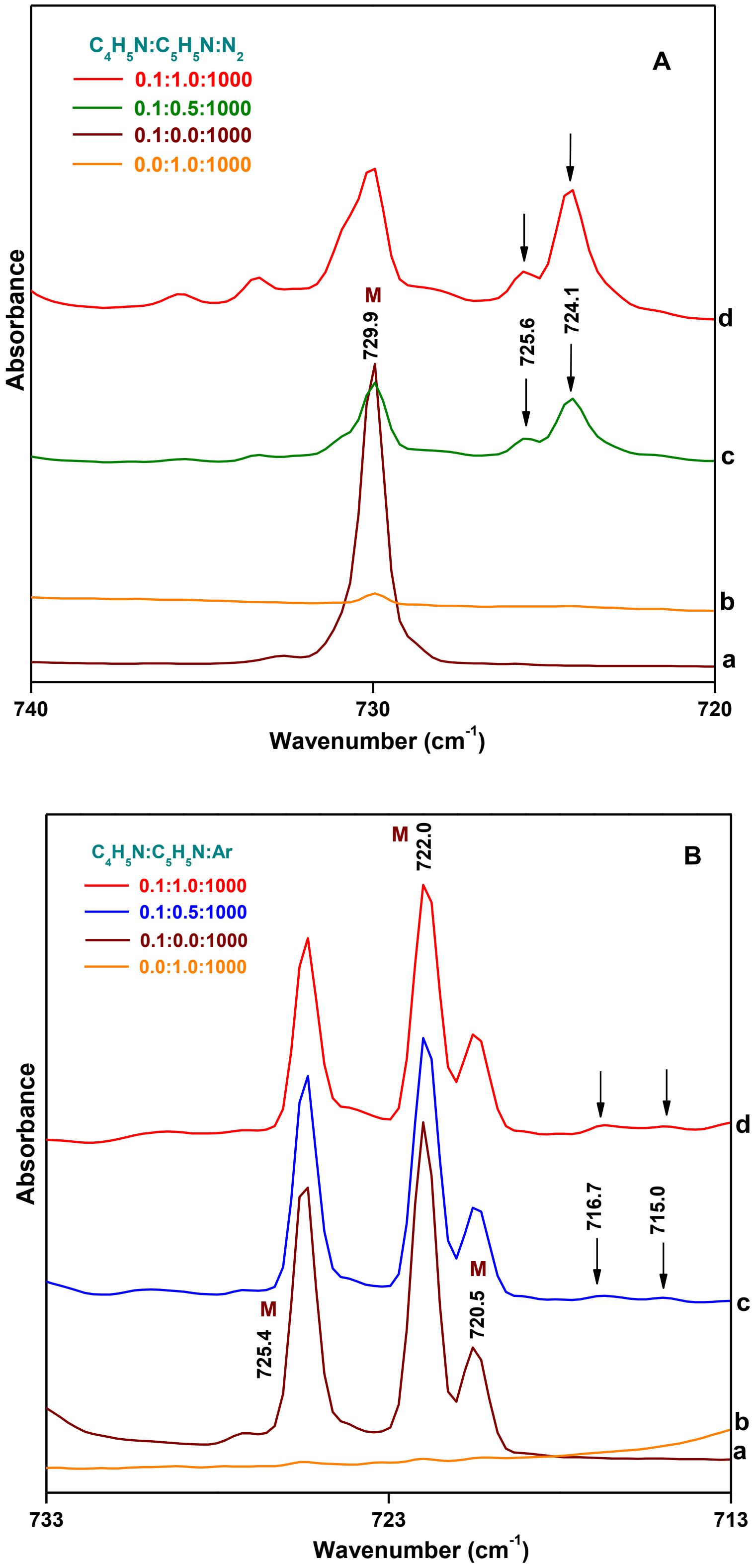

Figure 6.11 Infrared spectra correspond to the C-H bending region of C_4H_5N in the heterodimers of (A) C_4H_5N-C_5H_5N in N_2 matrix, (B) C_4H_5N-C_5H_5N in Ar matrix. All the spectra shown above were annealed at 30 K (N_2) and 35 K (Ar).

C_5H_5N molecule, favoring a secondary interaction between H10 of C_5H_5N and N14 of C_4H_5N with a bond distance of 2.831 Å. The ZPE corrected stabilization energy of ~-7.95 kcal mol^{-1} suggests a strong hydrogen bond formation. In case of PPy-D heterodimer, the bond angle ∠N4-H21-N14 is 179.9°, indicating a linear structure with a hydrogen bond distance of 1.911 Å. The first local minimum corresponds to PPy-B heterodimer with N-H···N and C-H···π interactions and the second local minimum PPy-C heterodimer with N4···H20, N4···H17 and C-H···π interactions are shown in Figure 6.12. The BSSE corrected reorganization energy showed no major changes in the energies of the heterodimers. Since, the PPy-B heterodimer has N-H···N and C-H···π interactions on BSSE geometry optimization, this heterodimer converts to a more stable global minimum PPy-A. The free energy of all the heterodimers computed at 10 K showed similar trend as ZPE corrected energies, except that the PPy-A becomes slightly more stable than the PPy-D heterodimer. This in turn clearly authenticates that PPy-A geometry is the global minimum heterodimer.

6.2.2.3 Vibrational Assignment in ν_1 and ν_{16} modes of C_4H_5N

Upon increasing the concentration of C_5H_5N, new features were observed as site split multiplets at 3264.7, 3251.7 and 3242.6 cm^{-1} (traces b and c in grid A of Figure 6.9) with an average red-shift of -260.2 cm^{-1} in N_2 matrix and in Ar matrix at 3266.7 and 3239.2 cm^{-1} (traces b and c grid B of Figure 6.9) with a red-shift of -267.3 cm^{-1} from the bare C_4H_5N absorption that compares well with the computed red-shift of -289.0 cm^{-1} for the PPy-A heterodimer (Table 6.4). It is interesting to discern from the experimental spectrum that the infrared features of PPy-A heterodimer are broad and its intensity is significantly higher in N_2 than in Ar matrix.

On analyzing the N-H bending mode, the spectral bands at 611.8, 610.8 and 602.6 cm^{-1} in N_2 and at 611.6, 599.3 cm^{-1} in Ar matrix were found to increase in intensity on

Table 6.3 Stabilization energies ([a]Raw/[b]ZPE/[c]BSSE/[d]Reorg) and Gibbs free energy (ΔG) at 10 K of 1:1 C_4H_5N-C_5H_5N heterodimers computed at MP2/aug-cc-pVDZ Level of Theory.

Heterodimers	**Stabilization energies**	**ΔG**
PPy-A	-9.95/-9.05/-7.95/-8.00	-8.88
PPy-B	-9.35/-8.55/-6.32/-[e]	-8.37
PPy-C	-4.49/-4.06/-2.38/-2.56	-3.88

[a]Raw interaction energies refer to energies not corrected for either ZPE or BSSE.
[b]ZPE -Zero point energy
[c]BSSE- Basis set superposition error
[d]Reorg– BSSE with Geometry optimization
[e]Converts to PPy-A heterodimer
All energies are in kcal mol^{-1}

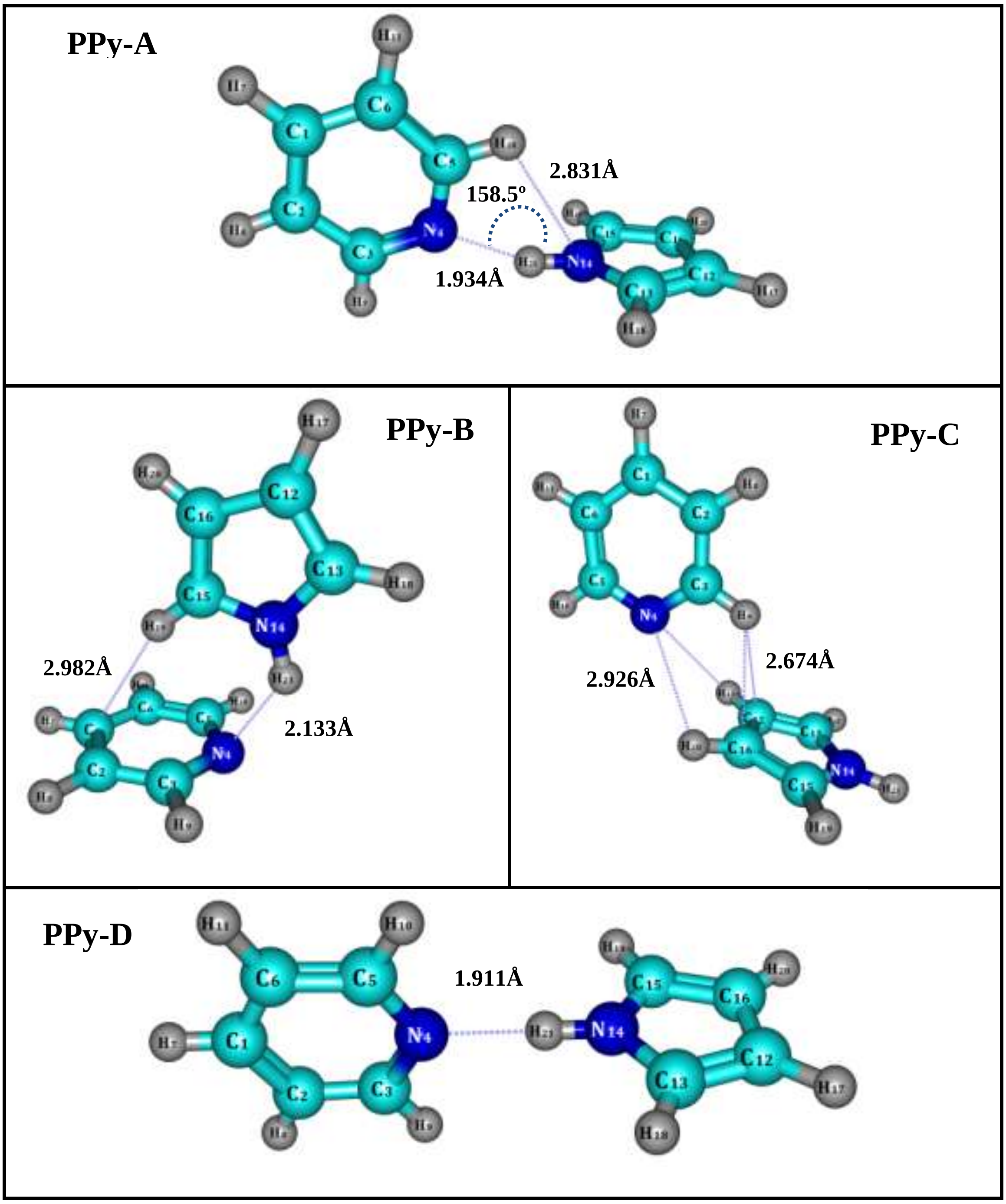

Figure 6.12 Structures of C_4H_5N-C_5H_5N heterodimers, PPy-A, PPy-B, PPy-C and PPy-D, optimized at MP2/aug-cc-pVDZ level of theory.

co-depositing the precursors followed by annealing (Figure 6.10). These bands with an average blue-shift of 84.7 in N_2 and 122.7 cm^{-1} in Ar, compares well with the computed shift of 95.1cm^{-1} for the global minimum PPy-A heterodimer (Table 6.4).

6.2.2.4 Vibrational Assignment in C-H bending mode of C_4H_5N

Figure 6.11 grids A and B show the C-H bending mode of C_4H_5N in N_2 and Ar matrixes respectively. Co-deposition of precursors and subsequent annealing indicated the formation of new spectral bands at 725.6, 724.1 cm^{-1} in N_2 and at 716.7, 715.0 cm^{-1} in Ar matrix. The bands showed a red-shift of -5.1 and -6.4 cm^{-1} in N_2 and Ar matrixes, respectively and match well with the computed red-shift of -4.7 cm^{-1} for the PPy-A heterodimer.

6.2.2.5 Higher Clusters of C_4H_5N-C_5H_5N

It is to be noted that features for the higher aggregates of C_4H_5N-C_5H_5N were not observed in the low temperature matrixes. In C_5H_5N, the absence of acidic hydrogen precludes the formation of C_5H_5N-clusters. Also, the formation of dimers or trimers of C_5H_5N was highly unlikely at the low concentrations used in our experiments. Hence, the higher clusters of C_4H_5N-C_5H_5N were not formed in matrixes.

6.2.3 Pyrrole···Quinoline

6.2.3.1 Experimental Results

Figure 6.13 grids A and B, traces ‘a’ and ‘b’ show the infrared spectra of bare C_4H_5N and C_9H_7N in N_2 and Ar matrixes, while the traces ‘c’ and ‘d’ show the spectra where the concentration of C_4H_5N has been kept constant but the concentration of C_9H_7N has been incremented gradually. Figure 6.14 shows the infrared spectra of the N-H bending region of C_4H_5N in N_2 matrix. C_9H_7N has no absorption in this region. As the concentration of C_9H_7N were varied, new features at 604.3/596.8 cm^{-1} with a blue-shift of ~77.0 cm^{-1} increase in intensity and matches with the computed shift of 101.0 cm^{-1} for the PQ-A heterodimer. No new features could be observed for the PQ-A heterodimer in Ar matrix.

Table 6.4 Comparison of experimental vibrational wavenumbers of the 1:1 heterodimers of C_4H_5N-$C_5H_5N$with computed wavenumbers at MP2/aug-cc-pVDZ Level of Theory.

Calculation		**Experimental**				**Mode Assignment**
		N_2 Matrix		Ar Matrix		
ν (cm^{-1})	**Δν**[a]	**ν (cm^{-1})**	**Δν**	**ν (cm^{-1})**	**Δν**	
			C_4H_5N			
514.9 (59)[a]	-	527.2/520.2	-	483.8/482.8/481.6	-	N-H bending-C_4H_5N
718.4 (176)	-	729.9	-	722.2	-	C-H bending-C_4H_5N
3672.4 (76)	-	3513.2	-	3520.2	-	N-H stretching-C_4H_5N
			C_5H_5N			
709.1 (57)	-	702.3	-	701.0	-	C-H bending-C_5H_5N
737.6 (17)	-	708.7	-	705.6	-	
			PPy-A			
610.0 (9)	95.1	611.8/610.8/602.6	84.7[c]	611.6/599.3	122.7[c]	N-H bending-C_4H_5N
713.7 (111)	-4.7	725.6/724.1	-5.1[c]	716.7/715.0	-6.4[c]	C-H bending-C_4H_5N
3383.4 (1166)	-289.0	3264.7/3251.7/3242.6	-260.2[c]	3266.7/3239.2	-267.3[c]	N-H stretching-C_4H_5N
610.0 (9)	95.1	611.8/610.8/602.6	84.7[c]	611.6/599.3	122.7[c]	N-H bending-C_4H_5N
711.7 (43)	2.6	-[c]	-	-[c]	-	C-H bending-C_5H_5N
741.6 (25)	4.0	-[c]	-	-[c]	-	

[a] $\Delta\nu = \nu_{heterodimer} - \nu_{monomer}$.

[b] Intensities (in km mol^{-1}) are given in parenthesis.

[c] Average of multiplet experimental wavenumbers of the monomers and multimers were taken to compute the experimental shift in the heterodimers.

[d] Experimental features were not observed.

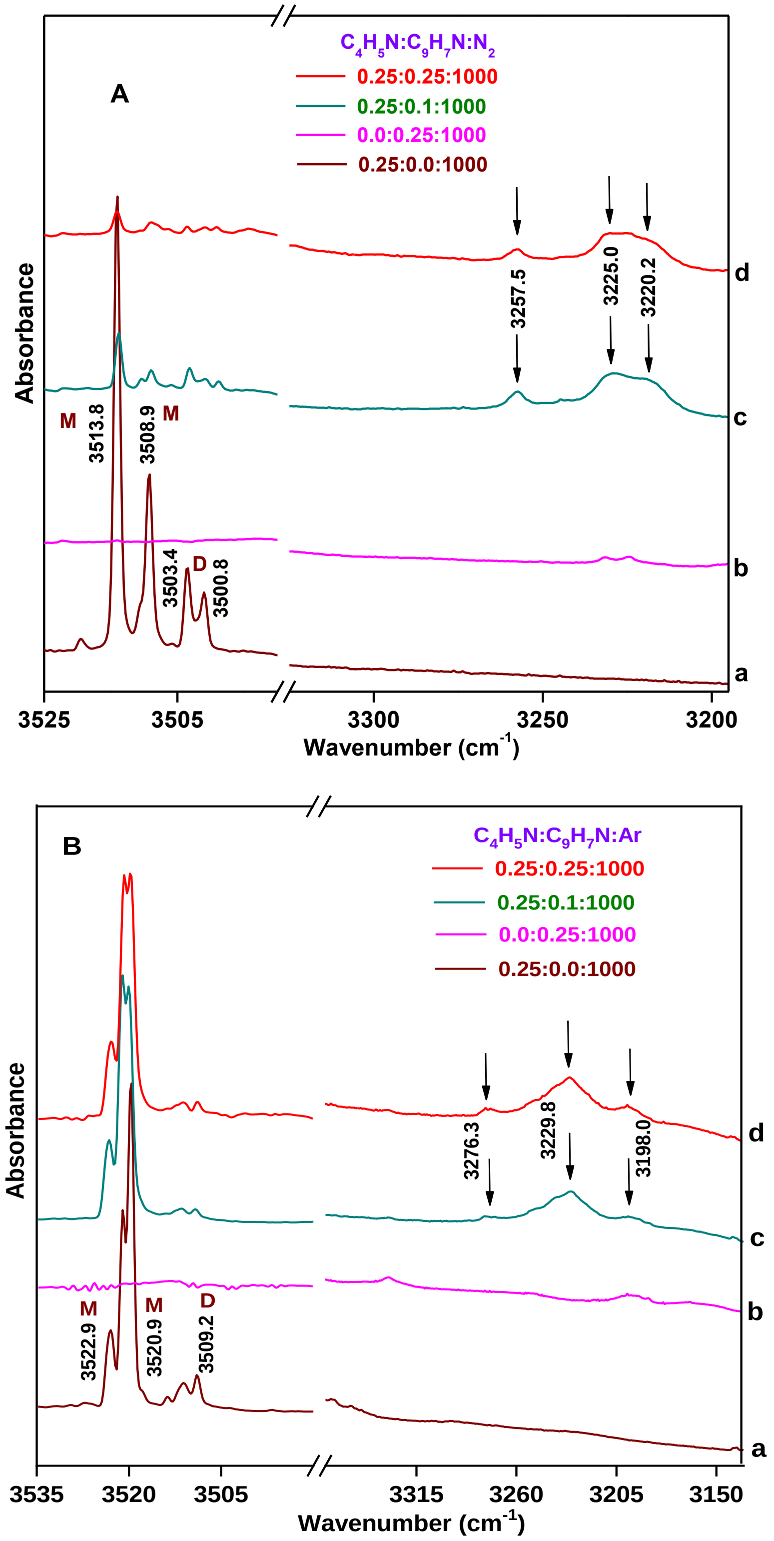

Figure 6.13 Infrared spectra correspond to the N-H stretching region of C_4H_5N in the heterodimers of (A) C_4H_5N-C_9H_7N in N_2 matrix, (B) C_4H_5N-C_9H_7N in Ar matrix. All the spectra shown above were annealed at 30 K (N_2) and 35 K (Ar).

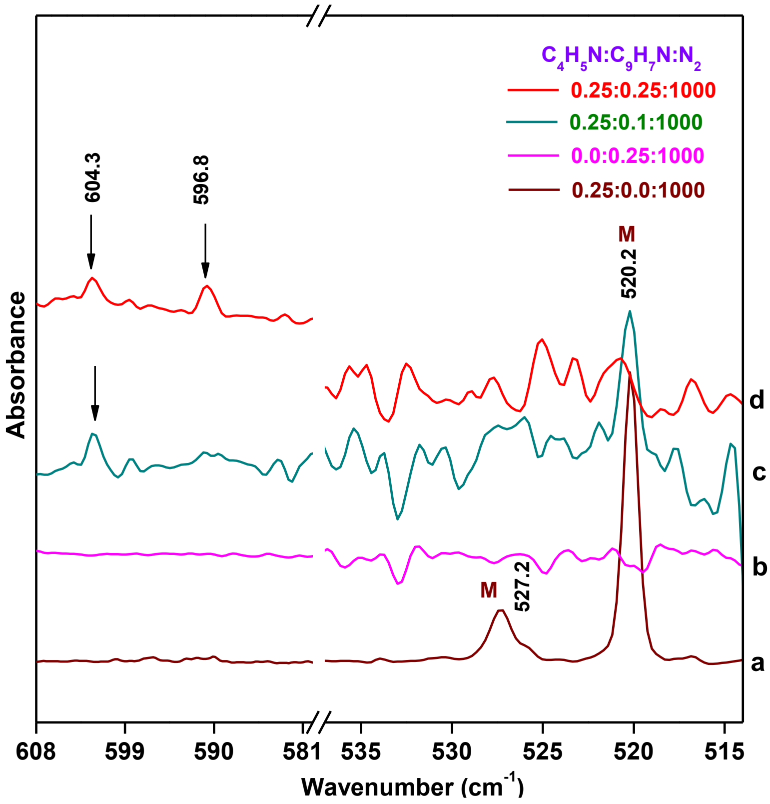

Figure 6.14 **Infrared spectra correspond to the N-H bending region of C_4H_5N in the heterodimers of C_4H_5N-C_9H_7N in N_2 matrix. All the spectra shown above were annealed at 30 K (N_2).**

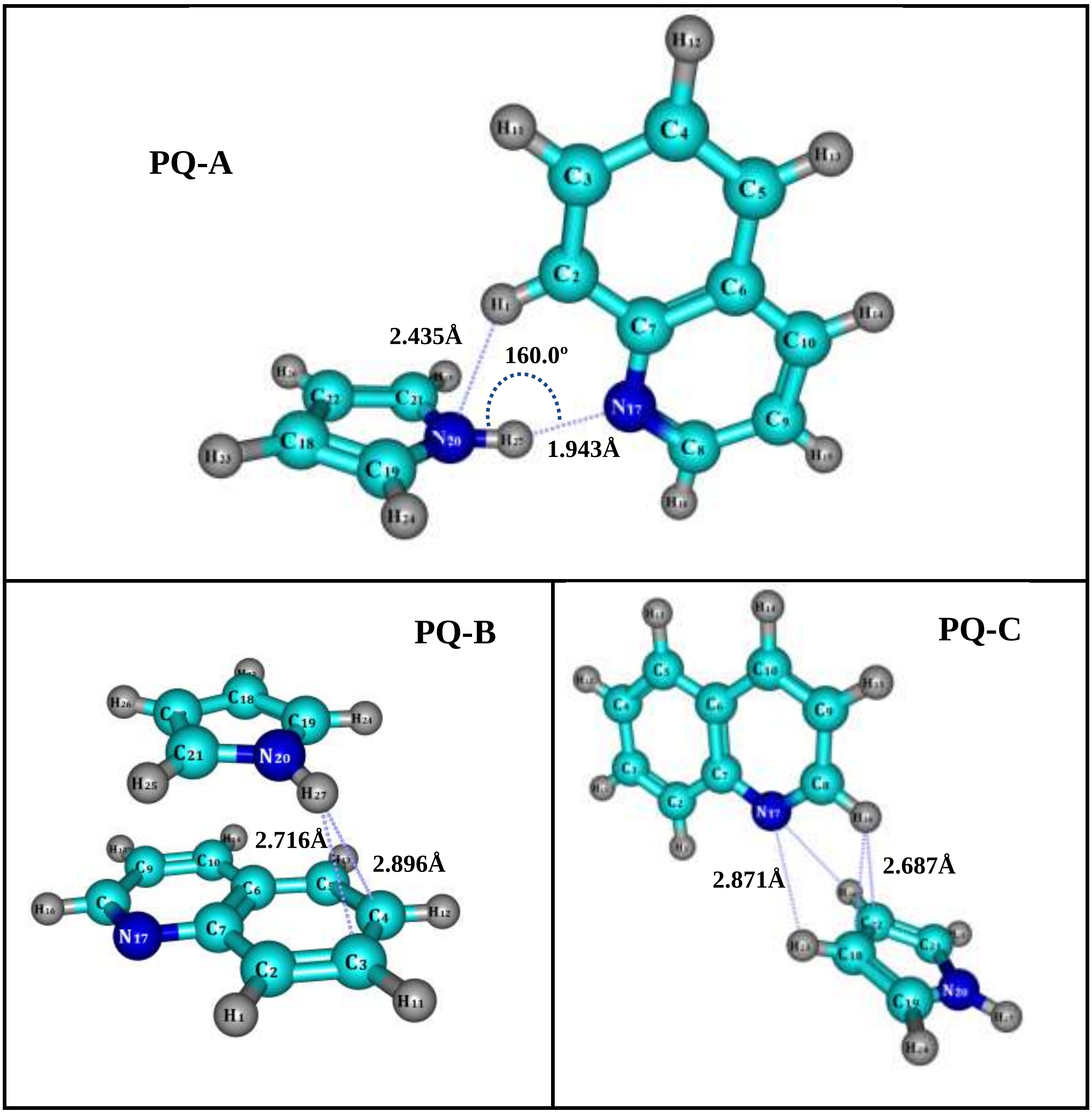

Figure 6.15 Structures of C_4H_5N-C_9H_7N heterodimers, PQ-A, PQ-B and PQ-C optimized at MP2/aug-cc-pVDZ level of theory.

Table 6.5 Stabilization energies ([a]Raw/[b]ZPE/[c]BSSE/[d]Reorg) and Gibbs free energy (ΔG) at 10 K of 1:1C_4H_5N-C_7H_9N heterodimers computed at MP2/aug-cc-pVDZ Level of Theory.

Heterodimers	**Stabilization energies**	**ΔG**
PQ-A	-11.41/-10.39/-8.56/-8.67	-10.18
PQ-B	-14.10/-13.44/-7.72/-8.14	-13.21
PQ-C	-4.96/-4.47/-2.59/-2.78	-4.26

[a] Raw interaction energies refer to energies not corrected for either ZPE or BSSE.
[b] ZPE -Zero point energy
[c] BSSE-Basis set superposition error
[d] Reorg-BSSE with Geometry optimization
All energies are in kcal mol^{-1}.

6.2.3.2 Computational Details

Three minima were accomplished for the 1:1 C_4H_5N-C_9H_7N heterodimer, with the global minimum structure corresponding to PQ-A heterodimer, having a strong N-H···N interaction between N17 of C_9H_7N and H27 of C_4H_5N with a bond distance of 1.943 Å. Due to this interaction, the change in N-H bond length of C_4H_5N submolecule was found to be 0.016 Å and computations indicated a red-shift of -311.7 cm^{-1} in the N-H stretching region from the C_4H_5N monomer. Furthermore, the bond angle of ∠N17-H27-N20 is 160.0º, favoring a secondary interaction between the H1 of C_9H_7N with N20 of C_4H_5N with a bond distance of 2.435 Å as shown in Figure 6.15. The first and second local minima PQ-B and PQ-C have N-H···π/π···π*, and C-H···N/C-H···π interactions, respectively. The stabilization energies of 1:1 C_4H_5N-C_9H_7N heterodimers are listed in Table 6.5.

There was a substantial deviation of linearity of N-H···N bond angle on moving from C_4H_5N-NH_3 to C_4H_5N-C_5H_5N and C_4H_5N-C_9H_7N. From a linear geometry with the ∠N-H···N angle of ~180˚ in PAm-A, the bond angle changed to ~158˚ in PPy-A to 160˚ in PQ-A, indicating the formation of a secondary interaction in the latter heterodimers.

6.2.3.3 Vibrational Assignment in v_1 and v_{16} modes of C_4H_5N

When C_4H_5N and C_9H_7N were co-deposited and annealed, new features were observed at 3257.5, 3225.0 and 3220.0 cm^{-1} in N_2 matrix and in Ar matrix at 3276.3, 3229.8 cm^{-1} (Figure 6.13). These shifts compare well with the computed red-shift of -311.7 cm^{-1} for the 1:1 C_4H_5N-C_9H_7N PQ-A heterodimer (Table 6.6). It is interesting to observe that the PPy-A and PQ-A heterodimers have both N-H···N as well as C-H···N interactions, further, the pattern of the infrared spectra for the heterodimer indicators in this mode looks alike, which shows that the two heterodimers have structural similarities, and the broadening could be due to a dispersed distribution of nearly equivalent classes of oscillators [14].

Figure 6.14 shows the infrared spectra of the N-H bending region of C_4H_5N in N_2

Table 6.6 Comparison of experimental vibrational wavenumbers of the 1:1 Heterodimers of C_4H_5N-C_9H_7N with computed wavenumbers at MP2/aug-cc-pVDZ Level of Theory.

Calculation		**Experimental**				**Mode Assignment**
		N_2 Matrix		**Ar Matrix**		
ν (cm^{-1})	**Δν[a]**	**ν (cm^{-1})**	**Δν[a]**	**ν (cm^{-1})**	**Δν[a]**	
C_4H_5N						
514.9 (59)[a]	-	527.2/520.2	-	483.8/482.8/ 481.6	-	N-H bending-C_4H_5N
718.4 (176)	-	729.9	-	722.2	-	C-H bending-C_4H_5N
3672.4 (76)	-	3513.2	-	3520.2	-	N-H stretching-C_4H_5N
C_9H_7N						
811.5 (81)	-	814.5	-	804.5	-	C-H bending-C_9H_7N
PQ-A						
615.9 (10)	101.0	604.3/596.8	77.0[c]	-[c]	-	N-H bending-C_4H_5N
717.2 (110)	-1.2	723.6/717.8	-9.5[c]	-[c]	-	C-H bending-C_4H_5N
3362.5 (1097)	-311.7	3225.0	-288.2	3229.8	-290.4	N-H stretching-C_4H_5N
816.0 (75)	4.2	-[c]	-	-[c]	-	C-H bending-C_9H_7N

[a] $\Delta\nu = \nu_{heterodimer} - \nu_{monomer}$.

[b] Intensities (in km mol^{-1}) are given in parenthesis.

[c] Average of multiplet experimental wavenumbers of the monomers and multimers were taken to compute the experimental shift in the heterodimers.

[d] Experimental features were not observed.

matrix. C_9H_7N has no absorption in this region. As the concentration of C_9H_7N was varied, new feature at 604.3/596.8 cm^{-1} with a blue-shift of ~77.0 cm^{-1} increase in intensity and matches with the computed shift of 101.0 cm^{-1} for the PQ-A heterodimer. No new features could be observed for the PQ-A heterodimer in Ar matrix.

It is important to point out that the secondary interaction (C-H···N) aids in the formation of the heterodimers, but it leads to a compromise on the strength of the N-H···N bond formation. Hence even if the proton affinities and binding energies of the heterodimers of pyridine and quinoline are higher than ammonia, the $\Delta\nu_{N\text{-}H}$ is somewhat similar and in N_2 matrix $\Delta\nu_{N\text{-}H(NH3)}$ exceeds that of $\Delta\nu_{N\text{-}H(C5H5N)}$.

6.3 Nature of Interaction

6.3.1 Atoms-in-Molecules Analysis

As mentioned in previous chapters, the aim of AIM analysis is to find the nature of interaction between the approaching molecules along the atomic interaction line through the presence of a *bcp*. From Table 6.7, the magnitude of $\rho(r_c)$ is found to increase from PAm-A to PPy-A to PQ-A, while the small positive value of $\nabla^2\rho(r_c)$ of the order ~ 10^{-2} a. u. signifies a closed shell type interaction. The increase of electron density at the bcp from PAm-A to PPy-A is around ~0.004 a. u., while that from PPy-A to PQ-A is only ~0.0002 a. u. Figure 6.16 illustrates the AIM plot of the heterodimers and PQ-A indicates an additional *bcp* and *rcp*, apart from the one *bcp* between the C_4H_5N -N-H and C_9H_7N-N.

6.3.2 Natural Bond Orbital Analysis

NBO analysis is a useful tool to understand the stabilizing charge-transfer hyperconjugative interactions prevailing between the two or more sub-molecules in a heterodimer. Table 6.8 lists the electron occupancies of the donor and acceptor orbitals and the second order perturbation energies (E_2 in kcal mol^{-1}) of the delocalization interactions of the PAm-A, PPy-A and PQ-A heterodimers. In all the heterodimers, the N-H···N is the

Table 6.7 Properties of (3,-1) bond critical point (BCP) of the heterodimers of Pyrrole with Ammonia, Pyridine and Quinoline computed at MP2/aug-cc-pVDZ Level of Theory.

Heterodimer	**Interaction**	**$\rho(r_c)$**	**$\nabla^2\rho(r_c)$**	**λ_1**	**λ_2**	**λ_3**
PAm-A	N-H…N	0.027139	0.07626	-0.034674	-0.033752	0.144686
PPy-A	N-H…N	0.030941	0.09131	-0.04099	-0.04097	0.173269
PQ-A	N-H…N	0.031168	0.08889	-0.041136	-0.040950	0.170981
	N…H-C	0.011978	0.03564	-0.009864	-0.009182	0.054691

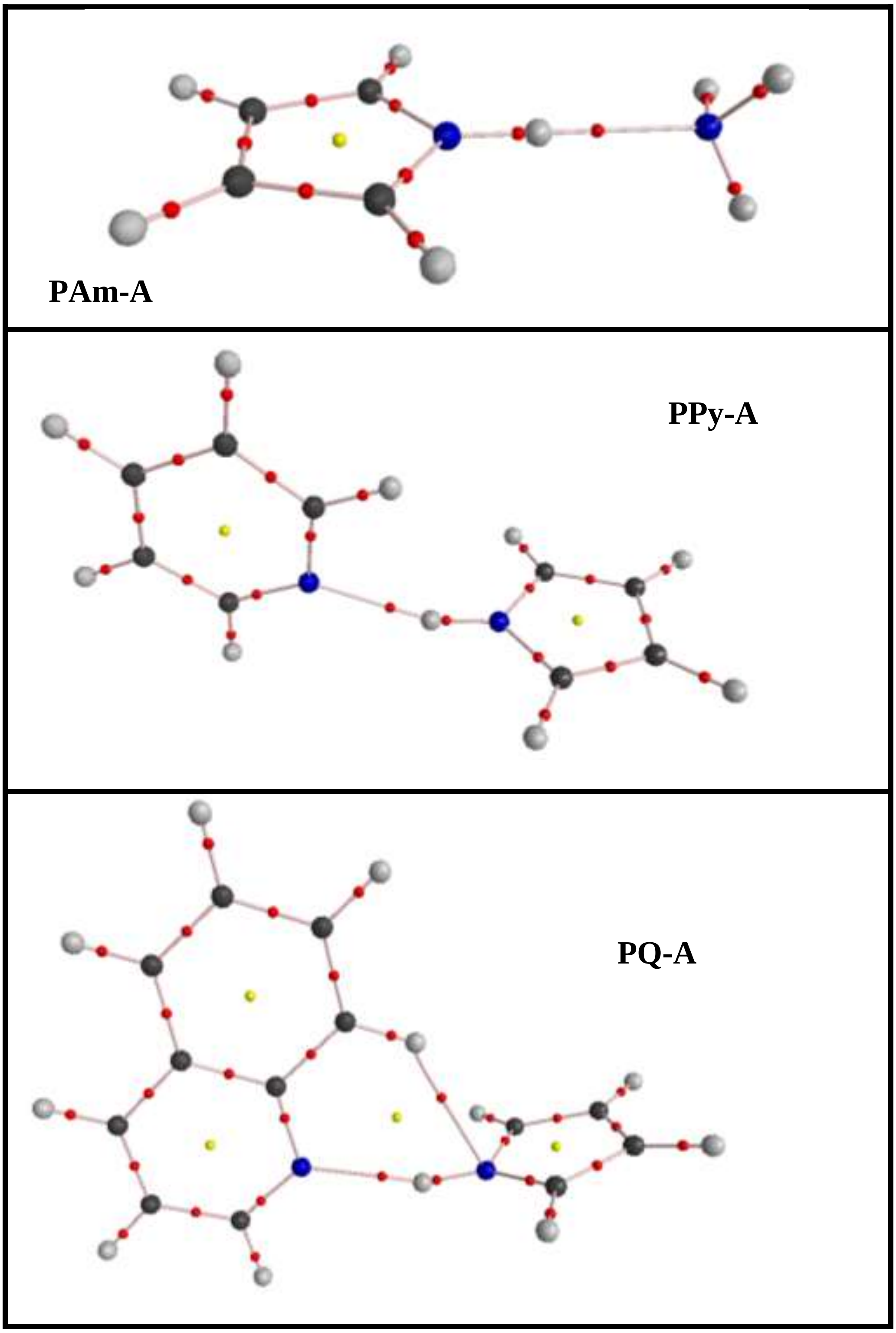

Figure 6.16 AIM plot of the global minimum heterodimers of C_4H_5N-NH_3 (PAm-A), C_4H_5N-C_5H_5N (PPy-A) and C_4H_5N-C_9H_7N (PQ-A) computed at MP2/aug-cc-pVDZ level of theory.

Table 6.8 Electron occupancies of various NBOs of 1:1 Pyrrole-Ammonia, Pyrrole-Pyridine and Pyrrole-Quinoline heterodimers computed at MP2/aug-cc-pVDZ level of theory. The donor-acceptor delocalization interaction and second order perturbation energies (E_2, kcal mol^{-1}) are also shown.

NBO	Occupancy	Donor-acceptor delocalization interaction	E_2
PAm-A			
σ*(N15-H22)	0.03841(0.01370)	n^1(N1)→σ*(N7-H14)	21.23
n^1(N1)	1.96806(1.99530)		
PPy-A			
σ*(N14-H21)	0.03726(0.01370)	n^1(N4)→σ*(N14-H21)	17.41
n^1(N14)	1.60158(1.63057)	n^1(N14)→σ*(C5-H10)	0.19
n^1(N4)	1.92499(1.94346)		
PQ-A			
σ*(N20-H27)	0.03997(0.01370)	n^1(N17)→σ*(N20-H27)	18.19
n^1(N20)	1.60253(1.63057)	n^1(N20)→σ*(H1-C2)	1.05
n^1(N17)	1.92182(1.94213)		

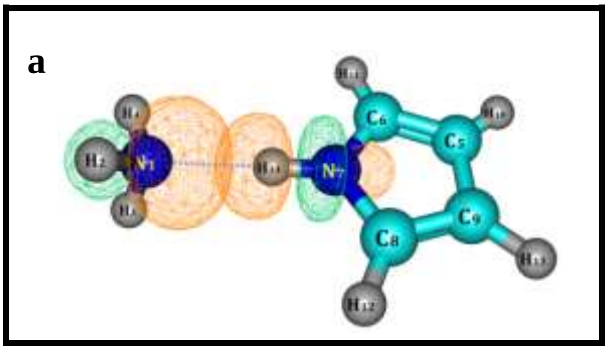

$n^1(N1)\rightarrow\sigma^*N7\text{-}H14 = 21.23$ kcal mol^{-1}

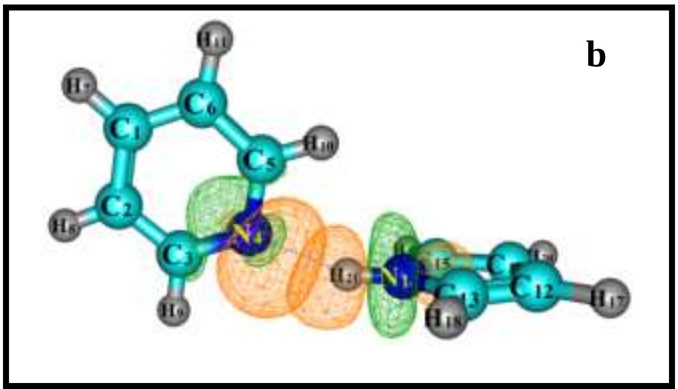

$n^1(N4)\rightarrow\sigma^*N14\text{-}H21 = 17.41$ kcal mol^{-1}

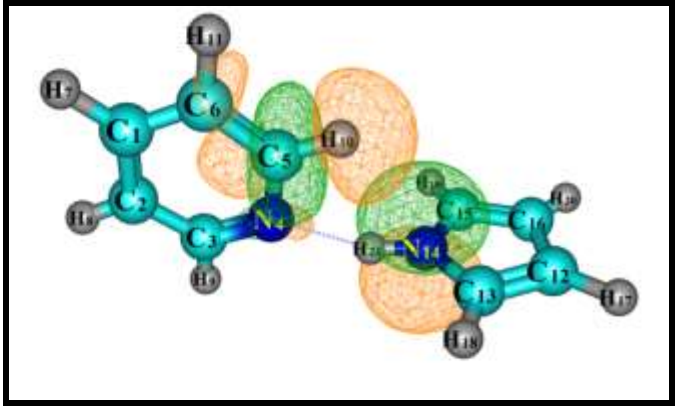

$n^1(N14)\rightarrow\sigma^*C5\text{-}H10 = 0.19$ kcal mol^{-1}

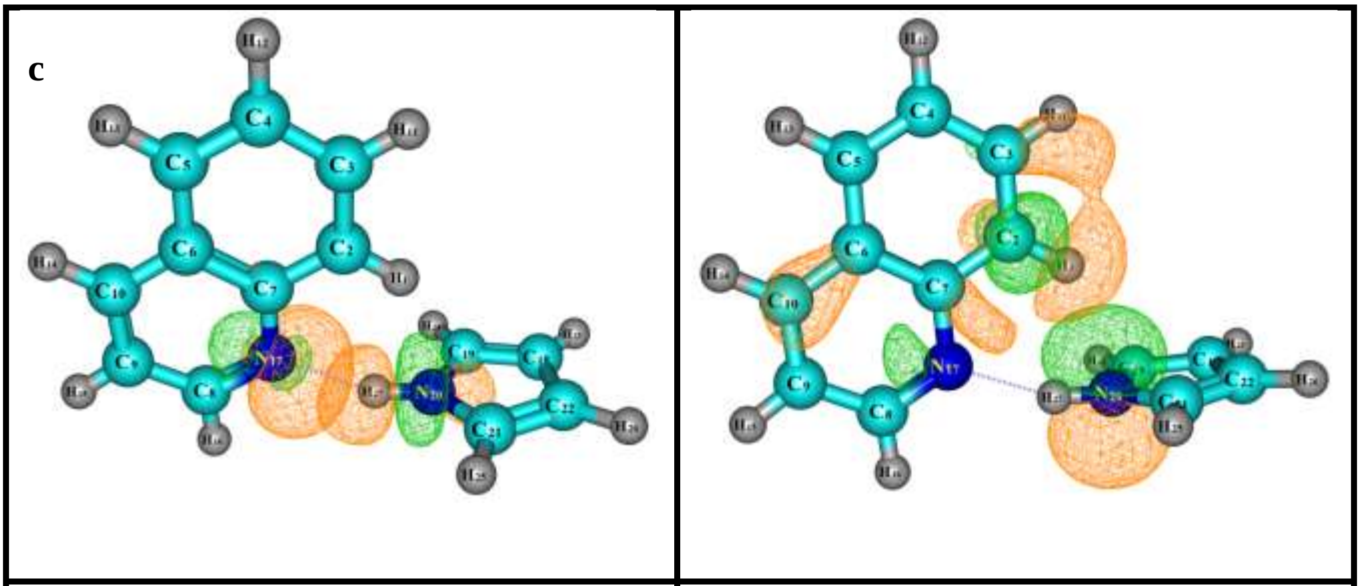

$n^1(N17)\rightarrow\sigma^*(N20\text{-}H27) = 18.19$ kcal mol^{-1}

$n^1(N20)\rightarrow\sigma^*(H1\text{-}C2) = 1.05$ kcal mol^{-1}

Figure 6.17 Natural bond orbitals of the interacting orbitals have been presented for the heterodimers (a) C_4H_5N-NH_3 (PAm-A), (b) C_4H_5N-C_5H_5N (PPy-A), (c) C_4H_5N-C_9H_7N (PQ-A) along with the second order perturbation energy at MP2/aug-cc-pVDZ level of theory.

primary interaction, and due to this interaction, the magnitude of electron occupancies of σ*(N-H) of C_4H_5N in the heterodimer is higher than the C_4H_5N monomer, and the corresponding electron occupancies of the lone pair of nitrogen in ammonia, pyridine and quinoline is lower than the corresponding monomers. As a consequence of this hyperconjugative interaction, there is a lengthening of N-H bond length with the corresponding red-shift in the N-H mode of C_4H_5N sub-molecule in all the heterodimers. The E_2 energies of this hyperconjugative interaction is 21.23, 17.41 and 18.19 kcal mol^{-1}, respectively for the PAm-A, PPy-A and PQ-A heterodimers, respectively. For the PPy-A and PQ-A heterodimers, apart from the primary N-H···N interaction, there is a secondary C-H···N interaction, the E_2 energies of n^1(N14)→σ*(C5-H10) and n^1(N20)→σ*(C2-H1) interaction are 0.19 and 1.05 kcal mol^{-1} respectively. Figure 6.17 shows the orbital picture of the hyperconjugative interactions prevailing in the PAm-A, PPy-A and PQ-A heterodimers.

6.3.3. Energy Decomposition Analysis

The energy decomposition analysis was performed on the optimized geometry (MP2/aug-cc-pVDZ) of PAm-A, PPy-A, and PQ-A heterodimers at B3LYP-D3/TZ2P level of theory using ADF-2016 package. Figure 6.18 shows the bar graph of the attractive (electrostatic, dispersion, and charge transfer) and repulsive (Pauli-repulsion) contributions to the total bonding energies of the 1:1 heterodimers. As can be seen from the graph that the stabilizing contributions from electrostatic interaction is maximum for all the 1:1 heterodimer followed by charge transfer and dispersion interactions. NBO analysis also revealed the hyperconjugative interaction between the non-bonding electrons on nitrogen of NH_3, C_5H_5N and C_9H_7N with antibonding orbital of N-H of C_4H_5N is quite dominant in all the 1:1 heterodimer. Among the 1:1 heterodimer, Pauli repulsion contribution is significantly larger for PQ-A heterodimer, which is likely due to the approach of two bulkier groups in forming this heterodimer.

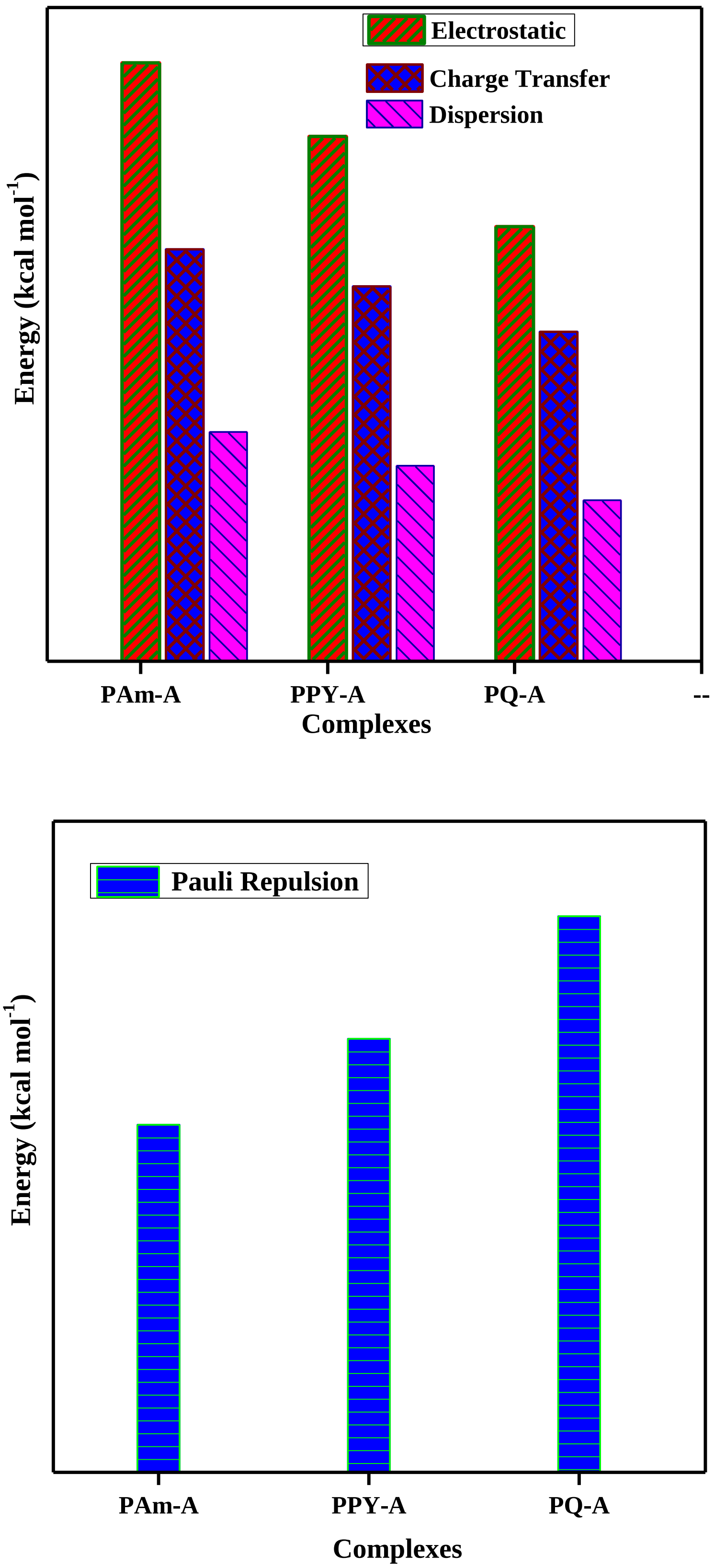

Figure 6.18 Bar graph showing the electrostatic, exchange, dispersion and Pauli repulsion contribution to the total binding energy of the C_4H_5N with NH_3, C_5H_5N and C_9H_7N heterodimers computed at B3LYP-D3/TZ2P level of theory.

6.4 Summary

The 1:1 heterodimer of C_4H_5N with NH_3, C_5H_5N and C_9H_7N, stabilized by N-H···N interaction are trapped and studied using matrix isolation infrared spectroscopy. In case of C_4H_5N with NH_3, the NH_3 higher clusters $(NH_3)_n$ [n = 1, 2, 3, 4] were found to form heterodimers with C_4H_5N and $(C_4H_5N)_2$, in low temperature inert matrixes. Computations performed at MP2/aug-cc-pVDZ level of theory gave five, four and three minima for the $C_4H_5N \cdots NH_3$, $C_4H_5N \cdots C_5H_5N$ and $C_4H_5N \cdots C_9H_7N$ heterodimers, respectively, while nine structures were optimized for the $C_4H_5N \cdots NH_3$ higher aggregates. NBO analysis revealed the hyperconjugative charge transfer interaction between the lone pair of electrons on nitrogen of NH_3, C_5H_5N and C_9H_7N to the antibonding N-H orbital of pyrrole. In $C_4H_5N \cdots C_5H_5N$ and $C_4H_5N \cdots C_9H_7N$ heterodimers, an additional cooperative strength was provided by the C-H···N interaction. EDA analysis showed that electrostatic interaction was the dominant interaction followed by charge transfer, leading to the N-H···N interaction in the global minimum heterodimers.

On comparing the various computed parameters with the experimental shifts (Table 6.9), it was found that there was a steady increase of computed wavenumber shift from PAm-A to PPy-A to PQ-A, which was reflected in the experimental wavenumber shifts in Ar matrix. But the wavenumber shift in N_2 matrix was highest for PAm-A, followed by PQ-A and PPy-A. The reason could be the effect of nitrogen matrix on the guest molecules and so on the PAm-A heterodimer, leading to a stronger bonding, thus a higher shift. Such observation was also seen in the heterodimer of pyrrole with methnol (PM-A) in Chapter 5. The pattern in the increment of shifts from PAm-A< PPy-A< PQ-A, correlates with the trend of the BSSE corrected binding energies, change in the N-H bond length and electron densities at the intermolecular bond critical points. However the second order perturbation energy is seemingly highest for PAm-A, followed by PQ-A and PPy-A. The interacting angle ∠N-H-N is ~180˚ , while that for PPy-A and PQ-A are 158.5° and 160°, respectively. Hence a linear geometry was responsible for a better overlap of orbitals and thus higher charge transfer in PAm-A heterodimer.

Table 6.9 Comparison of some selected computed parameters of C_4H_5N with NH_3, C_5H_5N, and C_9H_7N with Experimental Shift in N_2 and Ar Matrixes. Computations were performed at MP2/aug-cc-pVDZ Level of Theory.

Heterodimers	[a]$\Delta\nu_{N-Hstr(calc)}$	[b]$\Delta\nu_{N-Hstr(N2)}$	[c]$\Delta\nu_{N-Hstr(Ar)}$	[d]$d_{N-H\cdots N}$	[e]Δr_{N-H}	[f]ΔS.E.	[g]E_2	[h]ρ_{bcp}
PAm-A	-265.5	-291.2	-263.8	1.426	1.999	-6.61	21.23	0.0271
PPy-A	-289.0	-260.2	-267.3	1.539	1.934	-8.00	17.14	0.0309
PQ-A	-311.7	-288.2	-290.4	1.652	1.943	-10.18	18.19	0.0312

[a] $\Delta\nu_{N-H(calc)} = \nu_{N-H(heterodimer)} - \nu_{N-H(monomer)}$ at MP2/aug-cc-pVDZ.
[b] $\Delta\nu_{N-H}$ (N_2) = $\nu_{N-H(heterodimer)} - \nu_{N-H(monomer)}$ in N_2 matrix in cm^{-1}.
[c] $\Delta\nu_{N-H}$ (Ar) = $\nu_{N-H(heterodimer)} - \nu_{N-H(monomer)}$ in Ar matrix cm^{-1}.
[d] H-Bond distance (Å).
[e] $\Delta r_{(N-H)} = r_{heterodimer} - r_{monomer}$ (picometer)
[f], S.E. (BSSE) = Basis set superposition error corrected stabilisation energy in kcal mol^{-1}.
[g] E_2 = Second order perturbation energy in kcal mol^{-1} obtained from NBO Analysis.
[h] Electron Density in a. u. obtained from AIM Analysis.

References

---

1. Self-Aggregation in Pyrrole: Matrix Isolation, Solid State Infrared Spectroscopy, and DFT Study, A. Gomez-Zavaglia, R. Fausto, *J. Phys. Chem. A*, **2004**, 108, 6953-6967.

2. Vibration–Rotation Bands of Ammonia: II. The Molecular Dimensions And Harmonic Frequencies Of Ammonia And Deuterated Ammonia, J. A. Cugley, A. D. E. Pullin, *Spectrochimic. Acta*, **1975**, 29A, 1665-1672.

3. Matrix infrared and Raman spectra of the inequivalent submolecules in the ammonia dimer, J. P. Perchard, R. B. Bohn, L. Andrews, *J . Phys. Chem*., **1991**, 95, 2707-2712.

4. Identification of ammonia clusters in low-temperature matrixes using the FTIR short-pulsed matrix isolation technique, T. Nishiya, N. Hirota, H. Shinohara, N. Nishi, *J. Phys. Chem*., **1985**, 89, 2260-2264.

5. Identification of ammonia clusters in low-temperature matrixes using the FTIR short-pulsed matrix isolation technique, P. E. Janeiro-Barral, M. Mella, *J. Phys. Chem. A*, **2006**, 110, 11244-11251.

6. Study on structures and properties of ammonia clusters (NH3)n (n=1–5) and liquid ammonia in terms of *ab initio* method and atom-bond electronegativity equalization method ammonia-8*P* fluctuating charge potential model, L. Yu, Z. Z. Yang, *J. Chem. Phys*., **2010**, 132, 174109.

7. Complex between water and ammonia, B. Nelander, L. Nord, *J. Phys. Chem*. **1982**, 86, 4375-4379.

8. Infrared spectra of ammonia suspended in solid nitrogen, G. C. Pimentel, M. O. Bulanin, M. Van Thiel, *J. Chem. Phys*., **1962**, 36, 500-506.

9. Rotational tunnelling and ammonia sites in Ar and N2 matrixes, M. Havighorst, M. Prager, W. Langel, *Physica B*, **1992**, 180 & 181, 674-676.

---

10. Vibration–Rotation Bands of Ammonia: II. The Molecular Dimensions And Harmonic Frequencies Of Ammonia And Deuterated Ammonia, J. A. Cugley, A. D. E. Pullin, *Spectrochimic. Acta*, **1975**, 29A, 1665-1672.

11. Infrared Spectra of Crystalline and Matrix Isolated Pyridine and Pyridine-D5, E. Castellucci, G. Sbrana, F. D. Verderame, *J. Chem. Phys.*, **1969**, 51, 3762-3770.

12. An infrared Study of Pyridine-Pyridine and Pyridine-H_2O Interactions by the Matrix Isolation Method, G. Maes, *Bull. Soc. Chim. Belg*., **1981**, 90, 1093-1107.

13. Matrix isolation FT-IR studies and ab initio calculations of hydrogen-bonded complexes of molecules modeling cytosine or isocytosine tautomers. 1. Pyridine and pyrimidine complexes with water in argon matrixes, A. Destexhe, J. Smets, L. Adamowicz, G. Maes, *J. Phys. Chem.*, **1994**, 98, 1506-1514.

14. Incremental NH stretching downshift through stepwise nitrogen complexation of pyrrole: a combined jet expansion and matrix isolation study, S. Oswald, M. A. Suhm, S. Coussan , *Phys. Chem. Chem. Phys*., **2019**, 21, 1277-1284.

List of Keywords in Thesis

1. Hydrogen Bonding
2. Pyrrole
3. Acetylene
4. Ethylene
5. Benzene
6. Water
7. Methanol
8. Diethyl ether
9. Phenol
10. Ammonia
11. Pyridine
12. Quinoline
13. N-H···π
14. N-H···O
15. N-H···N
16. π ···π*
17. Weak interactions
18. Strong Interactions
19. *ab initio* Computations
20. Matrix Isolation Infrared Spectroscopy

Thesis Highlight

Name of the Student: Shubhra Sarkar

Name of the CI/OCC: Indira Gandhi Centre for Atomic Research

Enrolment No.: CHEM 02 201504010

Thesis Title: N-H···X (X=O, N, π) Hydrogen-bonded Interactions of Pyrrole: Matrix Isolation Infrared and Computational Studies

Discipline: Chemical Sciences; **Sub-Area of Discipline:** Matrix Isolation Infrared Spectroscopy

Date of viva voce: 15-03-2021

Hydrogen bonding is ubiquitous and one of the most important non-covalent interactions. In diverse biological systems, the nitrogenous compounds are omnipresent and as an example, the derivatives of pyrrole are found in haemoglobin, chlorophyll, alkaloids, tryptophan and proteins.

One of the highlights of this thesis is to study the spectroscopic properties of pyrrole monomer and multimers in N_2 and para-hydrogen (p-H_2) matrices and compare the vibrational wavenumbers of the pyrrole aggregates in different matrices (Ne, Ar, Xe and Kr) with the gas phase spectra.

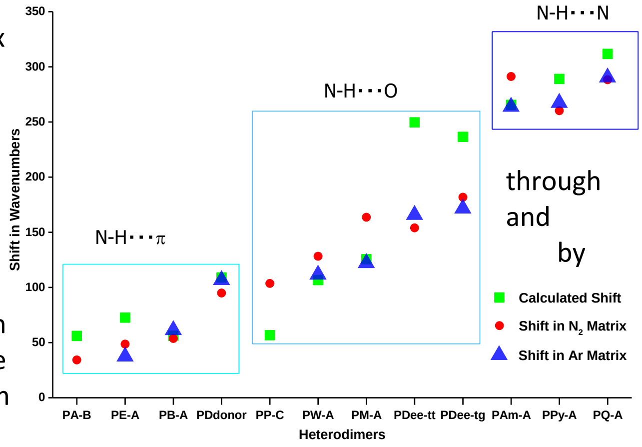

Figure 1 The graph depicting shift in wavenumber against the heterodimers of pyrrole with benzene, ethylene, acetylene, phenol, water, methanol, diethyl ether, ammonia, pyridine and quinoline shows there is a gradual increase of computed and experimental vibrational shifts from the N-H···π →N-H···O →N-H···N complexes, clearly demonstrating the strength of the dimers follows the order weak →moderate →strong.

Secondly, hydrogen bonding interactions of pyrrole with different bases are explored using matrix isolation infrared spectroscopy supported by *ab initio* computations. The N-H···π interaction is studied in pyrrole-acetylene, pyrrole-ethylene and pyrrole-benzene systems. The N-H···O interaction is probed through interaction of pyrrole with water, methanol, phenol and diethyl ether and the N-H···N interaction is explored by interacting pyrrole with ammonia, pyridine and quinoline. In all the systems, the global minimum complexes are primarily stabilized by N-H···X (where X= π, O, N) interaction and the local minimum geometries are stabilized by C-H···π, π···π* and O-H···π interactions. Among the N-H···π complexes, pyrrole dimer shows the highest shift in N-H stretching vibrational wavenumber followed by PB-A, PP-B, PE-A and PA-B. The strong pyrrole dimer shows highest shift, while the weakest complex PA-B shows the lowest in both Ar and N_2 matrices. Comparison of the various computed parameters with experimental vibrational wavenumbers of the N-H···O complexes of pyrrole revealed that the successive replacement of the protons of water with alkyl group leads to the strengthening of the N-H···O hydrogen bond whereas the substitution of phenyl group weakens the interaction. Hence PP-C is the weakest complex, while py-DEE-*tt/tg*$^{\pm}$ is the strongest complex. In case of N-H···N complexes, computations indicated that the magnitude of computed shift ($\Delta\nu_{N\text{-}H}$) in the vibrational wavenumber follows the order PQ-A >PPy-A >PAm-A. Experimentally, the above trend resonates in Ar matrix, but in N_2 matrix, due to the interaction of matrix with the complexes a deviation was observed. It is experimentally observed that among the different types hydrogen bonding interactions of pyrrole studied in this thesis, the N-H···N type of interaction was the strongest, N-H···O is the moderate and N-H···π is the weakest hydrogen bonded interaction.